PALACKÝ UNIVERSITY

DEPARTMENT OF PHYSICAL CHEMISTRY

OLOMOUC

Structural, electronic, and magnetic properties of nanomaterials for potential magnetic, energy storage, and catalytic applications

Mgr. Rostislav Langer

A thesis is submitted in fulfillment of the requirements for the degree of
Doctor of Philosophy

Supervisor: doc. Mgr. Piotr Błoński, Ph.D.

Olomouc 2022

Declaration

I declare that I elaborated my dissertation independently under the supervision of doc. Mgr. Piotr Błoński, Ph.D., and all sources are included in the bibliography. Neither the thesis nor any of its parts was previously used for obtaining any academic degree.

In Olomouc, date: 12. 08. 2022

Mgr. Rostislav Langer

Acknowledgement

A huge acknowledgement goes to my supervisor doc. Mgr. Piotr Błoński, Ph.D. for his time, patience, attitude, valuable advice, and leadership during the studies.

I would like to thank prof. RNDr. Michal Otyepka, Ph.D. for valuable advice, recommendation, and for giving me the opportunity to participate in several projects.

Many thanks to all the colleagues who participated in joint projects.

V neposlední řadě bych chtěl poděkovat mé rodině za podporu při mém studiu.

Bibliographical identification

Author:	Mgr. Rostislav Langer
Title:	Structural, electronic, and magnetic properties of nanomaterials for potential magnetic, energy storage, and catalytic applications
Type of Thesis:	Dissertation
Department:	Department of Physical Chemistry, UP Olomouc
Supervisor:	Doc. Mgr. Piotr Błoński, Ph.D.
The year of presentation:	2022
Keywords:	graphene derivatives, DFT, magnetism with and without transition metals, electronic structure, single-atom catalysts, supercapacitors, lithium-ion batteries
Number of Pages:	235
Language:	English

List of abbreviations

two-dimensional	2D
single atom	SA
single-atom catalysis	SAC
lithium-ion-batteries	LIBs
supercapacitors	SCs
fluorographene	FG
fluorinated graphenes	FGs
cyanographene	G–CN
single-atom catalysts	SACs
graphene acid	G–OOH
room temperature	RT
magnetic anisotropy energy	MAE
transition metal	TM
spin-orbit coupling	SOC
one-dimensional	1D
metal-oxide-silicon field-effect transistor	MOSFET
Information Technology	IT
scanning tunneling microscope	STM
carbon nanotubes	CNTs
zero-dimensional	0D
carbon dots	CDs
transition metal dichalcogenides	TMDCs
solid-state drives	SSD
hard disc drives	HDDs

magnetoresistance	MR
giant magnetoresistance	GMR
ferromagnetic	FM
non-magnetic	NM
tunneling magnetoresistance	TMR
magnetic tunnel junction	MTJ
magneto-electric spin–orbit logics	MESOs
torque nano-oscillators	STNOs
magnetic random-access memory	MRAM
information and communication technology	ICT
bit-patterned media	BPM
Rudermann–Kittel–Kasuya–Yoshida	RKKY
density of states	DOS
Fermi level	E_F
hydroxofluorographenes	GOHF
paramagnetic	PM
antiferromagnetic	AFM
density functional theory	DFT
single molecule magnets	SMMs
single-chain magnets	SCMs
atomic force microscopy	AFM
three-dimensional	3D
scanning probe microscopy	SPM
N-doped graphene acid	N-G–OOH
oxygen reduction reaction	ORR
Standard Oil of Ohio	SOHIO

Nippon Electric Company	NEC
lithium–sulfur batteries	LSBs
arginine	Arg
Schrödinger equation	SE
Hartree-Fock	HF
Thomas-Fermi	TF
scanning transmission electron microscopy	STEM
spin-polarized density functional theory	SP-DFT
graphene oxide	GO
chemical vapor deposition	CVD
near edge X-ray absorption spectroscopy	NEXAFS
generalized gradient approximation	GGA
Monte Carlo	MC
metal-organic-frameworks	MOF
ferrimagnetic	FIM
bond dissociation energy	BDE
nearest-neighbor	NN
graphene nanoribbons	GNRs
graphene nanoflakes	GNFs
graphene quantum dots	GQDs
scanning tunnelling spectroscopy	STS
electron paramagnetic resonance	EPR
nearest-neighbor	NN
Bethe-Peierls-Weiss	BPW
mean-field approximation	MFA
cluster mean-field	CMF

correlated cluster mean-field	CCMF
quantum Monte Carlo	QMC
high-temperature series-expansion	HTSE
self-consistent field	SCF
Hohenberg–Kohn	HK
Kohn-Sham	KS
Kohn-Sham equations	KSE
Born-Oppenheimer	BO
local density approximation	LDA
homogeneous electron gas	HEG
local spin density approximation	LSDA
Vienna Ab-initio Simulation Package	VASP
long-range-corrected	LC
periodic boundary condition	PBC
Brillouin zone	BZ
projected augmented wave	PAW
full-linearized augmented-plane-wave	FLAPW
the natural bond orbital	NBO
climbing image nudged elastic band	CI-NEB
phosphorus doped graphene	Gr-P
adsorbed P adatoms onto graphene	Gr-adP
spin-polarized scanning tunnelling spectroscopy	SP-STS
partial densities of states	PDOS
high resolution-transmission electron microscopy	HR-TEM
high-angle annular dark-field-STEM STEM	HAADF-

energy-dispersive spectroscopy	EDS
high-resolution photoelectron spectroscopy	HR-XPS
atomic absorption spectroscopy	AAS
X-ray photoelectron spectroscopy	XPS
cyclic voltammetry	CV
electrochemical impedance spectroscopy	EIS
van der Waals	vdW
random phase approximation	RPA
Lifshitz−Zaremba−Kohn	LZK
adiabatic connection and fluctuation dissipation theorem	ACFDT
polyaromatic hydrocarbons	PAHs
paramagnetic	PM
nuclear magnetic resonance	NMR
galvanostatic charge/discharge measurements	GCD
cross polarization magic angle spinning	CP MAS
infra-red	IR
energy dispersive X-ray spectroscopy	EDXS
cyclic voltammograms	CV
1-ethyl-3-methylimidazolium tetrafluoroborate	EMIM-BF$_4$
1,1,2,2-tetrafluoroethyl-2,2,3,3-tetrafluoropropyl ether	TTE

Table of Contents

Preface

The traditional costly and time-consuming, trial-and-error experimental approaches to develop novel (nano)materials with desired properties are being complemented and often overtaken by new strategies based on a detailed understanding of the materials' properties down to the level of individual atoms with the help of theoretical modeling.

Graphene [1], a two-dimensional (2D) material comprising of covalently bound sp^2 carbon atoms arranged in a hexagonal (honeycomb) lattice sandwiched between two π-electron clouds, has attracted great interest because of its remarkable properties and numerous potential applications [2]–[5]. However, despite extensive research efforts, a limited number of graphene-based products have so far been successfully commercialized. The potential range of graphene applications can be greatly enhanced by covalent modification, including doping of the graphene lattice with foreign atoms [6], [7] and sp^3 functionalization [8]–[12].

The work presented here concerns modeling and theoretical description of graphene-based materials for potential applications in spintronics and information-storage, single-atom (SA) and molecular magnets, single-atom catalysis (SAC), lithium-ion-batteries (LIBs), and supercapacitors (SCs) **[13]–[18]**. There was a strong synergy between theory and experiments throughout the work. All references to the works I am a co-author are in **bold** throughout the text.

Fluorinated graphenes (FGs) are key precursors to the synthesis of many graphene derivatives, so a better comprehension of fluorographene (FG) reactivity and the nature of the C-F bond is key to unlocking the application potential of graphene-based materials **[19]**.

Indeed, understanding the mechanism of thermal decomposition of a fully fluorinated graphene in the presence of a reducing hydrogen atmosphere has helped to develop novel electrode materials for SCs aimed at practical applications **[20]**. Further, the radical-based chemistry of FG, which enables the combination of sp^2 and sp^3 carbon bonds in the same network, along with very high nitrogen doping and vacancies, has enabled the discovery of a new class of carbon-based materials comprising nitrogen doped graphene with diamond-like tetrahedral bonds for high energy-density SC electrodes, and with the help of theoretical modeling, the materials' properties has been better understood **[16]**.

Controllable atom substitution and defluorination of FG enables the synthesis of cyanographene (G–CN) [9], which has proven to be a perspective material for anchoring Pt

adatoms with potential implications as single-atom catalysts (SACs) **[15],** and the use of complex chemistry of −CN groups makes it possible to synthesize a wide range of graphene derivatives with a very high degree of functionalization, including graphene acid (G–OOH), which emerges as a stable and high-energy organic LIB anode material **[17]**.

The substitution of fluorine atoms in FG with hydroxyl groups **[21], [22]** and simultaneous doping of graphene by phosphorus atoms and its functionalization with P-containing groups **[13]** can lead to materials with magnetic features sustainable up to room temperature (RT), which creates perspectives for the design of metal-free graphene-based spintronic devices.

Doping of the graphene lattice with Fe and Mn atoms results in a high magnetic anisotropy energy (MAE) corresponding to a theoretical blocking temperature of 34 K assuming a relaxation time of 10 years, enhancing the application potential of graphene in spintronics, including data storage in magnets of the size of SAs **[14]**.

In porphyrin molecules with coordinated transition metal (TM) atoms, the ligand field coordinated with the central metal atom governs the magnetic anisotropy due to spin-orbit coupling (SOC) in a close analogy to the TM atoms anchored in N-decorated defects in the graphene lattice **[14],** [23]. The possibility of tailoring the magnetic state in such nanostructures is highly desirable for potential spintronic applications. Theoretical calculations revealed the mechanism of the MAE modification in Au(111) supported one-dimensional (1D) metalloporphyrin polymers depending on the structural conformations of the molecular units **[18]**.

The first part of this thesis, following the historical timeline of the most important milestones in the development of materials science, presents the main ideas behind the work. Afterwards, the studied materials and the theoretical methods applied in my research are described. Finally, the theoretical results of the six selected papers are discussed in more detail, along with the experiments carried out at the University of Vienna and the RCPTM in Olomouc. The appendices contain reprints of these papers that constitute the basis of the doctoral thesis.

Introduction

The development of material science in a nutshell

The history of mankind is contemporaneous with the evolution of tools and technology development, ultimately bringing our civilization to the point where we are today. In a nutshell, the earliest primitive tools made of stone date back 2.6 million years, ushering in the Stone age. Later, other raw materials like bones, antlers, or ivory were used. The turning point in the technological evolution of early humans was the control of fire 1.7–2.0 million years ago. Fire provided a source of warmth, heat for cooking food, and lighting, made it possible to create more advanced hunting tools and allowed for geographic dispersion of human, cultural innovations, and changes in diet and subsequently behavior.

The transition from the Stone Age to the Bronze Age occurred between 6000 and 2500 BC with the discovery of the ore smelting technique. The first evidence of human metallurgy dates to the 6th–5th millennium BC, and the first regions to enter the Bronze Age were West Asia and the Middle East, whose ancient peoples practiced year-round agriculture, developed writing systems, created centralized governments, economic and civil administration, social stratification, and slavery. They also laid the foundations for mathematics and astronomy.

Abundant terrestrial iron, due to its high melting point of 1811 K was out of common use until the end of the second millennium BC. The Iron Age begins when the production of iron or steel has reached the point where iron tools and weapons replace their bronze counterparts. The end of the Iron Age is generally considered to coincide from the Roman Conquests and last up to the Middle Ages about 500 AD.

For thousands of years, directions at sea were determined primarily by the position of celestial bodies. This changed with the emergence of the navigational compass in China in 11th century, which by about 1300 appeared in Europe and the Middle East. With a compass in hand, Europeans set sea routes to China, Japan, and the Indonesian Islands, and established the trade of tea, spices, silk, and, importantly, knowledge of that time. It was also the time when conquistadors encountered and destroyed the Aztec and Inca civilizations of Central and South America. The increase in sea travel and trade routes, made possible by the compass, led to European settlements in the Americas.

Another great technological and social change was brought by the Industrial Revolution in 1760–1840 triggered by the development of thermodynamics born out of a few important questions like: What is temperature? What is heat? Why do some reactions happen, and others do not? Is it possible to convert heat in useful energy? The practical impetus for development of the science of thermodynamics in the nineteenth century was the advent of heat engines. The increasing reliance on machines to do our work required better understanding of the basic principles underlying conversion of heat to work, thermodynamic laws, thermodynamic cycles and, interestingly, led to abstract ideas like entropy.

The eighteenth and nineteenth century also brought great discoveries in the field of electricity and magnetism. In 1752, Benjamin Franklin tied a kite on string during a thunderstorm and proved that static electricity and lightning are one and the same. Following this important experiment, people were eager to tame the power of electricity primary for lighting their homes in a cheap and safe way trying to replace flammable and dangerous oil and gas lamps. In 1758, Charles-Augustin de Coulomb presented three reports discussing the interaction between the two electrified bodies, explained the attraction and repulsion between electric charges and magnetic poles.

In 1800, Alessandro Volta constructed the first battery. The discovery of Hans Christian Ørsted on April 21, 1820, showing that an electrical current moves a compass needle, and several weeks later by André-Marie Ampère and François Arago showing that the current-carrying coil was equivalent to a magnet, launched the electromagnetic revolution. By demonstrating the principle of the electric motor in 1821, Michael Faraday laid the foundation for modern electromagnetic technology. Ten years later, he discovered electromagnetic induction. In 1831, German physicists Johann Carl Friedrich Gauss and Wilhelm Weber established the representation for the unit of magnetism in terms of mass and charge and explored the nature of the Earth's magnetism.

One of the first experiments to show the close relationship between a magnetic field and light was carried out by Faraday in 1845. In 1877 John Kerr discovered the counterpart of the Faraday effect in reflection, now widely used to study the magnetization of materials. In the 1860s, James Clerk Maxwell unified the theory of electricity, magnetism, and light into a system of partial differential equations known as Maxwell's equations [24]. In 1888, Heinrich Hertz, through experimental verification and validation of Maxwell's work, made it possible to later invent radio, television, radar, and other devices dependent on electromagnetic radiation. In 1879, Thomas Edison brought to life the world's first electric

light bulb. Household electrification in Europe and North America began in the early 20th century.

The modern understanding of magnetic phenomena in condensed matter originates from the work of Pierre Curie and Pierre Weiss, who investigated the effect of temperature on magnetic materials and observed that magnetism disappeared suddenly above a certain critical temperature in materials like iron, thus defining the Curie temperature and Curie-Weiss law [25].

However, further technological development would not be possible without quantum mechanics and relativity, two pillars of modern physics that erected in the early years of the 20th century. For instance, today, our understanding of the phenomenon of magnetism is inextricably linked with the concept of spin, jointly proposed in 1925 by Samuel Goudsmit and George Uhlenbeck [26], which results from the relativistic description of the electron in an external electromagnetic field. The motion and interaction between electrons, the later called exchange energy, are of purely quantum-mechanical and quantum electrodynamics origin, and their understanding is derived from the work and theoretical models of Ernest Ising and Werner Heisenberg [27].

During World War II and in the post-war period, material research became a priority for the development of military and space technology. It set the onset of the Silicon Age, which began with the invention of the metal-oxide-silicon field-effect transistor (MOSFET) by Mohamed M. Atalla and Dawon Kahng at Bell Labs in 1959 [28]. The Silicon Age meant revolutionary changes in technology, economy, culture, and thinking, leading to a rapid shift from the traditional industry established by the Industrial Revolution to an economy primarily based upon Information Technology (IT), often referred to as the Information Age.

The further development of IT is inextricably linked with the advance of nanotechnology. The concept of a *nanometer* was first elaborated by Richard Zsigmondy; he coined the term *nanometer* explicitly for characterizing particle size and was the first person who measured the size of particles such as gold colloids with a microscope in 1898 [29]. In 1959, at an American Physical Society meeting at Caltech, Richard Feynman gave a lecture *There's Plenty of Room at the Bottom*, in which he envisioned the possibility of direct manipulation of SAs as a more powerful form of synthetic chemistry than those used at the time. Almost 15 years later, a Japanese scientist, Norio Taniguchi, was the first to use the term

nanotechnology as a field mainly consists of the processing, separation, consolidation, and deformation of materials by one atom or one molecule [30]. The term nanotechnology was also applied by Eric Drexler in his book from 1986 *Engines of Creation: The Coming Era of Nanotechnology*, which proposed the idea of a nanoscale "assembler" which would be able to build a copy of itself and of other items of arbitrary complexity.

The golden era of nanotechnology began in 1980s with the invention of the scanning tunneling microscope (STM) [31], followed by the discovery of fullerenes in 1985 [32] and carbon nanotubes (CNTs) in 1991 [33]. The STM development in 1981 earned its inventors, Gerd Binnig and Heinrich Rohrer the Nobel Prize in Physics in 1986. Harald Kroto, Robert Curl, and Richard Smalley were awarded the 1996 Nobel Prize in Chemistry for their roles in the discovery of fullerenes. The crowning achievement was in 2004 the isolation of graphene [1], called the wonder material of the 21st century, which is a monoatomic layer of sp^2-hybridized carbons atoms tightly arranged into a 2D honeycomb lattice sandwiched between two π-electron clouds, which awarded Andre Geim and Konstantin Novoselov the Nobel Prize in Physics in 2010.

The discovery of zero-dimensional (0D) fullerenes, 1D nanotubes, and 2D graphene raised the question of whether other low-dimensional materials could be prepared. Indeed, in 2004, the group of Xiaoyou Xu [34] discovered carbon dots (CDs) as a waste material during the synthesis of single-wall carbon nanotubes. The tunable photoluminescence, low-toxicity, convenient solubility in many solvents, and biodegradability predestined CDs for plethora of applications including bioimaging, sensing, cancer therapy, optoelectronic devices, and photocatalysis [35].

Further, 2D transition metal dichalcogenides (TMDCs), isolated for the first time in 2010 [36], exhibiting a unique combination of direct bandgap, strong spin–orbit coupling, and auspicious mechanical properties, have become interesting for electronics, spintronics, optoelectronics, and energy harvesting [37].

Another intriguing group of materials, MXenes consisting of a-few-atoms-thick layers of TM nitrides, carbides, or carbonitrides appeared in 2011 [38]. The variable arrangement and type of TM atoms enables their properties to be tailored, which makes MXenes applicable in many fields, *e.g.,* batteries, SCs, composites, and optoelectronic devices [39]–[41].

Another 2D material, hexagonal boron nitride, is a wide-gap insulator whose boron and nitrogen atoms are arranged in a honeycomb lattice, analogous to graphene. It is mainly used in electronics or piezoelectronics [42], [43].

A single layer of black phosphorus, phosphorene, was isolated in 2014 and attracted a lot of attention mainly due to its direct bandgap, tunable by the material's thickness form 1.88 eV (monolayer) up to 0.3 eV (bulk) [44].

Other graphene-like materials isolated from bulk analogues are silicene [45], germanene [46], stanene [47], borophene [48], and 2D iron oxide (hematene) [49].

However, we do not have to go far from graphene to look for new materials with enhanced properties. Covalent and non-covalent graphene modifications have led to multitude of graphene derivatives that have increased its application potential as discussed in detail in **Chapter 1**.
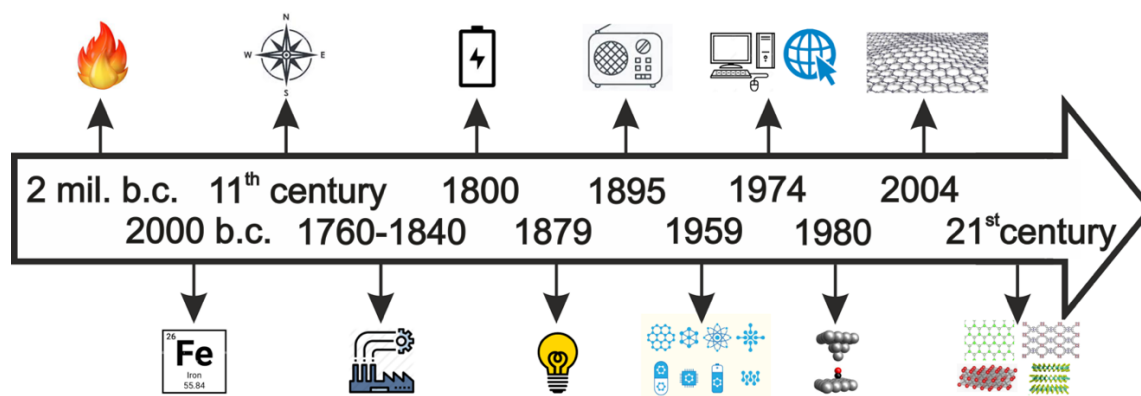
Figure 1 Timeline indicating important technological milestones in human history coeval with the development of science.

Information storage

The progress of human civilization would not be possible without the storage and sharing of information. The stored data in a person's brain are volatile. The exponentially decreasing forgetting curve shows that humans tend to halve their memory of newly learned knowledge in a matter of days or weeks unless they consciously review the learned material, the biggest loss of memory comes in first ten minutes.

By 20 000 BC, primitive cultures had developed methods of storing information mechanically. By notching a stick, knotting a string, weaving a pattern, carving, painting images in caves, information could be stored by one person for transmission to others.

The ability to store information as symbols representing sounds, rather than as pictures representing concepts, was a major transition point in improving communications and storage efficiency. Another major step in the development of information storage was printing. The early documents were printed with cylinder seals in clay by Sumerian civilization. Other techniques including hammered coinage, pottery imprints, cloth printing, woodblock printing, or letterpress printing aroused in mid-15th century. Finally, the development of lithography and screen printing boomed the spread of information.

The capturing sound on a recording medium began during the Industrial Revolution. Many pioneering efforts to record and reproduce sound were made during the latter half of the 19th century, resulting in Scott's phonautograph of 1857, followed by more famous invention of the phonograph by Thomas Edison in 1877. As the industrial revolution dawned, owners of machinery began to store information in ways that a machine could use it directly. In some cases, the information could be stored as patterns. The studded cylinder or disk of a music box is an example of pattern stored data interpreted by a machine, in this case to reproduce music. In 1898, danish engineer Valdemar Poulson patented the first magnetic recording device, a magnetic wire recorder called telegraphone. First modern technologists would acquire read-only memory, *i.e.*, the data can be stored and read, but not modified afterwards.

Current computer systems store data in digital format in the form of zeros and ones. One of the most widely used types of digital data storage is the magnetic one. Another option to store the date is electrical, as used for example in solid-state drives (SSD). However, in contrast to magnetic storage, the data from SSD can hardly be restored when damaged.

Magnetic storage devices, both magnetic tapes and hard disc drives (HDDs), have been used as a crucial recording media since the birth of the information age in 1950s. Introduced by IBM in 1956, HDDs became the dominant secondary storage device for general-purpose computers by the early 1960s, whereas magnetic tapes are predominantly used for backups. Data centers, which are the primary platforms for cloud computing and big data storage, still rely heavily on magnetic storage technology.

The basic approach to magnetic data storage, such as magnetic wires, magnetic tapes, floppy disk, and later HDDs is very similar. The magnetic surface is divided into magnetic domains which has mostly a uniform magnetization. In current commercialized HDDs, about 100 000 atoms are needed to store a bit [50]. As the read-write head moves along the surface,

the changes in magnetization are detected and recorded as zeros and ones depending on the orientation of the magnetic moments within the domain (**Figure 2**). So, the head can register the changes in the magnetic field and convert it into an electrical signal. More specifically, hard drives depend on a phenomenon called magnetoresistance (MR) [51] where a magnetic field alters the electrical resistance in a material, causing measurable changes in the electric current. MR is proportional to the strength of the magnetic field, with a larger field producing a higher resistance. The magnetic data is processed by applying a potential difference to a wire that is placed close to the magnetic material on a disk or tape. As the magnetic field representing data on the material passes by the wire, the resistance of the wire changes with the magnetic field of the data. This change in resistance alters the current through the wire. Monitoring this current provides a reading of the magnetic field on the tape or disk.
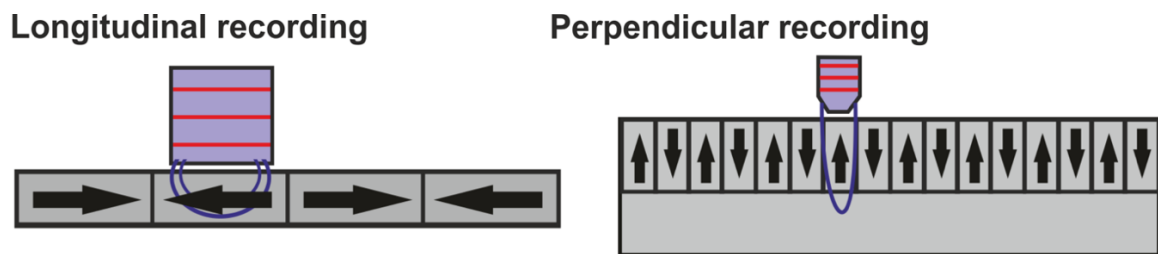

Figure 2 The longitudinal and perpendicular magnetic recording. Changes in magnetization are detected and recorded as zeros and ones depending on the orientation of the magnetic moments (indicated by arrows) within the domain.

Following the discovery of the giant magnetoresistance (GMR) effect in the late 1980s by Peter Grünberg and Albert Fert [52], [53] who awarded the 2007 Nobel Prize in Physics, GMR heads began to replace MR heads. The GMR effect is observed as a significant change in the electrical resistance that is induced by the application of a magnetic field to the thin films composed of alternating ferromagnetic (FM) and non-magnetic (NM) layers, *i.e.*, the change in electrical resistance depends on whether the magnetization of adjacent FM layers is parallel or antiparallel (**Figure 3**). The overall resistance is relatively low for parallel alignment and relatively high for antiparallel alignment. Thus, in a GMR based system, very feeble magnetic variations give rise to large differences in electrical resistance and provides almost three times the data density than MR devices.

Today, though, the read head no longer uses GMR but giant tunneling magnetoresistance (TMR) [54]. TMR is a magnetoresistive effect that occurs in a magnetic tunnel junction (MTJ) where electrons can tunnel from one ferromagnet into another thorough a very thin

insulator. The direction of the two magnetizations of the FM films is tuned by an external magnetic field. The electrons more likely tunnels through the insulating film when FM films have parallel alignment of the magnetization than with an antiparallel orientation. Consequently, the antiparallel alignment of the films corresponds to higher resistance. TMR extended the concept of GMR with both effects being based on spintronics.
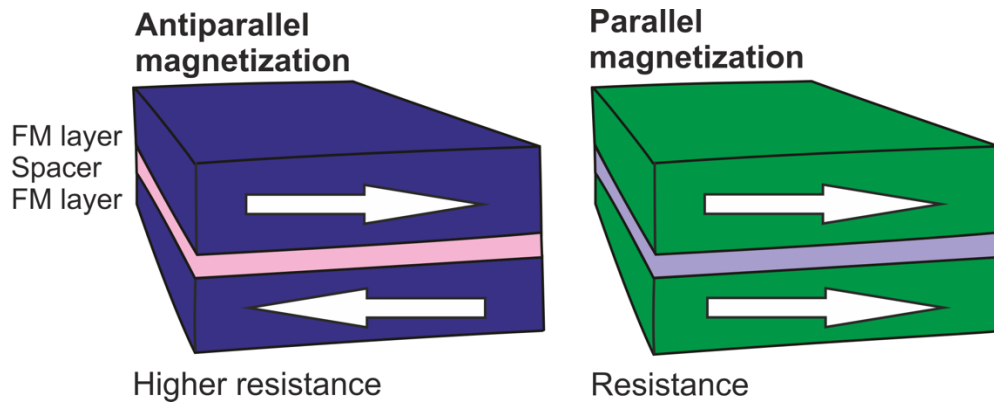
Figure 3 GMR effect. Change in electrical resistance depends on whether the magnetization of adjacent ferromagnetic layers is parallel or antiparallel. The overall resistance is relatively low/high for parallel/antiparallel alignment, respectively.

Spintronics and new prospects for data storage

Spin transport electronics, or spintronics for short – which was coined in the 1990s – is a rapidly developing field that combines the electronic and magnetic properties of materials. In addition to the electronic charge in solid-state devices, the intrinsic spin of the electron and/or holes, and the associated magnetic moment add another degree of freedom allowing for better performance as opposed to classical electronics, *i.e.*, reduction of their power consumption and increase of their data storage and processing efficiency. With the wide applications of spintronics in mind so far, including spin-valves [55], [56], magneto-electric spin–orbit logics (MESOs) [57], spin torque nano-oscillators (STNOs) [58], spin-mediated energy harvesting, spin thermoelectric generation, or spin-polarized photovoltaic cells [59], intense research efforts have been made in this field to improve existing and develop emerging applications, including spintronic devices for quantum computing, ultra-dens data storage, and flexible electronics [59], [60].

The origins of spintronics date back to the pioneering experiments by Richard Meservey and Paul Tedrow in the early 1970s on spin-dependent tunneling current between FM and superconducting films [61], [62], followed by Michel Julliere's experiment on MTJs [63]. Spintronics flowered following the discovery of the GMR effect in the late 1980s [52], [53],

which went on to be used in HDDs, now using the TMR effect though (*vide supra*) [64], [65], where magnesium oxide MgO layer being sandwiched between two FM layers acts as a spin filter that only allows electrons of one spin direction through it. The electron current flowing through MgO is almost 100% spin-up or spin-down polarized, depending on the magnetic orientation of the surrounding magnetic layers. Thus, the TMR signal is many times greater than that from a GMR spin valve. TMR is also the basis of magnetic random-access memory (MRAM) [66], a non-volatile memory that uses magnetic moments to retain data instead of electrical charges.

Over past decade, we have witnessed a tremendous increase in the rate of digital data production. The amount of data in the global datasphere was estimated to be 44 zettabytes at the dawn of 2020; by 2025, the amount of data generated each day is expected to reach 463 exabytes globally. Google, Facebook, Microsoft, and Amazon themselves store at least 1200 petabytes of information. Electronic Arts process roughly 50 terabytes of data every day [67]. It is expected that the ICT (information and communication technology) industry will consume 20% of the world's electricity and emit up to 5.5% of the world's carbon dioxide by 2025 [47]. Therefore, today's research is largely driven by the goal to develop IC devices that are smaller, faster, low-energy-consuming, and cheaper than ever before. However, advances in magnetic data storage capacity and miniaturization of the storage devices as we know it is coming to an end due to the so-called superparamagnetic limit [48], [49] that dictates the highest possible storage capacity limited by the superparamagnetism, a type of magnetism occurring in single-domain nanoparticles that possess a single giant magnetic moment that can randomly flip its direction under the influence of thermal effects. In contrast to (anti)ferro/ferri magnetism, superparamagnetism can occur below the Curie temperature of the material.

Because of the nanoparticle's magnetic anisotropy, the magnetic moment has usually only two stable magnetic orientations separated by an energy barrier, *i.e.*, easy and hard magnetization axes. At finite temperature, there is a finite probability for the magnetization to flip. The state of the nanoparticle depends on the measurement time, τ_m, and Néel relaxation time, τ_N, which corresponds to the mean time between the flips due to thermal fluctuations. If $\tau_m \gg \tau_N$ the nanoparticle magnetization will flip several times during the measurement, then the measured magnetization will average to zero, which is known as a superparamagnetic state. If $\tau_m \ll \tau_N$, the magnetization will not flip during the measurement and this refers to as a blocked state. In several experiments, the measurement

time is kept constant, but the temperature is varied, so the transition between superparamagnetism and blocked state is seen as a function of the temperature (**Figure 4**). Then, the blocking temperature is defined as $T_b = \frac{KV}{k_B(ln\frac{\tau_m}{\tau_0})}$, where K is the nanoparticle's MAE density and V its volume. Together, KV is the energy barrier associated with the flipping between the magnetization axes, the MAE of the material [68]. The blocking temperature is the temperature below which a material shows slow relaxation of magnetization and remains in the preferred magnetization direction.
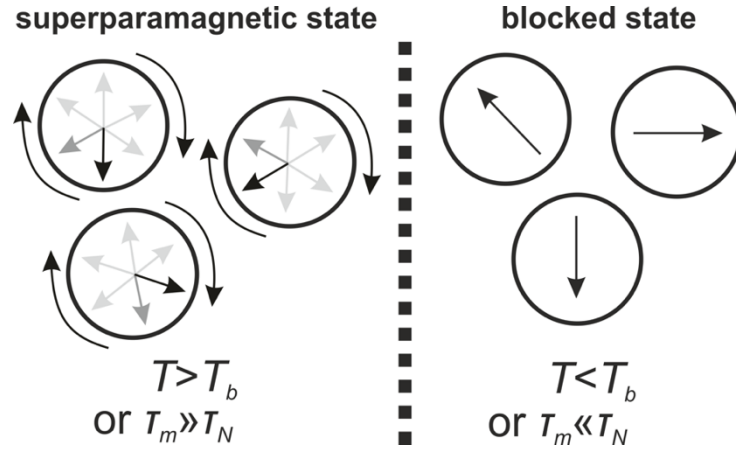
Figure 4 Blocked and superparamagnetic state, T_b stands for blocking temperature, τ_m and τ_N stands for measurement time and Néel relaxation time, respectively.

How the superparamagnetic limit can be suppressed? A fundamental constrain for the ultimate limit of classical data storage is imposed by the MAE determining the energy required to flip the spin of a SA. However, the magnetic field needed to write the bit increases with the magnetic anisotropy, unless the magnetization per bit rises too. A convenient possibility to manipulate the value of MAE (and possibly also the spin state) *via* electric fields [69]–[71] – a large MAE is needed to stabilize a magnetic bit against thermal agitation; a low MAE is desired during magnetization reversal while writing information – can solve this issue while gaining a lot in energy efficiency.

From a material perspective, the bit-patterned media (BPM), proposed in 1989 by Akira Kikitsu *et al*. [72], represents a promising approach to overcoming the superparamagnetic limit. BPM stores data on a uniform array of magnetic cells that act as single-domain magnets, each holding one bit of information (**Figure 5**). Patterned media is predicted to enable areal densities up to 20-300 Tb/in^2 as compared to the 1 Tb/in^2 limit that exists with current HDD technology. However, the mass production of BPM and its integration with the HDD's recording system is perceived as the greatest challenge for its commercialization.
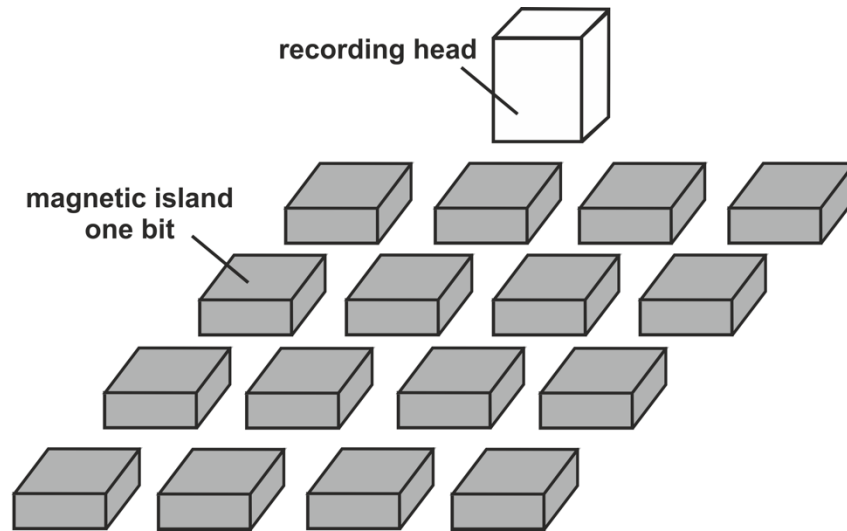
Figure 5 Bit-patterned media stores data in a uniform array of magnetic cells that act as single-domain magnets.

Pioneering work showing giant MAE for Co atoms adsorbed on the Pt(111) surface [73] has set the ultimate limit of magnetic data storage as a surface-supported atom-sized magnetic bit (**Figure 6**). Importantly, it has more recently been proven for an ensemble of Ho atoms on ultra-thin MgO(100) films coating Ag(100) that information processing in atom-sized bits is possible [74]. Still, this can only be achieved in ultra-high vacuum and very low temperatures, making them impractical in actual applications. If an atom-sized magnet was to be found with MAE corresponding to the temperature of at least 77 K, that of liquid nitrogen, which is abundant and cheap, applications in data centers could become realistic.
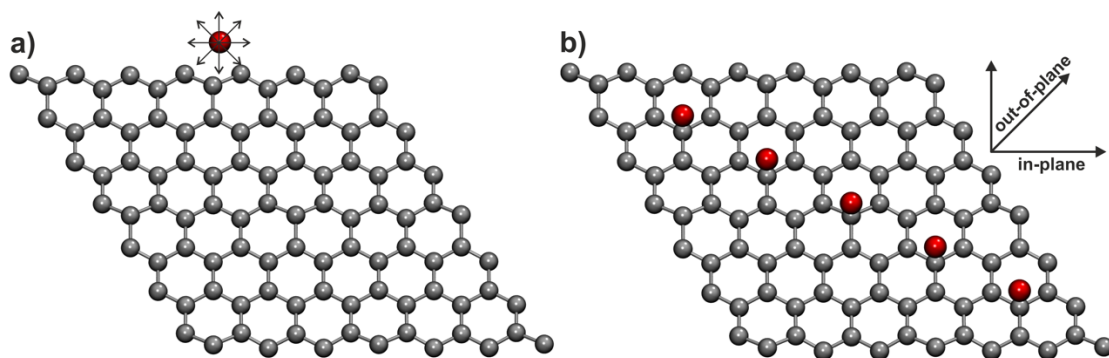
Figure 6 a) Due to the spherical symmetry of a free atom the magnetization is isotropic, and the magnetic anisotropy energy equals zero. b) Symmetry breaking and adatom–substrate hybridization induces strong anisotropy of the magnetization along the out-of-plane and in-plane direction.

Since the seminal paper by Pietro Gambardella *et al.*, [73] intensive research has focused on the magnetism of individual TM atoms and their clusters, up to the monolayers supported

on metal surfaces [75], [76]. Surprising theoretical results showing that the magnitude and even the sign of MAE [77]–[79] depend on the adsorption site and also that due to strong quenching of adatom's orbital moments and the formation of large, induced spin and orbital moments in the substrate, which contributes significantly to the MAE, have shifted the scientific interest to TM atoms and ultra-small TM clusters supported on NM graphene [80]–[84]. While the theory predicted the MAE for TM atoms embedded in graphene to reach only 7 meV [23], a huge MAE of up to 289 meV for a bimetallic IrCo dimer on the benzene molecule was calculated [85]. The MAE value was reduced to ~0.1 eV for IrCo on a free-standing graphene sheet [84].

The practical application of magnetic dimers on a graphene support would require the deposition of a carbon sheet on a solid substrate. Importantly, an increased MAE to 204 meV was predicted for the IrCo dimer deposited on graphene@Cu(111) [84], which based on Néel's theory, $MAE = k_B T_b (ln \frac{\tau_N}{\tau_0})$ [68], corresponds to the theoretical blocking temperature of 56 K. Increasing the MAE further to 285 meV would increase the blocking temperature to about 78 K, which is close to that of liquid nitrogen. On the other hand, the Pt atom and Pt–Pt dimer deposited on graphene@Ni(111) were NM [86]. From an experimental perspective, magnetic hysteresis and a spin lifetime of 1000 s at 2.5 K were measured for the self-assembled superlattice of dysprosium atoms on graphene@Ir(111) [87].

The mobility of single TM atoms or dimers in the ideal region of graphene [88]–[90] however, may limit their application potential. Lattice imperfections, such as vacancy defects can tightly anchor TM atoms or their clusters, preventing their diffusion and agglomeration on the surface [23], [91], [92], ultimately allowing a high MAE of up to 170 meV to be achieved for an OsPd dimer bound to a single nitrogen-decorated vacancy defect [76].

Our open question was whether the lighter TM atoms of Groups VI.-VIII.B of the Periodic Table and their clusters could also show significant MAE values, and to what extent graphene-mediated coupling between TM dopants could modify - preferentially increase - the MAE compared to that of SA impurities [14]. Because information can be stored and processed at the atomic scale if the atomic spins are coupled [69], [70], [93] understanding structural, electronic, and magnetic properties of graphene simultaneously doped with multiple TM atoms rather than a SA dopant is of paramount importance for spintronic applications.

Indeed, the Mn dopants bound to four carbon atoms, the presence of which in the graphene lattice has been experimentally confirmed, can create spots for the Fe–Mn dimers formation with a remarkably high value of ~120 meV per pair of Fe–Mn dimers due to the graphene-mediated RKKY (Rudermann–Kittel–Kasuya–Yoshida [94]–[96]) exchange between the dimers, which corresponds to blocking temperature of 34 K based on Néel's theory **[14]**. The conductive TM-doped graphene with robust magnetic features offers a new perspective on the design of graphene-based spintronic devices.

Importantly, inherently diamagnetic graphene can not only be a substrate for atom-sized metallic magnets, but also can be equipped with magnetic features without the presence of magnetic metallic elements, thus opening the way, *i.e.*, to *non-metallic* graphene-based spintronic devices [97]. Several methods has been employed to endow magnetic properties in graphene without the presence of TM atoms, *e.g.*, defects [98]–[102], edge engineering [103], [104], doping with *sp*-atoms [6], [7] *sp³* functionalization [10], **[19]**, **[21]**, **[22]**, [105], and/or non-covalent functionalization [106] (see **Chapter 2**).

The doping of graphene can be divided into two groups: electron doping by using *n*-dopants or hole doping by using *p*-dopants, the former with, *e.g.*, nitrogen atoms, the latter with boron atoms substituting C atoms in graphene, because nitrogen has one additional electron and boron has one electron less than carbon [107]. As the substitution of carbon by light elements (**Figure 7**) in the graphene lattice leads to changes in the electronic density of states (DOS), *i.e.*, graphitic dopants can provide π-electrons close to the Fermi level (E_F) of graphene, if the itinerant electrons occupy narrow bands at the E_F, Stoner magnetism can emerge, as has been recently shown for sulfur [7] and nitrogen [6].

Theoretical and experimental doping of sulfur and nitrogen onto graphene demonstrated FM arrangement with transition temperature of 62 K and 69 K, respectively and saturation magnetization ~5.5 emu g^{-1} (S-doped graphene), ~1.1 emu g^{-1} (N-doped graphene) [6], [7]. Below 4 at.% of sulfur atoms and 6 at.% of nitrogen, respectively, graphene exhibited diamagnetic character with paramagnetic (PM) centers around the dopant. The increased concentration and specific configurations of dopants led to the FM alignment where PM centers were coupled by π-electron system (see **Chapter 2.4** for more details). Hence, the magnetic ordering can resist thermal disruption to some extent depending on the chemical nature of the dopant and its concentration, and configurations of foreign atoms in the graphene lattice – as graphene can be regarded as a bipartite system with two interpenetrating triangular lattices [108].

Besides ferromagnetism triggered by graphitic nitrogen [6], graphene-containing extensive pyridinic N-doping acts as spin switch, in an "on-off-on" fashion, under microwave energy [55], which may lead to novel types of switches, filters, and spintronic devices using sp^2-only 2D systems.
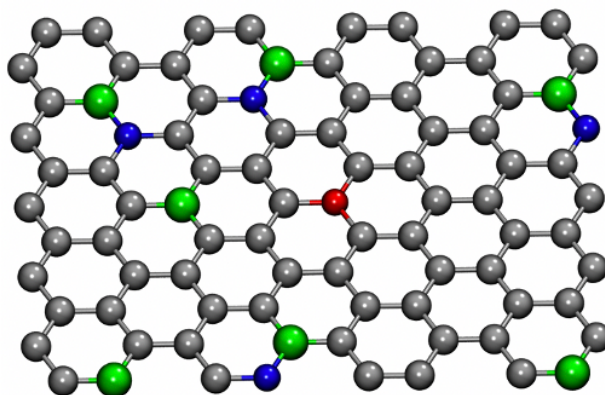
Figure 7 Doping of the graphene layer with *sp*-elements can lead to a stable magnetic ordering in graphene. Color code: carbon in gray, nitrogen in blue, boron in green, and oxygen in red.

FG chemistry has been shown to be convenient for the further development of magnetic graphene derivatives, hydroxyl-substituted FG, termed hydroxofluorographenes (GOHFs), exhibiting FM magnetic ordering up to 62 K and antiferromagnetic (AFM) alignment sustainable up to 372 K. The magnetism in GOHFs stemmed from the presence of aromatic islands forming diradicals that couple superexchange interactions mediated through OH-groups [10]. However, if defluorination pathways lead to the formation of sp^2 zig-zag motifs inside the sp^3 lattice, strengthening the role of itinerant π-electrons on top of the superexchange interactions mediated by −OH groups, GOHF exhibits RT FM ordering **[21]**. Theoretical calculation showed that the transition temperature could be tuned by substitution of hydroxyls by other functional groups **[22].**

With this in mind, we have theoretically explored whether phosphorus atoms could induce magnetism in the graphene lattice **[13]**. Why did we examine phosphorus? i) Phosphorus atom belongs to the same group as nitrogen but is heavier and larger. Therefore, it was an interest in comparing their electronic and magnetic properties. ii) Phosphorus atom was experimentally embedded into graphene by several technique, *i.e.,* chemical vapor deposition or ion implantation/irradiation [109], [110] however, no systematic studies have been carried out then focusing on different C/P ratio, configuration of P atoms, or transition temperature. iii) Recent experimental preparation of Gr-P with P concentration up to 6.40 at.% imprinted localized magnetic centers in graphene, which ultimately led to the

coexistence of AFM and FM phases, with the corresponding Neél and Curie temperature 125 K and 300 K, respectively [111]. iv) In addition to magnetism, phosphorus doped graphene could be used for oxygen reduction reaction [112], oxygen evolution reaction [113], hydrogen generation [114], batteries [115], sensing [116], or field effect transistors [117].

Employing density functional theory (DFT), we systematically investigated structural, electronic, and magnetic properties, including the theoretical transition temperatures of P-doped (Gr-P) and/or phosphono-functionalized graphene (Gr-PO_3H_2) at various doping concentrations and/or structural arrangements **[13]**. Our simulations of simultaneous P doping and $-PO_3H_2$ functionalization of graphene elucidated the origin of experimentally observed FM ordering up to RT and showed that the simultaneous substitution of C by P and the adsorption of P adatoms can lead to FM and AFM arrangements in line with experimental findings [111]. Such atomically tailored organic magnets may stimulate interest in exploiting them in spintronics or data-storage applications.

Molecular magnets

The coordination of TM atoms in porphyrin molecules, where the ligand field coordinated with the central metal atom governs the magnetic anisotropy, locally resembles the structure of TM atoms anchored in N-decorated defects in the graphene lattice **[14],** [23]. Porphyrins, which belong to the class of single molecule magnets (SMMs) and single-chain magnets (SCMs) are the subject of active research [118].

The SMMs and SCMs have potential applications in diverse fields and devices including molecular spintronics, nuclear spin resonance, molecular spin-valves, nano-memory devices, and quantum computing. SMMs and SCMs also exhibit many remarkable features that make them suitable for other applications, including quantum tunneling effects, quantum phase interference/coherence, and giant magnetic anisotropy [52]. Moreover, they can retain their magnetizations for a relatively long time in the absence of an applied field at low temperatures [119].

Although the first synthesis and physicochemical characterization of a molecular magnet, namely of diethyldithiocarbamate-Fe(III) chloride [120], took place as early as 1967, the wave of interest in molecular magnetism came nearly three decades later with the discovery of [$Mn_{12}O_{12}(OAc)_{16}(H_2O)_4$] in 1991 [121]. The term single-molecule magnet was used five years later for distorted $Mn^{IV}Mn^{III}_3$ cubane complex [122]. In the same year, the quantum

tunneling of magnetization was experimentally observed in the [Mn$_{12}$] complex, which was considered as a breakthrough in the SMM field [123]. In 2003, Naoto Ishikawa reported on a new type of SMMs based on large orbital and spin angular moments of a single lanthanide (Ln = Tb, Dy, and Ho) ion bonded to double-decker phthalocyanine (Pc) complexes [Ln(Pc)$_2$]$^{n-}$ [124]. These seminal works have greatly inspired the investigation of 4f-containing SMMs, such as 3d-4f complexes, pure 4f clusters, and 4f single-ion magnets (SIMs). The first reports on the actinide-based SMM came in 2009 [119], [125]. In 2013, it was shown that mononuclear SMMs can contain not only a single PM 4f or 5f center but also a 3d ion [126], [127]. The synthesis of such complexes with low coordination number (2–4) is an effective approach to preserve the orbital angular momentum and significantly enhances the magnetic anisotropy [119], [128]. However, further development of new molecular magnets would be slow and limited without advances in surface science and on-surface synthesis, which are used in many industries such as catalysis [129], the semiconductor industry [130], and biomedical devices [131].

Surface chemistry has its pros and cons though. On the one hand, the reactants have limited access to each other, which reduces the contact between them. Moreover, the confinement into two dimensions dramatically changes the range of chemical on-surface reactions. On the other hand, on-surface synthesis gives access to new reaction mechanisms that would not be easily accessible under standard chemistry conditions and enables reactions of non-soluble materials, consequently with an absolute absence of solvents. Further, it represents an efficient method to form robust organic networks and 2D polymers, or self-assembled building blocks [132]–[135].

Today's on-surface chemistry would not be possible without the development of experimental techniques. In the 1920s, Irving Langmuir advanced his theory of chemisorption, which plays an important role not only in heterogeneous catalysis but also in on-surface chemistry in general [136]. The huge development of surface chemistry took place in 1960s, when spectroscopic and structural probes were developed [137] that made it possible to investigate surfaces and on-surface processes. Twenty years later, surface studies have been reinforced with the discovery of a new class of microscopy tools, *i.e.*, STM and atomic force microscopy (AFM) that enable the observation of chemical changes of surfaces and direct three-dimensional (3D) mapping of the positions of atoms at surfaces, and even direct engineering and modification of surfaces. In 1981, the first direct visualization of surface atoms was made using an STM [31]. For the first time, many processes that occurred at surfaces and interfaces, such as catalytic reactions, could be

probed directly. While the STM enables to investigate metal and semiconductor surfaces, the non-conductive surfaces of oxides and biological materials can be studied by AFM [138], which also provides the surface mapping of materials. Additionally, STM and AFM can be used as a "nanowriter" that places and positions atoms and molecules on surfaces to make organized structures, as demonstrated by IBM as early as 1987 [139]. Despite the unprecedented chemical resolution provided by the high-resolution scanning probe microscopy (SPM), a detailed understanding of the mechanisms of on-surface chemistry reactions is still limited due to the temporal resolution. This is where theoretical simulations come in handy.

A beautiful example of such a combination of theory and experiment comes from our laboratory where the chemical evolution of the fluorinated free-base porphyrin (2H-4FTPP) adsorbed onto Au(111) surface, 2H-4FTPP → 2H-4FPP → Au-4FPP, was elucidated [140].

Another combined theoretical/experimental study revealed that the spin state of a single iron(II) phthalocyanine molecule on N-doped graphene can be locally controlled by weak non-covalent interaction with the dopant causing a reordering of iron d-orbitals without the use of an external stimulus such as an external magnetic field, electric field, light, pressure, or temperature [106].

We more recently provided theoretical insight into the reaction steps in experimental synthesis of porphyrin based 1D coordination polymers and explained the sudden drop of MAE upon their intramolecular rearrangements **[14]**. Controlling the chemical reactions and conformational and intrinsic magnetic characteristics of surface restricted porphyrin molecules by rational designing could open new possibilities in the field of molecular spintronics [140].

Single atom catalysis

Various noble-metal catalysts have been extensively exploited for industrial applications, including energy conversion, chemicals production, pharmaceutics, and automotive exhaust purification [141]–[143]. Noble metals are, however, expensive and of limited supply. Their industrial use, scarcity, limited supply and production, and global demand have driven their prices up over last decade. In addition, they are less eco-friendly compared to organic materials. Moreover, a large part of the metal surfaces is inactive for catalytic reactions. Therefore, in addition to potential applications in spintronics and information storage, TM atoms dispersed on graphene [144]–[147] or graphene-derivative supports **[15]**, [148] have

been extensively studied as the ultimate limit to size reduction of heterogeneous metal catalysts [149]–[151].

The first known reference to the use of inorganic catalysis dates back to 1552, when Valerius Cordus used sulfuric acid to catalyze the conversion of alcohol to ether [136]. In 1597, Andreas Libavius referred in his book *Alchemi* the term *catalysis* to describe the decomposition of base metals into silver and gold [136], but it was Jöns Jacob Berzelius who defined the term *catalysis* in 1835 in the sense used today [152]. The first *intentional catalysis* was presented by Elizabeth Fulhame in 1794, who suggested that a small amount of water was required to oxidize carbon monoxide [152].

However, all early catalytic studies were empirical. Only the introduction of a rate dependence of chemical reactions by Ludwig Wilhelmy in 1820, the first quantitative law of Cato Maximilian Guldberg and Peter Waage in 1864, the definition of the rate constant for the measurement of chemical change in 1877 by Jacobus Henricus Van't Hoff, and the dependence of the chemical reaction on temperature and pressure by Henry Louis Le Chatelier in 1884, established the needed theory for the flowering of catalysis. In 1927, Cyril Norman Hinshelwood presented his kinetic theory based upon earlier findings by Irving Langmuir, which is still being applied in today's catalytic modeling [136], [152].

Nowadays, 90% of chemical procedures use catalysts during the manufacture processes. The petroleum industry uses catalysis at almost every step, for alkylation, catalytic cracking, naphtha reforming, steam reforming, post-combustion exhaust gas treatment, *etc*. Even electrical cars use catalysts in both anodic and cathodic reactions. Natural catalysts, enzymes, are frequently used in food production such as baking, dairy and starch processing, brewing and beverages, and enable the processing and storage of food materials. The largest-scale chemicals such as nitric acid (from ammonia), sulfuric acid (from sulfur oxides), are produced by using catalysts in oxidation processes. Even one of the most energy-intensive Haber-Bosch process from World War I, producing ammonia as a source of explosives and fertilizes, still uses an iron oxide catalyst. Pharmaceutical processors use a variety of precious-metal-bearing catalysts in the manufacture of drugs and other products, mainly for hydrogenation reactions. The global demand for catalysts in 2014 was estimated as 33.5 billion USD, therefore, a reduction of the expenses is highly desirable. Today, over 80% of all commercially produced chemicals utilize a catalyst at some stage in the production process, including food processing, fine chemicals, bulk chemicals, or the energy industry to increase the rate of a desired reaction and enhance its selectivity [153].

For these reasons, it is very advantageous to reduce the amount of catalytically inactive atoms while increasing catalyst efficiency and reactivity. The ultimate limit is an atomically dispersed catalyst, also termed SACs, being at the frontier in atom economy thanks to the highest possible surface to volume area, and nearly 100% metal loading utilized to form accessible active sites (**Figure 8**). The SACs are one of the holy grails in catalysis as they bridge the gap between the homogeneous and heterogeneous catalysis, enabling the best use of rare and expensive noble metals. Moreover, the well-defined structure and strong interaction between the support and SACs ensure ease of reuse, recycling of the catalytic material, and prevents undesirable agglomeration and leaching [154]–[157].
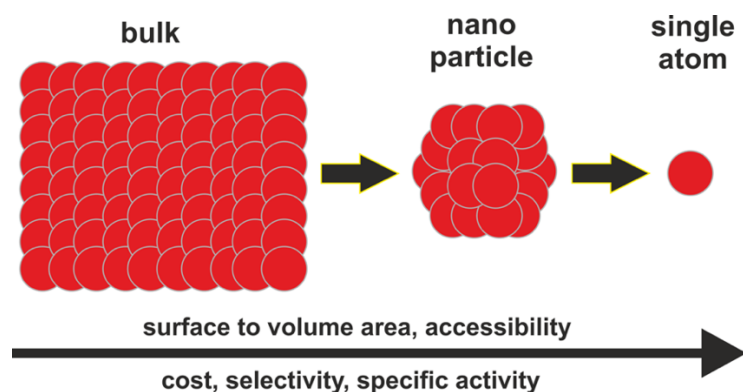
Figure 8 Miniaturization of the bulk catalyst into nanoparticles and ultimately SACs is advantageous due to the higher surface to volume ratio, accessible sites, selectivity, and specific activity.

Despite the fact that many metals are capable of catalytic reaction, one of the most interesting is continued to be platinum, which is still used in many research works as indicated by Nobel laureate Paul Sabatier [152]. It possesses a unique catalytic activity, especially for hydrogenation reactions, which ultimately became the basis for the rapid development of the petrochemical industry [152].

The huge surface area and relative ease of functionalizing graphene make it a promising material for heterogenous catalysis [149]. However, the stabilization of the individual metal atoms on the pristine graphene remains a significant challenge in further development of effectual and stable SACs due to the mobility of metal adatoms, agglomeration, or leaching [88]–[90], which make heterogeneous catalytic reactions typically unoptimized as concerns structure, morphology, theoretical description, and performance [158]–[160].

To overcome these difficulties, it is necessary to identify appropriate anchoring groups for single metal atoms, understand the nature of the metal-linker-graphene interaction, and the influence of the adatoms on the electronic structure of the graphene derivative.

It has recently been shown that N-doped graphene acid (N-G–OOH) with the basal plane densely covered by COOH groups exhibits excellent catalytic activity in oxygen reduction reaction (ORR) towards H_2O_2 generation [161]. With the help of DFT calculations, it was revealed that surface carboxylic acid functional groups play a significant role in achieving the high activity of N-G–OOH for $2e^-$ ORR.

In other study, the strong interaction between palladium and carboxylic groups of G–OOH ensured a nanoparticle growth mechanism entailing counterion metathesis followed by a G–OOH promoted reduction. The G–OOH-Pd nanohybrids mediated Suzuki–Miyaura cross coupling reaction under eco-friendly conditions [162].

We have also shown that G–CN, experimentally prepared for the first time in 2017 [9], is a suitable scaffold for the Pt adatoms, both in Pt^0 and Pt^{II} oxidation states [15]. Effective immobilization of Pt ions may enable a multitude of catalytic reactions, as has already been demonstrated for amine coupling and alcohol oxidation reactions on Cu@G–CN [148].

Energy storage

Given the significant growth of the world population, the demand for energy resources is projected to increase by 100% by 2050 [163], [164] and the ICT industry itself could account for 20% of global electricity consumption and 5.5% of the world's carbon dioxide emission already by 2025 [47]. In addition, the limited supply of fossil fuel resources and government restrictions on fuel cars due to carbon dioxide emissions, and the rapidly growing demand for electric vehicles, grid electric energy storage, powering portable electronics, and reliance on energy-based devices, it is legitimate to research focused on sustainable energy resources and suitable energy storage technologies using earth-abundant elements with minimal environmental impact [165]. In this context, rechargeable batteries and SCs have attracted immense attention [166].

The term *battery* was introduced by Benjamin Franklin in 1749 when he experimented with electricity using a set of linked capacitors. In 1780, Luigi Galvani's famous experiments on frog legs led to the discovery of the principle behind batteries. The first true battery, however, was invented by Alessandro Volta in 1800, which was essentially a stack of

alternating discs of copper and zinc separated by a cloth soaked in brine [167]. One of the most enduring batteries is the lead-acid battery, which was invented in 1859 by Gaston Planté and is still used today to start most cars with an internal combustion engine. It is the oldest example of a rechargeable battery. Then, in 1868, Georges Leclanché invented the Leclanché cell, later improved by Carl Gassner in 1886, which is known today as the dry cell. The first battery to use an alkaline electrolyte appeared in 1899 thanks to Waldemar Jugner using nickel-cadmium electrodes in potassium hydroxide.

LIBs currently dominate the contemporary energy storage landscape. This rechargeable battery laid the foundations for wireless electronics such as cell phones and laptops [168]. It is also used from powering electric cars to storing energy from renewable sources, which with the development of smart grids and networks for "Internet of Things," rapidly increases the demand for batteries with higher efficiency and lower cost [169]. John B. Goodenough, M. Stanley Whittingham, and Akira Yoshino for their contribution to the development of LIBs awarded the 2019 Nobel Prize in Chemistry.

However, LIBs suffer from long charging times and undergo irreversible processes during cycling that gradually reduce their energy density and thus their cycle-life [169]. Another LIBs bottleneck is that the cathode materials that determine the LIBs capacity contain non-sustainable Co or Ni elements [170]. At the same time, graphite, which is typically used on the negative electrode anodes, limit the rate performance and safety due to the slow Li-ion diffusion and operation potential window that is very close to the voltage of Li metal plating. This causes rapid aging of graphite anodes, especially in power-demanding applications such as electric vehicles and poses a risk of catastrophic battery failure due to the growth of lithium metal dendrites [171], [172].

The first capacitator to use a double-layer charge storage was reported in 1957 by Becker of General Electric [173], but the device was not commercialized due to the impractical design because of the need to immerse it in a pool of electrolytes. In 1966, Robert A. Rightmire at Standard Oil of Ohio (SOHIO) [174] developed another version of the capacitor as *electrical energy storage apparatus*, while working on experimental fuel cell designs, with the standard design used today. The first commercially effective electrochemical capacitor referred to as a *supercapacitor* was sold in 1975 by the Japanese company Nippon Electric Company (NEC). In 1991, Brian Evans Conway described the difference between SCs and batteries behavior in electrochemical energy storage [175], and in 1999 he defined the term *supercapacitor* [173].

The advantages of SCs over batteries or fuel cells are high power density, long life cycle, and small size [176], which means savings in material and cost. They can store more energy than classic conventional capacitors, while maintaining a similar cell design [176]–[178]. These attributes, together with high stability and rather low costs, makes them frontier candidates in the energy storage industry. However, commercial SCs have cell-level specific energies (and energy densities) several times lower that of lead-acid batteries and about one order of magnitude less than state-of-the-art LIBs [179]–[181]. **Table 1** compares advantages and disadvantages batteries and SCs.

Table 1 Pros and cons of batteries and supercapacitors.

Pros	Cons
Batteries	
Power density	Limited cycle life
Storage capacity	Voltage and current limitations
Better leakage current than capacitors	Long charging times
Constant voltage that can be turns off/on	More temperature sensitive than capacitators
Supercapacitors	
Long life cycle	Low specific energy
High load currents	Linear discharge voltage
Short charging times	High self-discharge
Excellent temperature performance	High cost per watt

Cost-effective and environmentally friendly nature, abundance, processability, and design versatility render organic materials subject to reversible electrochemical redox processes and coordinating lithium, attractive candidates for anodes in LIBs [179], [180]. Likewise, replacing the metal atoms in SC's electrode materials with non-metal and earth-abundant elements such as carbon would have significant environmental benefits, reducing our dependence on critical natural resources and increasing sustainability. Further, in order to take advantage of SCs in a broader range of applications, it is imperative to identify electrode materials that have much better energy density combined with long life and high power.

Graphene has attracted increasing attention as an interesting electrode candidate for energy storage due to its striking mechanical and electronic properties [1], and the ease of functionalization by various functional groups **[13]**, **[20]**, **[22]** boosting electrochemical stability and capacitive performance [182], [183].

For instance, thanks to the reach chemistry of FG [9], [184], sulfur chains with a particularly high sulfur content of 80 mass% covalently bonded to graphene resulted in an electrochemically active cathode material for lithium–sulfur batteries (LSBs) [185]. The sulfurized-graphene material exhibited excellent performance with only 5 mass% of conductive carbon additive and at a low temperature of 298 K. In combination with a fluorinated ether as electrolyte additive, the capacity persists at ca. 700 mAh g^{-1} after 100 cycles at 0.1 C, and at ca. 644 mAh g^{-1} after 250 cycles at 0.2 C. Thus, LSBs can offer a promising alternative in the energy storage field [185].

The covalent grafting of carboxyl groups on the conductive skeleton of graphene paves the way for an efficient and stable G–OOH anode for LIBs **[17]**. Experiments combined with our theoretical calculations revealed the excellent charge transport, particularly low charge transfer resistance and redox activity stemming from the carboxyl groups, and lithium intercalation properties due to the co-presence of significant content of *sp²* moieties of the G–OOH anode. The true potential of G–OOH as a LIB anode was confirmed by the practical capacity and rate capability of 800 mAhg^{-1} at 0.05 A g^{-1} and 174 mAhg^{-1} at 2.0 A g^{-1} **[17]**.

Recent studies have also shown that G–OOH is as a promising material for electrochemical sensing [186], catalysis [161], [162], [187], electrocatalysis [188], and eco-friendly electrode material for SCs [178] [9]. The charging/discharging rate stability test revealed that G–OOH can be repeatedly measured at current densities ranging from 1 to 20 A g^{-1} without capacitance loss, making this material suitable for lightweight electrode materials for SCs with extremely high durability [178].

The FG chemistry made it also possible to homogeneously graft the amino acid arginine (Arg) via its guanidine group on both sides of graphene [177]. More specifically, having the guanidino functional group, Arg acted as a nucleophile and was grafted onto electrophilic radical centers of FG forming the zwitterionic arginine-functionalized FG (FG/Arg). This material showed a high capacitance of ≈390 F g^{-1} at 0.25 A g^{-1} and, importantly, after ≈30 000 galvanostatic charging/discharging cycles under typical operation conditions, the

capacitance retention remained at around 82.3%. An eco-friendly FG/Arg offers promising properties for an efficient supercapacitor in aqueous electrolytes [177].

Further, using combined experimental and theoretical approaches, a simple and up-scalable method was developed for the preparation of partially FGs based on thermal reduction of a fully fluorinated sample in a reducing hydrogen gas. The specific capacitance was influenced by the number of fluorine atoms and the hydrogenation process, as explained with the help of our computational modeling. An optimized material showed a specific capacitance of 539 F g^{-1} recorded at a current density of 0.25 A g^{-1} with 100% specific capacitance retention after 1500 cycles in a three-electrode configuration and 96.7% specific capacitance after 30 000 cycles in a two-electrode setup [20].

Finally, thanks to the radical-based FG chemistry enabling the presence of *sp^2* and *sp^3* carbon bonds in the same lattice, a new class of carbon-based materials was developed comprising nitrogen doping and diamond-like tetrahedral bonds for high energy density SCs [16]. Our theoretical calculations revealed that the C–C bonds develop between C-centered radicals, which emerge in the vicinity of the N dopants. This material achieved an ultra-high mass density of 2.8 g cm^{-3} and delivered unprecedented energy densities of 200 W h L^{-1} at a power of 2.6 kW L^{-1} and 143 W h L^{-1} at 52 kW L^{-1} – twice as high as that of top-rated materials and several-fold higher than commercial supercapacitor carbons – increasing the competitiveness of SCs in the portable energy storage landscape [16].

Outline

In the following chapter, the materials that form the basis of our research **[13]–[18]** are introduced. The common denominator is graphene and its derivatives. By modifying graphene with dopants, adatoms, or functional groups, unique materials with tailored structural, electronic, and magnetic properties can be obtained for potential applications in SCs, electrodes, spintronics, composites, photovoltaic devices, medicine, environmental treatment , and sensors [2], [189]–[196].

Another studied material in this thesis is porphyrin, whose main features are presented in **Chapter 1.5**, and thanks to its unique magnetic properties **[18],** it may find applications in catalysis, spintronics, molecular sensing, and biological applications [35], [197]–[201].

The magnetism of graphene derivatives is reviewed in **Chapter 2**.

Chapter 3 discusses the theoretical basis of the calculations upon which our study is based. Besides the description of Schrödinger equation (SE), Hartree-Fock (HF) method, and Thomas-Fermi (TF) model, the focus is on the concept of DFT and its exchange-correlation functionals. Further, the physics behind solid-state calculations is presented.

In **Chapter 4**, the possibilities of establishing magnetic ordering in phosphorus-doped and phosphono-functionalized graphene is discussed. For a single P substitution, the 3D reconstruction of the experimental geometry based on atomic-resolution aberration-corrected scanning transmission electron microscopy (STEM) imaging at multiple sample tilts is compared with the computational results **[13]**.

Chapter 5 deals with the doping of TM atoms (Cr, Mn, and Fe) with vacancy-containing graphene, both bare and nitrogen-decorated, which, based on spin-polarized DFT (SP-DFT) calculations including spin-orbit coupling, results in a high MAE due to the coupling between TM dopants through graphene. The computational findings are supplemented by an experimental atomic-resolution characterization of a Mn substitution, which may create spots for the formation of atom-sized magnets in graphene **[14]**.

In **Chapter 6**, the feasibility of adapting the MAE with conformational changes of 1D Au(111)-supported metalloporphyrin polymers is presented. DFT results are discussed in relation to scanning tunneling microscopy and spectroscopy, and high-resolution atomic force microscopy experiments **[18]**.

Chapter 7 discusses the theoretical prospective of graphene and its derivatives as a scaffold for SAC preventing the unwanted migration and agglomeration of SACs. Calculations from first-principles allowed to identify the cyano group as a convenient binding site for Pt adatom, which was additionally supported by the experimental result confirming that the – CN groups act as ligands immobilizing of 3.7 wt.% Pt adatoms **[15]**.

Chapter 8 focuses on the possibility of using G–OOH, a carboxyl derivative of graphene, as the LIB anode. While the experimental measurements showed excellent charge transport, redox activity, and lithium intercalation of the G–OOH anode, theoretical insight was needed into the mechanism underlying energy storage in G–OOH **[17]**. The results of finite (functionalized ovalene) and infinite (periodic) model calculations in the context of experimental data are discussed.

The reaction of FG with azide anions enables the preparation of a material connecting sp^2 layers of the graphene type with tetrahedral carbon-carbon bonds and superdoping with nitrogen. The resulting ultra-high mass density material is an excellent ion host, delivering unprecedented energy densities. Theoretical research allowed for a better understanding of the structural properties of this material, which is discussed in **Chapter 9 [16]**.

Finally, our research is concluded in **Chapter 10**, followed by References, and then Appendices containing reprints of these papers that constitute the basis of my dissertation.

1 Materials

1.1 Graphene

The concept of single layer graphite was first described by P. R. Wallace in 1947, who investigated the band theory of graphite [202]. The first mention of monolayer reduced graphene oxide (GO) flakes obtained experimentally by Hanns-Peter Boehm and co-workers was in 1962, who in 1986 established the term *graphene* by combining the word *graphite* and the suffix *ene* referring to polycyclic aromatic hydrocarbons [203]. However, graphene was first unambiguously produced and identified by Andre Geim and Konstantin Novoselov in 2004 [1]. Using micromechanical cleavage and the Scotch tape technique, the monolayer of graphite was exfoliated and transferred to silicone dioxide wafer. For their pioneering isolation and description of graphene, both scientists were awarded the Nobel Prize in Physics in 2010.

Besides mechanical exfoliation of graphene layers, graphene can be prepared by chemical vapor deposition (CVD), thermal decomposition of SiC, electrical arc discharge method, organic synthesis, or chemical syntheses from graphite dispersion [204].

Pristine graphene belongs to the group of 2D materials because it consists of only a single layer of carbon atoms arranged in hexagons (**Figure 9**). Each carbon atom forms three 1.42 Å long bonds with adjacent carbon atoms [205]. It was predicted that graphene as a 2D material would not be stable, however, the corrugation, sp^2 hybridization of the s, p_x, and p_y orbitals forming the σ bonds (**Figure 9**) make graphene stabile. While these σ C–C bonds are responsible for the extraordinary mechanical strength of graphene, the π-bonds (**Figure 9**) hybridized from the p_z orbitals are responsible for most of the graphene's excellent electronic properties [202].
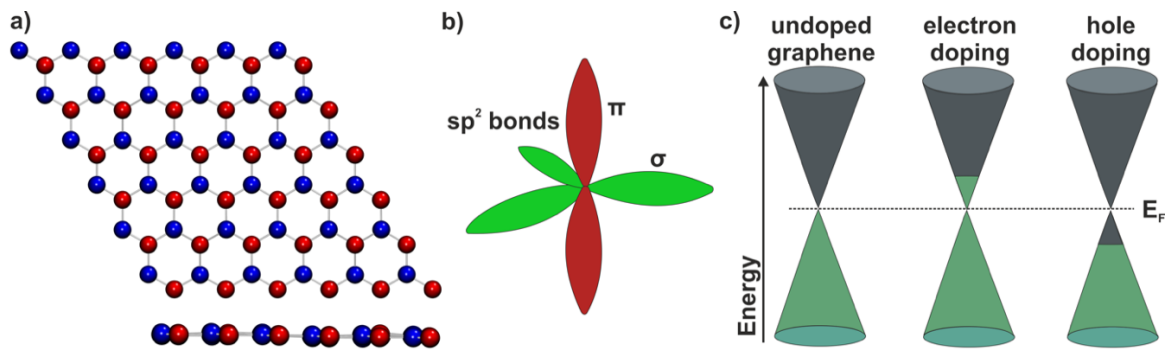
Figure 9 a) graphene bipartite lattice with A (red) and B (blue) sublattices, b) σ-bonds are responsible for the extraordinary mechanical strength of graphene, the π-cloud causes excellent electron mobility, c) semi-metallic electronic structure with the Dirac point is shifted by electron or hole doping.

Pristine graphene acquires a delocalized conjugated system with Dirac cones at the E_F (**Figure 9c**), *i.e.*, it is a zero-gap semiconductor, which results in an extraordinary electron mobility (2×10^5 $cm^2V^{-1}s^{-1}$) [1] and thermal conductivity of graphene (~5000 W $m^{-1}K^{-1}$) [206]. It attains excellent intrinsic strength with a breaking strength of 42 N m^{-1} and the Young's modulus of about 1 TPa [207], and a huge specific surface area (2675 m^2 g^{-1}) [208]. Moreover, graphene is optical transparent (97.7%) [209]. Due to its fascinating properties, graphene can be used in many applications, *e.g.*, field-effect transistors [210], optical devices [211], medicine [212], (bio)sensors [213], SCs [3] and/or in sport industry as a composite material.

Nevertheless, there are several drawbacks including high hydrophobicity and the lack of magnetic response that hinders its usage. Therefore, various methods have been developed to alter its properties, even though graphene is chemically inert. Covalent chemistry is an effective way of modulating the physico-chemical properties of graphene, *i.e.*, by converting *sp²* hybridized carbon atoms to *sp³* ones, new 2D materials with altered properties were obtained [214]. For instance, treatment of graphene with cold plasma [215] or irradiation of graphite with protons [216] produces hydrogenated graphene, called graphane, which is a wide-gap semiconductor. Oxidation of graphene, leading to GO containing hydroxy, epoxy, or carbonyl groups, turns hydrophobic graphene into a hydrophilic material [217]. More importantly for the further chemistry of graphene, exfoliation of graphite fluoride or fluorination of graphene gave rise to FG, which is considered to be the thinnest insulator. High reactivity of FG enables facile and scalable access to a wide portfolio of graphene derivatives [184], such as thioflurographene, which can be used as a biosensor [218], GOHF

exhibiting FM or AFM ordering at RT [10], **[21]**, G–CN which can be used in SACs [9], [148], [219] or G–OOH which can be used as a SC component [9], **[17]**, [178], [220].

1.2 Fluorographene

Fluorographene, also known as graphene fluoride, was first synthesized in 2010 [11], [221]. FG is a 2D derivative of graphene consisting of hexagonal carbon rings with covalently attached fluorine atoms in sp^3 hybridization, which can form four main configurations, *i.e.*, chair, boat, armchair, and zig-zag (**Figure 10**) [222]. FG can be prepared via two approaches: i) top-down method, which includes thermal, sonochemical, or microwave exfoliation of graphite fluoride [11], [221], [223] and ii) bottom-up approach where graphene is either directly fluorinated by XeF_6, F_2, and SF_6 [11], [224] or treated by fluorine radicals using SF_6, CF_4, or F_2 as plasma sources [225]–[227]. The remarkable FG properties predispose it in many application including electronics, electrochemistry, or biomedicine [228], [229].
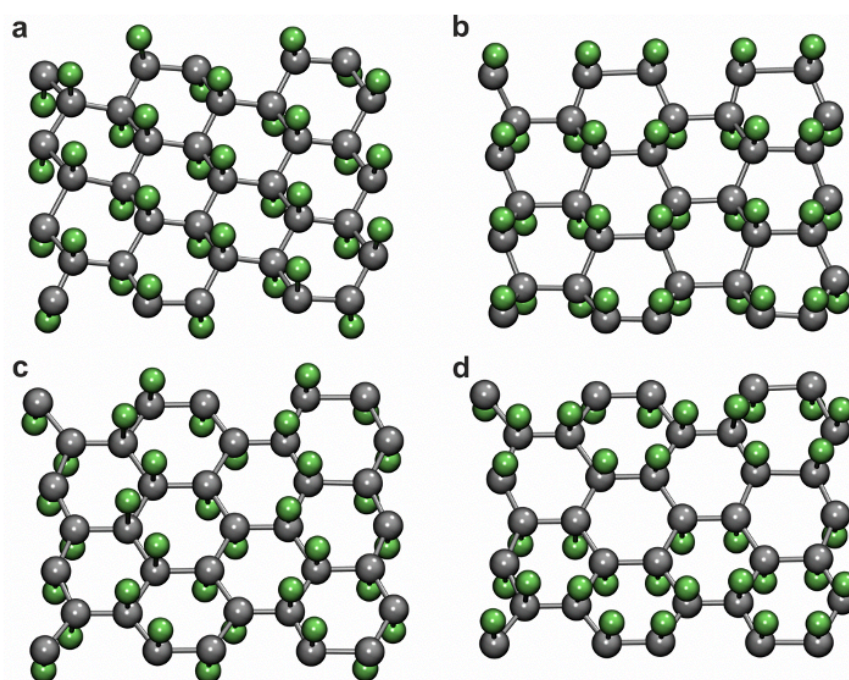
Figure 10 Four main configurations of fluorographene a) chair, b) boat, c) zig-zag, and d) armchair.

The presence of F atoms on both side of the graphene surface disrupts the π-electron cloud and modifies its electronic properties from a semi-metal into an insulator. The value of the bandgap of the FG is, however, ambiguous. While the experiments evaluate the bandgap to 3 eV using Raman spectroscopy [11] and 3.8 eV using near edge X-ray absorption spectroscopy (NEXAFS) [230], calculations at the generalized gradient approximation

(GGA) level estimate it at 3 eV **[19]** and the many-body GW theory, which accounts for single particle Green's function *G* and screened Coulomb interaction *W*, strongly overestimates the FG bandgap to 7-8 eV [231]. The combination of many-body GW and fixed-node diffusion Monte Carlo (MC) calculations gives the bandgap of 7.1 eV [232], which in combination with the exciton binding energy of 1.9 eV calculated using the Bethe-Salpeter equation [231] provides the gap of 5.2 eV.

FG is a highly important material for the further development of the graphene derivatives due to its propensity to react with electrophiles [233]. Initially, it was presumed that FG is chemically and thermally inert due to the strong covalent C–F bond, which resembles the one of very stable Teflon [11]. It was shown, however, that fully fluorinated graphene undergoes chemical transformation involving nucleophilic substitution and reductive defluorination under mild conditions, *e.g.*, FG can react with NaOH, NaSH, $NaNH_2$, CCl_2, which leads to new graphene-based materials [8], [184], [233]–[237].

FG is spontaneously defluorinated in the presence of nucleophilic solvents [234], which is attributed to the strong dipolar–dipolar interactions of the solvent molecules with the electron-deficient carbon atom of the C–F bond. The experimental-theoretical study of FG in *N,N'*-dimethylformamide has further revealed that the fluorine vacancies play the role of electrophilic radical centers that cause homolytic bond cleavages. In this way, point defects in FG can initiate its reactivity [238].

The reactivity of FG obviously depends on the strength of the C–F bonds. We found out that the bond strength varies from 1.11 to 5.13 eV depending on the configuration of the fluorine adatoms. FG is prone to form a specific pattern during fluorination and defluorination processes **[19]**. While defluorination favors the formation of zig-zag π-conjugated chains of sp^2 carbon along the fluorinated surface, various structural patterns can be formed by gradual fluorination (**Figure 11**). These specific patterns acquire either a metallic or semiconducting electronic structure and either FM or NM alignment **[19]**.
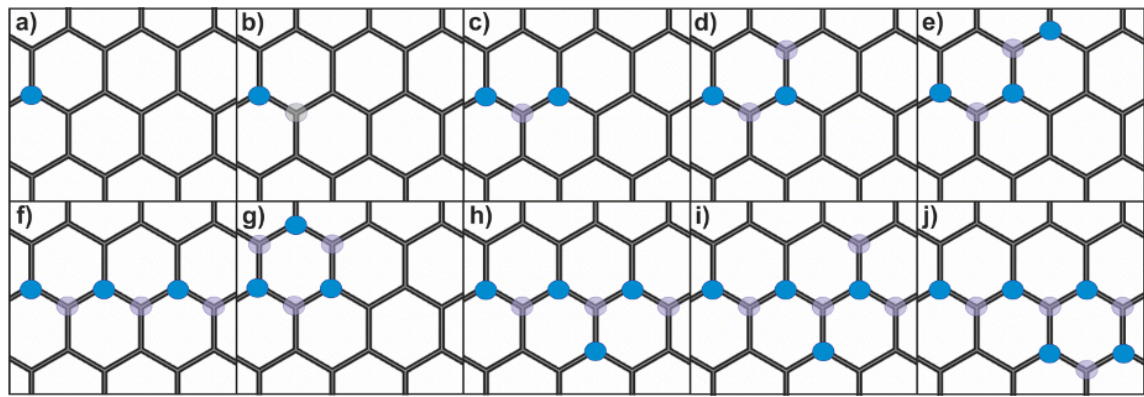
Figure 11 The preferable structural patterns during the gradual fluorination. The lowest-in-energy of a) $C_{18}F_1$, b) $C_{18}F_2$, c) $C_{18}F_3$, d) $C_{18}F_4$, e) $C_{18}F_5$, f) $C_{18}F_6$, g) $C_{18}F_6$, h) $C_{18}F_7$, i) $C_{18}F_8$, j) $C_{18}F_9$ [19].

The ability to tailor the electronic and magnetic properties of partially fluorinated FG samples by the proper positioning of F adatoms and different C/F ratios has also been demonstrated in other studies [224], [239]–[242]. The DFT calculations revealed that the precise location of the F adatoms on the graphene surface allows for tuning the bandgap from 0 to ~3.13 eV and establishing the magnetic alignment in FG **[19]**, [242]. The combined theoretical and experimental study has shown that monoatomic chains of fluorine atoms on graphene lead to strong magnetism in these purely organic graphene-based systems. The magnetic susceptibility data yielded behavior typical of a quantum spin-ladder system with FM legs and AFM rungs whose exchange coupling constant along the rungs was measured to be 450 K (**Figure 12**) [241].
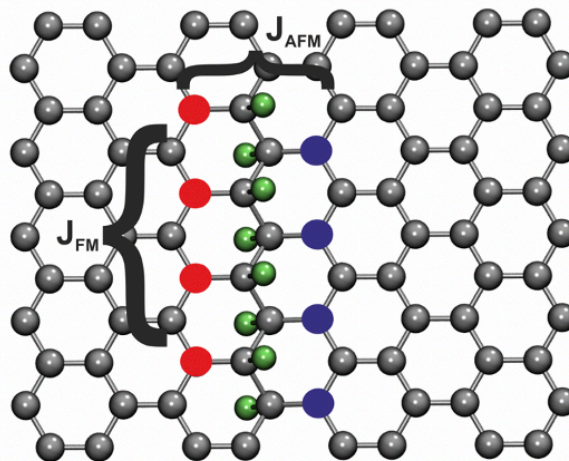
Figure 12 Monoatomic chains of fluorine atoms on graphene led to strong magnetism with exchange coupling of 450 K. The J_{FM} and J_{AFM} denotes ferromagnetic and antiferromagnetic coupling between the atoms. Red a green represents spin-polarized carbon atoms [241].

1.3 Cyanographene

The chemistry of FG turned out to be beneficial for the synthesis of a well-defined graphene derivative containing homogenously distributed –C≡N groups, *i.e.*, cyanographene (**Figure 13**) [9]. Reaction of FG with NaCN in dimethylformamide (DMF) leads to highly efficient nucleophilic substitution of F adatoms by nitrile groups. Simultaneous reductive defluorination partially re-establishes the delocalized π-electron cloud and thus increases the conductivity of G–CN.
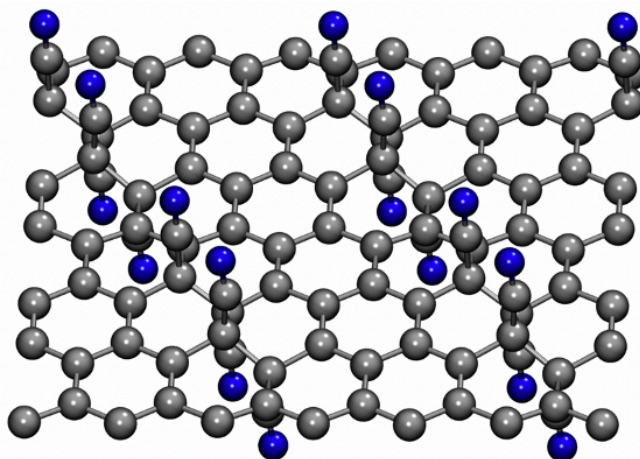
Figure 13 Theoretical model of cyanographene with –CN groups covalently attached to the graphene layer from both sides [9].

The well-defined stoichiometric G–CN can be used as a sensing material for the negatively charged analytes, for example for ascorbic and uric acid [186]. Further, the covalent –CN group turned out to be important for catalysis, particularly as a scaffold for SACs, *e.g.*, Pt **[15]** or Cu SAs [148].

Silver nanoparticles 4-8 nm of diameter covalently bound to G–CN has been proven to kill silver-nanoparticle-resistant bacteria at concentrations 30 times lower than stand-alone silver nanoparticles. The combined theoretical-experimental study showed strong and multiple dative bonds between –CN groups and silver nanoparticles. The G–CN prevents the leaching of silver nanoparticles, ascribing very high cytocompatibility to healthy human cells, which is a huge advantage over the commonly used ionic silver and free Ag nanoparticles [243].

The introduction of reactive homogeneously distributed functionalities over the graphene surface is highly desirable since it enables for further modifications as demonstrated during the synthesis of G–OOH [9].

1.4 Graphene acid

Various oxygen-containing functional groups are introduced into graphene through the oxidation processes [244]. These functionalities, particularly the carboxyl groups, increase the hydrophilicity of the material and provide many opportunities for further reactions and redox processes. However, the ambiguously defined structure of GO hinders further consistent and reproducible modifications of graphene [245]–[247], and the direct and exclusive attachment of −COOH groups to the graphene surface is very challenging.

Thus, a new approach to grafting −COOH functionalities with high degree of functionalization (13-15%), homogeneity, and selectivity has been developed, which led to a new graphene derivative, graphene acid (**Figure 14**) [9]. In the first stage, G–CN is synthesized from FG via reductive defluorination by using NaCN in DMF. The nitrile groups are then converted to carboxyl functionalities by acid hydrolysis with 20% HNO_3.
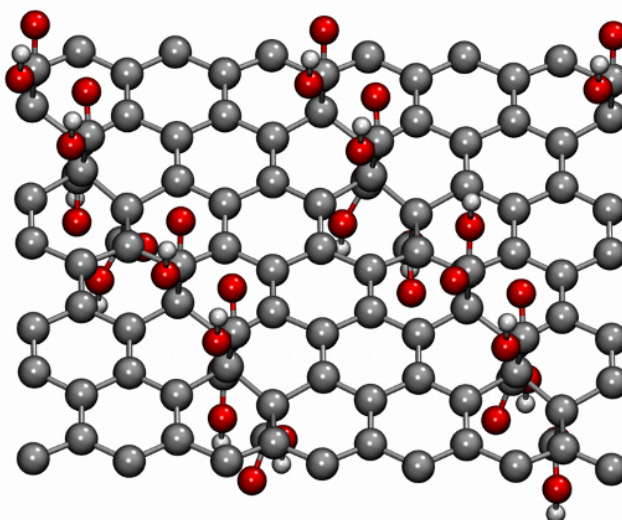
Figure 14 Theoretical model of graphene acid with –COOH groups covalently attached to the graphene layer from both sides [9].

G–OOH acquires extraordinary colloidal stability, biocompatibility, and low toxicity. Since the titration profile of G–OOH resembles the one of molecular organic acids, it is deemed as a 2D acid with pK_a of 5.2 [9]. Furthermore, theoretical calculations revealed that in some cases – depending on the functionalization degree, the distribution of functional groups, and the sublattice symmetry – the spin-up and spin-down states were split by exchange interaction indicating the possibility of stimulation of magnetic moments in some G–OOH. Specifically, the magnetic properties in G–OOH structures were triggered by a sublattice imbalance of the graphene bipartite lattice, caused by changes in its sp^2 hybrid states to sp^3 by covalent grafting of carboxyl groups. Importantly, many structural arrangements

led to a significantly reduced bandgap in the electronic structure of G–OOH with a quite pronounced density of states near the E_F, which indicates an appreciable conductivity [9]. Indeed, compared with GO, the conductivity of G–OOH increases, the sheet resistance of G–OOH was recorded as 6800 Ω sq^{-1}, which is five orders lower than the one of GO [186].

Despite that –COOH groups prefer to form chains over the graphene surface, they do not form intralayer hydrogen bond (H-bond) networks. However, molecular dynamics simulations demonstrated the formation of interlayer H-bonds when the pH is below the pK$_a$ of the system, and thus, the carboxylate groups are protonated. This agrees with the experiments showing the formation of spherulitic supramolecular G–OOH crystals after drying [9].

The carboxylic groups permit subsequent functionalization of the G–OOH system, the carbodiimide chemistry has been used to conjugate G–OOH with the aminothiol cysteamine, the aminoalcohol 2-(2-aminoethoxy)ethanol, and the diamine ethylenedioxy-bis(ethylamine) via the amide bond formation [9].

Further, the combined theoretical-experimental work has also shown that G–OOH can be used as an efficient and stable anode for LIBs **[17]**, [178], [186] as discussed in more detail in **Chapter 8**.

1.5 Porphyrins

Porphyrins belong to the group of heterocyclic macrocycle organic compounds, which are constituted of four pyrrole units interconnected via methine bridges. The parent component of porphyrins, porphine, is a planar continuous cycle with 18 π-electrons. Metals and/or ligands functionalized porphines are termed porphyrins. Porphyrin, being an aromatic system, absorbs in the visible region of the electromagnetic spectrum, hence the name porphyrin, which means *purple*.

TM coordinated porphyrins combine the inherent redox and magnetic properties of metal centers with those of the purely organic materials, making them promising materials for molecular magnets and molecular spintronics [248]–[250]. The combination of central TM atoms incorporated within the tetradentate ligand (**Figure 15**), tailored substituents, axial ligands, and the substrate influence the final performance and properties of these molecular assemblies [197]. Further, the SOC coupling of the central TM atom dictates the MAE of the porphyrin-based coordination polymer complexes [251]; free TM atoms bear large spin

and orbital magnetic moments, which, however, decrease in magnetic compounds due to electron delocalization and crystal field effects that compete with the intra-atomic Coulomb interactions. Such effects were found to decrease on surfaces and low-symmetry nanostructures [77], [86], [252], [253]. For instance, 1D metalloporphyrin chains prepared via a heat-assisted Ullmann-like coupling reaction of Fe(III)diphenyl-bromine-porphyrin (2BrFeDPP) on Au(111) **[18]** exhibit a MAE of 3.7 meV. Annealing at 600 K led to molecular planarization of poly-FePP on Au(111) leading to a decrease of MAE to 1.7 meV. SP-DFT calculations, including SOC, elucidated the origin of the molecules planarization and the reduction of MAE by reordering of the 3d levels of the central Fe atom (see **Chapter 6**) **[18]**.
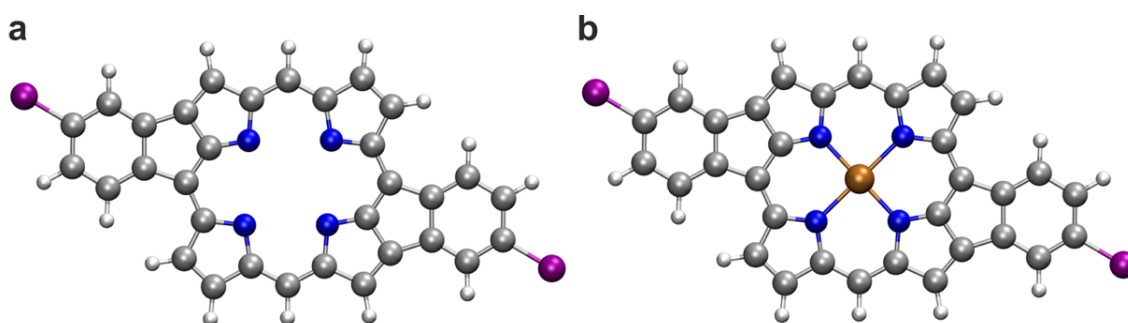

Figure 15 Stick-ball model of the 2BrFePP porphyrin molecule. a) metal-free molecule, b) molecule with an iron atom. Color code: carbon in grey, nitrogen in blue, hydrogen in white, bromine in purple, iron in ochre [18].

Due to numerous potential applications of porphyrins including catalysis, spintronics, molecular sensing, photosensitizers, and biological applications [35], [197]–[201], [254]–[257] many studies have focused on the self-assembly and self-metalation of porphyrin molecules on various surfaces [258]–[261]. Both freestanding and supported conjugated porphyrins oligomers and polymers with delocalized electronic networks [262], [263] have been the subject of research of many groups.

Due to the poor solubility of porphyrins, ultrahigh vacuum on-surface synthesis is performed (*cf.* **Chapter 6**) to obtain porphyrins molecules with TM-center, 1D molecular wires, or 2D porphyrin polymers on solid surfaces [197], [198], [264], [265] and characterized by microscopy techniques [140], [266]. For example, annealing of the fluorinated free-base 5,10,15,20-tetrakis(4-fluorophenyl)porphyrin (2H-4FTPP) deposited on the Au(111) surface at 500 K initiated its planarization via dehydrogenation and ring-closing reactions. Further annealing at 575 K allowed gold metalation from the Au(111) substrate. Final annealing at 625 K induced the activation of the C–F and C–H bonds, which

enabled intermolecular C–C coupling and the formation of porphyrin oligomers [267] (**Figure 16**).
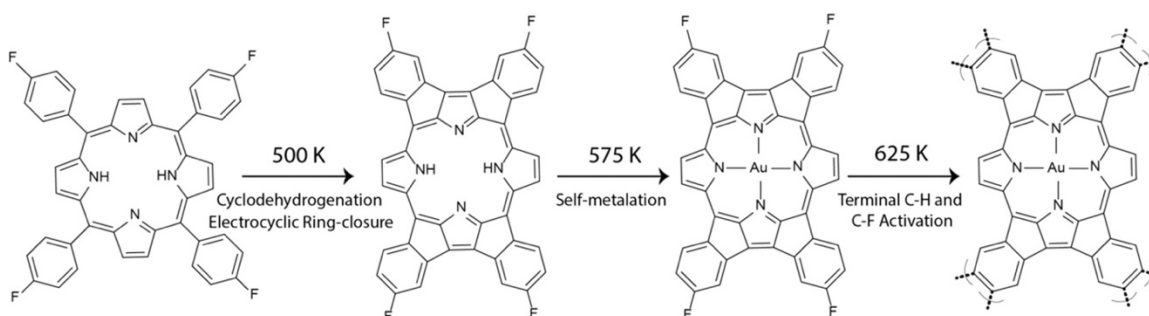
Figure 16 Thermal reaction pathways of 2H-4FTPP on Au(111). i) Planarization of the molecule via cyclodehydrogenation and electrocyclic ring closure, ii) self-metalation with an Au atom coming from the Au(111) surface, and iii) terminal C–H and C–F Bond activation. Reprinted with permission of [267]**.**

A gold metalation reaction was also experimentally carried out and theoretically described by Bruno de la Torre *et al.* [140]. The final configuration of the porphyrin molecule depends on the balance between the gain in the adsorbate–surface interaction energy and the deformation energy of the molecule. The theory showed that the heat induced planarization and electrocyclic ring closure of 2H-4FTPP were attributed to a reduction of the bond-dissociation energy of the pyrrole's C–H bonds of the Au(111)-supported porphyrin molecule compared to that in the gas phase. On the other hand, the C–F bond exhibited the highest bond dissociation energy (BDE), which makes it the least likely to be perturbed [140].

The redox properties of porphyrin molecules and polymers are utilized in oxidation reactions [268], *e.g.*, porphyrinic metal-organic-frameworks (MOF) have shown the ability to selectively catalyze the oxidation of cyclohexane under mild condition [269]. The conjugated electronic system and the strong absorption of visible light of the porphyrin are beneficial for plethora of applications: TiO_2-supported porphyrins are used in solar energy harvesting [270], porphyrin polymers in photodynamic therapy [271], [272], deposited on reduced graphene oxide or platinum are used for photochemical splitting of water [273], and porphyrin nanocomposites are utilized in photonics [274].

Last but not least, porphyrin molecules play a key role in many biological systems. One of the most important porphyrin compounds for human beings – heme – is the iron-containing oxygen-carrying metalloprotein in red blood cells, which transports oxygen from the respiratory organs to the rest of the body. Porphyrin molecule containing magnesium is an

important part of chlorophylls, which absorbs energy from light and participates in the CO_2 fixation process in plants.

2 Magnetism of graphene derivatives

For several centuries it was presumed that the phenomenon of magnetism only concerned TMs, their alloys, rare earth elements and their compounds. This view has changed with the first reproducible experimental reports of magnetism in *p*-orbital based compounds from 1991 with the discovery of crystalline *p*-nitrophenyl nitrooxide (*p*-NPNN) [275] and the charged complex of C_{60}–TDAE (tetrakis(dimethylamino)ethylene) [276] displaying FM ordering due to the ion-radicals [101], but only at low temperatures (0.6 K and 16 K, respectively). These materials brought the attention of the scientific community to organic magnetic materials [97].
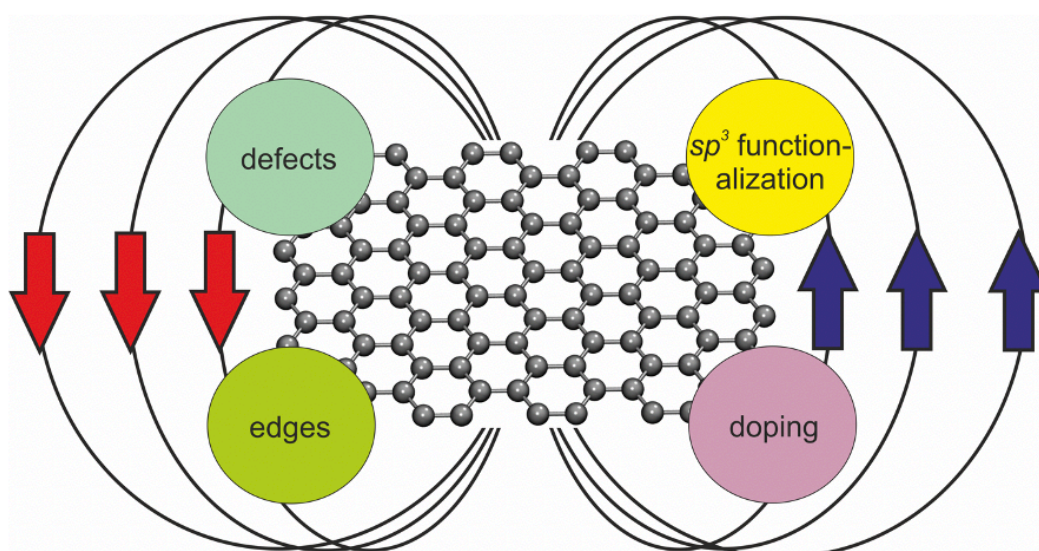
Figure 17 Diverse methods have been employed to imprint magnetic alignment in graphene, *e.g.*, vacancy defects, edge engineering, doping with foreign atoms, and *sp³* functionalization.

Since the discovery of graphene in 2004 [4], and later the synthesis of graphene derivatives, many groups have focused on imprinting and tailoring their magnetic properties (**Figure 17**).

The theoretical understanding of graphene magnetism can be described in terms of the tight-binding model, the Hamiltonian model, the Hubbard model, or the mean-field approximation. The one-orbital mean-field Hubbard model seems to be the simplest model to analyze the magnetic properties of sp^2 carbon nanostructures. The unhybridized p_z orbitals in graphene give rise to low energy π-symmetry electronic states. The mean-field

Hubbard model considers the π-symmetry electronic states [97] where the Hamiltonian is given as

$$H = H_0 + H_I \tag{1},$$

where H_0 and H_I are the kinetic and interaction parts of the Hamiltonian, respectively. The kinetic Hamiltonian characterizes the nearest-neighbor (NN) tight-binding Hamiltonian and is given as

$$H_0 = -t \sum_{\langle i,j \rangle \sigma} \left[c_{i\sigma}^\dagger c_{j\sigma} + h.c. \right] \tag{2},$$

where t indicates the hopping integral between neighboring i-th and j-th sites belonging to the A- and B-sublattice (**Figure 9a**), respectively, $c_{i\sigma}^\dagger$ and $c_{j\sigma}$ are the creation and annihilation operators, respectively, which create and annihilate an electron at site i with spin σ. The term $h.c.$ is the Hermitian conjugate part of the Hamiltonian. The consideration of nearest-neighbor atoms is denoted by the angular bracket. H_0 can predict the electronic structure of sp^2 carbon atoms.

The on-site Coulomb interaction (interaction part of the mean-field Hubbard model) explains the emergence of magnetism and is expressed as

$$H_I = U \sum_i n_{i\uparrow} n_{i\downarrow} \tag{3},$$

where U is the magnitude of the on-site Coulomb interaction. The spin-resolved electron density at the i-site is given by $n_{i\sigma} = c_{i\sigma}^\dagger c_{j\sigma}$. This model involves only the nearest neighbor interactions, which means that only two electrons that occupy the same p_z atomic orbital are considered. This could be overcome by the mean-field approximation where a spin-up/-down electron at the i-site interacts with an average electron density. The Hamiltonian is then defined as

$$H_{mf} = U \sum_i \{ n_{i\uparrow} \langle n_{i\downarrow} \rangle + \langle n_{i\uparrow} \rangle n_{i\downarrow} - \langle n_{i\uparrow} \rangle \langle n_{i\downarrow} \rangle \} \tag{4}.$$

The induced magnetic moment in graphene depends on the parameter U/t. With a correct choice of U/t, one can obtain similar solutions compared to those from the first-principles calculations.

Alternatively, the magnetism in graphene can be described based on Lieb's theorem [277], the counting rule [101], and the Stoner criterion [278]. The number of zero-energy states in the tight-binding model is then given, based on the counting rule, as

$$\eta = 2\alpha - N \tag{5},$$

where N denotes the total number of sites and α is the maximum possible number of non-adjacent sites [101]. According to Lieb's theorem [277], the total spin of a bipartite system can be calculated as

$$S = \frac{1}{2}|N_A - N_B| \tag{6},$$

where N_A, N_B are the numbers of sites in sublattices A and B, respectively. Together, the counting rule and Lieb's theorem are connected as

$$\eta \geq |N_A - N_B| \tag{7}.$$

Further, the Stoner criterion decides about the magnetic character of the materials. It is based on the competition between the loss of kinetic energy and the gain in exchange energy due to spin polarization of a system. The exchange splitting of the electronic states in a spin polarized system can cause a gain in the exchange energy [279]

$$\Delta S = \varepsilon_\uparrow - \varepsilon_\downarrow = \frac{U}{2}\sum_i n_i{}^2 \tag{8},$$

where $\sum_i n_i{}^2$ determines the degree of localization of the corresponding state. The loss of kinetic energy is proportional to this state. If $U > 0$, the material becomes spin polarized and zero-energy states appears in DOS plot. Thus, spin polarization prevents the instability of low-energy states in the system.

Usually, the s- and p-block elements have higher kinetic energy than the exchange energy. Thus, they tend to be NM as the loss of kinetic energy dominates over the gain in exchange energy. The reduction of the dimension, the presence of defects and other atoms at the interface or surface eventually overcome this obstacle, and organic-based materials may become magnetic.

2.1 Defects in graphene

Defects crafted in the graphene structure (**Figure 18**) alters its chemical, mechanical, and electronic properties. Moreover, defects can induce magnetic moments in naturally

diamagnetic pristine graphene as was shown in numerous theoretical and experimental studies [97]. In principle, both vacancy and adatoms remove p_z orbital from graphene π-cloud leaving unpaired electrons [101]. These defect states were experimentally confirmed with STM. Theoretically, zero-energy states, also called quasi-localized states or midgap states, appear at the E_F in the electronic structure of graphene and spread around the defects, forming the characteristic $\sqrt{3} \cdot \sqrt{3}R30°$ patterns in the spin density distribution plots [98]. First-principles calculations for defect-induced magnetism have shown that itinerant magnetism is sustainable over the wide range of defect concentrations [279], [280]. However, while hydrogen adsorption demonstrated narrow states at E_F, bond reconstruction due to a single vacancy defect resulted in partial suppression of the magnetic moments and broadening of the states around E_F. This has also been shown experimentally as a profound peak in STM measurements [280].
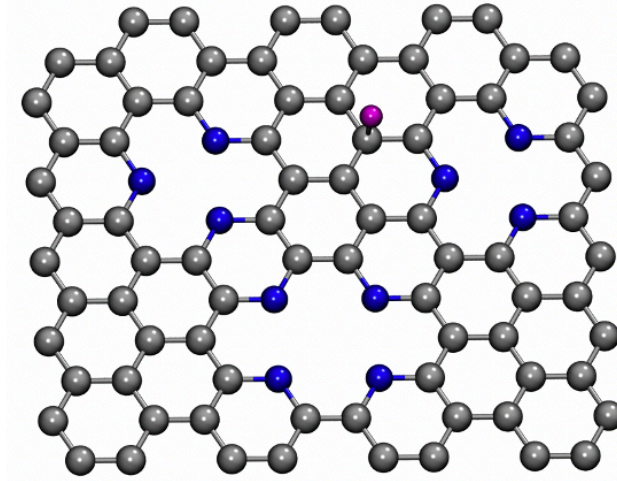
Figure 18 Vacancies and adsorbed adatoms can induce magnetic moments in graphene. Color code: Carbon atoms in grey, atoms around vacancy defects in blue, adatom in purple.

Furthermore, the position of hydrogen adatoms on the graphene lattice can be precisely manipulated by using STM, which allowed for tuning of magnetic properties based on disbalancing of the graphene bipartite lattice. The conductance *dI/dV* spectra of two hydrogen adatoms adsorbed to graphene showed two regimes: i) no midgap states were observed when hydrogens were bound onto the different sublattice (NM regime) and ii) H adatoms adsorbed to the same sublattices showed midgap states at E_F (magnetic regime). Moreover, a large extension of the local magnetic moments related to H adatoms indicated long-range magnetic interactions mediated by direct exchange [281]. Additionally, SAs were implanted and manipulated into the graphene lattice by electron-beam irradiation and

STM [109], [282], which enables the positioning of individual dopants or specific groups in graphene, thus, tailoring its final properties.

2.2 Edge modification of graphene

Generally, three spatially confined carbon forms derived from graphene can be distinguished: graphene nanoribbons (GNRs), graphene nanoflakes (GNFs), and graphene quantum dots (GQDs). The magnetism in these materials depends on its shape and edge type, which also influences their stability and electronic band structure [283].

Theoretical calculations revealed that zig-zag edges (**Figure 19**) are exhibited as non-bonding π-electron edge states with energy levels appearing at E_F; the presence of such states has also be recognized in several experimental studies [104]. These states emerge due to the broken symmetry of the pseudospins; the unpaired electrons (with $S = 1/2$) in the non-bonding π-orbital of the zig-zag edge are localized, thus forming a strongly spin-polarized region. As a result, the finite-sized graphene with zig-zag edges becomes magnetic. These states are absent in the case of the NM armchair edges (**Figure 17**). The edges can be terminated by hydrogen atoms which creates edges without s-dangling bonds promoting the stability of these materials [104].
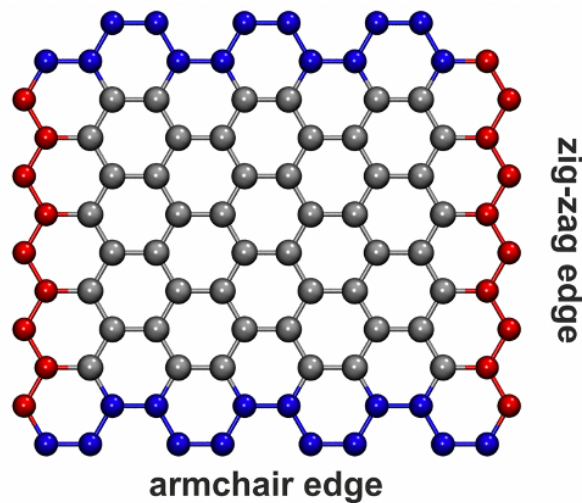

Figure 19 In contrast to armchair edges (in blue), zig-zag edges (in red) imprints magnetism in graphene.

GNRs are commonly produced by chemical unfolding of CNTs by oxidation reagents, electrical current or high-pressure, organic synthesis, or CVD technique [189]. For an arbitrarily shaped sheet of GNRs with a combination of armchair and zig-zag edges, a ferrimagnetic (FIM) alignment can be established. Basically, two types of interaction between edge-state spins are recognized: i) intra-edge interaction between spins lying along

the same edge, which is strong and of FM character [189] and ii) inter-edge interaction between spins on opposite edges, which is moderate and can be either FM or AFM depending on the mutual geometry between the edges [189]. The width between the edges, edge saturation, doping, and defects further affect the final properties of GNRs [283]–[285], which naturally complicates the interpretation of experimental observations of edge magnetism in this material.

GNFs are, in contrast to 1D GNRs, considered as 0D sp^2 carbon allotropes, which can bear magnetic ordering depending on their size, shape, and symmetry [286], [287]. Theoretical calculations revealed FM, AFM, and mixed states in GNFs according to Lieb's theorem [277] Moreover, doping, applied strain, or external field further alters their properties [285]. The combined experimental-theoretical study of GNFs revealed a low-temperature FM ordering with an experimental Curie temperature, T_c, of 37 K. The magnetic measurement at 5 K showed a coercivity of 72 Oe and a magnetization of 0.45 emu g^{-1} [285]. DFT calculations taking into account various size and shape models of GNFs revealed that, regardless of the GNF shape, the zig-zag edges induce spin-polarized electronic states, whereas the armchair edges are non-magnetic. The nearest-neighbor carbon atoms residing different sublattices were coupled in the AFM manner in line with the theorem by Lieb [277], the atoms localized inside the carbon flake were NM, but on the other hand the zig-zag edges led to the local imbalance of graphene lattice, establishing edge FM [285]. Such localized states have been observed by scanning tunnelling spectroscopy (STS) [288]. As with GNRs, while intra-edge coupling could be of FM or AFM alignment, inter-edge coupling was responsible for suppressing FM ordering. Theoretical calculations revealed morphology-driven magnetism of GNFs, resulting from synergistic effects of size, geometry, edge terminations, and angle between adjacent edges. As shown in **Figure 20,** the lowest T_C was found for rectangular and trapezoidal flakes that contain both magnetic zig-zag edges and NM armchair edges. The largest T_C of 107 K was calculated for the triangular flake which possess a predominant intra-edge coupling between the zig-zag edges and sharp corners. A median T_C of ≈47 K calculated for various GNF morphologies and sizes corresponds well with the experimentally observed T_C [285].
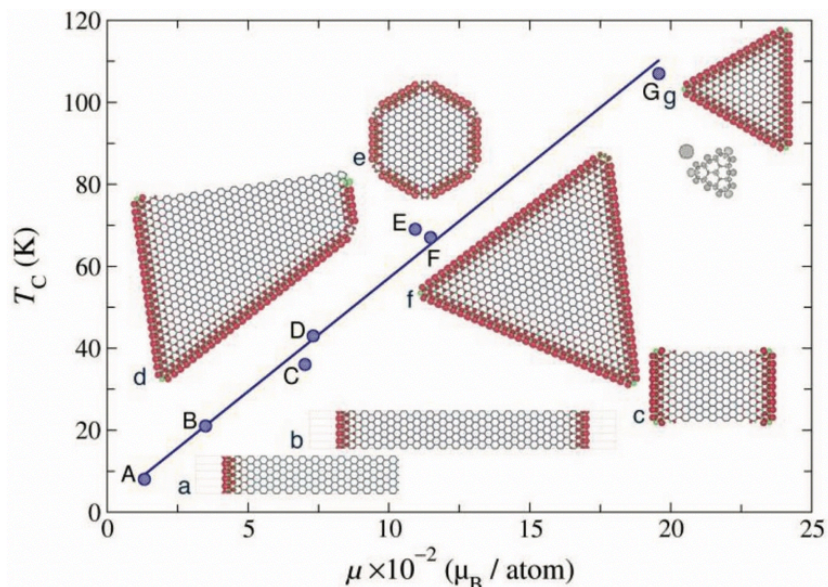
Figure 20 Predicted T_C values of various GNR and GNP structures: The calculated T_C for graphene flakes of various shapes and sizes (as shown in the insets) versus magnetic moments (normalized per number of atoms) indicating stability of the ground FM state. The graphene flakes are labeled by small letters; the corresponding point on the plot is indicated by a capital letter. Reprinted with permission from [285].

2.3 Functionalization of the graphene layer

The sp^3 functionalization of the graphene layer (**Figure 21**) is another effective strategy to adjust its physicochemical properties for a given application. Particularly, it tunes the bandgap and the hydrophobicity/hydrophilicity of graphene, and prevents aggregation of graphene layers [97]; it also imprints magnetic features into graphene.

DFT calculations indicated that any molecule attached to the graphene layer through a weakly polar single bond imprints a magnetic spin moment of 1 μ_B [289] in agreement with the theorem by Lieb [277]. The magnetic moments align ferromagnetically on the same sublattice. In contrary, sp^3 functionalized opposite sublattices tend to couple antiferromagnetically.
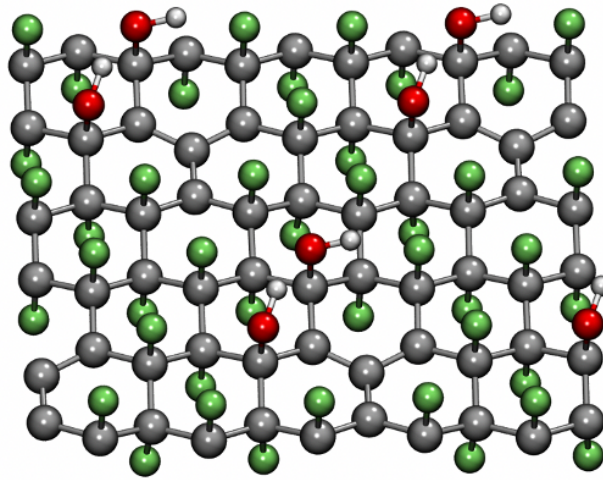
Figure 21 The *sp³* functionalization of graphene can lead to a magnetic ordering that is stable up to room temperature. Color code: carbon in grey, fluorine in green, oxygen in red, hydrogen in white [10].

Graphane, the fully hydrogenated graphene derivative, is a NM semiconductor with a wide bandgap of 3.5 eV. The strong covalent C–H bonds cause transition from sp^2 to sp^3 states and confines the p_z electrons into the chemical bonds, which is manifested by the disappearance of the π-bands. The σ-bands move to the top of the valence band, which is accompanied by a large opening of the bandgap [12]. A single H-vacancy defect in the graphane lattice leads to the formation of a localized state with an unpaired spin and, accordingly, the formation of a defect level in the energy gap (*vide supra*) [290]. Subsequent hydrogenation, the C/H ratio, and the configuration of H adatoms further tune the properties of graphane. For example, first-principles calculations for single-side hydrogenated graphene with H adatoms distributed over the same graphane sublattice, also known as graphone, predicted FM alignment with the estimated Curie temperature between 278 and 417 K [291]. Since the strong C–H bonds break the π-bonding network and leave the electrons in the unhydrogenated C atoms localized and unpaired, the magnetic moments are presented on the unhydrogenated sp^2 C-atoms. The long-range magnetic coupling in graphone can be ascribed to the large spatial extension of the valence electrons in the *p*-states [291].

Similarly, the properties of fully fluorinated graphene, which is considered as the thinnest insulator, could be modulated by the degree of F coverage and its configuration **[19]**, [242]. The spin number increases monotonically with the higher degree of fluorination [100]. More recently, a combined experimental–theoretical work demonstrated that monoatomic chains of fluorine atoms attached to graphene led to strong magnetism with exchange coupling of

450 K (see **Subchapter 1.2**). Two edges were separated by a nearly impenetrable CF-nanoridge which acted as a high-energy barrier for the graphene π-electron cloud. Magnetic susceptibility data revealed a behavior typical of a quantum spin-ladder system with FM legs and AFM rungs (see **Figure 12**) [241].

Resembling graphone, a recently prepared single-side semi-fluorinated graphene (C_2F) should be FM according to Lieb's theorem since the fluorine atoms are adsorbed on the same sublattice of graphene [292]. However, dissimilarly to graphone, C_2F was shown to be at the edge of the AFM–FM instability, which in combination with the Dzyaloshinskii–Moriya interaction can lead to a skyrmion state [293].

The tendency of FG to nucleophilic substitution reaction enabled to prepare a new graphene derivative, GOHF (**Figure 22a,b**), via the ultrasonic exfoliation of fluorinated graphite in DMF and subsequent treatment of FG with aqueous tetramethylammonium hydroxide [10]. At the proper chemical composition, sp^3/sp^2 coverage, and the position of the –F and –OH groups, GOHF exhibits FM magnetic ordering up to 62 K and AFM alignment sustainable up to 372 K (**Figure 22e,f**). Theoretical calculations elucidated these observations by diradical motifs – m-xylylene and trimethylenemethane motifs – embedded in the sp^3 lattice of GOHF, where the –OH groups mediate the coupling between carbon atoms through superexchange interactions as indicated in atom-resolved DOS (**Figure 22c,d**), showing the spin-split midgap states at E_F with a significant contribution of –OH-derived states [10]. These diradical motifs emerge only above the site percolation limit of the graphene lattice, *i.e.,* the sp^3 functionalization must reach a defined level for both the generation of diradical motifs and suppression of the lateral diffusion of adatoms that would ruin the periodic pattern of sp^2 magnetic islands over the graphene sheet. The presence of diradical motifs has also been experimentally proved by electron paramagnetic resonance (EPR) spectra [10].
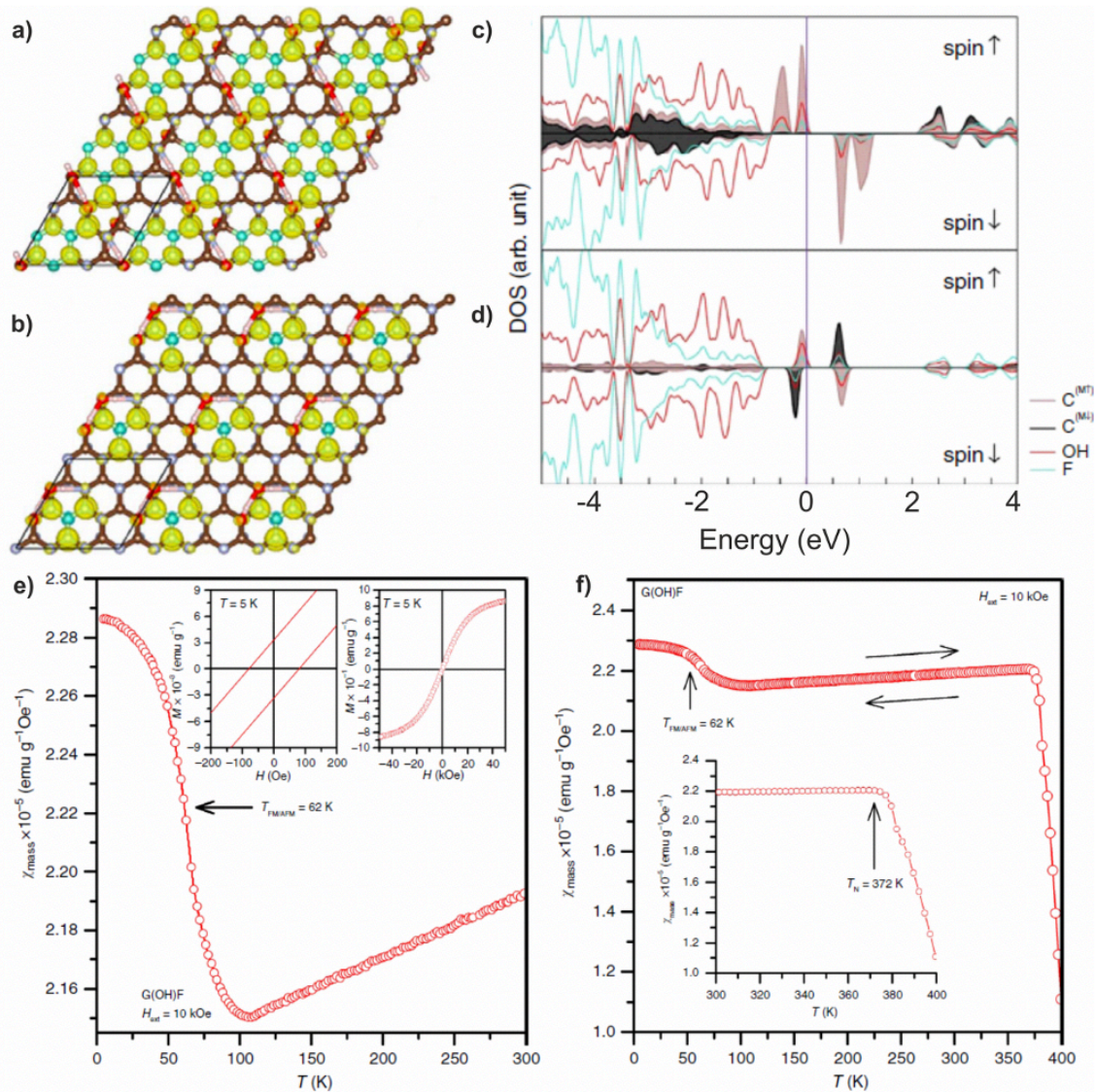
Figure 22 a) The *m*-xylylene-like motif (green) of GOHF embedded in an *sp³* lattice with up/down spin densities shown in yellow/blue. b) The *sp³*-embedded trimethylenemethane-like motif with the corresponding FM spin density. Brown/green, blue, red and pink balls represent carbon, fluorine, oxygen and hydrogen atoms, respectively. c,d) DOS of the GS FM phase corresponding to the *m*-xylylene-like motif and the trimethylenemethane-like motif, respectively. e) Temperature evolution of the mass magnetic susceptibility (χ_{mass}) of GOHF showing the FM-AFM transition at 62K, and f) the AFM-PM transition at 372 K [10].

However, the reaction of FG with KOH in ethanol led to the formation of GOHF, in which the zig-zag motifs of *sp²* carbon atoms passing through the *sp³* carbon lattice with the –F and –OH groups attached were observed by STEM validating the computational structural models (**Figure 23a,b**) and they provide a suitable matrix to stabilize the FM ordering up to RT (**Figure 23c**). Nucleophilic substitution promotes the formation of radical centers in the s*p³* region and the emergence of superexchange interactions, whereas the defluorination

pathways lead to the formation of sp^2 zig-zag motifs that act as communication pathways between radical motifs involving itinerant π-electrons (**Figure 23d–f**) [21].
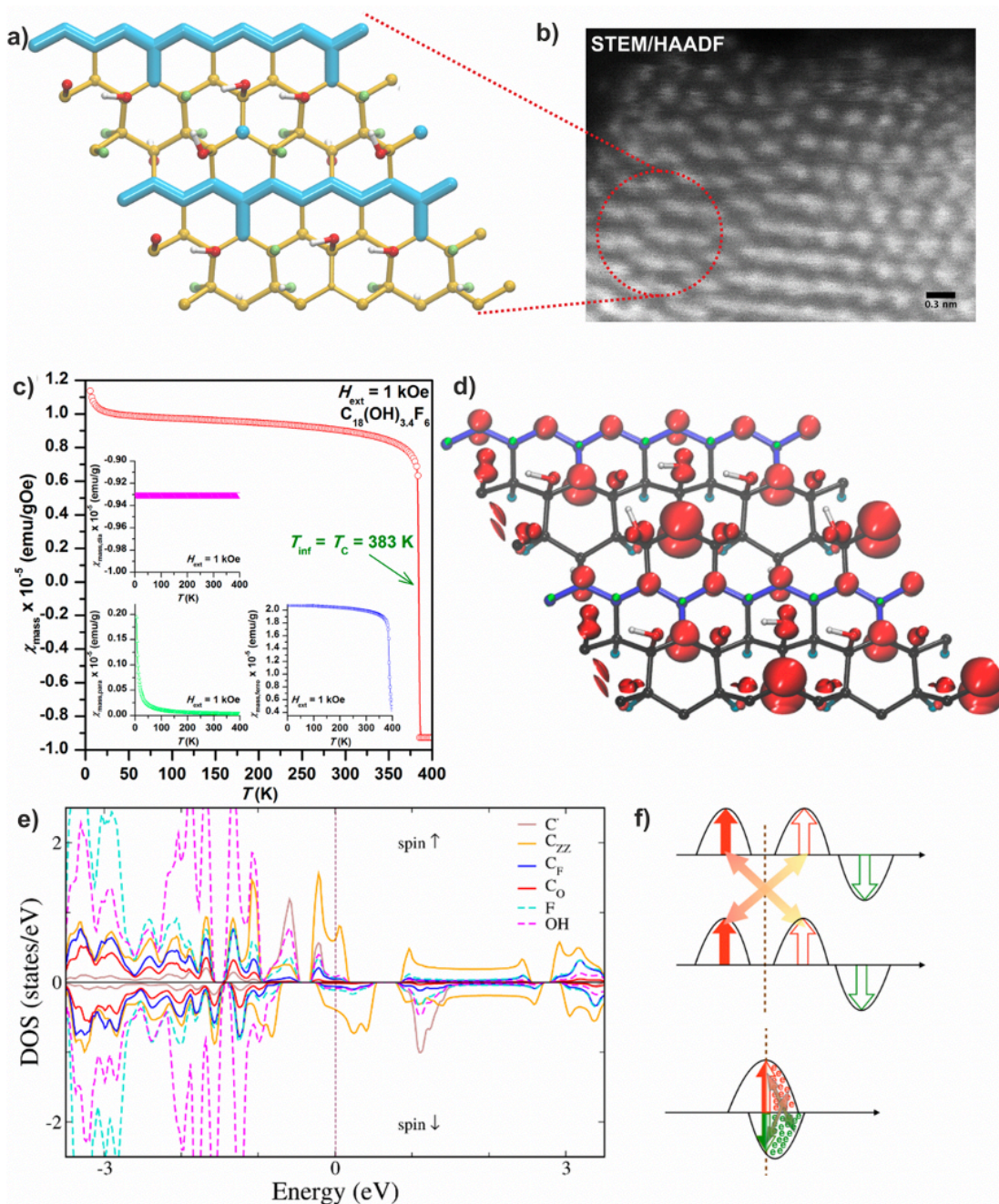
Figure 23 a,b) Scanning transmission electron microscopy/high-angle annular dark-field imaging (STEM/HAADF) with evident zigzag patterning in agreement with the theoretical model. c) Temperature evolution of the mass magnetic susceptibility (χ_{mass}) recorded for the $C_{18}(OH)_{3.4}F_6$ showing FM-PM transition at 383 K, d) GOHF model with spin density distribution (positive shown in red and negative in green) plotted for isosurfaces at 5×10^{-3} eÅ^{-3}, e) corresponding atom-resolved spin-polarized DOS plot showing a continuum of states at E_F predominantly composed of π-chain states and the electronic states of the radicals, −OH groups, and −F adatoms. f) schematic DOS of

the two parallel-aligned magnetic moments with a FM superexchange interaction (top) and itinerant electron magnetism with the interaction of magnetic spins mediated by conduction π-electrons (bottom) Reprinted with permission from [21].

2.4 Doping with foreign atoms

Foreign atoms introduced into the graphene lattice during synthesis processes can lead either to electron doping using *n*-dopants [112], [294] or hole doping using *p*-dopant [295]. Both type of dopants modifies electronic structure of graphene by changing the position of E_F (**Figure 9c**). Such doping has been theoretically and experimentally demonstrated for doping graphene with nitrogen and boron atoms [107], and while the Dirac point of graphene has been downshifted in N-doped graphene, in B-doped graphene it has been upshifted with respect to E_F [107].

Further, the substitution of carbon by light elements in the graphene lattice can induce FM ordering in diamagnetic graphene. The combined theoretical-experimental studies have shown that depending on the position and concentration of sulfur [7] and nitrogen atoms [6], the FM alignment can occur [108]. Below 4 at.% of sulfur and 5 at% of nitrogen, even though PM centers were imprinted upon doping, they did not lead to magnetically active configurations. However, the increased concentration of dopants led to higher number of induced PM centers eventually forming magnetically active motifs (**Figure 24**). The theoretical calculations confirmed FM long-range ordering between PM centers mediated via π-electron system sustainable up to 62 K (S-doped graphene, [7]) and 69 K (N-doped graphene, [6]) with graphitic dopants playing the principal role.
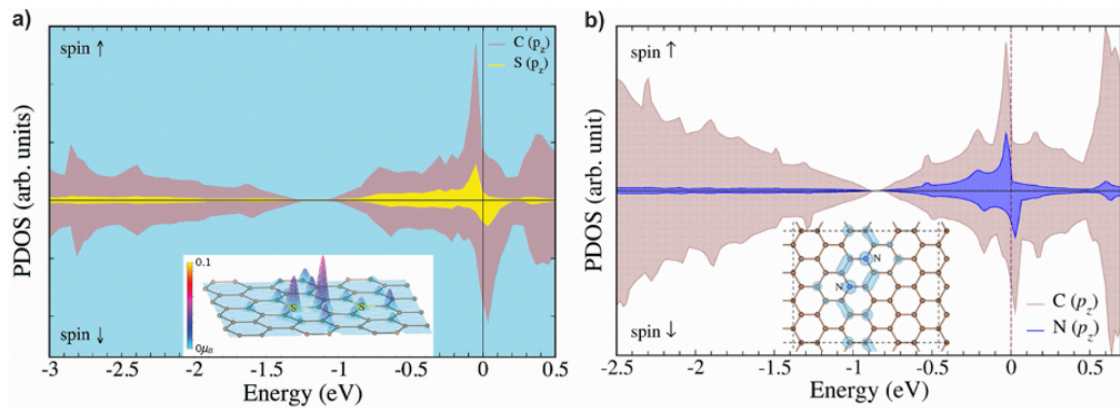
Figure 24 a) Partial density od states (PDOS) of graphene doped by 4.2 at.% of sulfur; b) PDOS calculated for graphene doped with nitrogen embedded in the lattice at *para* positions at a concentration of 4.2 at.%. The supercells are shown in the insets. Reprinted with permission from [6] and [7].

Besides the FM-imprinting graphitic nitrogen atoms, N-doped graphene with only pyrrolic nitrogen at relatively high concentration of 11 at.% of nitrogen was shown to stabilize FM ordering up to 678 K [296]. Pyridinic N-atoms at 9.8 at.% doped into the graphene lattice imprinted localized spin-polarized centers, S_L, and spin-containing sites with itinerant-like spins, S_I. These two spin domains, separated by diamagnetic region, are coupled via exchange interaction which drives the spin-switch effect under microwave irradiation at X-band frequency [55] (**Figure 25**). Under the application of large microwave flux density, P_a, the exchange interaction, J_{ex}, exceeds a thermal barrier and causes a spin-flip-flop transitions between S_I and S_L sites (**Figure 25**). This makes such material convenient for transistors or spintronic devices without the need of spin-injecting FM substrate.
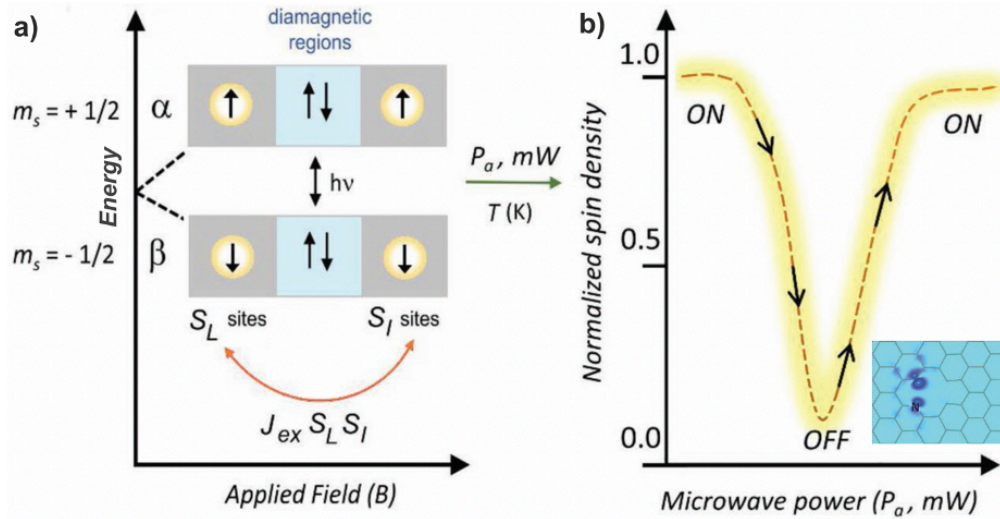
Figure 25 a) Model of two distinct spin systems (the S_L and S_I sites) embedded in nitrogen-doped graphene, separated by a diamagnetic region. When the exchange interaction (J_{ex}) exceeds $k_B T$ and under the application of large microwave flux density (P_a), b) spin-flip-flop transitions from uncoupled and saturated S_I and S_L sites intercross the energy band of the coupled system ($S_I S_L$). Theoretical structure of N-doped graphene is shown as inset. Reprinted with permission from [55].

Besides doping with light elements, $3d$ elements from Group 4 of the periodic table and from Group 6 $5d$ Pt and Au have also been considered in graphene [80], [297], [298]. High resolution-transmission electron microscopy (HR-TEM) revealed easy diffusion of Pt and Au along the pristine graphene lattice at 873 K [88] with an activation barrier from vacancy centers of 2.2-2.5 eV and a much lower barrier of 0.14 eV (theoretical value for Pt) and 0.28 eV (experimental value for Au) on pristine graphene. This was further corroborated by theoretical calculations for Ag, Cu, and Au clusters on graphene [299] and $4d$ and $5d$ TMs on Graphene/Ru(0001) [300]. Thus, lattice imperfections such as atomic vacancies may prevent them from diffusing [23]. DFT calculations revealed strong binding of $3d$ elements in vacancy defects with migration barriers around $2-4$ eV for metals at SV and slightly higher for DV [80]. Further, V, Cr, Fe, Co, and Ir atoms induced magnetic moment in defective graphene [23], [298] which can be explained by a simple local-orbital picture, involving the hybridization and electron filling of sp^2 carbon atoms and spd orbitals of TM [80]. Interestingly, while Fe@SV and Cu@DV are NM, the Fe@DV and Cu@SV complexes have high magnetic moments [80].

Recent ion beam implantation and electron-beam manipulation of foreign atoms into graphene [109], [282], [301], [302], as well as STM [281], which enables precise positioning of foreign atoms, make doped graphene promising for spintronics and magnetic

data storage. It is worth recalling that that several studies have focused on the MAE of TM atoms and the MAE enhancement by embedding TM dimers into defects in the graphene lattice [23], [76], [84] (*cf.* **Introduction**). MAE in graphene with vacancy defects, both bare and nitrogen-decorated, doped by Cr, Mn, and Fe atoms and TM dimers was also a subject of our study **[14]**. Mn dopants experimentally observed in the graphene lattice by STEM may create spots for the Fe–Mn dimer formation with a large MAE of 120 meV corresponding to the blocking temperature of 34 K **[14]**.

2.5 Theoretical calculations of magnetic transition temperature

The magnetic transition temperature is an important parameter determining the suitability of a magnetic material for practical applications. Raising the temperature to the Curie point disrupts the FM alignment of the material, leading to random alignments of the magnetic moments, an analogous AFM-PM transition is reached at the Néel temperature. Since it is generally difficult to find an exact solution to an interacting many-body system [303], several approaches have been proposed for calculating the Curie temperature, T_C.

One option to calculate the T_C is to use the mean-field approximation (MFA), which assumes that each spin only interacts with the average spin number from neighboring atoms via exchange interactions that decay very quickly with a distance, so in practice only the NN spins are assumed to interact. Then, one can express the exchange interaction using the Heisenberg model and the Hamiltonian operator as [304]

$$H = -J \sum_{\langle kl \rangle} S_k S_l \tag{9},$$

where J denotes the exchange interaction constant and the brackets under the sum sign suggests that the sum is taken only on the NN pairs.

By using the Langevin and Brillouin functions, a general formula can be derived [305], [306]

$$T_C = \frac{S(S+1)Jz}{3k_B} \tag{10},$$

where S is the spin number, z denotes the coordination number, and k_B is the Boltzmann constant. The exchange interaction is expressed as [307], [308], [306], [309]

$$J = \frac{\Delta E}{2zS^2} \tag{11},$$

where ΔE is the energy difference between FM and AFM phases.

By combining Eq. 10 and Eq. 11 for $S = 1$, the mean-field approximation yields the equation [22], [310], [311]

$$T_C = \frac{2\Delta E}{3k_B N_m} \tag{12},$$

where N_m is the number of considered magnetic atoms. The MFA typically provides a higher T_c estimate compared to the experimental one. For example, MFA provided even 2–7 times higher values compared to experimental results for 1D quantum-dots arrays of BN nanoflakes [310]. In our calculations of sp^3 functionalized graphene with sp^2 diradical islands the values were 2–11 times higher than the experimental values. The MFA therefore offers a rather upper-limit for the T_C estimate at relatively low cost **[22]**.

Several improvements to the MFA have been proposed. A natural step beyond the standard MFA approach is to consider a spin cluster under the effective field instead of individual spins as applied in the cluster mean-field (CMF) method or the correlated cluster mean-field (CCMF) theory, which account for small clusters under the effect of correlated self-consistent mean fields [303]. These methods allow a very accurate estimation of critical temperatures at a low computational cost for systems with $S = \frac{1}{2}$.

Another model, the Ising model, takes into account the up or down orientation of spin moments with $S = \frac{1}{2}$. Taking into account the interaction of the spin moments of individual atoms in the graphene lattice, the Ising model on a triangular lattice [22], [312] can be expressed as

$$T_C = \frac{0.3797J}{k_B} \tag{13}.$$

It can provide excellent agreement with measured magnetic FM-AFM transition temperatures as shown for G(OH)F systems [22], [313].

In the Ising model, the magnetic exchange coupling constant is usually associated with the energy difference between the FM and AFM spin arrangements, $J = \Delta E/2z$. However, in complex system such as in G(OH)F [313], spin-flip of the FM phase led to ferrimagnetic states instead of the AFM phase. To solve this issue, the PM state is calculated by a spin singlet with all electrons paired, although the PM state can be maintained by thermal effects with local moments pointing in random directions. The use of PM states instead of AFM

phase usually yields an upper estimate of T_C as shown for G(OH)F whose T_C was two and five times higher compared to the experimental value **[22].**

Replacing the system of spin moments of individual magnetic atoms with a super-spin with $S = ½$ on the square lattice ($z = 4$), T_C is given as [13], [314]

$$T_C = \frac{0.567 J}{k_B} \tag{14},$$

and the exchange interaction J as [307]

$$J = \frac{E_{FM} - E_{AFM}}{2zS^2} \tag{15},$$

where E_{FM} and E_{AFM} are the total energies of the FM and AFM phases, respectively, and z is the coordination number in the super-spin system. For $S = 1$, $S = 3/2$, and $S = 2$, and the square lattice [13], [303], [314], T_C can be expressed by Eqs. (16)–(18), respectively

$$T_C = \frac{1.674 J}{k_B} \tag{16}.$$

$$T_C = \frac{3.278 J}{k_B} \tag{17}.$$

$$T_C = \frac{5.351 J}{k_B} \tag{18}.$$

We applied the above model with Eqs. 14-18 for P-doped graphene as described in **Chapter 4,** obtaining reasonable values of T_C and RT FM or AFM alignment of magnetic moments in agreement with experiments **[13]**, [111]. For other lattices such as linear, plane square, and cubic, similar equations with different pre-factors has been derived [315].

Other, more demanding techniques to study the critical temperatures has been developed [303], *e.g.*, thermodynamic perturbation theory [315], Quantum Monte Carlo (QMC) [305], Bethe-Peierls-Weiss (BPW) approximation [316], Oguchi's method [317], or high-temperature series-expansion (HTSE) method [318] whose critical temperature is practically exact.

3 Theoretical backgrounds

The interactions between atoms and electrons are governed by the laws of quantum mechanics. Hence, it was necessary to develop accurate and efficient techniques for solving quantum-mechanical equations for complex many-electron systems. The SE for such systems is not analytically solvable, therefore numerical approaches have become invaluable for physics, chemistry, and materials science, *e.g.*, HF method (1928) [319], Configuration interaction method (1928) [320], Møller–Plesset perturbation theory (1934) [321], Coupled-Clusters (initially created in 1950s and developed in 1966) [322], and/or Multi-configurational self-consistent field (SCF) method (1964) [323]. The breakthrough in computational efforts came in 1970s with the Hohenberg–Kohn (HK) theorems [324] defining electron density as the key element of DFT. The electron density in DFT is a function of only three spatial coordinates as opposed to many-body SE (**Figure 26**). HK work was further developed by Walter Kohn and Lu Jeu Sham, which led to Kohn–Sham (KS) DFT [325]. The KS equations (KSE), a set of coupled one-electron equations, transform the complexity of the electron–electron interactions into an effective single-particle potential, determined by the exchange-correlation functional that describes the complex kinetic and energetic electron-electron interactions. Although the form of this functional is unknown, approximate functionals have proven highly successful in describing many material properties. The hierarchy of exchange-correlation functionals after John Perdew is usually referred to as the "Jacob's ladder" of DFT [326] (**Figure 26**).

One of the most important roles of the DFT modeling is to provide information that is difficult to access in experiments. This became possible with an unprecedented increase of computer power. Historically, one of the first topics in materials science that successfully applied DFT was the phase and lattice stability of ideal crystals, which were in excellent agreement with the experiment [327]. Hence, DFT marked a decisive breakthrough in these efforts, and in the past decade, DFT has had a rapidly growing impact not only on fundamental but also industrial and material research, such as catalysis, surface science, nanomaterials, biomaterials, and geophysics [328].
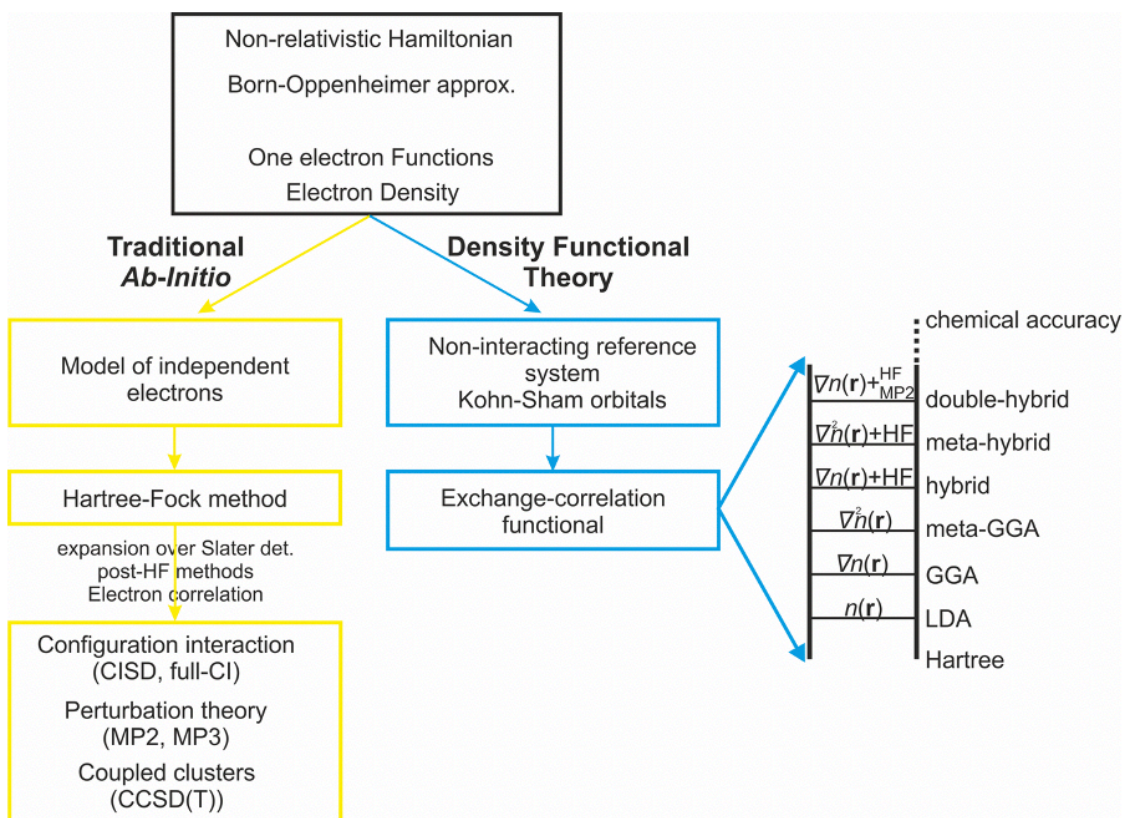
Figure 26 Scheme showing the hierarchy of ab-initio methods and density functional theory.

The computational experiments can basically be applied in three areas, i) as a double-check for experimental results, ii) to explain experimental observations down to atomic resolution, and iii) as a tool to discover new phenomena and materials, and their properties, such as structural, electronic, magnetic, catalytic, and other properties. Moreover, they help to understand and optimize laboratory experiments and thus reduce chemical costs. The focus of this dissertation was to predict the novel materials' properties and to explain experimental observations, mainly in graphene-related materials.

3.1 Schrödinger equation

In the electronic structure theory, we are interested in the theoretical description of atomic-scale objects. Since this scale is dominated by quantum effects, quantum theory must be applied to obtain reliable results. For this, the eigenvalue problem is solved, known as the stationary SE [329], [330] written in bracket notation as

$$\hat{H}|\Psi_i\rangle = E_i|\Psi_i\rangle \tag{19},$$

where Ψ_i refers to the wave-function, $\hat{H}$ is the Hamiltonian, E_i denotes the eigenvalue of the Hamiltonian.

In non-relativistic quantum mechanics, a molecular Hamiltonian is defined that describes the system of N electrons and M nuclei (without external fields), which is in fact the total energy operator

$$\hat{H} = \hat{T}_e + \hat{T}_n + \hat{V}_{ee} + \hat{V}_{en} + \hat{V}_{nn} \tag{20},$$

expressed as the sum of operators corresponding to the kinetic and potential energies, *i.e.*, the kinetic energy operator of the electrons, $\hat{T}_e$, and the nuclei, $\hat{T}_n$, the Coulomb electronic repulsions operator $\hat{V}_{ee}$, the Coulomb attractive interactions operator among the electrons and the nuclei $\hat{V}_{en}$, and the nuclear Coulomb repulsion term $\hat{V}_{nn}$.

Solutions to the stationary SE with the full molecular Hamiltonian are exceedingly complicated due to the presence of non-separable interaction terms and contain a fully quantum description of electrons and nuclei. The mass of the nuclei is much larger than that of the electrons (about 10^5) and the electrons move much faster than the nuclei (about 100-1000 times), therefore, the complexity of the problem may be significantly reduced by separating the electron and nuclear motion

$$\psi(\boldsymbol{R}, \boldsymbol{R}_n) = \psi_e^{R_n}(\boldsymbol{R})\psi_n(\boldsymbol{R}_n) \tag{21},$$

where $\boldsymbol{R} = (\boldsymbol{r}_1, \boldsymbol{r}_2, \dots, \boldsymbol{r}_N)$ is the $3N$ dimensional electron position vector, and $(\boldsymbol{R}_n = (\boldsymbol{R}_1, \boldsymbol{R}_2, \dots, \boldsymbol{R}_N)$ is the $3M$ dimensional nuclear position vector.

Since electrons are in the field of moving nuclei and the nuclei "feel" the mean interaction with electrons, it is useful to introduce the Born-Oppenheimer (BO) approximation, where the masses of nuclei in the term $\hat{T}_n$ are formally set to infinity [329], [330]. Hence the positions of the electrons are given explicitly, and the positions of the nuclei are given parametrically. The BO Hamiltonian is defined as

$$\hat{H}^{BO} = \hat{T}_e + \hat{V}_{en} + \hat{V}_{ee} + V_{nn} \tag{22}.$$

Since only the electronic terms require solutions to the eigenvalue problem, the equation has the form

$$\hat{H}^{BO} = \hat{H}_e + V_{nn} \tag{23}.$$

And one looks for the solutions to the eigenvalue problem

$$\hat{H}_e|\Psi_{e,i}\rangle = E_{e,i}|\Psi_{e,i}\rangle \tag{24}.$$

Note that the parametric dependence on the nuclear coordinates have been omitted for the sake of convenience. The variation method is an important approach to the approximate solution to the eigenvalue problems and the stationary SE for electrons. The variation principle means that the total energy expectation value of any approximate normalized trial wave function $|\tilde{\psi}\rangle$ is the upper bound to the exact solution for a given state

$$\langle\tilde{\psi}|\hat{H}|\psi\rangle = \tilde{E} \geq E \tag{25}.$$

In other words, the variation method allows one to minimize the total energy expectation value with respect to the parameters of the trial wave function and find the lowest value of the total energy that corresponds to the variational estimate of the exact energy.

3.2 Hartree-Fock method

HF method, also known as the SCF method, is a one-electron approximation that properly accounts for the permutation symmetry of fermions [329], [330]. The HF method relies on the variational optimization of a single-determinant N-electron ground-state wave function. One starts with a Slater determinant

$$\Psi_0(\chi_1, \chi_2, ..., \chi_N) = |\chi_1(\boldsymbol{x_1})\chi_2(\boldsymbol{x_2}) ... \chi_N(\boldsymbol{x_N})\rangle \tag{26}.$$

and the spin-orbitals χ_i are varied to minimize the ground-state energy expectation value

$$E^{HF} = min_{\{\chi_i\}}\langle\Psi_0|\hat{H}|\Psi_0\rangle \tag{27},$$

with the assumption that the wave-function is orthogonal and normalized.

In the HF method, the electron "feels" an interaction with the average potential from all other electrons; this is called mean-field-particle interaction or the mean-field method. However, HF ignores inter-particle correlations, and the total energy is increased due to neglect of the repulsion. The HF method relies on solving an eigenvalue problem

$$\hat{f}(x_i)\chi_k(x_i) = \varepsilon_i\chi_k(x_i) \tag{28},$$

which is a set of *N*-coupled non-linear eigenvalue equations instead of one equation for *N* fully interacting electrons that would be much more difficult to solve, and $\hat{f}(x_i)$ is the effective one-electron Fock operator

$$\hat{f}(x_i) = -\frac{1}{2}\nabla_i^2 - \sum_{A=1}^{M}\frac{Z_A}{r_{iA}} + v^{HF}(x_i) \tag{29}$$

with a mean electronic potential $v^{HF}(x_i)$ acting on an electron *i*

$$v^{HF}(x_i) = \sum_j \int dr' \frac{|\phi_j(r')|^2}{|r-r'|}\phi_i(r) - \sum_j \delta_{\sigma i,\sigma j} \int dr' \frac{\phi_j^*(r')\phi_i(r')}{|r-r'|}\phi_j(r) \tag{30}.$$

The first term (the Hartree term) is responsible for the electrostatic repulsion of electron "clouds". The second term (the exchange term) is the sum over all pairs of orbitals with the same spin projection, keeping electrons with the same spin apart, so that the Pauli principle is obeyed. While the HF method combined with the Slater determinant correctly describes the exchange effects arising from the permutation symmetry of the fermions, it lacks the correlation energy that was introduced in the post-HF methods. To solve the problem, an iterative procedure should be used until the self-consistency is obtained. Due to its low computational demands, HF is also used as a starting point for more demanding calculations.

3.3 Thomas-Fermi model

Working independently, in 1927 Llewellyn Thomas and Enrico Fermi used a statistical model to approximate the distribution of electrons in an atom [331], [332]. Although electrons are distributed non-uniformly in an atom, the local density approximation (LDA) has been made such that the electrons are uniformly distributed in each small-volume element *ΔV*, but the electron density can still vary from one small-volume element to the next. The energy in the TF is defined in terms of electron density as

$$E = T + v_{ext}(\boldsymbol{r})n(\boldsymbol{r})dr + \frac{1}{2}\iint \frac{n(r_1)n(r_2)}{r_{12}}dr_1dr_2 + \frac{1}{2}\iint \frac{n(r_1)n_{XC}(r_1,r_2)}{r_{12}}dr_1dr_2 \tag{31},$$

where *T* is the kinetic energy, $v_{ext}(\boldsymbol{r})$ is the external potential and $n_{XC}(\boldsymbol{r_1},\boldsymbol{r_2})$ is the exchange-correlational density. Thomas and Fermi applied the LDA to Eq. 31 and neglecting the exchange-correlation effect, obtained

$$E_{TF}[n(\boldsymbol{r})] = T_{TF}[n(\boldsymbol{r})] + v_{ext}(\boldsymbol{r})n(\boldsymbol{r})dr + \frac{1}{2}\iint \frac{n(r_1)n(r_2)}{r_{12}}dr_1dr_2 \tag{32},$$

with the TF kinetic energy functional

$$T_{TF}[n(\boldsymbol{r})] = C_F \int n(\boldsymbol{r})^{5/3} dr^3 \tag{33},$$

where kinetic constant $C_F = \frac{3h^2}{10m}\left(\frac{3}{8\pi}\right)^{2/3}$, h is the dimension and m is the mass.

When equation (32) and (33) are combined, the TF energy is obtained as

$$E_{TF}[n(\boldsymbol{r})] = C_F \int n(\boldsymbol{r})^{5/3} dr^3 + v_{ext}(\boldsymbol{r})n(\boldsymbol{r})dr + \frac{1}{2}\iint \frac{n(r_1)n(r_2)}{r_{12}} dr_1 dr_2 \tag{34},$$

which can be minimized with the constraint

$$\int n(\boldsymbol{r})dr = N \tag{35}$$

to obtain the approximate ground state electron density of an atom.

While the TF model is suitable for calculating system's ground state energy, its accuracy is limited due to the inaccurate representation of kinetic energy, exchange energy, and the complete neglect of electron correlation. TF model yields poor quantitative predictions for realistic systems, no molecular bonding is predicted, and molecules are less stable than their fragments. However, the basic concept and the kinetic energy expression of the TF theory has been used as a component in a more sophisticated density-approximation to kinetic energy within the DFT. A more realistic evaluation of one-electron orbitals and the introduction of non-interacting electrons (reference potentials) led to a proper description of the chemical bond.

3.4 Density functional theory

Over the past 40 years, DFT has become a very popular method in computational quantum chemistry. Its popularity is due to the lower computational demands compared to the wave-function based methods while still achieving a reasonable precision. Compared to SE, DFT means finding the function of the three spatial variables instead of the $3N$ variables of the wave function, which significantly reduces the complexity of DFT-based calculations. The DFT method relies on two fundamental mathematical theorems from Walter Kohn and Pierre Hohenberg in 1964 [324].

The first theorem states that the external potential, $v_{ext}(\boldsymbol{r})$, and hence the total energy, is a unique functional of the electron density $n(\boldsymbol{r})$. The energy functional $E_{[n(r)]}$ in the first Hohenberg-Kohn theorem can be written in terms of the external potential $v_{ext}(\boldsymbol{r})$ as follows

$$E_{[n(r)]} = \int n(r)v_{ext}(r)dr + F_{[n(r)]} \qquad (36),$$

and

$$v_{ext}(r) = -\sum_i \frac{Z_i}{|r-r_i|} \qquad (37),$$

where $F_{[n(r)]}$ is the unknown functional of the electron density $n(r)$ and Z_i denotes the charge of the nuclei.

The second theorem states that the ground-state energy can be obtained variationally, *i.e.*, the density that minimizes the total energy is the exact ground-state density. In other words, the ground-state and its properties are uniquely determined by the electron density. If we know the exact form of $F_{[n(r)]}$, we could vary the electron density until the energy functional $E_{[n(r)]}$ is minimized. Nevertheless, we do not know the exact form of the $F_{[n(r)]}$.

The energy functional, $E_{[n(r)]}$

$$E_{[n(r)]} = T_{[n(r)]} + \frac{1}{2}\iint \frac{n(r_1)n(r_2)}{r_{12}}dr_1 dr_2 + E_{XC} + \int v_{ext}n(r)dr \qquad (38),$$

consists of $T_{[n(r)]}$ which denotes the kinetic energy of electrons, the second term stands for the electron-electron repulsion (divided by two to avoid their self-interaction), E_{XC} is the exchange-correlation potential, and the last term describes the interaction between electrons and nuclei [330].

Electrons are fermions that must obey the Pauli exclusion principle. If the coordinates of two identical particles are exchanged the total wavefunction, $\psi_{i,j}$, changes its sign. This gives rise to the exchange energy:

$$E_x = -\iint \psi_i(r_1)\psi_j(r_2)\frac{1}{r_{12}}\psi_i(r_2)\psi_j(r_1)dr_1 dr_2 \qquad (39).$$

The correlation is defined as the difference between the exact eigenvalue of the time-independent SE and the solution of the HF limit [330]

$$E_C = E - E_{HF} \qquad (40).$$

The most problematic is the expression of the functional for the kinetic part. We can express the kinetic energy of N electrons in the form of their molecular orbitals, φ_i, as

$$E_{kin} = -\frac{1}{2}\sum_{i=1}^{N} \int \varphi_i \Delta_i \varphi_i dr_i \qquad (41).$$

The kinetic energy for each electron is thus described by the one-electron wave function (orbital), and their energies are summed.

The energy functional can be re-written as

$$E_{[n(r)]} = T_{[n(r)]} + \int n(r)V_{eff}(r)dr \tag{42},$$

where the effective potential, V_{eff}, is expressed as

$$V_{eff} = v_{eff}(r) + \int \frac{n(r_2)}{|r-r_2|}dr + V_{XC}(r) \tag{43}.$$

Now, we can solve the Kohn-Sham equations (KSE)

$$\left(-\frac{1}{2}\Delta_i + V_{eff,i}\right)\varphi_i = \varepsilon_i\varphi_i \tag{44},$$

in the same way as the HF equations.

The self-interaction of electrons is treated by a functional derivative of exchange-correlation energy

$$V_{XC}(r) = \frac{\delta E_{XC}(r)}{\delta n(r)} \tag{45}.$$

The KSEs are iteratively and self-consistently solved as follow: i) define a trial electron density, $n(r)$ ii) solve the KSEs using the trial electron density to find the single-electron wave function, $\varphi_i(r)$ iii) calculate the electron density defined by the Kohn-Sham single-particle wave function iv) compare the calculated electron density, $n_{KS}(r)$, with the trial electron density used in solving the Kohn-Sham equations, $n(r)$. If these densities match, the ground-state electron density is obtained that can be used to compute the total energy. Otherwise, the trial electron density must be updated (**Figure 27**).
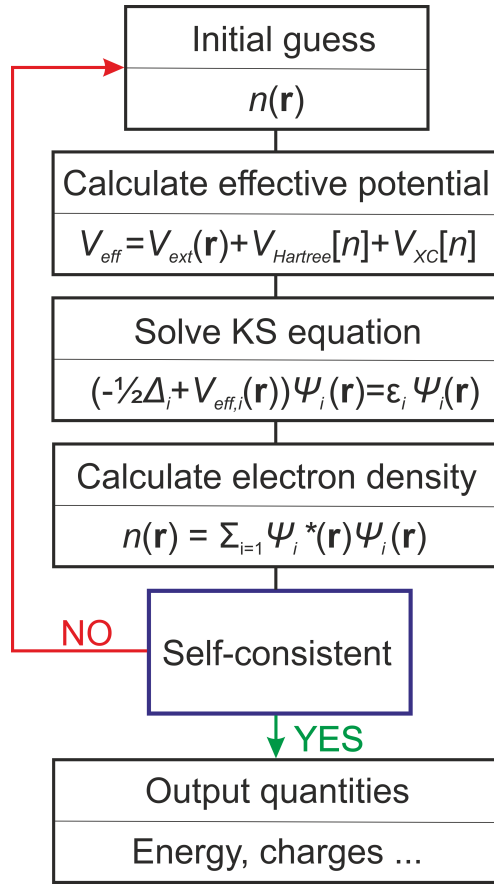
Figure 27 The workflow of DFT calculations from the initial guess of electron density to calculation of energy density and desired properties.

The form of the exchange-correlation functional, E_{XC}, is not known. Therefore, many attempts and approximations have been made that can be gathered into two groups. The first approach focuses on deriving E_{XC} from first principles, the second one is more pragmatic, *i.e.*, the E_{XC} contains parameters obtained from experimental measurements. The accuracy and speed of DFT-based methods depend crucially on the form of the exchange-correlation functional whose hierarchy is depicted in **Figure 26** [326].

Local Density Approximation (LDA) functional

The LDA assumes that the local exchange-correlation energy density is the same as in the homogeneous electron gas (HEG), which is the hypothetical physical state with the constant density. At any point in space the local exchange-correlation energy of the HEG is used for the corresponding density, ignoring the non-locality of the true exchange-correlation energy. The LDA functional is mathematically expressed as

$$E_{XC}^{LDA}[n] = \int n(\boldsymbol{r})\varepsilon\big(n(\boldsymbol{r})\big)dr \qquad (46),$$

where $\varepsilon(n(r))$ is the HEG exchange-correlation energy, which can be separated into the exchange and correlation part

$$\varepsilon(n) = \varepsilon_x(n)\varepsilon_c(n) \tag{47}.$$

For the exchange part, the analytic solution was derived in [333] and written as

$$\varepsilon_x(n) = -\frac{3}{4}\left(\frac{3}{\pi}\right)^{\frac{1}{3}}\int n(r)^{4/3}dr \tag{48}.$$

The correlation part of HEG energy has no analytic solution, and it was determined numerically by the quantum MC simulations [334] and fitted to the analytic form by Vosko, Wilk, and Nusair (VWN) [335]. The local spin density approximation (L(S)DA) [335]–[337] is an extension of the LDA that accounts for the electron density with spin α and with spin β

$$\varepsilon(n) = \varepsilon(n_\alpha, n_\beta) \tag{49}$$

and usually implies the VWN correlation. L(S)DA uses Slater exchange plus Vosko, Wilk, Nusair correlation (S-VWN) [333], [335].

L(S)DA calculations provide better results than the HF method for geometries, vibrational frequency, or dipole moments. The description of energetics is worse though, it tends to overestimate the bond strength and cohesive energies [326]. The ionization energies and bandgaps in semiconductors and insulators are utterly underestimated. It must be noted that the L(S)DA fails badly to predict the ground magnetic state for TMs, for example the L(S)DA predicts the ground state of iron to be hexagonal close-packed and NM instead of body-centered cubic and FM [328].

Generalized Gradient Approximation (GGA) and meta-GGA functionals

The GGA introduces a dependence of E_{XC}^{GGA} on the local gradient of the electron density $\nabla n(r)$

$$E_{XC}^{GGA}[n] = \int n(r)f(n, \nabla n)dr \tag{50}.$$

The exact form of the GGA functionals is more complex and can also include parameters. A popular exchange functional is the Becke functional B88, also noted as B [338], and the correlational functional is LYP by Lee, Yang and Paar [339] or P86 by Perdew [169]. The Vienna Ab-Inition Simulation Package (VASP), which is the main software used for our

calculations, includes PBE (Perdew-Burke-Ernzerhof) [340], PW91 (Perdew-Yang) [341], [342], RPBE (revised PBE) [343], AM05 (Armiento-Mattson) [344], and PBEsol [345]. The PW91 functional was derived by using MC for the uniform electron gas and the exact properties of the exchange-correlation hole. PBE was derived by using the exact properties of the exchange-correlation energy. RPBE represents a revised version of the PBE functional to improve binding and adsorption energies. AM05 was designed to take into account surface effects. PBEsol represents revised PBE density-functional which improves predictions of equilibrium properties of solids [346].

The GGA functionals are more precise than the LDA ones, correct the over-binding tendency of the LDA, however, they usually underestimate the bandgaps [347].

The meta-GGA extends the GGA method with the second derivation of the electron density $\nabla^2 \rho(\boldsymbol{r})$

$$E_{XC}^{meta-GGA}[n] = \int n(\boldsymbol{r})f(n, \nabla n, \nabla^2 n)dr \qquad (51).$$

The B95 correlation functional by Becke [348] and the TPSS exchange-correlation functional by Tao, Perdew, Staroverov, and Scuseria [349] belong to the most common meta-GGA functionals. TPSS was shown to improve the description of solids and surfaces [350]. The non-empirical SCAN (strongly constrained and appropriately normed semilocal density functional) [351] includes 17 known exact constraints of meta-GGA which are mentioned in the supplementary material of [351]. SCAN improves the description of geometries, energies, and bandgaps of various materials at almost-GGA cost [352].

Hybrid functionals

Hybrid functionals incorporate a portion of exact exchange from the HF theory to local or semilocal DFT exchange in certain proportion. The aim is to improve the calculation of many molecular properties, such as atomization energies, lattice parameters, bond lengths, vibration frequencies as well as band structure in semiconductors and insulators [353], since underestimating the DFT bandgap can be corrected by overestimating the bandgap by the HF method. The most popular hybrid functional is the three-parameter B3LYP, which consists of

$$E_{XC}^{B3LYP} = (1 - a_0 - a_x)E_X^{LDA} + a_0 E_X^{exact} + a_x E_X^{B88} + (1 - a_c)E_C^{VWN} + a_c E_C^{LYP} \quad (52),$$

with tunable parameters $a_0 = 0.2$, $a_x = 0.72$, and $a_c = 0.81$, where a_0 defines the percentage of HF exchange energy, *e.g.*, in B3LYP $a_0 = 20$ %. Since the mixing coefficients were derived by fitting them to a large test set of molecules, this is a general and accurate functional. However, the correlation part of the functional turned out to be incorrect in the HEG limit [346].

The parameter-free PBE0 functional [354] mixes the PBE exchange energy and HF exchange energy in a set 3:1 ratio

$$E_{XC}^{PBE0} = 0.25E_X^{HF} + 0.75E_X^{PBE} + E_C^{PBE} \tag{53}.$$

Since PBE0 is empirical-parameters-free which predicts correctly the structural, thermodynamic, kinetic, and spectroscopic properties of various materials, it is widely used in both quantum chemistry and condensed matter physics [354].

In periodic boundary condition (PBC) calculations, obtaining the HF exchange energy is very expensive because of the slow decay of the exchange interaction with distance. Therefore, the HSE (Heyd–Scuseria–Ernzerhof) exchange–correlation functional [355] has been proposed to separate Coulomb potential into a long-range and short-range part. In general, HSE can be written as

$$E_{XC}^{\omega PBEh} = aE_X^{HF,SR}(\omega) + (1-a)E_X^{PBE,SR}(\omega) + E_{XC}^{PBE,LR}(\omega) + E_C^{PBE} \tag{54},$$

where ω is the adjustable parameter controlling short-range (SR) and long-range (LR) interactions, and a is the mixing parameter.

The HSE03 and HSE06 functional mixes HF exchange and DFT exchange only to the short-range interaction

$$E_{XC}^{HSE03} = 0.25E_X^{HF,SR}(\omega) + 0.75E_X^{PBE,SR}(\omega) + E_{XC}^{PBE,LR}(\omega) + E_C^{PBE} \tag{55},$$

and range-separation parameter $\omega = 0.2$ and 0.3 Å^{-1} for HSE03 and HSE06, respectively [356].

All functionals exist in spin-degenerate and spin-polarized versions. The GGA calculations represent a systematic improvement over the LDA, although for the heavy elements a certain tendency for the GGA to overcorrect the LDA error is observed. The meta-GGA leads to only moderate progress as compared with the GGA. Hybrid functionals demonstrate

great promise for insulating and semiconducting systems, but also show the need to develop new hybrid functionals better suited to metal description [328].

There are certain issues in using some functionals for specific systems. For itinerant magnets, only the GGA provide reliable results, the LDA often predicts the wrong GS. Hybrid functionals tend to overestimate the magnetic moments and exchange splitting because in metallic systems the screening of the HF exchange is underestimated. For systems with localized magnetic moments, the GGA underestimates the exchange-splitting, while hybrid functionals or the DFT+U approach leads to improved results.

The nature of DFT tends to over-delocalize valence electrons and over-stabilize metallic ground states [357] and therefore it fails to predict the properties of systems whose GS is characterized by a more pronounced localization of electrons. The DFT+U method describes the "strongly correlated" electronic states of a system – typically localized d or f orbitals – by using the Hubbard model [358], while the rest of valence electrons are treated by standard DFT functionals [357]. The Hubbard model enables to include the so-called on-site repulsion, which stems from the Coulomb repulsion between electrons at the same atomic orbitals [359]. Thus, by simply adding a semiempirical numerical parameter U, which is the Coulomb potential responsible for localization, the underestimated electronic interactions are corrected. The U correction enhances the description of structural, electronic, or magnetic properties of correlated systems, the electron transfer energetics, and chemical reactions. However, it fails in predicting the properties of systems with more delocalized electrons, such as metals [360].

Modern functionals

The development of new functionals improving the DFT results is an active filed of quantum chemistry, hundreds of different functionals have been proposed to date. Pure DFT exchange-correlation functionals use only local quantities at a reference point: *e.g.,* electron density, density gradient. It is therefore presumed that pure functionals overestimate local contributions and underestimate non-local contributions. The most significant non-local contribution neglected in pure functionals may be the long-range electron-electron exchange interaction because it may be impossible to represent this interaction as a functional of a one-electron quantity.

In atoms and molecules, the exchange-correlation potential of semilocal functionals decays exponentially, while the asymptotic form of the exact potential is $-1/r$ [361]. For hybrid

functionals mixing exact and GGA exchange, the exchange-correlation potential decays asymptotically as $-a/r$ where a is the fraction of HF exchange. To recover the exact $-1/r$ asymptote, it has been suggested to separate the Coulomb kernel into a short- and long-range part.

In the long-range-corrected functionals (LC-functionals), the local functional can be used for short-range exchange interaction, and long-range part is treated with HF exchange

$$E_{XC}^{LC-DFT} = E_X^{DFT,SR} + E_X^{HF,LR} + E_C^{DFT}$$ (56),

where DFT stands for any possible flavor of DFT. The LC-functionals effectively minimize the self-interaction error in DFT and overcome the tendency of over-delocalization of the electron density typically found in local DFT approaches. The LC-functionals improves the description of charge transfer excitation energies, oscillator strengths in time-dependent Kohn–Sham calculations, optical response properties or activation energies such as hyperpolarizability in coupled-perturbed Kohn–Sham and finite-field calculations. They are commonly used for the simulations of excited states [362]. However, the HOMO-LUMO gaps are approaching to HF values and are grossly overestimated [363]. As an example, one can use ωB97XD [364] which includes empirical dispersion.

3.5 Spin-polarized DFT

The basic variables of the spin-density-functional theory are the scalar density *n(r)* and the vector of the magnetization density *m(r)*. Alternatively, to these variables, the 2 × 2 spin density matrix $n^{\alpha\beta}$*(r)* can be used, where α and β can have positive (spin up) and negative (spin down) value. The *n(r)*, *m(r)*, and $n^{\alpha\beta}$*(r)* are connected by

$$n(\boldsymbol{r}) = \sum_\alpha n^{\alpha\alpha}(\boldsymbol{r})$$ (57),

$$m(\boldsymbol{r}) = \sum_{\alpha\beta} \boldsymbol{\sigma}^{\alpha\beta} n^{\alpha\beta}(\boldsymbol{r})$$ (58),

and by

$$n^{\alpha\beta}(\boldsymbol{r}) = \frac{1}{2}\left(n(\boldsymbol{r})\delta^{\alpha\beta} + m_x(\boldsymbol{r})\sigma_x^{\alpha\beta} + m_y(\boldsymbol{r})\sigma_y^{\alpha\beta} + m_z(\boldsymbol{r})\sigma_z^{\alpha\beta}\right)$$ (59),

where $\boldsymbol{\sigma} = (\sigma_x, \sigma_y, \sigma_z)$ is a vector consisting of the Pauli spin matrices.

The exchange part is derived from the general spin-scaling relation and expressed as

$$E_x^{SDFT}[n_\uparrow, n_\downarrow] = \frac{1}{2}\left(E^{DFT}[2n_\uparrow] + E^{DFT}[2n_\downarrow]\right) \tag{60}.$$

The Hohenberg-Kohn-Sham spin-density functional is given as

$$E[n^{\alpha\beta}(\boldsymbol{r})] = T_S[n^{\alpha\beta}(\boldsymbol{r})] + \frac{e^2}{2}\int\int \frac{n(r)n(r')}{|r-r'|}d\boldsymbol{r}d\boldsymbol{r}' + \sum_{\alpha\beta}V_{ext}^{\alpha\beta}(\boldsymbol{r})\,n^{\alpha\beta}(\boldsymbol{r})d\boldsymbol{r} +$$

$$E_{xc}[n^{\alpha\beta}(\boldsymbol{r})] \tag{61}.$$

The variation and minimization of $T_S[n^{\alpha\beta}(\boldsymbol{r})]$ and $E[n^{\alpha\beta}(\boldsymbol{r})]$ with respect to the single-particle wave-function lead to the Kohn-Sham equations

$$-\frac{\hbar^2}{2m}\nabla_r^2\varphi_i^\alpha(\boldsymbol{r}) + \sum_\beta V_{eff}^{\alpha\beta}(\boldsymbol{r})\varphi_i^\beta(\boldsymbol{r}) = \epsilon_i\varphi_i^\alpha(\boldsymbol{r}) \tag{62},$$

where ϵ_i stands for Langrange parameters which guarantee the normalization of the wave-function. The potential $V_{eff}^{\alpha\beta}$ can be expressed as

$$V_{eff}^{\alpha\beta}(\boldsymbol{r}) = \delta^{\alpha\beta}e^2\int\frac{n(r')}{|r-r'|}d\boldsymbol{r}' + V_{ext}^{\alpha\beta}(\boldsymbol{r}) + V_{xc}^{\alpha\beta}(\boldsymbol{r}) \tag{63}$$

and represents an effective one-particle potential.

The exchange-correlation potential is given as

$$V_{xc}^{\alpha\beta}(\boldsymbol{r}) = \frac{\delta E_{xc}[n^\alpha(r), n^\beta(r)]}{\delta n^{\alpha\beta}(\boldsymbol{r})} \tag{64}$$

The spin-density-functional theory is exact; however, the functionals E_{xc} and $V_{xc}^{\alpha\beta}$ are not known and must be approximated. The most common approximations are LSDA and spin-polarized GGA.

3.6 Dispersion corrections in DFT

A shortcoming of the standard DFT is that it lacks correct description of London dispersion interactions (or loosely van der Waals (vdW) interactions) coming from dynamical correlations between fluctuating charge distributions [346]. Therefore, several dispersion corrections have been proposed [365].

The vdW interactions between a molecule and a metal surface have a leading contribution of the type C_3/z_3 where z is the distance between the molecule and the surface [366]. The dipole-dipole C_3 coefficients resulting from the polarization of the atoms were then estimated from the polarizability of the molecule and the dielectric function of the surface

[367]. The semiempirical DFT-D2 correction by Stefan Grimme [368], often used due to its low computational cost, introduces the dispersion correction by means of pairwise interactions from the London formula [369] leading to a sum over the term C_6/R^6. The C_6 parameters were tabulated for all atoms in the periodic table [370]. The DFT-D2 method overestimates the interactions with metals [371]. The systematic improvement of the DFT-D2 method, DFT-D3 [372], includes successive terms C_8-C_{10} in the expansion, which incorporates a range of precalculated coefficients for various elements in different reference states. For instance, the C_6 coefficients are assigned to each pair of atoms, taking into account the number of neighbors. However, DFT-D3 still largely overestimates the water−metal interaction [373]. For the interaction of substrate with metals, a method based on the determination of static polarizabilities together with the ionization potentials has been developed. This simple model based on the response of the dipole to the presence of an electric field was shown to provide reliable values for the C_6 coefficients for surface atoms on low-coordinated centers and alloys [365].

In an alternative formulation, known as DFT-vdW [374], the C_6 coefficients and radii are determined nonempirically from the electron density, and effective atomic volumes are used to obtain environment dependency. However, since scaling of the coefficients with volume yielded unclear results concerning the accuracy for more complex systems, Victor Ruiz [375] has introduced the DFT-vdW$^{\text{surf}}$ method [376], which determines a metal surface C_6 coefficient, which accounts for the collective response of the substrate electrons using the Lifshitz−Zaremba−Kohn (LZK) theory [366], [376].

Alternatively, a nonlocal correlation functional vdW-DF proposed by Bengt Lundqvist [377], [378] accounts for dispersion interactions approximately. The key to the vdW-DF method is the inclusion of a long- range correlation energy and a fully nonlocal functional of the density. The results depend on the combination between the exchange and the nonlocal correlation functionals [379]. Despite its success for describing dispersion better than any other non-empirical method [380], vdW-DF overestimates equilibrium separations and underestimates hydrogen-bond strength [381].

Last but not least, a random phase approximation (RPA) [382] and an adiabatic connection and fluctuation dissipation theorem (ACFDT) [383], [384] rigorously account the vdW energy. However, these methods are computationally very demanding and better serves as benchmark method for reactivity of large molecules on metal surfaces.

3.7 Finite models versus periodic boundary conditions

Modelling of graphene derivatives, which is the main subject of our research, can be carried out using a finite model or a PBC model. Each of them has its pros and cons, and the choice of the approach depends on what properties one aims to investigate. Both finite and infinite graphene models can be described using quantum-chemical or molecular mechanic (empirical) methods.

Often used as finite models are polyaromatic hydrocarbons (PAHs), benzene (C_6H_6), coronene ($C_{24}H_{12}$), ovalene ($C_{32}H_{14}$), or circumcoronene ($C_{54}H_{18}$) [385]. The C–H dangling bonds at the edges of the PAH affect the electron density distribution in the system as the electrons of the hydrogen atoms are drawn to the carbon skeleton, generating a positive electrostatic potential on the hydrogens and a negative electrostatic potential above and below the carbon sheet where the π-electron cloud resides. Thus, the finite model acquires quadrupole potential which is not presented in real corrugated graphene. The main advantage of using finite models is that they can be studied using a wide portfolio of electronic structure methods developed for molecular systems. It must be noted, however, that the electronic band structure of graphene and its derivatives can only reasonably be studied using PBC models because models that do not account the inherent extended nature of graphene neglect correlation contributions from the bands close to the Dirac point.

It is convenient to use atomic orbitals as building blocks for construction of wave function or electron density of a PAH. For example, one-electron Kohn-Sham orbitals φ_i composing the Slater determinant are expanded as a linear combination of atomic basis functions χ_i

$$\varphi_i = \sum_{\mu=1}^{L} c_{\mu i} \chi_i \tag{65}.$$

If a complete basis set is used ($L = \infty$), an exact solution is obtained.

Ideal graphene is an infinite 2D material which can be naturally modelled using PBC. It is a method of choice for calculating the electronic band structure of graphene and its derivatives [385]. The infinite model may also better describe the situations encountered in some experiments, as compared to the simulations employing the final models. The theory behind PBC solid-state calculations is described in the next subchapter.

3.8 Solid-state calculations

Modern calculations for solids are determined by several technical choices: i) The expansion of the Kohn-Sham eigenfunctions can be done either by plane waves or localized basis functions, *e.g.*, Gaussian-type orbitals. ii) The interactions between the ionic core and the valence electrons can be described either by a full-potential approach or by pseudopotentials. iii) The description of the electron-electron interactions depends on the choice of the exchange-correlation functional. In this subchapter I shall focus on plane waves and the pseudopotential approach due to the use of the VASP package [386]–[388] in most of my research.

Bloch's theorem, plane waves, and cut-off energy

Bloch's theorem [389], [390] is applied on the wave functions of electrons inside a crystal and relies on the periodicity of the Coulomb potential in a crystalline solid. Therefore, the potential energy function, $V(r)$, in Schrödinger's equation can be expressed as:

$$V(r) = V(r + R_n) \tag{66},$$

where R_n represents an arbitrary translation vector of the crystallographic lattice.

Bloch's theorem determines that the wave function $\psi k(r)$ in a crystal, obtained from the SE, can be expressed as the product of a plane waves and a function $u_k(r)$ with the same periodicity as the lattice, *i.e.*,

$$\psi_k(r) = e^{ik \cdot r} u_k(r) \tag{67},$$

where the space of vectors r is called the real space, and the space of vectors k is called the reciprocal space (or simply k-space). The periodicity of $u_k(r)$ means that it can be expanded in terms of a special set of plane waves:

$$u_k(r) = \sum_G c_G e^{iG \cdot r} \tag{68},$$

where the summation is over all vectors defined by $G = m_1 b_1 + m_2 b_2 + m_3 b_3$.

The expansion of electrons as plane waves e^{ikr} is very efficient in the solid state physics whose materials have atoms arranged in the periodic space [346]: i) It is easy to switch from the real-space to the momentum-space via the Fourier transform, which enables faster computations. ii) The basis-set convergence control is trivially determined by the cut-off

energy. iii) the basis-set superposition errors, which must be controlled in calculations based on local basis sets, can be naturally avoided.

Cutoff-energy

The softness of the pseudopotentials (*vide infra*) is important for plane-waves; a softer pseudopotential requires a smaller number of plane-waves in the wave-function expansion. Despite the time-saving pseudopotentials approach, the result of the single-particle equations would still require diagonalization of a large matrix, the size of which is assigned by the number of plane-waves in the expansion of the wave-functions. This issue has been grasped by the so-called cut-off energy [391].

By combining equations (67) and (68), a wave function $\psi\, k(r)$ in a crystal can be expressed as

$$\psi_k(r) = \sum_G c_{k+G}\, e^{i(k+G)r} \tag{69}.$$

The evaluation of this expression even at a single point in the *k*-space involves summing over an infinite number of possible values of G. Fortunately, this function has a simple interpretation as solutions of the Schrödinger equation

$$E = \frac{h^2}{2m}|k+G|^2 \tag{70}.$$

It is reasonable to expect that the lower energy solutions are physically more important than solutions with very high energies. As a result, it is usual to truncate the infinite sum above to include only solutions with kinetic energies less than the cut-off energy

$$E_{cut} = \frac{h^2}{2m}G_{cut}^2 \tag{71}.$$

The infinite sum is then reduced to

$$\psi_k(r) = \sum_{|G+k|<G_{cut}} c_{k+G}\, e^{i(k+G)r} \tag{72}.$$

k-points

A primitive cell in the reciprocal space is called the Brillouin zone (BZ) [391], [392]. The BZ plays a central role in the band theory of materials. The volume of the BZ, V_{BZ}, and the volume of the primitive cell in the real space defined by the Wigner–Seitz construction, V_{cell}, are related by

$$V_{BZ} = \frac{(2\pi)^3}{V_{cell}} \qquad (73).$$

To determine the total energy of a crystal, still a summation over the lowest eigenvalues has to be performed. For infinite periodic systems, this band structure energy in the total energy expression should be replaced by the integral over the first BZ, which is defined in the reciprocal space and integrates over the possible values of $\boldsymbol{k}$ in the Brillouin zone

$$g = \frac{V_{cell}}{(2\pi)^3} \int_{BZ} g(\boldsymbol{k}) dk \qquad (74).$$

Fortunately, this integral can be quite accurately approximated by the sum over a finite set of k-points. As the number of k-points increases, the results become more accurate. At the limit of a very large number of points, these numerical methods converge to the exact result for the integral.

The key ideas related to getting well-converged results in k-space include: i) Calculations should be converged with respect to the number of k-points. ii) The number of k-points used in the calculation should be reported to ensure reproducibility of the results. iii) Increasing the volume of the supercell reduces the number of k-points needed to achieve convergence because the increased volume in the real space correspond to a decreased volume in the reciprocal space.

Because the integrals take up so much of the computational effort of the DFT calculations, it is not surprising that the problem of efficiently evaluating these integrals has been studied very carefully. Most DFT packages offer the option of choosing k-points based on this method, and all that is needed is to specify how many k-points should be used in each direction in the reciprocal space. For calculations using a supercell that has the same length along each lattice vector and therefore the same length along each reciprocal lattice vector, it is natural to use the same number of k-points in each direction.

Pseudopotentials

Since chemistry per se is determined by valence electrons and the strongly bound inert core electrons are not crucial in defining chemical bonds and other physical characteristics of materials, pseudopotentials have been established so that the valence electrons are in the effective potential of the core electrons [346]. One usually refers to the frozen-core approximation. It is presumed that the core states are naturally localized within the augmentation spheres and that the core states of the isolated atoms are not influenced by the formation of molecules, only valence electrons are treated explicitly. The wave-function of

the electrons remain unchanged, and the simpler pseudo-wave-functions replace the oscillating wave-function of the core electrons. The real, the pseudo-wave-function, and potentials are identical above a cut-off radius r_c (**Figure 28**).
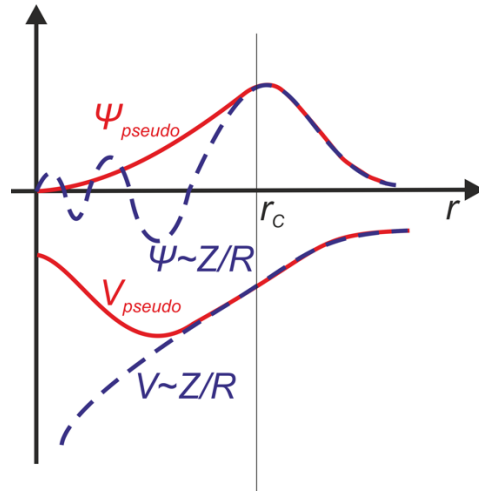
Figure 28 Illustration of the concept behind the pseudopotential. The pseudo-wave function coincides with the true or full valence wave function at the cut-off radius r_c.

Projected augmented wave (PAW) method

The PAW method [346], [393] achieves the efficiency of the pseudopotential method and the accuracy of the full-linearized augmented-plane-wave (FLAPW) method for solid-state calculations. The valence wavefunctions tend to oscillate rapidly near the ion cores. The PAW approach addresses this issue by transforming these rapidly oscillating wavefunctions into smooth wavefunctions that are computationally less demanding and provides a way to calculate all-electron properties from these smooth wavefunctions. Unlike the pseudopotential approach, the PAW method includes the nodal features of the valence orbitals and ensures orthogonality between the valence and core wave functions.

In principle, the linear transformation T transforms the $|\tilde{\psi}\rangle$ pseudo wavefunction into the all-electron wavefunction $|\psi\rangle$ of a Kohn–Sham single particle wavefunction

$$|\psi_i\rangle = T|\tilde{\psi}_i\rangle \tag{75}$$

The transformation operator T modifies the nodal structure in the core region of the all-electron wavefunction that is smooth beyond the r_c

$$T = 1 + \sum_R \hat{T}_R \tag{76}$$

where $\hat{T}_R$ denotes the difference between the pseudo and all-electron wavefunctions which are non-zero only in the core region because beyond the r_c the pseudo-wave function matches with the all-electron wave-function.

The pseudo-wavefunctions can be expanded to pseudo-partial waves in the core region with the coefficients c_i as

$$\left|\tilde{\psi}\right\rangle = \sum_i c_i \left|\tilde{\phi}_i\right\rangle \tag{77}.$$

For each partial wave, there exists an auxiliary pseudo-partial wave connect by transformation

$$\left|\phi_i\right\rangle = (1 + \hat{T}_R)\left|\tilde{\phi}_i\right\rangle \tag{78}.$$

An arbitrary pseudo wavefunction can be written in the pseudo-partial wave basis by

$$\tilde{\psi}(\boldsymbol{r}) = \sum_R \tilde{\phi}_i(\boldsymbol{r}) c_i = \sum_R \tilde{\phi}_i(\boldsymbol{r}) \langle \tilde{p}_i | \tilde{\psi} \rangle \tag{79},$$

where $|\tilde{p}_i\rangle$ is the set of the so-called projector functions satisfying completeness

$$\sum_R \left|\tilde{\phi}_i\right\rangle\langle \tilde{p}_i| = 1 \tag{80}$$

and fulfilling orthogonality

$$\langle \tilde{\phi}_i | \tilde{p}_i \rangle = \delta_{i,j} \tag{63}.$$

Then the transformation operator T can be expressed as

$$T = 1 + \sum_i \left(|\phi\rangle - \left|\tilde{\phi}_i\right\rangle\right)\langle \tilde{p}_i| \tag{81},$$

where the index i goes over all the partial waves corresponding to all atoms. Then the true all-electron wave function can be expressed as

$$|\psi\rangle = \left|\tilde{\psi}\right\rangle \sum_i \left(|\phi\rangle - \left|\tilde{\phi}_i\right\rangle\right)\langle \tilde{p}_i | \tilde{\psi} \rangle \tag{82},$$

The pseudo-wavefunctions $\tilde{\psi}$ are variational quantities in the PAW method that can be expressed by plane waves

$$\tilde{\psi}_{i,k}(\boldsymbol{r}) = \sum_G C_{i,k+G} e^{(k+G)r} \tag{83}.$$

In the regions between the PAW spheres surrounding the atoms, the pseudo-wavefunctions are identical to the all-electron wavefunctions. However, inside the spheres the pseudo-wavefunctions are only a bad approximation to the exact wave functions. Hence, partial waves were introduced that are solutions of the spherical scalar-relativistic Schrödinger equation [346].

3.9 Spin-polarized DFT including spin-orbit coupling

VASP accounts for the fully relativistic calculation for the core electrons and treats the valence electrons in a scalar relativistic approximation. The SOC of the valence electrons may be included using the second-variation method and scalar-relativistic eigenfunctions of the valence states. The inclusion of SOC enables the calculation of orbital moments, the determination of the easy/hard axis of magnetization, and the calculation of the magnetic anisotropy energy [346].

SOC has been implemented in VASP by Georg Kresse and Olivier Lebacq [394] following the approach of Leonard Kleinman [395] and Allan MacDonald *et al.* [396]. Calculations including SOC are performed in a non-collinear mode implemented in VASP by David Hobbs *et al.* [397] and Martijn Marsman and Jürgen Hafner [398]. The relativistic Hamiltonian given in a basis of total angular momentum eigenstates $|j, m_j\rangle$ with j = $l{\pm}1/2$ (containing all relativistic corrections up to order α^2, where α is the fine-structure constant) is recast in the form of 2×2 density matrix $n^{\alpha\beta}(\boldsymbol{r})$ in spin-space by re-expressing the eigenstates of the total angular momentum in terms of a tensor product of regular angular momentum eigenstates $|l, m\rangle$, and the eigenstates of the *z*-component of the Pauli spin matrices. The relativistic effective potential consists of a term diagonal in spin-space which contains the mass-velocity and Darwin corrections and the spin–orbit operator

$$\boldsymbol{V} = \boldsymbol{V}^{SC} + \boldsymbol{V}^{SO} = \sum_{l,m}[V_l \cdot \boldsymbol{1}_\sigma + V_l^{SO}\boldsymbol{L} \cdot \boldsymbol{S}]\,|l, m\rangle\,\langle l, m| \tag{84},$$

where $\boldsymbol{1}_\sigma$ is the unit operator in spin-space and

$$\boldsymbol{L} \cdot \boldsymbol{S} = \frac{1}{2}\begin{pmatrix} L_z & L_- \\ L_+ & -L_z \end{pmatrix} \tag{85}.$$

The *l*-components of the scalar V_l and spin-orbit V_l^{SO} potentials are weighted averages over the $l{\pm}1/2$ components, assuming that the magnetization is directed along the *z*-axis. The Hamiltonian is therefore a 2×2 matrix in spin-space. The non-diagonal elements arise from the spin–orbit coupling, but also from the exchange-correlation potential when the studied

system displays a non-collinear magnetization density. The electron density $n(\boldsymbol{r})$ is given by the trace of the density matrix which may be written as a linear combination of the 2×2 unit matrix and the vector $\boldsymbol{\sigma} = (\sigma^x, \sigma^y, \sigma^z)$ of the three Pauli spin matrices,

$$n^{\alpha\beta}(\boldsymbol{r}) = \frac{[n(r)\delta_{\alpha\beta} + \boldsymbol{m}(r) \cdot \boldsymbol{\sigma}^{\alpha\beta}]}{2} \tag{86},$$

with the local magnetization density $\boldsymbol{m}(\boldsymbol{r}) = \sum_{\alpha\beta} n^{\alpha\beta}(\boldsymbol{r}) \cdot \boldsymbol{\sigma}^{\alpha\beta}$. For a local magnetization $\boldsymbol{m}(\boldsymbol{r})$ directed along the unit vector $\boldsymbol{n} = (sin\theta \cos\phi, \sin\theta \sin\phi, \cos\theta)$ the exchange splitting is $b(\boldsymbol{r})\boldsymbol{n} \cdot \boldsymbol{S}$, where $b(\boldsymbol{r}) = \frac{\delta E_{xc}[n^{\alpha,\beta}(r)]}{\delta m(r)}$ is the functional derivative with respect to the spin density $m(\boldsymbol{r}) = |\boldsymbol{m}(\boldsymbol{r})|$. The spin-orbit interaction is transformed using the Wigner spin-rotation matrices. The Kohn–Sham equations with the relativistic effective potential is being solved self-consistently. Both spin–orbit coupling and non-collinearity lead to a mixing of different spin-components.

3.10 Computational details

In our DFT-based calculations, we used the PBC model **[13]**–**[18]** and the finite model **[14], [15], [17]** which are briefly discussed in **Chapter 3.7**, the first using the VASP package [386]–[388], the second with Gaussian software [399] with the long-range-corrected ωB97XD functional [364] which includes empirical dispersion, plus we considered an implicit solvent model **[17]**.

As PBC models of graphene, we used both a 3×3 (6×3) orthorhombic cell containing 48 (96) carbon atoms (**Figure 29a**) **[13]**, **[14]**, **[17]** and a 3×3 (6×6) triclinic cell containing 18 (72) carbon atoms **[15]** (**Figure 29b**). For modeling the structure of GN3 we used graphene flakes **[16]** shown in **Figure 29c**. As finite graphene models, we used coronene ($C_{24}H_{12}$) and larger ovalene ($C_{32}H_{14}$) **[14]**, **[15]**, **[17]** depicted in **Figure 29d,e**. The PBC model was used to study the freestanding and Au(111)-deposited porphyrin molecules (**Figure 29f**).
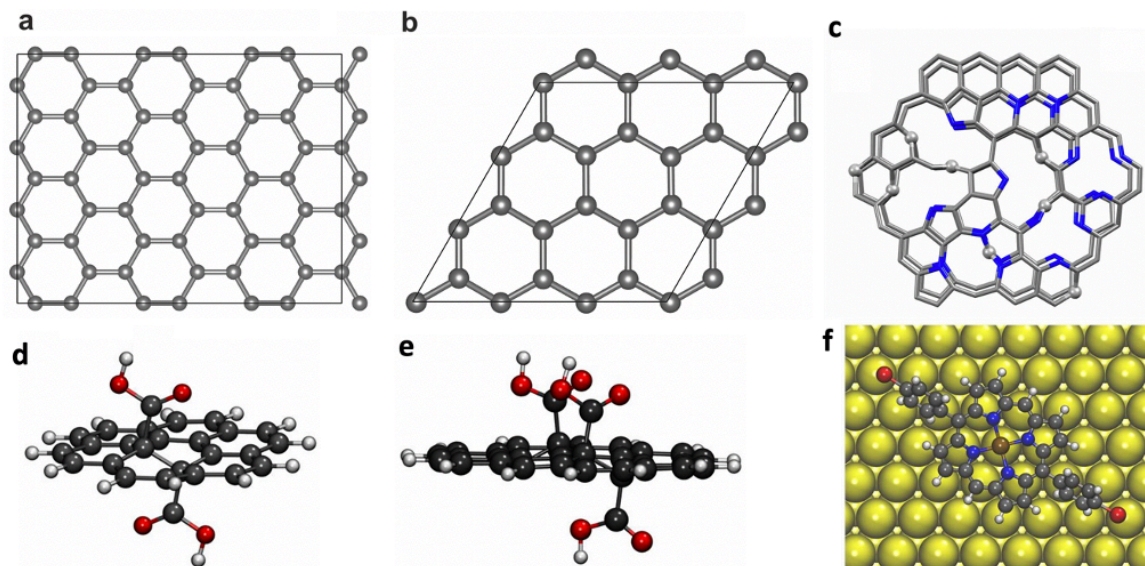
Figure 29 PBC and finite models used in our computational modeling. a) 3 × 3 orthorhombic cell of pristine graphene [14], b) 3 × 3 triclinic cell of pristine graphene [15], c) GN3 graphene flake [16], d) coronene model of G–OOH [17], e) ovalene model of G–OOH [17], f) porphyrin molecule deposited on Au(111) [18]. Color code: carbon in gray/black, nitrogen in blue, oxygen in red, hydrogen in white, iron in ochre, and gold in yellow. Reprinted with permission from [13]–[18].

All PBC calculations were spin-polarized and were executed with PAW potentials [346], [393]. The convergence tests allowed us to determine the cut-off energy and the number of *k*-points to obtain the best compromise between the accuracy of the calculations (**Table 2**) and the time needed to perform them.

Table 2 An example of convergence tests for Gr-P using the PBE functional. Reprinted with permission from [13].

system		total energies (eV)	total magnetic moment (μ_B)	total energies (eV)	total magnetic moment (μ_B))
		400 eV		**600 eV**	
$C_{47}P_1$	$3 \times 3 \times 1$	-439.2767	1.00	-435.1998	1.00
	$6 \times 6 \times 1$	-439.2866	1.00	-435.2098	1.00
	$9 \times 9 \times 1$	-439.2862	1.00	-435.2099	1.00
	$11 \times 11 \times 1$	-439.2865	1.00	-435.2099	1.00
	$15 \times 15 \times 1$	-439.2865	1.00	-435.2099	1.00
	$21 \times 21 \times 1$	-439.2865	1.00	-435.2099	1.00
$C_{46}P_2$-NM	$3 \times 3 \times 1$	-432.5935	0.00	-430.7406	0.00
	$6 \times 6 \times 1$	-432.6008	0.00	-430.7477	0.00
	$9 \times 9 \times 1$	-432.6008	0.00	-430.7477	0.00
	$11 \times 11 \times 1$	-432.6064	0.00	-430.7532	0.00
	$15 \times 15 \times 1$	-432.6074	0.00	-430.7541	0.00
	$21 \times 21 \times 1$	-432.6074	0.00	-430.7542	0.00
$C_{46}P_2$-FM	$3 \times 3 \times 1$	-430.5273	2.00	-429.8078	2.00
	$6 \times 6 \times 1$	-430.5296	2.00	-429.8105	2.00
	$9 \times 9 \times 1$	-430.5293	2.00	-429.8105	2.00
	$11 \times 11 \times 1$	-430.5295	2.00	-429.8105	2.00
	$15 \times 15 \times 1$	-430.5294	2.00	-429.8105	2.00
	$21 \times 21 \times 1$	-430.5295	2.00	-429.8105	2.00

The maximum plane-wave cutoff energy was 600 eV **[13]**. The Brillouin zone integrations were performed with maximum $21 \times 21 \times 1$ k-point mesh **[13]**. Electronic exchange and

correlation effects were treated with GGA-PBE [340]. However, it is known that semi-local GGA functionals tends to underestimate bandgaps [231] due to the self-interaction error and overdelocalization of the electronic system,. For this reasons, for selected systems **[13]** we also performed single-point calculations using the meta-GGA SCAN [351], which has been shown to improve band gaps of diversely bonded materials [352] or more demanding hybrid PBE0 functional [353], which by mixing exact exchange (HF) with PBE exchange may eliminate the—in some sense complementary—deficiencies of HF and DFT and, thus, provide a better description of band gaps.

In systems were non-covalent interactions plays an important role, the empirical dispersion of Grimme [368], [372] was taken into account in both PBC **[16]**, **[17]** and finite **[15]** models. The charge transfer was evaluated *via* Bader charge analysis (PBC) [400]–[402] and natural bond orbital (NBO) analysis (finite model) [403]. The climbing image nudged elastic band method (CI-NEB) [404], [405] was used to determine the reaction transition states.

For graphene-supported TMs **[14]**, and 1D Au(111)-supported metalloporphyrin polymers **[18]** we performed DFT $+ U$ [357], [358] calculations with U–J of 2 eV and 4 eV, respectively. The DFT $+ U$ method depends on semiempirical values of U–J [406] whose transferability between different systems is questionable. However, if moderate values of the on-site Coulomb repulsion are admitted, they introduce only modest changes with respect to conventional DFT calculations [407], whereas large values of the on-site repulsion led to unrealistic eigenvalue spectra of TM dimers [408].

We calculated MAEs following the implementations of David Hobbs [397] and Martijn Marsman and Jürgen Hafner [398] in the VASP package (see **Chapter 3.9**). The MAE per computational cell was evaluated as the difference in total energies between different orientations of the magnetization. In addition to fully self-consistent calculations of MAE, the magnetic force theorem [409] was applied allowing to approximate the MAE by the difference in the band energies from non-self-consistent calculations, thus significantly reducing the computational efforts.

All other calculation details can be found in the Appendices.

# 4 Tailoring Electronic and Magnetic Properties of Graphene by Phosphorus Doping

Rostislav Langer, Piotr Błoński*, Christoph Hofer, Petr Lazar, Kimmo Mustonen, Jannik C. Meyer, Toma Susi*, and Michal Otyepka, *ACS Appl. Mater. Interfaces* 2020, 12, 34074–34085, DOI: 10.1021/acsami.0c07564.

Doping of the graphene lattice by light elements, sulfur [7], nitrogen [6], and boron [410] *opens possibilities for tailoring its electronic and magnetic properties toward spintronic and optoelectronic applications. Further, recent experimental preparation of phosphorus doped graphene (Gr-P) led to the AFM phase below 125 K and the FM phase up to 300 K* [111]. *Although the sp^3-phosphono $-PO_3H_2$ groups were supposed to be the main magnetic sources* [111] *because the oxidation of substituent P is highly exothermic* [411]*, no insight into the influence of particular phosphorus chemical forms on the magnetic properties of Gr-P was presented, which motivated us to investigate the origin of magnetism in this system in more depth including the theoretical estimate of transition temperatures. In particular, we focused our research on the structural, electronic, and magnetic properties of Gr-P and Gr-PO_3H_2 at different levels of doping and structural arrangements. We compared our simulation for the single P-substitution to a 3D reconstruction of the experimental geometry based on atomic-resolution aberration-corrected scanning transmission electron microscopy (STEM) imaging at multiple sample tilts. We also provided a catalogue of theoretical core-level binding energies of variously bonded P that may be present in P-doped graphene to facilitate X-ray photoelectron spectroscopy-based identification of its chemical forms in graphene.*

Our DFT calculations revealed that either P atoms embedded in the graphene lattice or $-PO_3H_2$ functionalized graphene modulated structural, electronic, and magnetic properties of graphene depending on the C/P ratio and bonding configurations ultimately leading to the FM ordering sustainable at RT. This finding possibly elucidates the origin of experimentally observed FM ordering at RT [111]. *Interestingly enough, simultaneous adsorption of P adatoms and substitution of carbon atoms by phosphorus can lead to RT FM and AFM structures in line with experimental findings* [111]. *The co-existence of AFM and FM phases is assigned to the occupations of the graphene bipartite lattice, i.e., the magnetic moments are AFM coupled when the P-moieties are equally located on both sublattices of graphene and the FM phase appears when the P adatoms are located only on one sublattice.*

The unique electronic and magnetic properties of P-doped graphenes, which can be ultimately fine-tuned by the manipulation of P dopants, predispose these materials for various technological applications including catalysis, sensing, energy storage, electronics, and spintronics.

DFT calculations showed that the substitution of carbon atoms by phosphorus (2.13 at.%, $C_{47}P_1$, **Figure 30a**) led to a geometric distortion of the graphene lattice with a C–P bond length of 1.76 Å and a C–P–C angle of 101°, which agrees well with the experimental estimate of 1.61 ± 0.25 Å and $99.6 \pm 11.5°$ [110]. 3D reconstruction of a single P substitution in pristine graphene has been experimentally shown *via* STEM (**Figure 31**). This confirmed that the large atomic radius of P as compared to C cannot be confined by the graphene lattice, which led to the protrusion of the P atom above the graphene plane (**Figure 30b**).
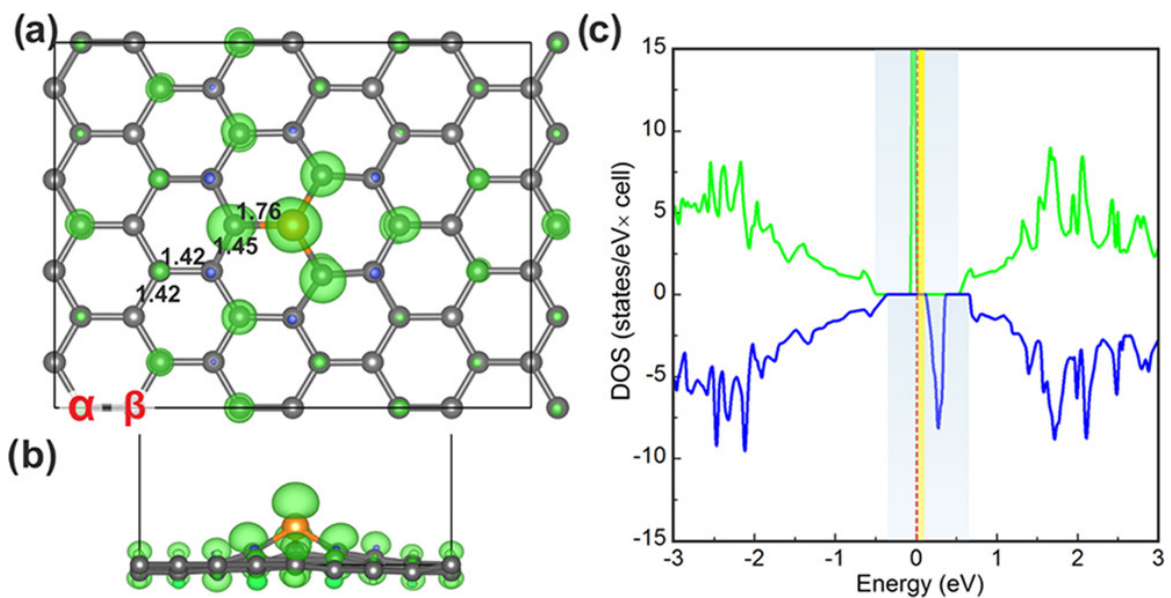
Figure 30 Spin-density distribution plot of Gr-P (2.13 at.%): a) top view and b) side view. Isosurface ± 4 meÅ^{-3}. Positive/negative magnetic moments are shown in green/blue. α and β denote the two sublattices of the graphene bipartite lattice. Numbers correspond to the bond length in Ångstrom. Carbon atoms are shown in gray, and phosphorus atoms are in orange. c) Spin-resolved DOS of Gr-P (2.13 at.%). The Fermi level marked with a vertical red dashed line is set to zero. Blue and yellow bars represent the bandgap and the spin-flip gap, respectively. Reprinted with permission from [13].
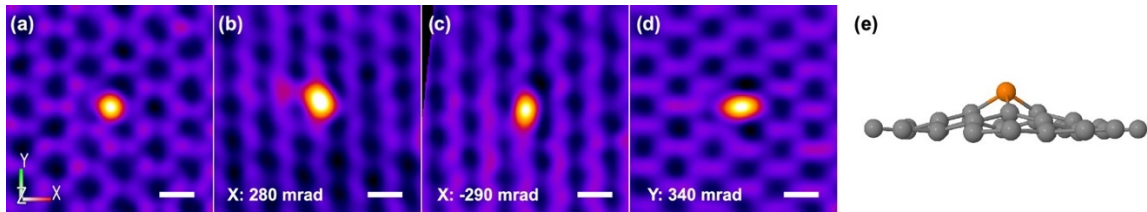
Figure 31 a–d) Atomically resolved STEM projections of a P substitution in graphene at specimen tilt angles of 0, 280, −290, and 340 mrad along the x-axis b, c) and the y-axis d). The scale bars are 2.5 Å. e) 3D reconstruction from multiple images recorded at different tilt angles and with threefold averaging. Reprinted with permission from [13].

Having one additional electron compared to a carbon atom, a single P atom adds an extra electron when substituted into the graphene lattice, thus disrupting its π-delocalized system and opening a 1 eV wide bandgap.

Moreover, doping-induced imbalance of the bipartite graphene lattice, $N = N_\alpha - N_\beta$, where N_α and N_β are the number of atoms belonging to each sublattice, with the total spin of the bipartite lattice given by the formula $2S = |N_\alpha - N_\beta|$ [277], in the case of $C_{47}P_1$ $S = 0.5$, led to two spin-polarized mid-gap states in the vicinity to the E_F separated by a gap of 0.12 eV (**Figure 30c**). The spin-density distribution plot revealed a large spatial extension of the magnetic state (**Figure 30a,b**) around the P dopants and forming a characteristic $(\sqrt{3} \times \sqrt{3})$R30° superstructure recognizable in STM [98]. The orbital/atom decomposed DOS (**Figure 32**) and spin density distribution plots thus demonstrated the direct coupling between the p-orbitals of P and NN C atoms, extending over long distances.
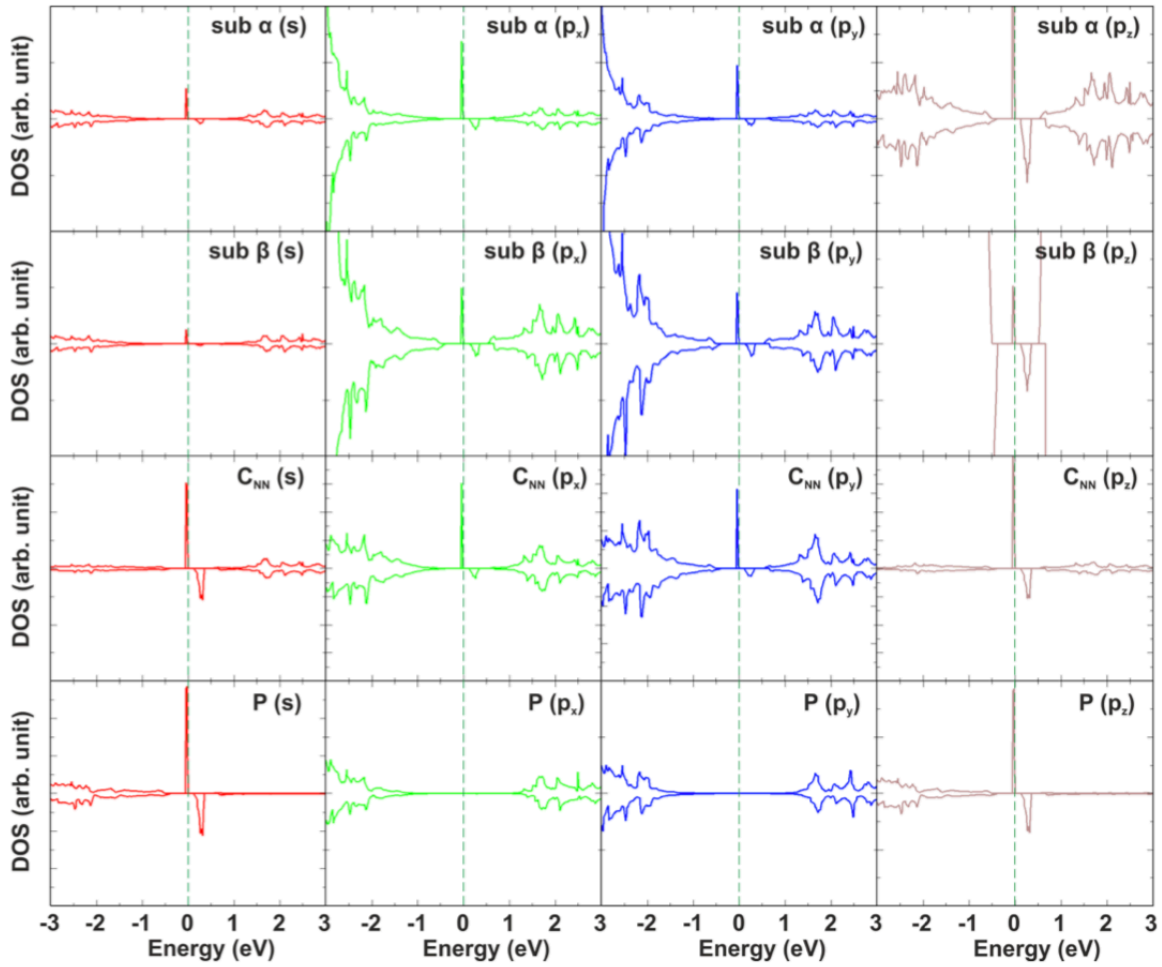
Figure 32 Orbital/atom-decomposed DOS of Gr-P (2.13 at.%). Fermi energy is set to zero (dashed green line). Sub α/β denotes the two graphene sublattices (see Figure 30), C_{NN} denotes nearest neighbor carbon atoms to the P atoms. Reprinted with permission from [13].

The magnetic transition temperature, T_c, is a key material parameter determining its potential industrial applications. If the T_c of a material exceeds the temperature of liquid nitrogen (77 K), the material becomes interesting for real devices and applications. We used the Ising model and a MFA [304] to estimate T_c of P-doped graphene using a C_{96} supercell (denoted as 6 × 3 cell, **Figure 33**) which enabled exchange interactions between single spins comprising magnetic moments induced by doping/functionalization in the C_{48} supercell (3 × 3 cell) (**Figure 30**). The magnetic transition temperatures (normalized per 3 × 3 cell) were evaluated using the Ising model on a square lattice [314] as $T_{C(IS)}^{FM-AFM} = \frac{0.567J}{k_B}$ for spin $S = 0.5$ ($C_{47}P_1$, $C_{48}P_1$, $C_{45}P_3$, Gr-P-O$_x$). For higher spin systems, we used the following expressions: $T_{C(IS)}^{FM-AFM} = \frac{1.674J}{k_B}$ for $S = 1$ ($C_{46}P_2$, $C_{47}P_2$), $T_{C(IS)}^{FM-AFM} = \frac{3.278J}{k_B}$ for $S = 1.5$ ($C_{45}P_3$), and $T_{C(IS)}^{FM-AFM} = \frac{5.351J}{k_B}$ for $S = 2$ (Gr-P-O$_x$), where k_B stands for Boltzmann constant

and J denotes the magnetic exchange coupling, evaluated [307] as $J = \frac{E_{FM} - E_{AFM}}{2zS^2}$, where E_{FM} and E_{AFM} are total energies of FM and AFM phases, respectively, and z is the coordination number in systems of *single* spins (**Figure 33**). Within the MFA [305] T_c was estimated as $T_{C(MF)}^{FM-AFM} = \frac{JS(S+1)}{3k_B}$, where $J = \frac{E_{FM} - E_{AFM}}{2}$ per pair of single spins S. Depending on the mutual configuration of the P atoms in the larger 6×3 cell, T_c of P-doped graphene with coverage of 2.13 at.% may be as high as 86 K (Ising model), which makes it promising material for potential spintronics applications. In the case of Gr-P, the MFA provided rather unrealistic T_C values as opposed to the reasonable values from the Ising model.
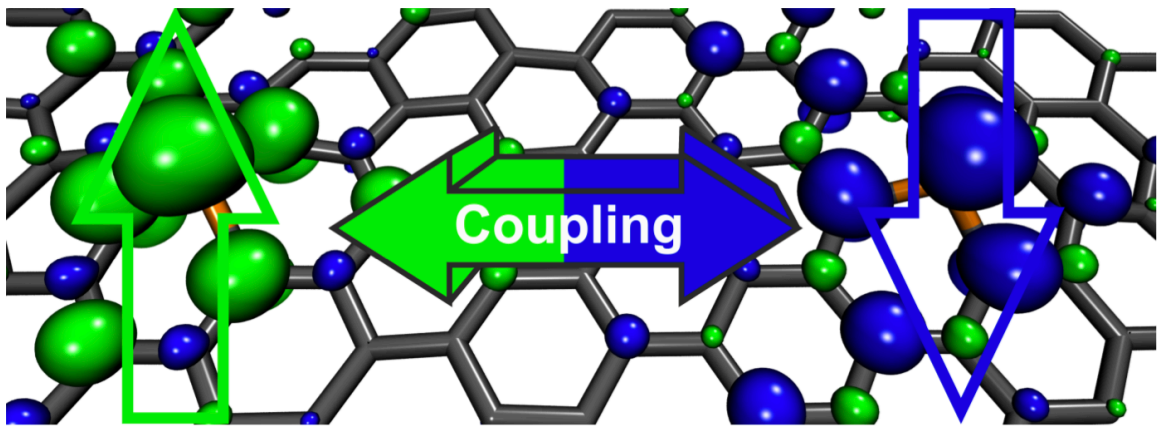
Figure 33 Scheme of calculating the transition temperature between the FM and AFM phases. A 6 × 3 supercell enabled the AFM interaction (positive/negative magnetic moments are depicted in green/blue) of magnetic islands by flipping their spin alignment (green/blue arrows). Reprinted with permission from [13].

The increased concentration of P atoms in the graphene lattice (4.35 at.% and 6.67 at.%) slightly modified the C–P bond lengths and C–P–C angles (1.76–1.78 Å and 99–102°). The stability of Gr-P depends on the mutual positions of the P atoms; in the GS phosphorus atoms taken the nearest-neighbor positions in the graphene lattice (4.34 at.%, **Figure 34**) and at a higher concentration (6.67 at.%, **Figure 34**) they occupied the para-positions in the graphene lattice. In experimental samples, the configuration of P dopants depends on the presence and type of defects, reactive sites, and contaminations during synthesis, therefore, the system is likely to differ from the energetically most stable configurations [109], [110].

The bipartite nature of the graphene lattice dictates whether or not Gr-P has magnetic properties, so the electronic and magnetic properties of Gr-P vary significantly both with the concentration and configurations of P atoms in the graphene lattice. Whereas P atoms evenly substituting C atoms in both sublattices at 4.35 at.%, led to the NM structure

(**Figure 34a**), the imbalance of the graphene lattice gave rise to the long-range FM ordering as evident in the spin-density plots (**Figure 34b,c**) with T_c reaching 192 K calculated using the Ising model. However, increasing the P doping level to 6.67 at.% significantly lowered T_c to a maximum of 46 K.

The Gr-P at at 4.35 at.% and 6.67 at.% exhibited either metallic or semiconducting electronic structure. The bandgap of NM Gr-P was smaller than those for magnetic structures, however, the presence of mid-gap states effectively lowered their electronic gaps. Moreover, a pronounced DOS near E_F in some of the theoretical structures indicated a possibility of appreciable conductivity. It should be noted that experimental samples may contain various arrangements of P atoms, and their electronic structure would therefore reflect a statistical averaging of the different configurations.
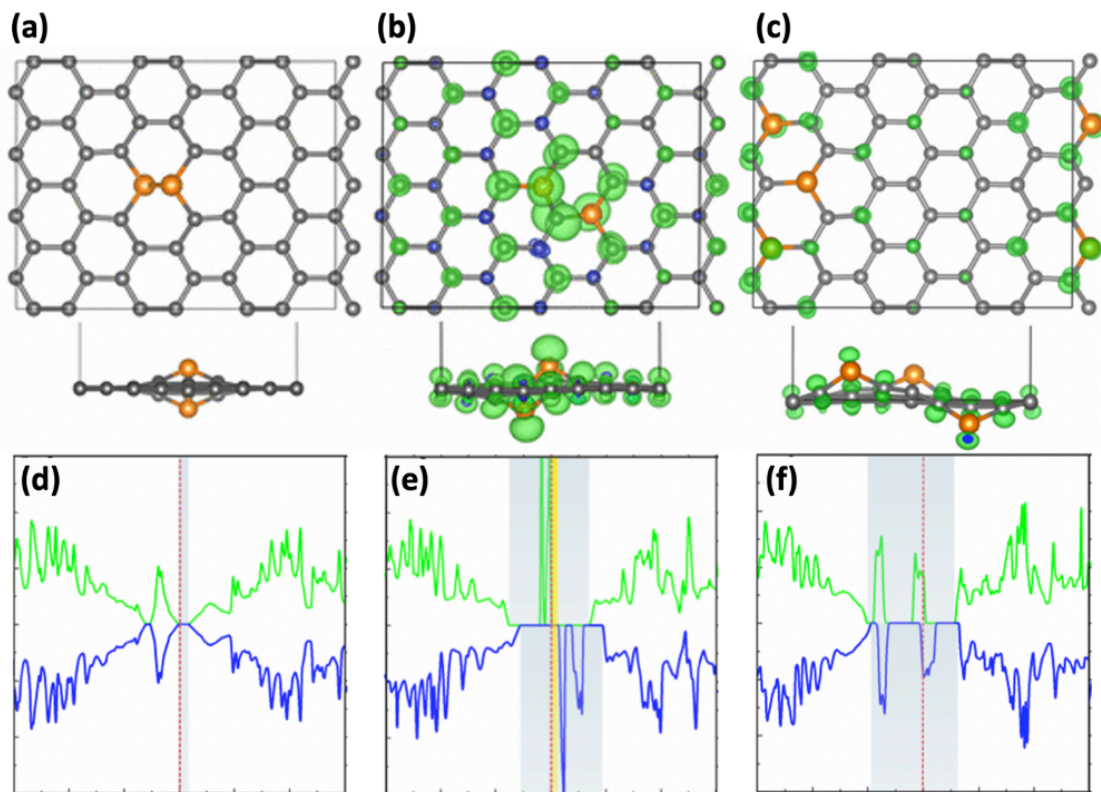
Figure 34 Structures and spin textures of a) the most stable Gr-P at 4.35 at.%, b) the most stable magnetic arrangement at 4.35 at.%, and c) the most stable Gr-P at the 6.67 at.%. Reprinted with permission from [13].

In addition to the substitution of the C atoms in the graphene lattice with P atoms, we considered adsorption of P adatoms onto graphene (Gr-adP). Among the high-symmetry sites of the graphene, only the bridge (B) site (**Figure 35**) appeared to be stable (-0.46 eV), while the on-top (T) and the hollow (H) sites were unstable. Consequently, the diffusion of

P adatoms along B–T–B or B–H–B paths is unlikely, as P adatoms would rather spontaneously desorb from graphene.

A tiny bandgap was opened in Gr-adP doped at 2.08 at.% as shown in DOS plot (**Figure 35**) and the spin value was $S = 0.5$, which can be understood by electron counting: two valence electrons formed covalent bonds with C atoms below, two electrons formed a lone pair, and the fifth valence electron induces a magnetic moment in Gr-adP. However, the carbon atoms in the vicinity of P adatom were NM, indicating PM in Gr-adP (2.08 at.%). This was further corroborated by the calculated T_c of 2 K showing excellent agreement with the experiments [111] where PM behavior was witnessed at a low P concentration.
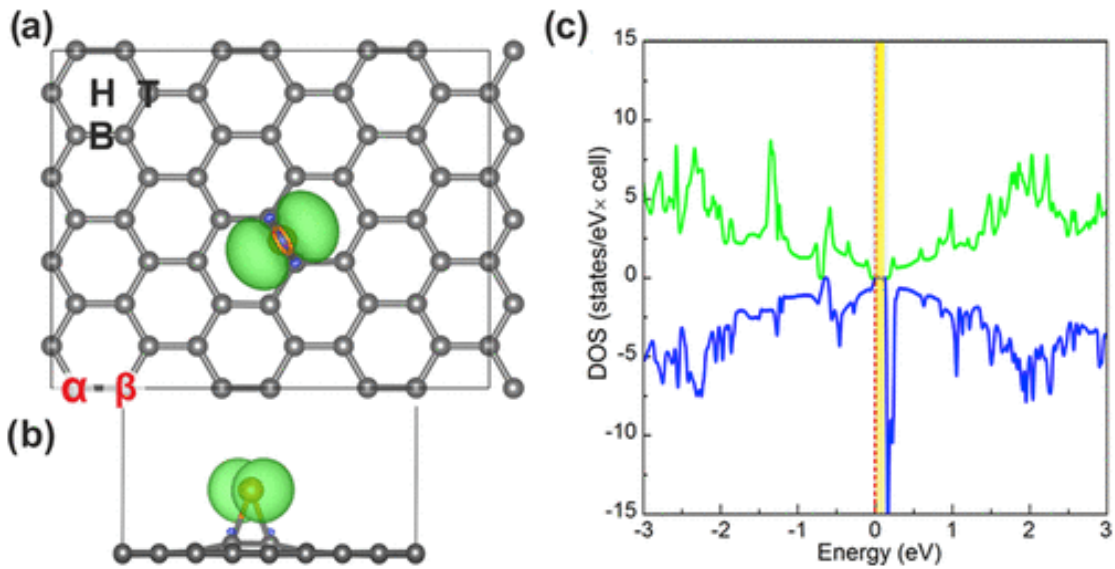
Figure 35 Spin-density distribution plot of Gr-adP (2.08 at.%): a) top view and b) side view. Isosurface is ±4 meÅ⁻³. c) Density of states of Gr-adP (2.08 at.%). α and β denote the two sublattices of the graphene bipartite lattice. T, B, and H stand for on-top, bridge, and hollow site, respectively. Reprinted with permission from [13].

We also studied the adsorption of a P adatom onto P-doped graphene. The adsorption energy depended on the mutual distance between the P adatom and the P-dopant, and the P adatom showed a tendency to adsorb next to the P atom substituting C in the graphene lattice. The adsorption configurations determined the electronic and magnetic properties of the considered structures. The Gr-adP structures possessed semiconducting electronic structure. We found FM structures with $S = 1$ and T_C of 18–303 K (Ising model) and, interestingly, the GS AFM structure at RT. Importantly, the co-existence of FM and AFM structures has been observed in experimental samples of P-doped graphene [111].

In the light of the experimental P-doped graphene [111], we theoretically considered also various oxidized phosphorus groups and functional groups adsorbed onto pristine graphene or onto Gr-P (**Figure 36**). While phosphate $-OPO_3H_2$ or $-OPO_2$ groups were unstable and desorbed from the graphene lattice, the relatively weakly bound phosphono $-PO_3H_2$ group (-0.42 eV) induced FM in the system with $S = 1$ and $T_c = 44$ K, and a similar spin texture and electronic structure to the single P-doped graphene. For two $-PO_3H_2$ in meta configuration on the graphene lattice, T_c increased to 148 K.

Finally, we considered the simultaneous effect of Gr-P, Gr-P-O_x, and Gr-PO$_3$H$_2$ on the electronic and magnetic properties of functionalized graphene. All structures were semiconducting. Depending on the composition and configurations of the theoretical structures, FM can emerge with midgap states at E_F and the theoretical T_c reaching 242 K. Thus, in line with experimental findings [111] magnetism with high T_c may result from a synergistic effect of phosphorus in various bonding configurations.
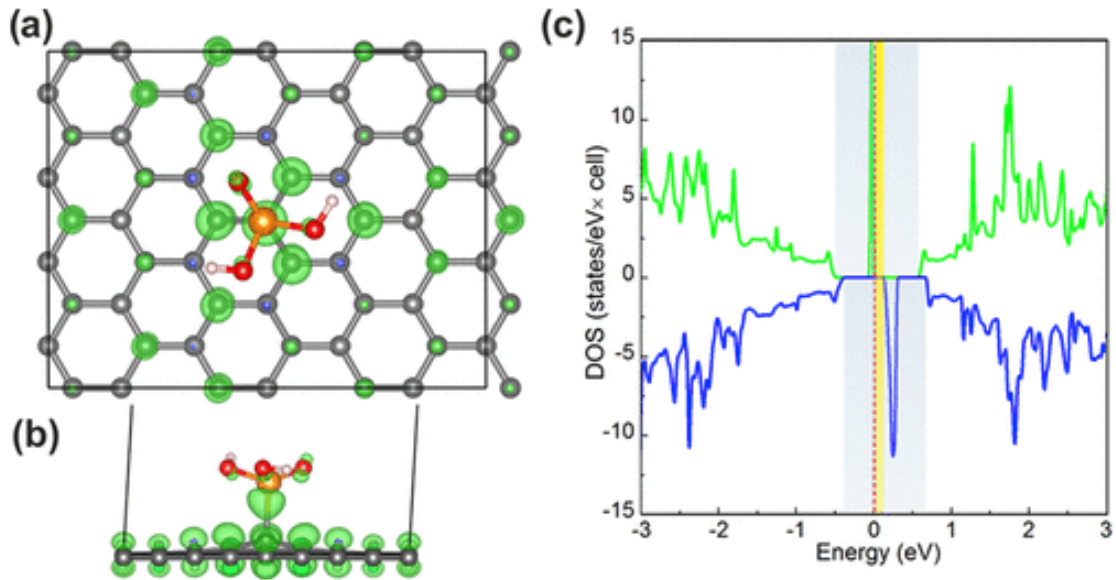
Figure 36 Spin-density distribution plot of Gr-PO$_3$H$_2$: a) top view and b) side view. Isosurface is ±4 meÅ^{-3}. c) Density of states of Gr-PO$_3$H$_2$. Reprinted with permission from [13].

Since semi-local GGA functionals tend to underestimate bandgaps due to self-interaction error and excessive delocalization of the electron system [231], [412], we calculated the bandgaps of several Gr-P structures using the meta-GGA functional SCAN [351] and hybrid functional PBE0 [353]. Both functionals resulted in wider bandgaps as compared with GGA-PBE. The bandgaps of the FM structures increased by 0.4-0.7 eV and the spin-flip gaps by 0.7-1.2 eV. For NM structures, the SCAN functional predicted wider bandgaps by

approximately 0.1 eV, and for PBE0 by 0.6-0.7 eV. The values of T_c increase up to 90-times (SCAN) and up to 50-times (PBE0), and thus did not lead a realistic estimate. This can be attributed to the larger exchange distribution 100-3450% relative to the GGA-PBE value.

In summary, we theoretically investigated the structural, electronic, and magnetic properties of Gr-P. We considered the P atoms embedded in the graphene lattice as well as on-surface adsorbed the P adatoms and the POx functional groups. The simultaneous P-doping and sp^3 functionalization of graphene by the –PO$_3$H$_2$ groups as well as adsorption of the P adatoms may lead to the RT FM or AFM alignment in accordance with the experimental findings [111]. The electronic structure calculations revealed that the magnetic ordering of Gr-P can be attributed to a combined direct coupling in an antiparallel fashion of an electron cloud of partially filled π-orbitals of neighboring carbon atoms that extends over a large distance from the P dopant, and the RKKY interaction. Our theoretical research was supported by an experimental reconstruction of the 3D geometry of the single P substitution. Our results may further encourage research into graphene-based magnets with C/P-tuned properties, or ultimately through the direct manipulation of P dopants. The unique and tunable electronic and magnetic properties of P-doped graphene predestine these materials for plethora of applications including spintronics.

5 Graphene Lattices with Embedded Transition-Metal Atoms and Tunable Magnetic Anisotropy Energy: Implications for Spintronic Devices

Rostislav Langer, Kimmo Mustonen, Alexander Markevich, Michal Otyepka, Toma Susi*, and Piotr Błoński*, *ACS Appl. Nano Mater.* 2022, 5, 1562–1573, DOI: 10.1021/acsanm.1c04309.

Big Data with a complex structure and large, aggressively growing volume challenges the storage capacity of data centers, thus spurring the drive to store information at the atomic scale. One of the great challenges in this field is preventing thermally induced reorientation of the magnetic moments between the easy and hard magnetization axis or, in other words, increasing the blocking temperature, which is enforced by magnetic anisotropy energy, i.e., the energy barrier for magnetic moments to flip their directions. Single-atom magnets represent the ultimate limit of the magnetic data storage [73], [87], [413]. Identifying substrates anchoring magnets the size of atoms firmly and, thus, conserving their size, symmetry and, accordingly, a large MAE, is at the core of the frontier magnetic materials research. If a system with an MAE could be found at least corresponding to the temperature of liquid nitrogen, data centers applications would become more feasible. To this end, transition metal atoms and their nanoclusters adsorbed on graphene were extensively studied and single-layer graphene with vacancy defects was identified as a suitable anchoring platform for magnetic TM atoms with remarkable MAE values [23], [76]. Atomic vacancies in graphene can be created intentionally, by irradiation.

In the light of recent advances in experimental manipulation of foreign atoms in the graphene lattice [282], [414], [415], we chose Cr, Mn, and Fe as prototypical metals from Groups VI.-VIII.B for the systematic study under SP-DFT with SOC and on-site Coulomb repulsion of 2 eV, changes in electronic and magnetic properties of doped defective graphene, including MAE, in relation to the arrangement and distances between TM atoms, both of the same element and two different TM atoms.

We found that doping of graphene with two different TM atoms and the formation of upright TM dimers lead to a vast increase in MAE compared to SA-doped graphene, and the value and even the sign of MAE as well as the electronic structures are sensitive to the distribution of doping atoms in the graphene lattice. In particular, two upright Fe–Mn dimers bound to two separate DVs reach an MAE of 120 meV due to the graphene-mediated RKKY exchange

between dimers, which modifies the occupations of states near E_F such that a changed splitting of energy bands that have degenerated in the absence of SOC lowers the total energy. The MAE of 120 meV corresponds to a blocking temperature of 34 K assuming a relaxation time of 10 years.

We first focused our investigation on the stability and structural, electronic, and magnetic properties of SAs of Cr, Mn, and Fe embedded in SV and DV defects in the graphene lattice, both bare and nitrogen-decorated (NSV and NDV). All TM atoms were strongly bound in vacancy defect, which is consistent with previous reports on TM@SV and TM@DV [80] (**Figure 37a,b**). The presence of N atoms on the edges of defects in the graphene layer increased the binding energies of TM atoms compared to TM@NSV and TM@NDV.

The presence of TM in a defective area of the graphene lattice, specifically Mn@DV, was experimentally recognized by STEM (**Figure 37c**) and its identity was confirmed by electron energy-loss spectroscopy, which also allowed to determine the Mn L_3/L_2 white-line ratio.
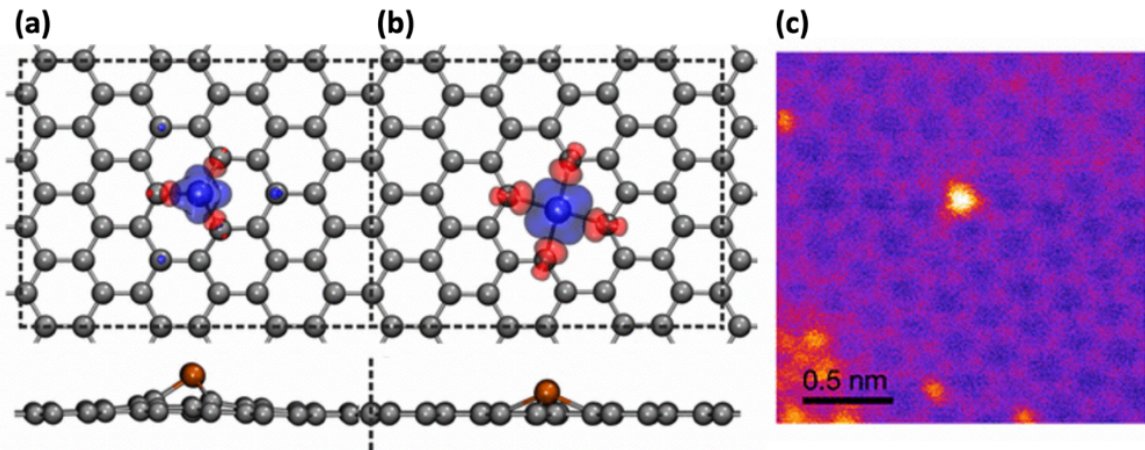
Figure 37 Top and side view of a) TM@SV and b) TM@DV where TM stands for Cr, Mn, and Fe. Carbon atoms are depicted in gray, and TM atoms in ocher. Spin densities corresponding to positive/negative magnetic moments are displayed in blue/red at isosurface values of ±0.035 eÅ^{-3}. Supercells are marked by dashed lines. After the cell was doubled in the x-direction, a second defect was introduced into the lattice. c) STEM image of an Mn@DV impurity (bright contrast) bonded to four carbon atoms in a disordered patch of graphene. Reprinted with permission from [14].

All considered TM atoms induced magnetic moments in graphene of 2 μ_B or 3 μ_B for TM@S(D)V and in the range of 1 μ_B to 4 μ_B for TM@NS(ND)V. Depending on the spin and symmetry of the interacting states [416], [417] the coupling of states with energies above and below E_F through spin-orbit interaction promotes either perpendicular or in-plane

magnetization, as shown in **Figure 38**. However, MAE was small in the range between ±0.1 meV and 1.1 meV and increasing within the Cr–Mn–Fe order in line with the low orbital moment anisotropy at isotropic spin moments. No significant changes of MAE were observed for TM@NS(ND)V.

In agreement with other studies, the electronic structure of graphene changed from semimetal to metal (Mn@DV and Fe@DV), half-metal (Fe@SV [298]), and/or semiconductor (Cr@SV [298], Mn@SV [418], and Cr@DV [419]), whereas N-impurities acting as *n*-dopants shift the density of states toward lower energies causing the semiconductor (Cr@SV and Mn@SV) to metal transition (Cr@NSV and Mn@NSV), half-metal (Fe@SV) to semiconductor transition (Fe@NSV), and metal (Mn@DV and Fe@DV) to semiconductor transition (Mn@NDV and Fe@NDV).
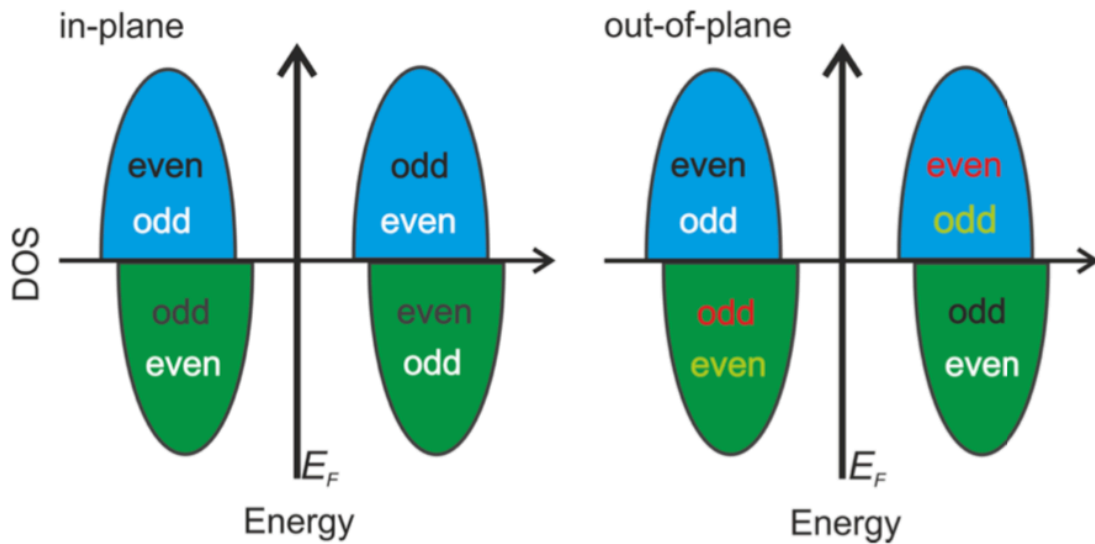
Figure 38 Coupling of eigenstates with energies above and below E_F through spin-orbit interaction, which favors either perpendicular or in-plane magnetization, depending on the spin and symmetry of the interacting states. For the five *d* states (per spin), in-plane magnetization is favored if the E_F is located between even $m_l = 0, \pm2$ and odd $m_l = \pm1$ states of the same spin, or between even or odd states of opposite spin. A perpendicular magnetization is favored if E_F is located between even (or odd) and odd (or even) states with opposite spins. Reprinted with permission from [14].

Information can be stored and processed on the atomic scale if the atomic spins are coupled. Indeed, the possibility to tailor the sign and strength of the magnetic coupling between atomic spins by the RKKY interaction mediated by conduction electrons in a metallic substrate has been demonstrated by spin-polarized scanning tunnelling spectroscopy (SP-STS) [407]. More recent time-resolved SP-STM experiments and DFT calculations [420]

further confirmed the role of the RKKY interaction in enhancing the atomic spin stability. The capability of the RKKY interaction to transfer and process information between atomic spins of adatoms on a NM metallic surface has been proven experimentally by realizing few-atom spin-based logic gates [93]. This sparked our interest in examining the property changes along with the mutual distances of TM atoms. To this end, we employed a larger 6×3 orthorhombic cell with two defects, and by changing the distance between the defects, we simulated the mutual interaction of TM atoms at different separations within the graphene lattice.

Whilst no structural changes of TM_1TM_2@SV and TM_1TM_2@DV were spotted compared to TM@SV and TM@DV, the magnetic moments were appreciably different from those of SA-doped graphene and, except CrCr@SV and MnMn@SV, the magnetic moments of the larger 6×3 cells were not the sum of the magnetic moments of the smaller cells. Notably, an increased magnetic moment of CrCr@DV and MnMn@DV indicating a synergistic effect between TM atoms. Moreover, depending on the distribution of the TM atoms in the graphene lattice, the AFM order was more energetically preferred than the FM one in line with other studies [418], [421], for instance, MnMn@SV and CrCr@DV. Nonetheless, the MAE values of the graphene-doping homoatomic pairs were still in the sub-meV range, and the highest MAE found for CrCr@DV was only 1.6 meV.

For the graphene doping heteroatomic pairs TM_1TM_2@SV and TM_1TM_2@DV calculated at a fixed distance of 12.87-13.24 Å between TM_1 and TM_2, the magnetic moments were the sum of the magnetic moments of individual TM atoms, and the electronic band gaps reached approximately the mean values obtained for the TM-SAs, but noteworthy, their MAE per computational cell increased significantly compared to TM-SAs. We found an MAE of –23.0 meV for CrFe@DV (**Figure 39**), 16.0 meV for CrMn@DV, and –15.8 meV for FeMn@DV. For Cr and Mn atoms of CrMn@DV separated by 6.55 Å, we found the MAE increased to 47.5 meV due to a strong anisotropy of the spin moments. Among the TM_1TM_2@NSV and TM_1TM_2@NDV systems, FeMn@NSV exhibited the highest MAE of 5.2 meV. The enhanced MAE in DV-graphene doped with two different TM atoms, which contrasts with SA-doped graphene, is a changed splitting of energy bands that were degenerate in the absence of SOC, and the downshift in binding energies of the d_{z^2} states, both leading to a lowering of the total energy (see the Appendix for more details) upon the reorientation of the magnetization direction.

The TM atoms induces magnetic moments in the surrounding carbon atoms of the graphene lattice due the sharing of electrons between the magnetic atoms and the lattice (**Figure 39**). Moreover, a (half)metallic DOS of (CrMn@DV) and FeMn@DV can enable the conduction electrons to couple to magnetic moments, which indicates the presence of an RKKY exchange [94]–[96] across the graphene lattice (**Figure 40**). The energy gap at E_F in CrFe@DV indicates that the RKKY interaction is suppressed in this system, and the coupling between the TM atoms is due to superexchange within the carbon atoms.
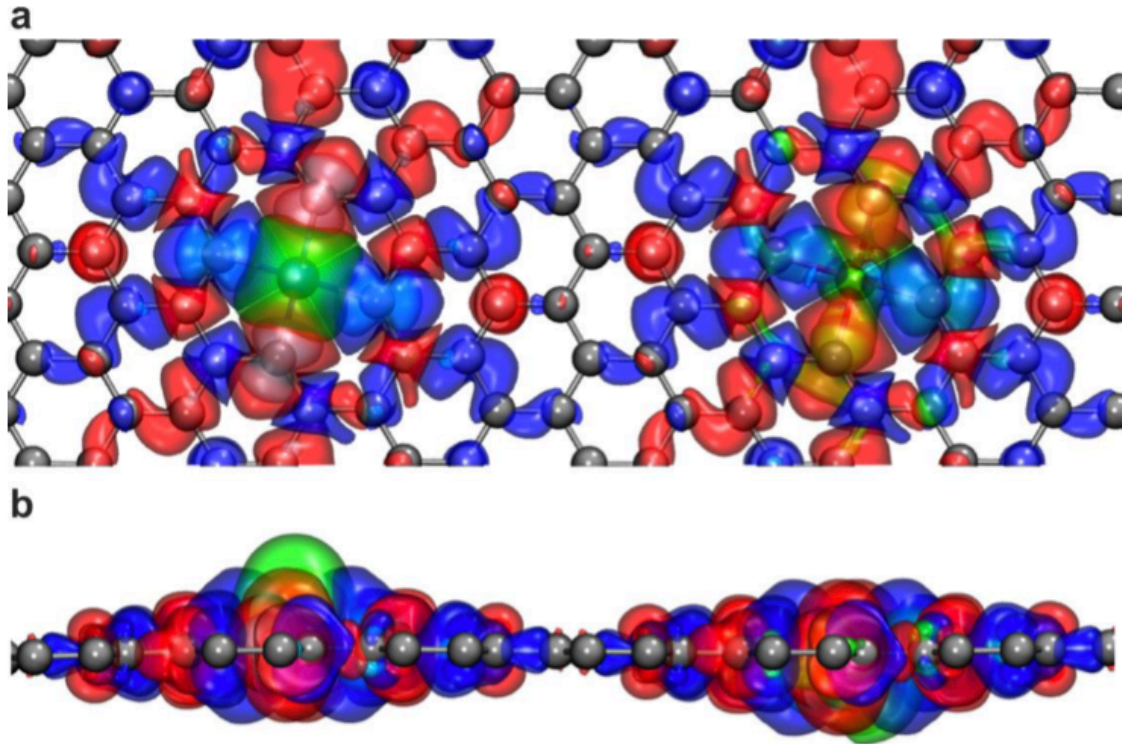
Figure 39 a) Top and b) side view of spin densities for the system of Cr and Fe atoms bound to separate DV defects plotted at ±0.01 eÅ^{-3} isovalues for Cr and Fe (displayed in green/cyan for spin densities corresponding to positive/negative magnetic moments) and ±0.001 eÅ^{-3} (shown in blue/red) for DV-graphene. Reprinted with permission from [14].
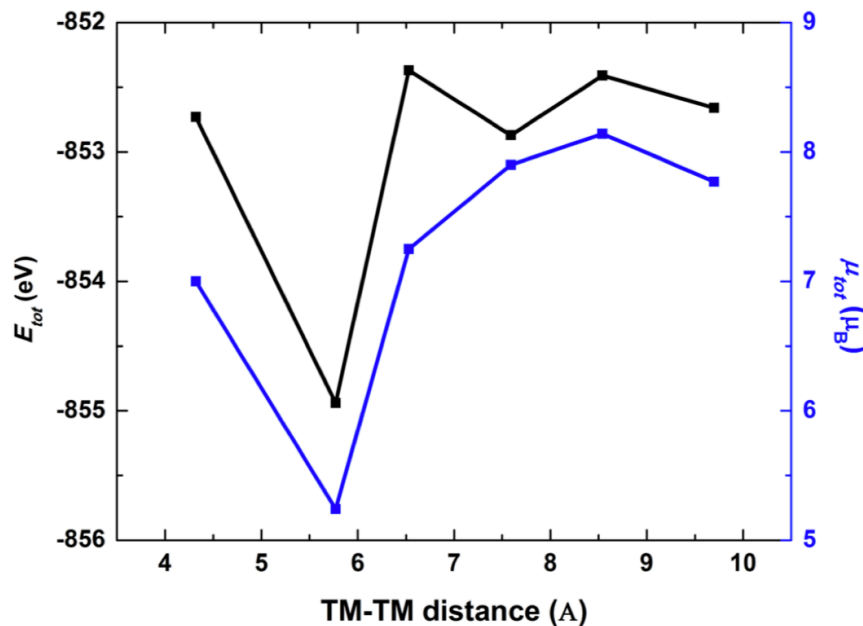
Figure 40 Variation in the calculated total energies (in black) and magnetic moments (in blue) with the distance between TM atoms in the CrFe@DV system. Reprinted with permission from [14].

In the view of theoretical calculations showing MAE enhancement in TM dimers on graphene [23], [408], [422], we investigated the possibility of creating TM–TM upright dimers embedded into defective graphene and their MAEs. We found the exothermic binding energy of the second TM atom on top of TM@DV and TM@SV ranging from −4.05 to −0.04 eV with a TM_1–TM_2 bond length of 1.98–2.85 Å and magnetic moments of 1.4–8.0 μ_B. The Fe@Mn@DV and Mn@Mn@SV systems have large positive MAEs of 9.8 meV and 14.9 meV respectively, and Fe@Fe@SV a large negative MAE of −12.4 meV. Earlier studies [23], [84] revealed that the dominant part in the MAE is enforced by the upper TM atom even despite the opposite MAE of the lower TM atom.

The introduction of a second Fe@Mn dimer into the DV defect at a distance of 12.9 Å from Fe@Mn@DV (**Figure 41**) resulted in an MAE increase to ~120 meV due to the spin anisotropy of −1.6 μ_B and the graphene-mediated RKKY-like exchange interactions between the dimers. **Figure 42** shows that the dominant positive contribution to the enormous MAE of ~120 meV is brought about the presence of partially occupied quasi-degenerate states at E_F and which is lifted for axial magnetization. This appears to be a general feature of the mechanism favoring the large MAE formation [423]. The giant MAE of ~120 meV corresponds to the blocking temperature of 34 K with a relaxation time of 10 years based on Néel's theory [68].

It is noteworthy that the phonon frequency calculations and the calculated Gibbs energy of −1.36 eV at 373 K for the Fe@Mn dimers indicate that they may be stable in the DV defects.
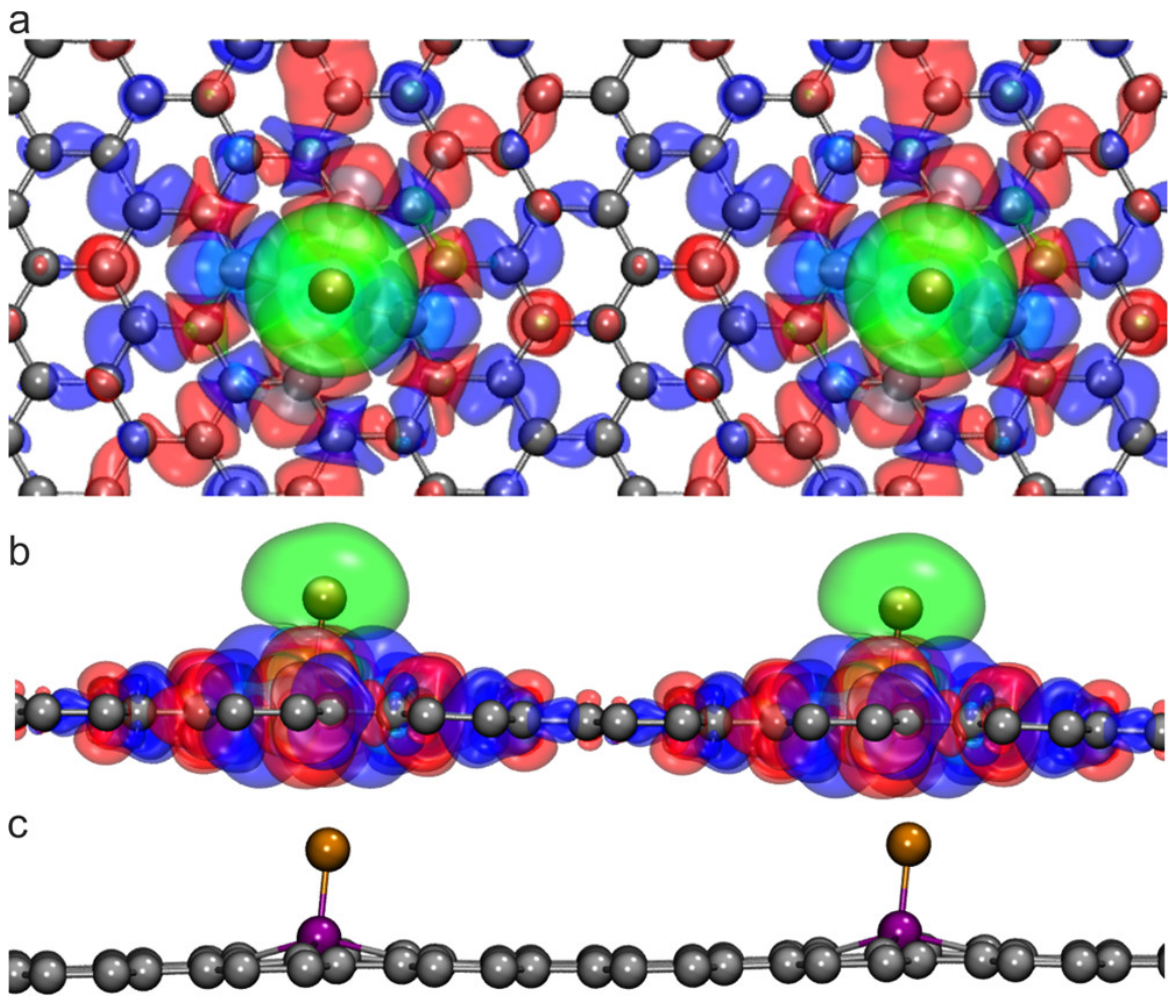
Figure 41 a) Top view and b) side view of spin densities plotted at ±0.01 e⁻Å⁻³ isovalues for Fe@Mn (displayed in green/cyan for spin densities corresponding to positive/negative magnetic moments) and ±0.001 eÅ⁻³ (shown in blue/red) for DV-graphene for the system of two Fe─Mn dimers bound to separate DV defects. c) Side view of the corresponding structure. Gray, purple, and ocher colors represent carbon, manganese, and iron atoms, respectively. Reprinted with permission from [14].
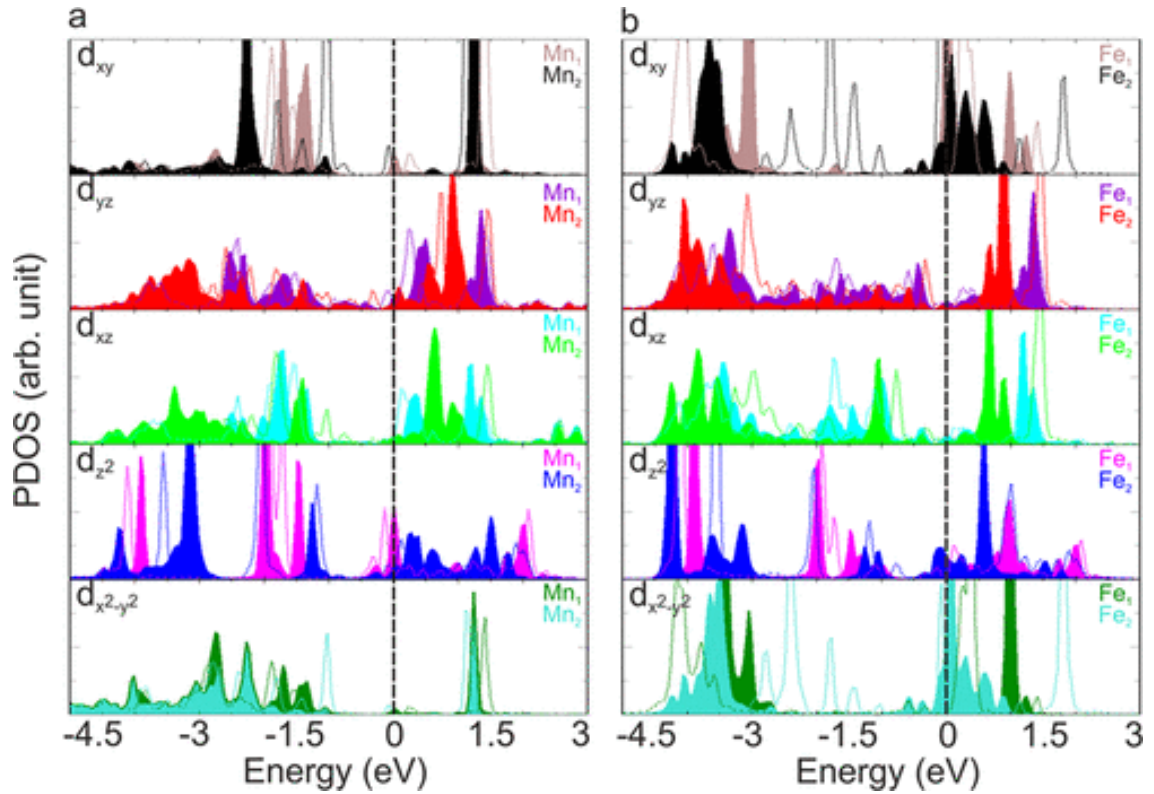
Figure 42 Relativistic partial atom/orbital-resolved densities of states for two Fe–Mn dimers bound to separate DV defects for in-plane (solid lines) and perpendicular magnetization (dashed lines): a) Mn atoms and b) Fe atoms. Reprinted with permission from [14].

In conclusion, in this work, we theoretically investigated the stability and the electronic and magnetic properties of TM atoms and dimers of the elements Cr, Mn, and Fe in (N)SV and (N)DV in the graphene lattice. We focused our study on the MAE dependence on i) the distances between TM atoms in the single-layer graphene; ii) homo- and heteroatom doping of graphene; iii) the formation of upright TM dimers of the same and different elements.

One of the most significant findings of our work is that, unlike the low MAE of up to 2 meV for TM SA-doped graphene, doping of graphene with two different TM atoms and the formation of upright TM dimers leads to a huge increase in MAE. The combination of graphene-mediated RKKY-like superexchange interactions between TM dopants and the presence of partially occupied degenerate states at E_F favors large MAE, which for the Fe@Mn@DV system can reach ~120 meV. TM-doped conductive graphene with robust magnetic properties therefore offers a new perspective in the design of graphene-based spintronic devices.

6 On-Surface Synthesis of One-Dimensional Coordination Polymers with Tailored Magnetic Anisotropy

Benjamin Mallada, Piotr Błoński*, Rostislav Langer, Pavel Jelínek, Michal Otyepka, and Bruno de la Torre*, *ACS Appl. Mater. Interfaces* 2021, 13, 32393–32401, DOI: 10.1021/acsami.1c04693.

1D organic polymers with regularly distributed magnetic centers are desirable for next-generation electronic and spintronic devices for their long spin coherence length and mechanical flexibility. However, the experimental synthesis of such 1D magnets is still a significant challenge. Advances in this field require the selection of an appropriate functional molecule to form a large 1D polymeric framework. Porphyrin frameworks with coordinated TM atoms appear promising thanks to their high thermal stability and propensity to form well-ordered assemblies on various solid surfaces.

A thermally assisted Ullmann-like coupling reaction of Fe(III)diphenyl-bromine-porphyrin (2BrFeDPP-Cl) on Au(111) successfully led to synthesized 1D porphyrin chains. In addition, the thermally controlled C–H bond activation of this material resulted in molecular planarization driven by the 2D surface confinement on the gold substrate. Based on theoretical calculations, we described the mechanism of heat-induced intramolecular planarization and the related change in MAE of metalloporphyrin polymers. Thermal activation of the C–H bond leads to conformational changes in the porphyrin units, which results in on-surface molecular planarization, changing the symmetry of the Fe environment leading to rearrangement of the 3d levels of the central Fe atom.

Before discussing the calculation results, let us first briefly talk over the experimental data. The molecular precursor used in this study – iron(III)5,15-(di-4-bromophenyl)porphyrin chloride, 2BrFeDPP-Cl (**Figure 43**) – possesses phenyl groups functionalized with C−Br groups at the para position, which ensures the linearity of the polymeric product after dehalogenation on the Au(111) substrate.

At 300 K, 2BrFeDPP-Cl adsorbed onto the Au(111) substrate in the form of spatially extended close-packed islands, as shown by STM (**Figure 44a-c**). These are dechlorinated species 2BrFeDPP in the saddle conformation with twisted aryl moieties. DFT calculations of 2BrFeDPP@Au(111) revealed that the Fe ion is above the Au atom and 3.53 Å from the surface, and the adsorption energy is −77.4 kcal/mol.

At 500 K the C−Br bonds were cleaved and large 1D poly-FeDPP wires (that extend up to ~40 monomers) were formed due to the surface-assisted aryl–aryl cross-coupling of adjacent porphyrin molecules, as demonstrated by STM/non-contact AFM (**Figure 43** and **Figure 44d-f**).

At 600 K, the molecular units within the wires underwent an intramolecular transition via dehydrogenation and electrocyclic ring closure of their aryl termini and the macrocyclic pyrroles, resulting in isoindole motifs inducing planarization of the porphyrin monomers on the surface (FePP units, **Figure 43** and **Figure 44g-i**).

Our theoretical calculations revealed that the activation energy for Br removal was lower than that of H removal by 15 kcal/mol. The Br removal reduced the BDE of the H atom, thus facilitating the H abstraction at higher temperatures, resulting in ring closure of the aryl moieties steered by the 2D confinement of the surface. Hence, sequential annealing of 2BrFeDPP allows first the formation of poly-FeDPP structures via Ullmann bonding of aryl-halides, and then the formation of planar poly-FePP structures at higher temperatures.
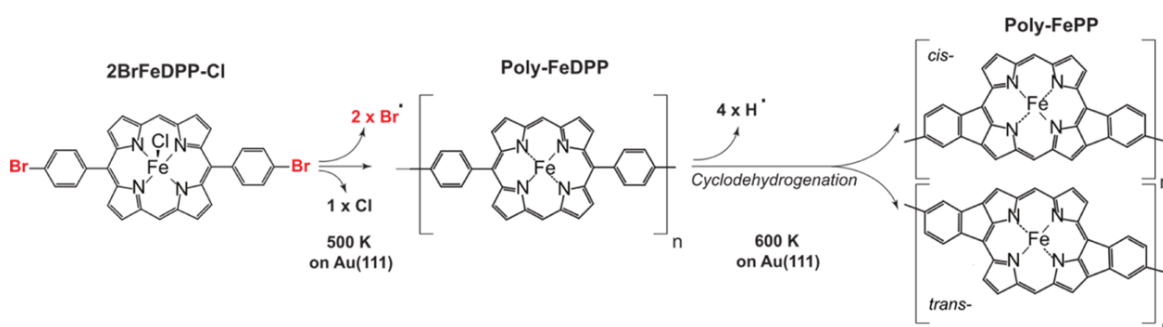
Figure 43 Thermal reaction mechanism of 2BrFeDPP-Cl on Au(111). Reprinted with permission from [18].
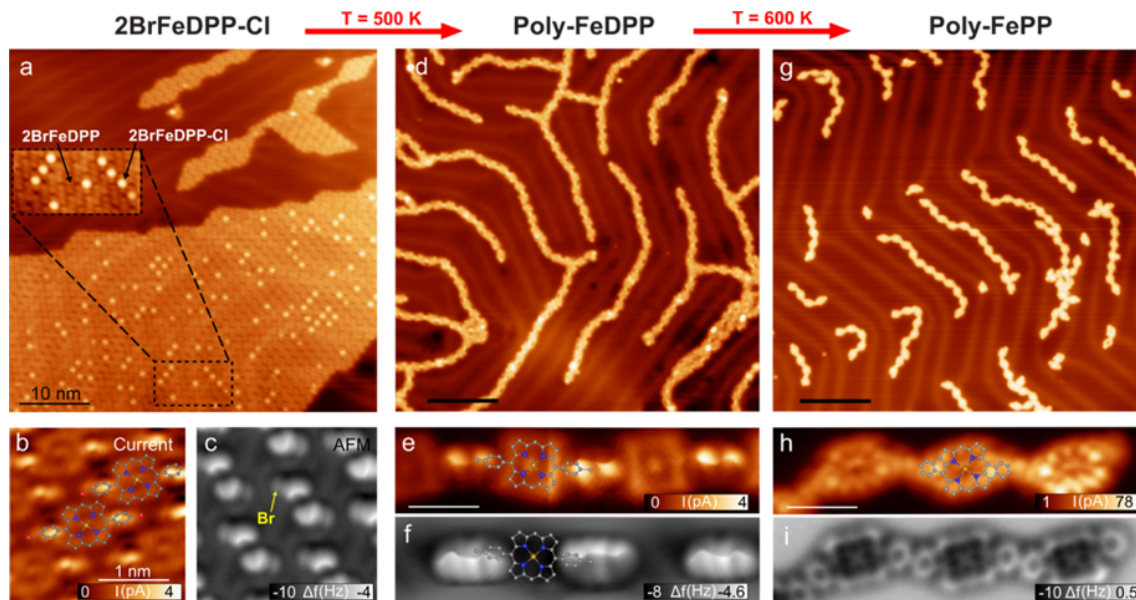
Figure 44 a) STM topography upon deposition of 2BrFeDPP-Cl on Au(111). b,c) STM/nc-AFM of 2BrFeDPP-Cl on Au(111). d) STM topography of poly-FeDPP annealing to 500 K. e,f) STM/nc-AFM of poly-FeDPP. g) STM topography of poly-FePP annealing to 600 K. h,i) STM/nc-AFM of poly-FePP. Reprinted with permission from [18].

Removal of the coordinated Cl atom from 2BrFeDPP-Cl reduced the oxidation state from Fe^{3+} to Fe^{2+} and lowered the total spin from $S = 3/2$ to $S = 1$. In addition, calculations predicted an MAE of -4.1 meV for 2BrFeDPP-Cl, where a negative MAE represents the easy-axis system as opposed to the MAE of dechlorinated 2BrFeDPP.

The first derivative of the dI/dV spectra acquired on the 2BrFeDPP molecules and FeDPP monomers showed excitation voltage onsets at $V_s = \pm 8.5$ mV and $V_s = \pm 7.5$ mV. While the polymerization process hardly affected the magnetic anisotropy of the FeDPP, the planarization of poly-FeDPP to poly-FePP reduced the onset of the excitation energy from ± 7.5 to ± 3.5 mV.

In order to investigate the origin of the experimentally observed MAE reduction of planarized FePP molecules, we performed SP-DFT with SOC calculations for 2BrFeDPP and 2BrFePP molecules as well as FeDPP and FePP polymers, both free-standing and Au(111)-deposited. Their MAEs are gathered in **Table 3**. The decrease in MAE for the planarized molecules was in semi-quantitative agreement with the experimental observations, regardless of whether they were deposited on the Au(111) surface and/or polymerized. This suggests that the origin of the MAE reduction is to be found in differences

in the symmetry of the Fe environment, which may lead to a different occupation scheme of the central Fe atom.

Table 3 MAE (meV) of freestanding and Au(111)-supported 2BrFeDPP and 2BrFePP [18].

	2BrFeDPP		2BrFePP	
	Freestanding	**On Au(111)**	**Freestanding**	**On Au(111)**
Single molecule	6.2	2.0	1.0	0.3
Dimer	4.8		1.1	
Wire	1.5	3.7	0.4	1.7

In a freestanding 2BrFeDPP molecule with all Fe–N distances equal to 2.01 Å, the occupations of Fe $3d$ levels in the SR limit and for the axial (hard) magnetization direction were similar, while upon the rotation of magnetic moments into the in-plane (easy) direction, the lifting of the degeneracy of the $d\pi$ states and the reordering and change in the occupation of the $3d$ levels were observed (**Figure 45a**).

Since for a freestanding 2BrFePP molecule the square-planar symmetry was broken with two short and two long Fe–N bonds in the length of 1.94 and 2.04 Å, the lifting of the degeneracy of the $d\pi$-states was already observed in the SR limit. There were no significant changes in the eigenvalue spectra for different orientations of magnetic moments using SOC (**Figure 45b**), which explains the reduced MAE in planarized 2BrFePP.

Projected density of states (PDOS, **Figure 46**) for an Au(111)-deposited single-molecule of 2BrFeDPP and 2BrFePP indicates that the spin polarization originated predominantly from the contribution of d_{z^2} and $d\pi$. As with the freestanding molecules, the degeneracy of $d\pi$ was largely broken for planarized 2BrFePP/Au(111) (**Figure 46b**), and the effect of SOC on the occupations of the $3d$ electronic states was lower than that of the freestanding molecules as a consequence of the hybridization with the substrate, which led to a small MAE of 0.3meV, while in 2BrFeDPP on Au(111) the in-plane magnetic direction is favored by 2.0 meV. The reduced MAE of 2BrFePP on Au(111) is in line with the experimental observation.

It should be noted that although the occupation schemes of the $3d$-electronic states of Au(111)-supported poly-FeDPP and poly-FePP correspond well to those for single

molecules on Au(111) shown in **Figure 46c,d**, the MAE values are greater than for the latter case. The reason may be intrachain interactions at the expense of interaction with the substrate. The relative MAE reduction of the Au(111)-supported molecules and chains due to planarization is however similar and amounts to ~2 meV in-line with the experimental findings, although DFT inherently provides a lower limit to the actual MAE.
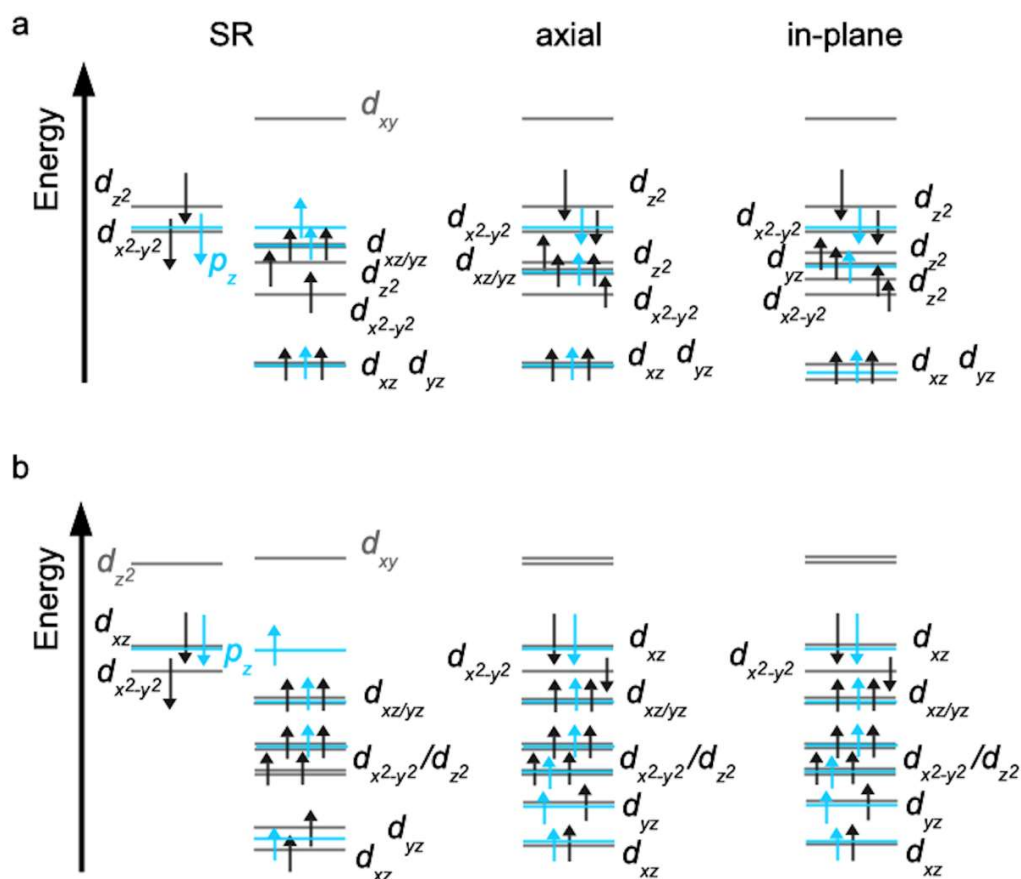
Figure 45 Simplified scheme of the occupation of Fe 3d levels of the freestanding 2BrFeDPP a) and 2BrFePP b). The left-hand part of each graph shows the spin-up and spin-down derived states from the scalar-relativistic (SR) calculations while the middle and right-hand part show the occupation for the axial and in-plane orientations of the magnetic moments after adding SOC. The relativistic states are not spin eigenstates. Reprinted with permission from [18].
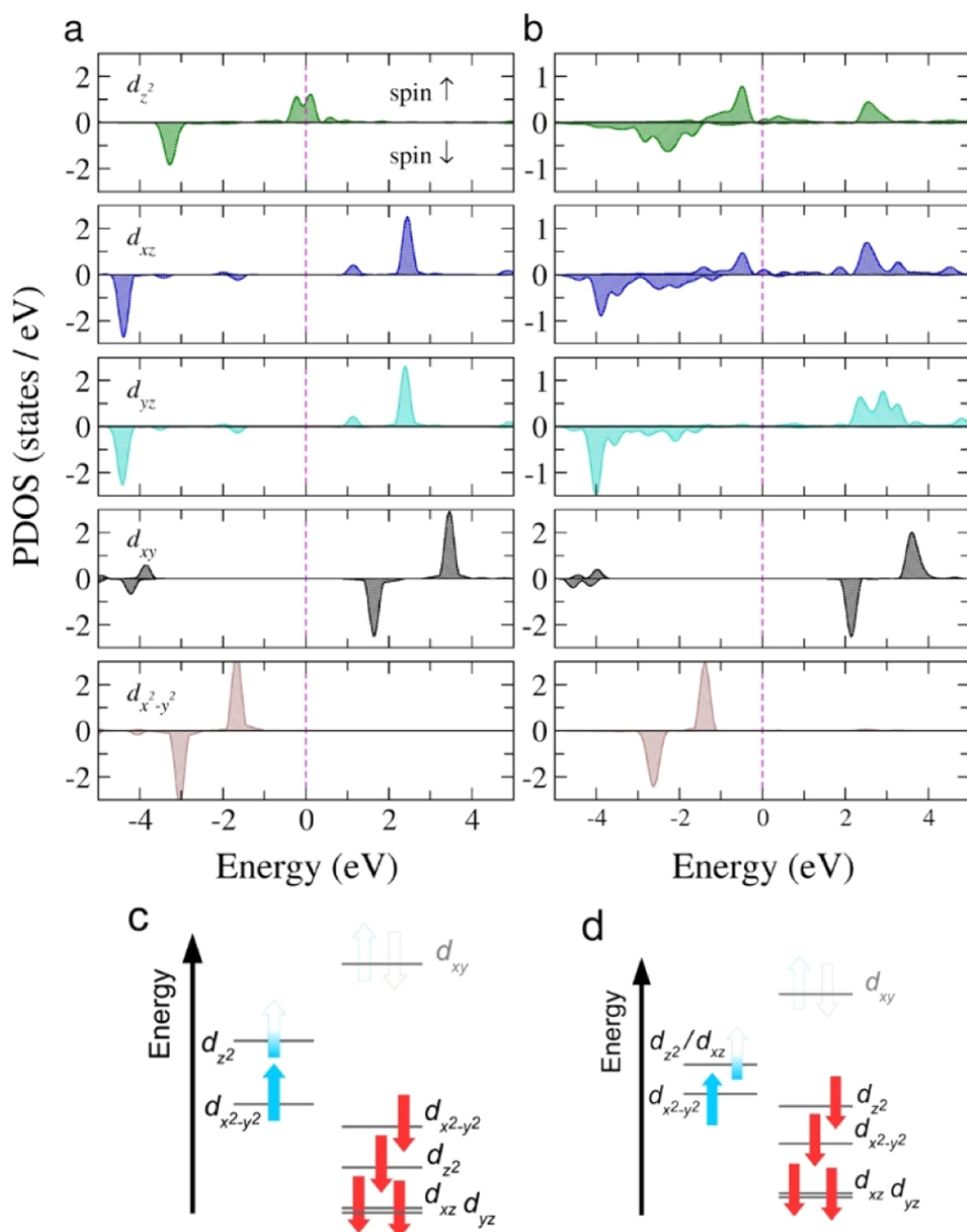
Figure 46 PDOS of the d orbitals of Fe for the Au(111)-supported 2BrFeDPP a) and 2BrFePP b). The corresponding PDOS-derived occupation schemes of Fe *3d* levels are shown in c,d). Due to two unpaired Fe-d electrons, the systems have S = 1 ground state. Reprinted with permission from [18].

To sum up, we theoretically investigated conformational changes of 1D metal-porphyrin wires on Au(111) as a result of sample annealing and the corresponding changes in magnetic properties, in particular the reduction of MAE related to the planarization of the porphyrin units. Upon planarization, the MAE of the triplet ground state of the central Fe ion dropped down due to the reduction of the ligand field symmetry and the subsequent change in the occupancy of the *3d* Fe electronic states. These results indicate new possibilities in the design of on-surface 1D organic magnets with tailored magnetic properties.

7 Anchoring of single-platinum-adatoms on cyanographene: Experiment and theory

Rostislav Langer, Edvin Fako, Piotr Błoński*, Miroslav Vavrečka, Aristides Bakandritsos, Michal Otyepka, Núria López*, *Appl. Mater. Today* 2020, 18, 100462, DOI: 10.1016/j.apmt.2019.100462.

Noble-metal catalysts have been extensively exploited for industrial applications, including energy conversion, chemicals production, and automotive exhaust purification, just to name a few. Noble metals are, however, expensive and of limited supply. Catalytic reactions take place on metal surfaces and, therefore, the metal in accessible to the reactants are not involved in the catalysis and it is very advantageous to reduce the amount of such inactive atoms. The dispersion of ultra-small metal-particles onto high-surface-area supports is an effective strategy to increase their usage efficiency and catalytic reactivity [151]. *The ultimate limit is atomically dispersed catalyst, also termed single-atom catalyst, with nearly 100% metal dispersion, making nearly every active site accessible* [149], [424], [425]. *To prevent the undesirable aggregation of SACs jeopardizing their catalytic reactivity, metal catalysts should be anchored onto a high-surface-area support, leaving the coordination sphere around SACs accessible for possible catalytic reactions. High specific surface area and reasonable price make graphene an attractive support for SACs. However, since TMs are prone to undesired migration and agglomeration on the graphene lattice, identifying the suitable ligand is of high importance. By using first-principles calculations, we found that among graphene covalently functionalized by –OH, –F, –CN and –H, only –CN groups were able to form stable complexes with Pt^0/Pt^{2+} atoms/ions. Our results were supported by the synthesis of cyanographene with 3.7 wt.% single Pt adatoms immobilized onto its surface.*

The relatively low interactions of the *d*-elements of the transition metals with graphene and their high mobility on its surface [426], [427], require finding an effective approach to stabilizing TM-SAs on graphene. Sp^3 functionalization of graphene seems to be a wise choice as it enables greater availability of SAs compared to when these atoms were embedded into vacancy defects in the graphene lattice. Therefore, the quest to identify suitable ligands for SAs, and a thorough understanding of the nature of the metal-ligand-graphene interaction and the influence of SA on the electronic structure of the graphene derivative is of great importance for the progress in the field of SAC.

We considered pristine graphene [216] and existing graphene derivatives in the diluted limit, *i.e.*, FG [221], graphane [216], GO [217], and G–CN [9] containing −F, −H, −OH, and −CN groups, respectively, as potential anchors for a single platinum atom **(Figure 47)**.
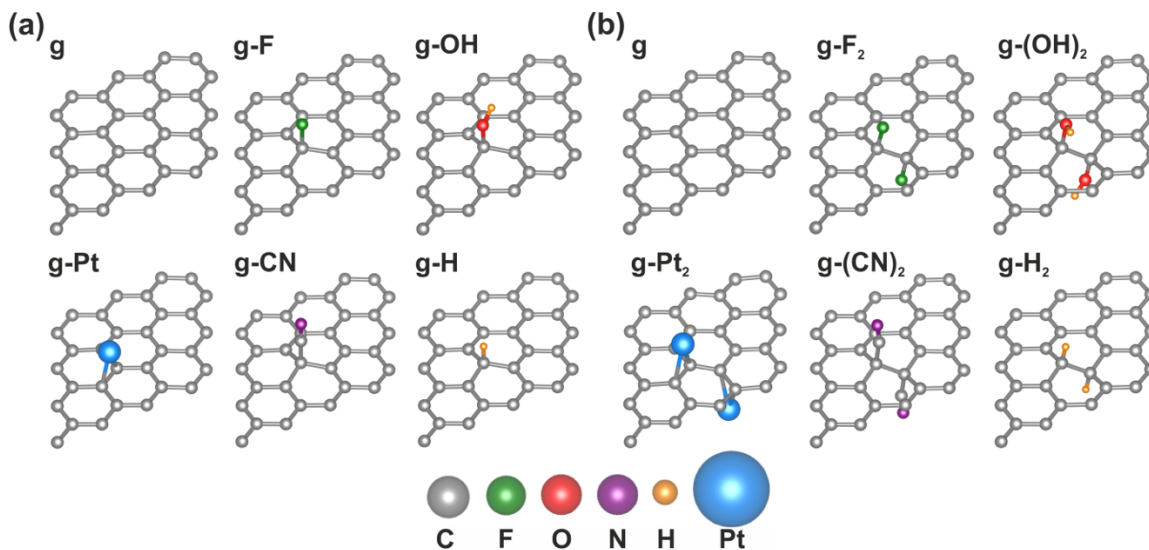

Figure 47 Relaxed structures of a) one-sided and b) two-sided functionalized graphene: pristine graphene (g), fluorinated (g-F, g-F₂), hydroxylated (g-OH, g-(OH)₂), nitrilated (g-CN, g-(CN) ₂), and hydrogenated (g-H, g-H₂) graphene and graphene deposited with platinum adatom (g-Pt, g-Pt₂) [15].

We focused on two-sided functionalized graphene g−X_2 (X = −F, −H, −OH, and −CN) with functional groups in *ortho*/*trans* positions, because adding another functional group next to the sp^3 carbon already bearing the functional group in a *trans* manner increased the C–X bond strength (**Table 4**), as well as their diffusion barriers **(Figure 48)**. While the adsorption on the carbon atom (top position) proved to be the most energetically stable for all the considered functional groups on graphene, a single Pt atom was preferentially bound between two C atoms (bridge position).

Table 4 Binding energies E_{bind}, magnetic moments μ_{tot}, Bader charges and C-X distances of g-F, g-OH, g-CN, g-H, g-Pt and g-F$_2$, g-(OH)$_2$, g-(CN)$_2$, g-H$_2$, g-Pt$_2$. Positive/negative values of Bader charges mean the loss/gain of electrons [15].

| Defect g–X	Preferred site	E_{bind} /eV	μ_{tot}/μ_B	Bader charges of functional group / e⁻	C–X distances / Å
g–F	top	-1.71	0.00	-0.55	1.55
g–OH	top	-0.73	0.73	-0.43	1.51
g–CN	top	-1.27	1.00	-0.23	1.50
g–H	top	-0.85	1.00	0.06	1.13
g–Pt	bridge	-1.80	0.00	0.07	2.10
g–F$_2$	top	-2.02	0.00	-0.58	1.46
g–(OH)$_2$	top	-1.12	0.00	-0.47	1.46
g–(CN)$_2$	top	-1.73	0.00	-0.23	1.49
g–H$_2$	top	-1.39	0.00	0.05	1.12
g–Pt$_2$	bridge	-1.68	0.00	-0.03	2.09
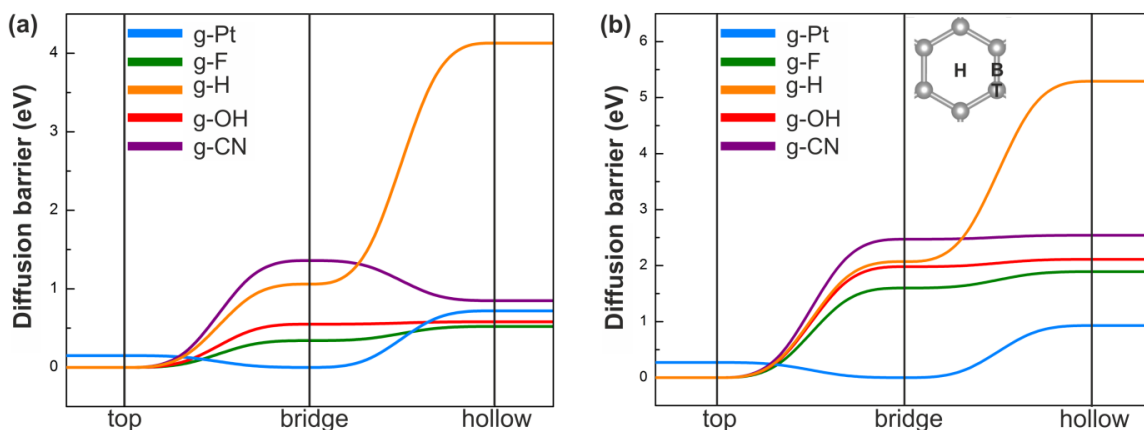
Figure 48 Diffusion paths between high symmetry sites on pristine graphene: a) one-sided and b) two-sided functionalized graphene. The high symmetry sites are depicted as inset [15].

All the unique adsorption positions of Pt SA onto g−X$_2$ were considered. The adsorption of Pt in the immediate vicinity of –F, −OH, and –H, cut their bonds with graphene and liberated the fluorine, hydroxyl, and hydrogen groups attached to the Pt atom, leading to the

graphene–Pt–F (–OH or –H) complexes (**Figure 49**). Such complexes can easily diffused along the top-bridge path with low diffusion barriers of 0.13-0.44 eV, similar to a single Pt adatom for which the diffusion barrier is 0.15 eV [88]. The release of the –OH group upon the Pt adsorption is in line with the experimental observations [428], [429]. Importantly, the Pt adatom did not cut off the –CN group from graphene but remained either coordinated next to the nitrile group or formed a linear g–CN–Pt complex (**Figure 49**). The release of –F, −OH, and –H and the formation of g–CN–Pt complex were predicted for both one-sided and two-sided functionalized graphene (**Figure 50**).

This predisposes G–CN as a suitable material to anchor Pt SAs with the Pt coordination sphere for potential catalytic reactions when it is bound at the top of the −CN group, and the 1.34 eV diffusion barrier may prevent thermal effects that could compromise the stability of this material.
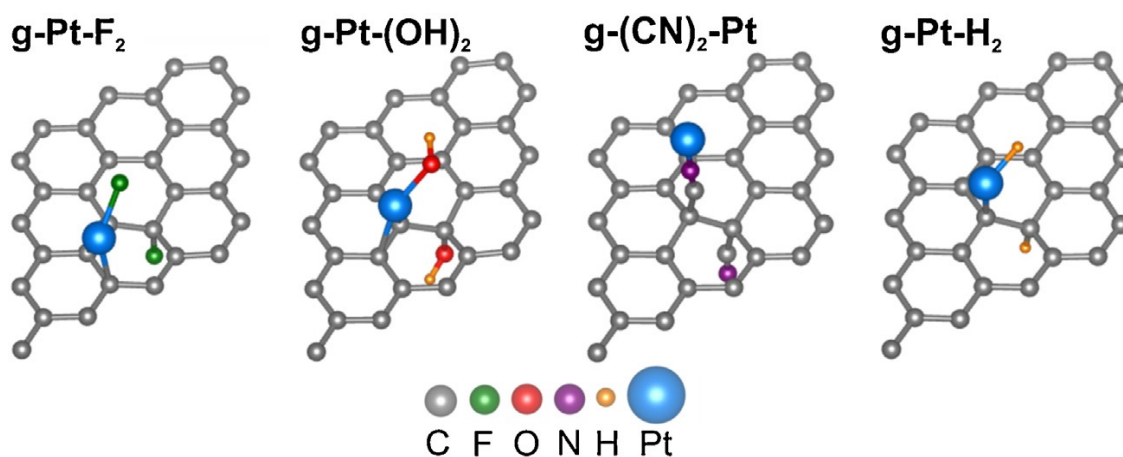
Figure 49 The most stable structures of g-X-Pt complexes: two-sided fluorinated g-Pt-F₂, hydroxylated g-Pt-(OH)₂, nitrilated g-(CN)₂-Pt and hydrogenated g-Pt-H₂ [15].
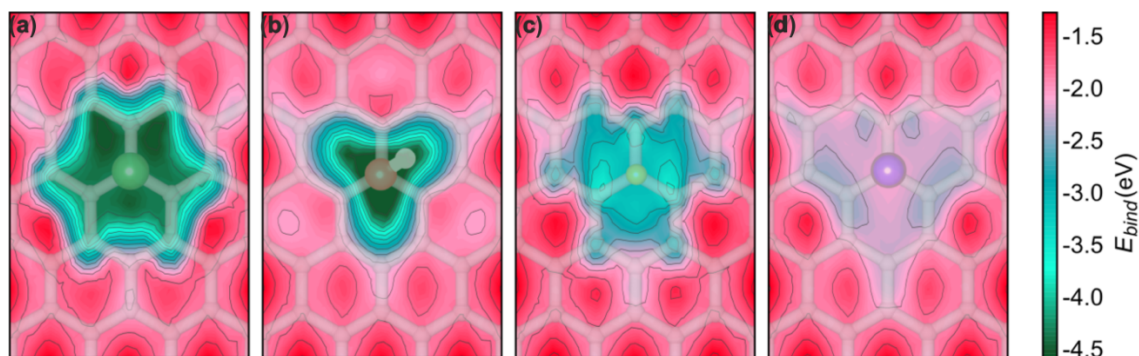
Figure 50 Binding energy mapping of single-Pt-adatom on one-sided functionalized graphene a) fluorinated g-F-Pt, b) hydroxylated g-OH-Pt, c) hydrogenated g-H-Pt and d) nitrilated g-CN-Pt [15].

Further, using the finite model calculations of g-$(CN)_2$-Pt performed with the Gaussian software [399] employing PBE exchange-correlation functional [340] and empirical dispersions D3 [372], we showed that the nitrile group is well suited for anchoring Pt^0 and Pt^{II} in both common oxidation states of platinum.

Indeed, the ability of G–CN to bind Pt SAs was experimentally confirmed by mixing aqueous dispersions of G–CN with a Pt^{II} salt and showed via HR-TEM and high-angle annular dark-field-STEM (HAADF-STEM) as atomic sized high-contrast, bright spots from metal atoms (**Figure 51**). Moreover, energy-dispersive spectroscopy (EDS) revealed that Pt atoms appear to be densely and homogeneously populated on nitrogen rich graphene sheets. The Pt^{II} oxidation state was confirmed by high-resolution photoelectron spectroscopy (HR-XPS). According to atomic absorption spectroscopy (AAS) analysis, G–CN was able to immobilize 3.7 wt.% of Pt.
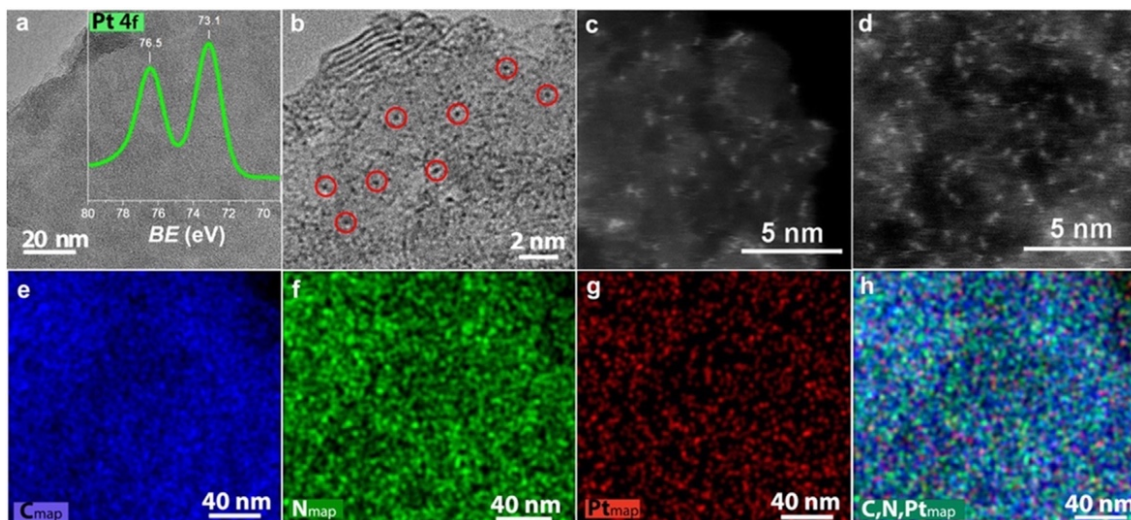
Figure 51 a) Representative HR-TEM image of a flake from the g-CN/Pt hybrid and HR-XPS of the Pt 4f region, b) higher magnification HR-TEM image showing high-contrast spots probably originating from embedded Pt(II) ions, c,d) HAADF-STEM images showing the heavier (and thus brighter) single metal ions embedded in the g-CN support and EDS elemental mapping performed on g-CN/Pt for e) carbon, f) nitrogen, g) platinum, and h) combined C, N and Pt [15].

Covalent bonding of –H, −OH, and –CN with graphene opened the graphene's zero-bandgap, while fluorinated graphene became a p-type metal. All g–X_2 systems were NM (**Figure 52**). The metallic character of the fluorinated graphene was further enhanced by the deposition of Pt adatoms and the formation of the g−Pt−F_2 complex, as was the electronic-gap closure in the g−Pt−$(OH)_2$ complex. The conductive nature of these materials can be beneficial in electrochemical sensors, capacitors, (photo) redox and (photo) electrocatalytic applications. The formation of the graphene−Pt−H_2 complex lowered the electronic gap of hydrogenated graphene from 0.27 to 0.19 eV. On the other hand, the 0.26 eV cyanographene electronic gap was hardly modified by the Pt bound at the top of the −CN group.
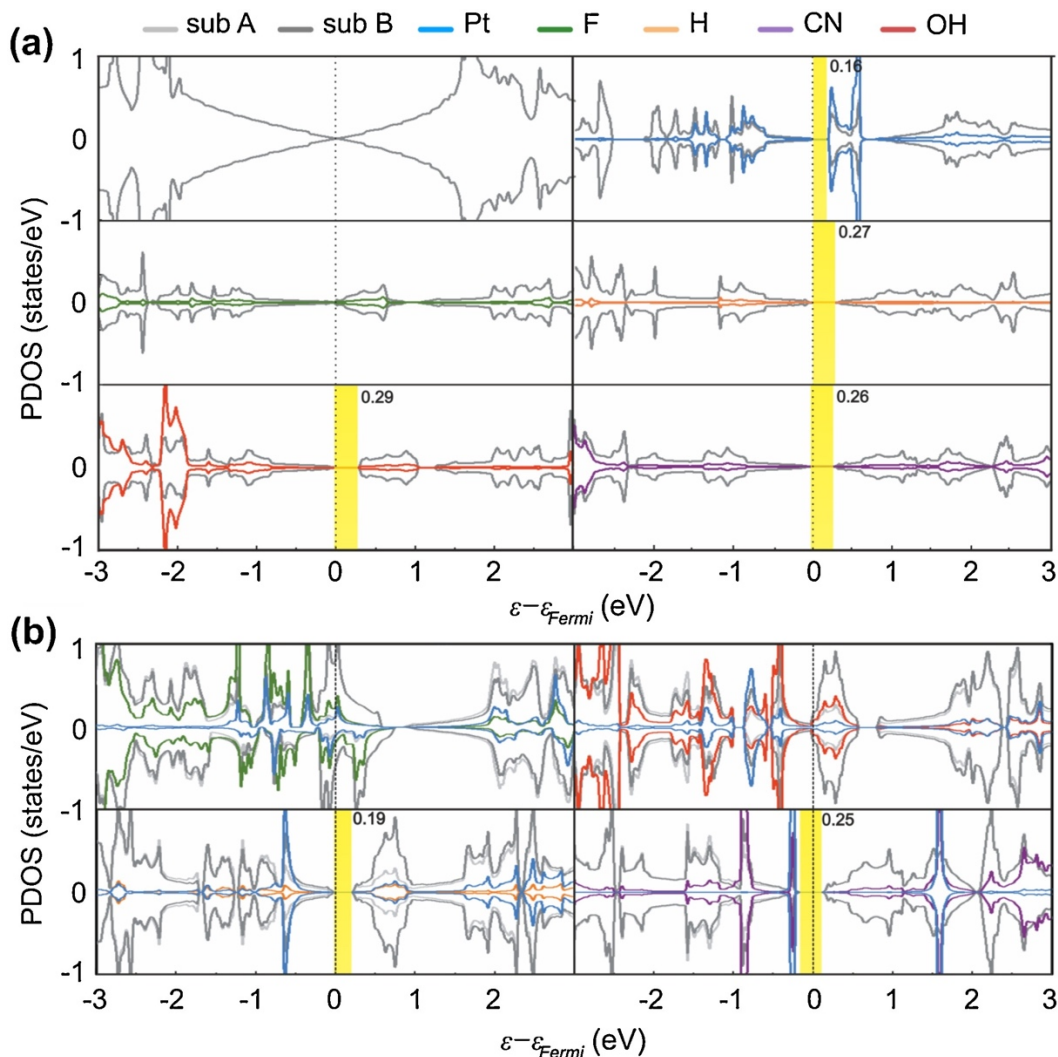
Figure 52 Spin-polarized PDOS plots of two-sided functionalized graphene a) g-X$_2$, b) g-X$_2$-Pt. The Fermi level is set to zero. Bandgaps are depicted by vertical bars; numbers correspond to the width of the bandgap (in eV) [15].

In conclusion, we investigated theoretically the possibilities of anchoring the Pt SAs onto graphene functionalized by –F, –OH, –CN and –H, which may otherwise easily diffuse onto the pristine graphene lattice. We found that on the one hand the Pt adatom cleaved the –F, –OH and –H bonds to graphene leading to the formation of graphene–Pt–F (–OH or –H) complexes, on the other hand the –CN group remained attached to the graphene lattice and anchored the Pt adatom with high energy barrier against –CN–Pt diffusion. The effective immobilization of Pt ions on g–CN was also confirmed experimentally [148]. Thus, g–CN is as a suitable scaffold for Pt SACs, enabling the efficient use of rare and expensive noble metals.

8 Graphene Acid for Lithium-Ion Batteries—Carboxylation Boosts Storage Capacity in Graphene

Ievgen Obraztsov, Aristides Bakandritsos*, Veronika Šedajová, Rostislav Langer, Petr Jakubec, Giorgio Zoppellaro, Martin Pykal, Volker Presser, Michal Otyepka*, Radek Zbořil*, *Adv. Energy Mater.* 2021, 12, 2103010, DOI: 10.1002/aenm.202103010.

Advances in materials design may lead to more efficient organic metal-ion batteries to meet the requirements of low-cost and environmental-friendly energy storage technologies. Among organic materials, carboxylic acids are attractive anode candidates in organic/LIBs owing to their low reduction potential and their coordination proclivity toward Li [430]. Since the capacity of organic materials can be expressed as the ratio of the number of coordinated lithium ions to the molecular mass of the organic molecule, an organic anode material with a high percentage of carboxyl groups is desirable for increasing the capacity. However, maintaining high conductivity upon imprinting high carboxyl content can be a problem limiting the development of organic LIB anode materials. This obstacle can be overcome by covalently grafting carboxyls into a highly conductive backbone such as graphene, leading to the carboxylic graphene derivative termed graphene acid [9].

The experimental measurements showed the excellent charge transport, redox activity, and lithium intercalation of the G–OOH anode, thus demonstrating the true potential of G–OOH anodes in advanced LIBs. However, the energy storage mechanism in G–OOH remained unclear. Therefore, we theoretically examined both Li-G–OOH (of both Li^0 and Li^+) binding and charge transfer using finite (functionalized ovalene) and infinite (periodic) models. The calculations revealed that up to 4 Li^0 atoms per one carboxyl group can be bound to G–OOH in two binding modes, i.e., the Li atom was either in contact both with the sp^2 carbon area and the carboxyl oxygens or, the Li atom was bound between the carboxyl oxygens. Weaker bonding of Li^+ ions to G–OOH than Li^0 allows for their easy migration to the cathode required during the discharge. The partial charge on Li indicated strong charge transfer processes between the Li species and the G–OOH skeleton.

G–OOH was prepared by selective acidic hydrolysis of G-CN as described in **Chapter 1.4**. The elemental analysis *via* X-ray photoelectron spectroscopy (XPS) revealed 79.9 at.%, 4.3 at.%, and 15.6 at.% of C, N, and O atoms, respectively, along with a trace amount of fluorine atoms. The oxygen atoms are exclusively from the –COOH groups.

G–OOH with a functionalization degree of 13 at.% possess a sheet resistance of 6800 Ω sq^{-1}, which is five orders of magnitude lower than that of GO [43]. G–OOH thus attains high redox capacity and extra charge storage due to the carboxyl groups bonded to the conductive sp^2 skeleton. For these reasons, in our combined theoretical-experimental study, we considered the G–OOH as the LIB anode.

Cyclic voltammetry (CV) and electrochemical impedance spectroscopy (EIS) revealed a high specific capacity of 747 mAh g^{-1} at 0.05 A g^{-1} (**Figure 53**). The composition-based capacity of G–OOH was 706 mAh g^{-1} for the reversible binding of four Li atoms per one carboxylic-sp^2 area according to our theoretical calculations (*vide infra*). Nyquist plots and EIS measurements further evidenced low resistance, fast kinetics of the carboxyls' group redox process, and high electronic charge transfer of the conductive graphene lattice. For comparison, the capacity of graphene and GNPs were measured as 476 mAh g^{-1} and 330 mAh g^{-1}, respectively at 0.05 A g^{-1} after the fifth cycle [431] (**Figure 53**).
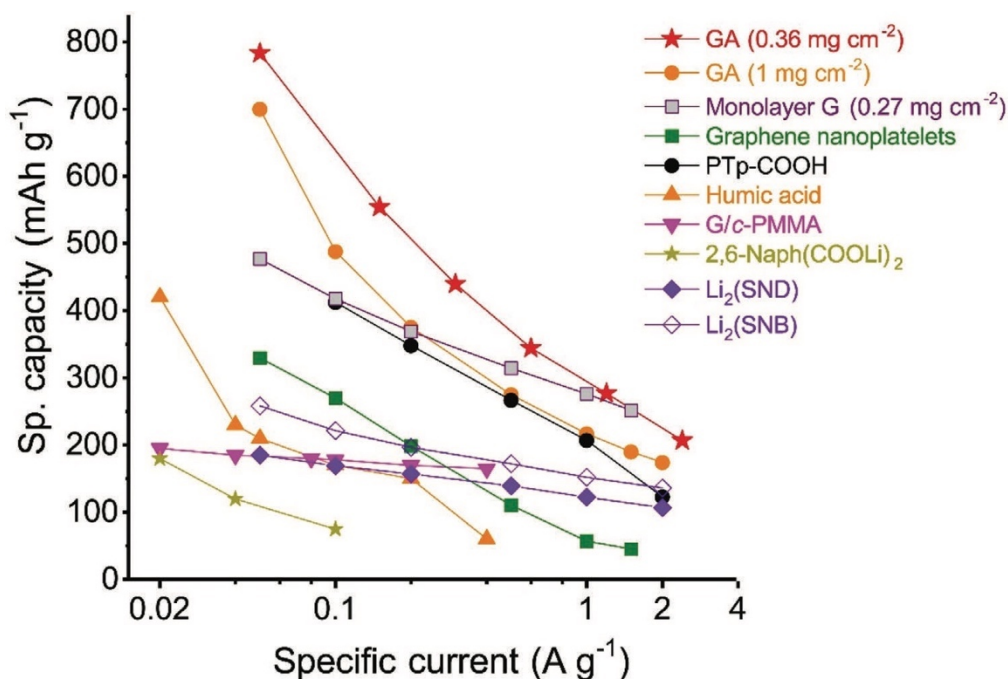

Figure 53 Performance comparison of organic materials [17].

Galvanostatic charge/discharge (GCD) cycles after 180 cycles showed a specific capacity of 475 mAh g^{-1} when cycled back from 0.2 to 0.05 A g^{-1}, which demonstrates the high stability and repeatability of its electrochemical properties. After 20 cycles, the oxygen content dropped to 11.5% and remained unchanged for the following 180 cycles as revealed by XPS. Differential capacity analysis shown three broad redox peaks: The first one below 0.5 V corresponds to lithiation-delithiation of the graphene lattice of G–OOH, the second between 1.0–2.0 V corresponds to carboxylate redox reactions, and the third above 2.5 V,

which was attributed to redox processes of nitrogen-containing graphene moieties from the synthesis.

We employed the first-principle calculations using both finite and periodic model of G–OOH to shed more light on the mechanism behind the high capacity and Li intercalation properties of this material. The calculations revealed that four Li^0 atoms can be bound per one carboxyl group in G–OOH with binding energy of –57.6 kcal/mol per Li^0 atom and without significant structural changes. Two binding modes of binding the Li atoms were distinguished: i) The Li atom is either bound between the carboxyl groups or ii) the Li atom is in contact both with the carboxyl groups and the sp^2 graphene lattice (**Figure 54**). The binding of four Li atoms per one –COOH group agrees with the experimental measurements, including Raman spectroscopy. Adding a fifth Li atom per carboxyl was not favored as it had positive adsorption energy. We predicted weaker bonding of the Li^+ ions to G–OOH than Li^0, which enabled their easy migration to the cathode required during discharging. The partial charge on Li 0.94-0.99 e^- on both oxidized/reduced states indicated strong charge transfer between Li-G–OOH.
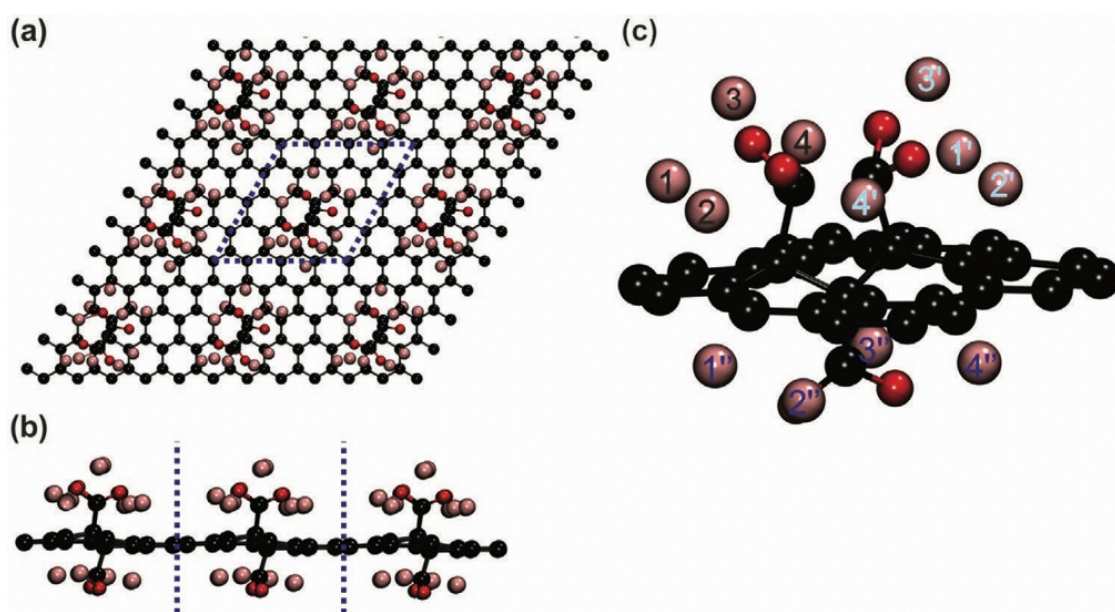
Figure 43 Theoretical model of Li-G–OOH according to DFT calculations; a) top and b) side view (the dashed line indicates the super-cell used in calculations). The zoom view c) shows two binding modes of Li atoms close to one (bottom) and two (up) carboxyl groups (C, O, and Li atoms are shown as black, red, and pink, respectively, balls). The atom numbering is arbitrary to highlight up to four Li atoms close to the nearest carboxyl group [17].

To summarize, G–OOH was identified as a highly efficient LIB anode material that possess excellent redox and intercalation properties and low charge transfer resistance, resulting from the conductive and selectively carboxylated graphene backbone. Our theoretical calculations and experimental operando Raman revealed an effective interactions and intercalation of lithium-ions with G–OOH. The calculations further elucidated the bonding preferences of Li atoms/ions with G–OOH and confirmed the direct charge transfer pathway between Li atoms/ions and the G–OOH host, where the experimental and composition-based capacitances match the theoretically calculated capacitances. The high competitiveness of G–OOH in comparison to other anode materials, combined with its easily reproducible and scalable composition, enables the effective use of this material as a LIB anode.

9 Nitrogen doped graphene with diamond-like bonds achieves unprecedented energy density at high power in a symmetric sustainable supercapacitor

Veronika Šedajová, Aristides Bakandritsos*, Piotr Błoński, Miroslav Medveď, Rostislav Langer, Dagmar Zaoralová, Juri Ugolotti, Jana Dzíbelová, Petr Jakubec, Vojtěch Kupka and Michal Otyepka*, *Energy Environ. Sci.* 2022, 15, 740-748, DOI: 10.1039/D1EE02234B.

The field of energy storage is currently dominated by lithium-ion batteries. To meet the United Nations' goal of affordable, reliable, and sustainable energy, the development of electrochemical energy storage devices with improved efficiency, safety, environmental friendliness, and lower costs is urgently needed. Supercapacitors offer safety, long cycle life, and ultra-fast charge-discharge, making them an attractive alternative to LIB. Moreover, the carbon based SCs ensure the independence of the critical elements. However, the energy content that can be stored per volumetric unit of the electrode is the Achilles' heel of contemporary SCs.

The radical-based chemistry of FG enabled the synthesis of nitrogen superdoped (16 at.%) graphene-type sp^2 layers with tetrahedral (sp^3) C–C bonds that exhibited unprecedented energy density twice as high as that of top-rated materials and several-fold higher than commercial SC carbons, making it highly desirable as a sustainable supercapacitor. This material (GN3) is characterized by a very high mass density compared to porous carbons, while keeping intact the ability to store energy carriers. Calculations based on DFT revealed that the diamond-like C–C bonds develop between carbon-center radicals that appear near nitrogen dopants, thus explaining the high mass density of the material and verifying the solid-state nuclear magnetic resonance (NMR) findings.

The energy density of the best currently available commercial supercapacitors is low, *i.e.*, their cell-level specific energies are 10 Wh kg^{-1}, while lead–acid batteries offer 20–35 Wh kg^{-1}, and LIBs reached $\sim$150 Wh kg^{-1} [432], [433]. However, LIBs suffer from long charging times and, unlike SCs, undergo irreversible processes during cycling that gradually reduce their energy density and life cycle. To exploit the benefits of supercapacitors in a wide range of applications, it is necessary to develop new electrode materials with high energy density, long life, and high power. At the same time, replacing metal atoms in electrode materials with earth-abundant elements, such as carbon, would bring significant

environmental benefits, reducing our dependence on critical natural resources and increasing sustainability.

Since FG chemistry allows the production of carbon derivatives with high mass density [434] and because the carbon atoms in the one-sided fluorinated carbon sheet in $(C_2F)_n$ in an FCCF manner adopt a diamond-like structure suggesting a high mass density [435], [436], FG was used as a starting point of our combined experimental-theoretical research. While it could be argued that the large bandgap of FG [11], [230] is unfavorable for supercapacitors, it has been shown that defluorination and functionalization of FG via radical reactions promoted by fluorine elimination [132], [238] diminishes its bandgap **[19]**.

A few-layered fluorographene reacted with sodium azide, NaN_3 in DMF at 403 K causing the defluorination and superdoping of nitrogen atoms into the graphene layer (**Figure 55**). DFT calculations demonstrated that the N_3^- anion commenced a nucleophilic reaction on carbon radical defects, which resulted in fluorine elimination and nitrogen superdoping, and subsequent N_2 release.

XPS analysis revealed almost complete defluorination of FG after a rection time of 72 hours when the nitrogen doping reached 16.1 at.%. The HR-XPS spectra of the N 1s envelope showed pyridinic, pyrrolic, and graphitic nitrogens of 44, 49 and 7 at.%, respectively. The $^1H \rightarrow {}^{13}C$ cross polarization magic angle spinning (CP MAS) solid-state NMR showed chemical shifts typical for sp^3 carbons in diamond and diamond-like carbon materials [437] while infra-red (IR) spectroscopy indicated on the formation of the π-conjugated aromatic network and aromatic C–N moieties [438]. These nitrogen dopants densely and homogeneously covered the GN3 sheets as revealed by energy dispersive X-ray spectroscopy (EDXS) and by elemental mapping with HAADF-STEM (**Figure 55a-e**). Further, as proved by thermogravimetric and evolved gas analyses in air, these N-atoms are indeed embedded in the lattice. The vacancies and holes in graphene lattice were showed by HR-TEM (**Figure 55**).
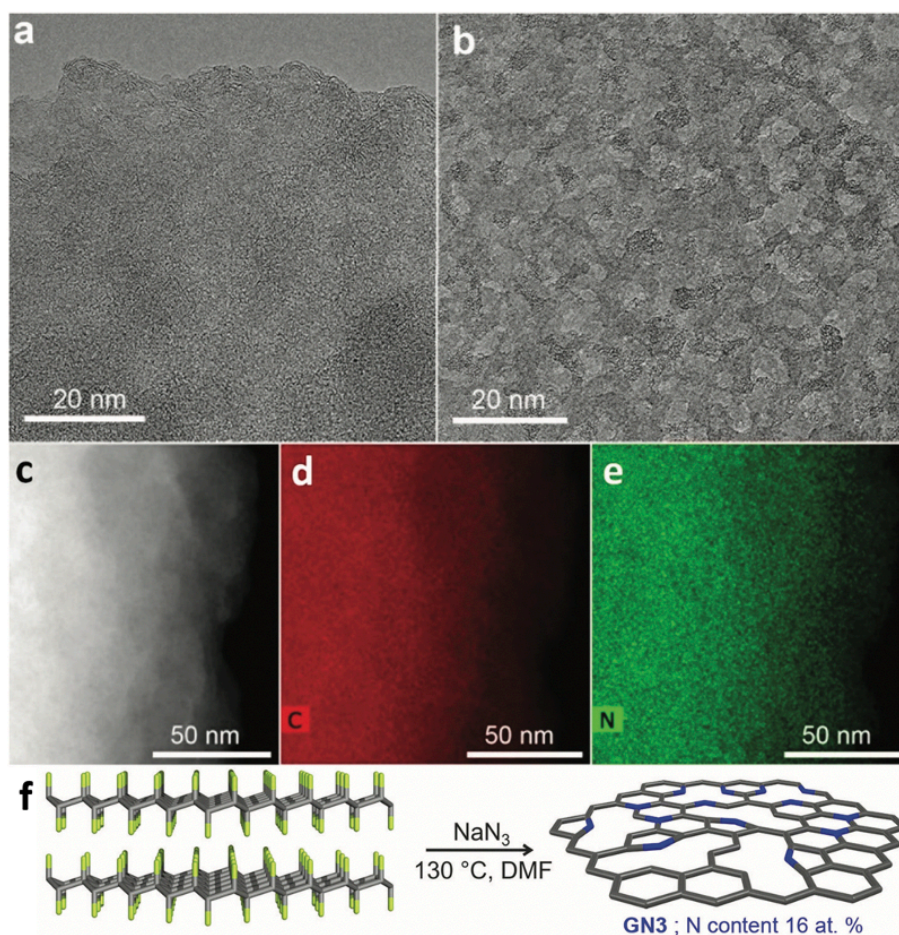
Figure 55 a), b) HR-TEM images of GN3 flakes, c) HAADF image of a GN3 flake used for EDXS mapping, along with the corresponding d) carbon and e) nitrogen map. f) Schematic synthesis of GN3 from sonicated FG [16].

To elucidate the structure of GN3 and the C–C tetrahedral bonds formation, DFT investigated theoretical models of bilayer graphene and GN3 bilayers containing vacancies and nitrogen dopants mainly in pyridinic and pyrrolic configurations (**Figure 56**) and thus in line with the experimental findings. While the final equilibrium interlayer distance between the pristine graphene flakes was approximately 3.45 Å (**Figure 56a**), graphitic-nitrogen doping stabilized the structure with a shorter interlayer distance of 3.08 Å (**Figure 56b,c**). In the GN3 bi-layer model (**Figure 56d**), the system upon relaxation spontaneously formed interlayer sp^3 tetrahedral C-C bonds. The interlayer bonds were formed by the carbons in the pyridinic vacancies in which the radicals were centered, as highlighted by the spheres in **Figure 56e**. Interestingly, similar interlayer bonds were suggested after the introduction of atomic vacancies and pyrrolic N atoms by N-ion beam irradiation of the graphene sheets, leading to the formation of carbon radicals around the vacancies [439]. The Raman spectrum and X-ray diffraction further confirmed the disordered structure with randomly developed tetrahedral C–C bonds in GN3.

130

To theoretically estimate the GN3 density, $\rho(NG)$, we used the following expression:

$$\rho(NG) = \frac{m(NG)}{V(NG)} = \frac{n(NG)*M(NG)}{S*h(NG)} = \frac{n(Gr)*1.05*M(Gr)}{S*f*h(Gr)} = \frac{1.05}{f}\rho(Gr),$$ where m, M, n, V, S, h,

$\rho(Gr)$ denotes respectively the mass, molar mass, amount of substance, volume, area, interlayer distance, density of bulk graphite (2.2-2.3 g/cm³), and $f = \frac{h(NG)}{h(Gr)}$ is the interlayer distance ratio. The obtained average interlayer distance and mass density were 2.9 Å and 2.8 g cm^{-3}, respectively, in agreement with experimental thickness measurements of pressed material performed using SEM and a digital micrometer.
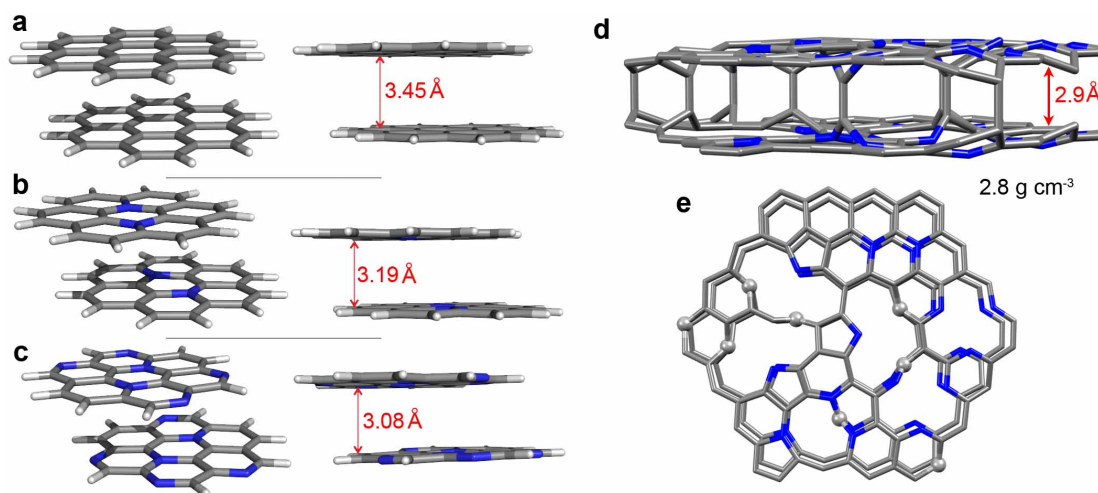
Figure 56 Decrease of the interlayer distance due to attraction and bond formation of N-doped graphene layers. a) A coronene dimer as a model for two-layered graphene. b) Bilayer graphene model with two graphitic nitrogens. c) Bilayer graphene model with two graphitic and four pyridinic nitrogens. d) Theoretical structure of GN3 at a C:N atomic ratio of *ca.* 84:16 obtained from first-principles spin-polarized DFT calculations. e) Top view of this structure with the carbons forming interlayer bonds highlighted as spheres [16].

The cyclic voltammograms (CV) and GCD measurements in a symmetric full cell using as the ionic-liquid electrolyte 1-ethyl-3-methylimidazolium tetrafluoroborate (EMIM-BF$_4$) with 1,1,2,2-tetrafluoroethyl-2,2,3,3-tetrafluoropropyl ether (TTE) in a 9:1 ratio, demonstrated fast charge transport within the GN3 system. Furthermore, a very low charge transfer resistivity was found. Volumetric performance of the material, particularly its energy density and power density, is important for modern energy devices. The former affects the amount of energy that can be stored, while the later enables fast charging and discharging. The GN3 cell demonstrated ground-breaking performance (**Figure 57**) with energy density of 200 Wh L^{-1} at a power of 2.6 kW L^{-1}, 170 Wh L^{-1} at 5.2 kW L^{-1}, or

143 Wh L^{-1} at 52 kW L^{-1} corresponding to improvements of 74% and 190%, respectively, over the previous record [440].
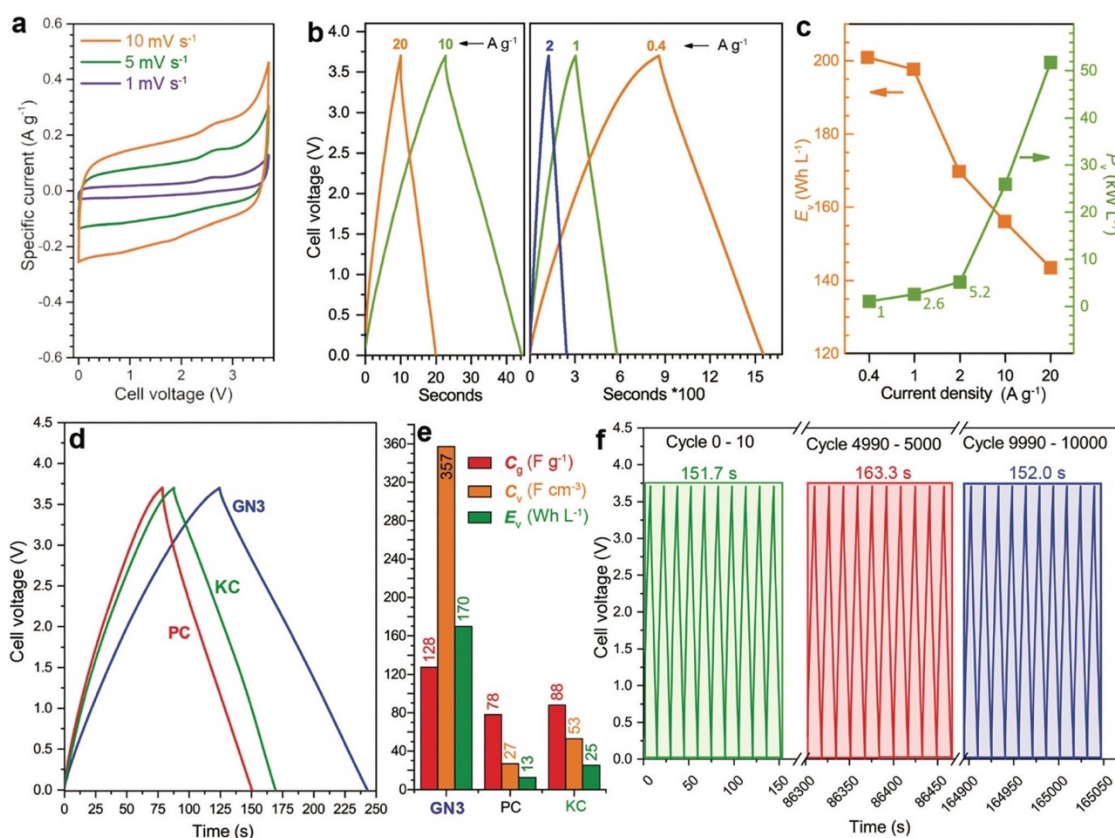
Figure 57 Electrochemical characterization of a symmetric supercapacitor cell with GN3 electrodes. a) CV curves in the EMIM-BF4 and TTE (9:1) electrolyte at low scan rates. b) GCD profiles at different specific currents. c) Energy and power density of GN3 at increasing specific currents. d) Comparison of the GN3 cell with symmetric cells made using commercial high surface area (2000 m^2 g^{-1}) porous carbons (PC and KC) at 2 A g^{-1} and e) the performance of these cells. f) Cyclic stability of GN3 showing the GCD profiles at the beginning, midpoint, and end of a 10 000 cycle test at 20 A g^{-1} current density [16].

To sum up, in our combined experimental-theoretical research, we discovered a new class of carbon-based materials, GN3, comprising nitrogen-doped graphene with diamond-like tetrahedral bonds formed between carbon-centered radicals that emerged near the nitrogen dopants and ultra-high mass density of 2.8 g cm^{-3}, as elucidated within DFT. GN3, prepared using FG radical chemistry, acquired a high energy density of 200 WhL^{-1} at a power of 2.6 kW L^{-1} and an efficient charge transport, ion penetration, diffusion, and storage. The discovery of such class of materials may stimulate research into other high-density conductive carbon-based materials to further enhance the competitiveness of SCs in portable energy storage.

10 Conclusion and perspective

Calculations within the SP-DFT framework provided an efficient tool to thoroughly characterize both existing and hypothetical graphene-based materials and to a better understand underlying phenomena in spintronics, magnetic data storage, single-atom catalysis, and energy storage. It is amazing that such a broad range of applications of materials based on graphene turned out to be possible thanks to the relatively easy modification and functionalization of graphene layers.

In this dissertation, special emphasis is placed on P-doped graphene, TM-doped graphene, and 1D porphyrin polymer with promise for spintronics and ultra-dens data storage, G-CN binding Pt-SAs for potential applications in SAC, and last but not least, Li-G–OOH and GN3 which may change the contemporary energy-storage landscape.

Due to the ability to tailor the properties of graphene-based materials through doping and sp^3 functionalization, the studied materials can be further optimized and many other applications still to be discovered. The computational design of materials with desired or optimized properties for a given application can be greatly accelerated by machine learning techniques.

For example, catalytic reactions on G-CN with Pt-SAs can be examined in the future. Another direction could be to further optimize the structure and composition of graphene-based materials towards the desired capacity value, energy density, and power density for SCs. Finally, forthcoming development directions of a wider family of high temperature 2D graphene magnets with application-specific properties must consider aspects of size and morphology with other magnetism sources, *e.g.*, defects, doping, and functionalization. Furthermore, for the practical applications of graphene magnets, the carbon sheet must be deposited on a solid substrate. Finding a suitable solid substrate for graphene magnets that will not compromise or even improve their properties remains one of the goals for the future.

References

[1]   Geim, A. K.; Novoselov, K. S. The Rise of Graphene. *Nat. Mater.* **2007**, *6* (3), 183–191.

[2]   Han, W.; Kawakami, R. K.; Gmitra, M.; Fabian, J. Graphene Spintronics. *Nat. Nanotechnol.* **2014**, *9* (10), 794–807.

[3]   Stoller, M. D.; Park, S.; Zhu, Y.; An, J.; Ruoff, R. S. Graphene-Based Ultracapacitors. *Nano Lett.* **2008**, *8* (10), 3498-3502.

[4]   Novoselov, K. S.; Geim, A. K.; Morozov, S. V.; Jiang, D.; Zhang, Y.; Dubonos, S. V.; Grigorieva, I. V.; Firsov, A. A. Electric Field Effect in Atomically Thin Carbon Films. *Science* **2004**, *306* (5696), 666–669.

[5]   Olabia, A. G.; Abdelkareem, M. A.; Wolberforce, T.; Sayed, E. T. Application of Graphene in Energy Storage Device – A Review. *Renew. Sustain. Energy Rev.* **2021**, *135*, 110026.

[6]   Błoński, P.; Tuček, J.; Sofer, Z.; Mazánek, V.; Petr, M.; Pumera, M. Doping with Graphitic Nitrogen Triggers Ferromagnetism in Graphene. *J. Am. Chem. Soc.* **2017**, *139* (8), 3171–3180.

[7]   Tuček, J.; Błoński, P.; Sofer, Z.; Šimek, P.; Petr, M.; Pumera, M.; Otyepka, M.; Zbořil, R. Sulfur Doping Induces Strong Ferromagnetic Ordering in Graphene: Effect of Concentration and Substitution Mechanism. *Adv. Mater.* **2016**, *28* (25), 5045–5053.

[8]   Ambrosi, A.; Urbanová, V.; Bourlinos, A. B.; Klára, C.; Loo, A. H.; Pumera, M.; Karlický, F.; Otyepka, M. Thiofluorographene – Hydrophilic Graphene Derivative with Semiconducting and Genosensing Properties. *Ad. Mater.* **2015**, *27* (14), 2305–2310.

[9]   Bakandritsos, A.; Pykal, M.; Boński, P.; Jakubec, P.; Chronopoulos, D. D.; Poláková, K.; Georgakilas, V.; Čépe, K.; Tomanec, O.; Ranc, V.; Bourlinos, A. B.; Zbořil, R.; Otyepka, M. Cyanographene and Graphene Acid: Emerging Derivatives Enabling High-Yield and Selective Functionalization of Graphene. *ACS Nano* **2017**, *11* (3), 2982–2991.

[10] Tuček, J.; Holá, K.; Bourlinos, A. B.; Błoński, P.; Bakandritsos, A.; Ugolotti, J.; Dubecký, M.; Karlický, F.; Ranc, V.; Čépe, K.; Otyepka, M.; Zbořil, R. Room Temperature Organic Magnets Derived from Sp^3 Functionalized Graphene. *Nat. Commun.* **2017**, *8*, 14525.

[11] Nair, R. R.; Ren, W.; Jalil, R.; Riaz, I.; Kravets, V. G.; Britnell, L.; Blake, P.; Schedin, F.; Mayorov, A. S.; Yuan, S.; Katsnelson, M. I.; Cheng, H.; Strupinski, W.; Bulusheva, L. G.; Okotrub, A. V; Grigorieva, I. V; Grigorenko, A. N.; Novoselov, K. S.; Geim, A. K. Fluorographene A Two-Dimensional Counterpart of Teflon. **2010**, *6* (24), 2877–2884.

[12] Sofo, J. O.; Chaudhari, A. S.; Barber, G. D. Graphane: A Two-Dimensional Hydrocarbon. *Phys. Rev. B - Condens. Matter Mater. Phys.* **2007**, *75* (15), 153401.

[13] Langer, R.; Błoński, P.; Hofer, C.; Lazar, P.; Mustonen, K.; Meyer, J. C.; Susi, T.; Otyepka, M. Tailoring Electronic and Magnetic Properties of Graphene by Phosphorus Doping. *ACS Appl. Mater. Interfaces* **2020**, *12* (30), 34074–34085.

[14] Langer, R.; Mustonen, K.; Markevich, A.; Otyepka, M.; Susi, T.; Błoński, P. Graphene Lattices with Embedded Transition-Metal Atoms and Tunable Magnetic Anisotropy Energy: Implications for Spintronic Devices. *ACS Appl. Nano Mater.* **2022**, *5* (1), 1562–1573.

[15] Langer, R.; Fako, E.; Błoński, P.; Vavrečka, M.; Bakandritsos, A.; Otyepka, M.; López, N. Anchoring of Single-Platinum-Adatoms on Cyanographene: Experiment and Theory. *Appl. Mater. Today* **2020**, *18*, 100462.

[16] Šedajová, V.; Bakandritsos, A.; Błoński, P.; Medveď, M.; Langer, R.; Zaoralová, D.; Ugolotti, J.; Dzíbelová, J.; Jakubec, P.; Kupka, V.; Otyepka, M. Nitrogen Doped Graphene with Diamond-like Bonds Achieves Unprecedented Energy Density at High Power in a Symmetric Sustainable Supercapacitor. *Energy Environ. Sci.* **2022**, *15* (2), 740–748.

[17] Obraztsov, I.; Bakandritsos, A.; Šedajová, V.; Langer, R.; Jakubec, P.; Zoppellaro, G.; Pykal, M.; Presser, V.; Otyepka, M.; Zbořil, R. Graphene Acid for Lithium-Ion Batteries—Carboxylation Boosts Storage Capacity in Graphene. *Adv. Energy Mater.* **2022**, *12* (5), 2103010.

[18] Mallada, B.; Błoński, P.; Langer, R.; Jelínek, P.; Otyepka, M.; De La Torre, B. On-Surface Synthesis of One-Dimensional Coordination Polymers with Tailored Magnetic Anisotropy. *ACS Appl. Mater. Interfaces* **2021**, *13* (27), 32393–32401.

[19] Langer, R.; Zaoralová, D.; Medved', M.; Banáš, P.; Błoński, P.; Otyepka, M. Variability of C-F Bonds Governs the Formation of Specific Structural Motifs in Fluorinated Graphenes. *J. Phys. Chem. C* **2019**, *123* (45), 27896–27903.

[20] Petr, M.; Jakubec, P.; Ranc, V.; Šedajová, V.; Langer, R.; Medveď, M.; Błoński, P.; Kašlík, J.; Kupka, V.; Otyepka, M.; Zbořil, R. Thermally Reduced Fluorographenes as Efficient Electrode Materials for Supercapacitors. *Nanoscale* **2019**, *11* (44), 21364–21375.

[21] Tuček, J.; Holá, K.; Zoppellaro, G.; Błoński, P.; Langer, R.; Medved, M.; Susi, T.; Otyepka, M.; Zbořil, R. Zigzag Sp2 Carbon Chains Passing through an Sp3 Framework: A Driving Force toward Room-Temperature Ferromagnetic Graphene. *ACS Nano* **2018**, *12* (12), 12847–12859.

[22] Langer, R.; Błoński, P.; Otyepka, M. Tuning the Magnetic Properties of Graphene Derivatives by Functional Group Selection. *Phys. Chem. Chem. Phys.* **2019**, *21* (23), 12697–12703.

[23] Navrátil, J.; Błoński, P.; Otyepka, M. Large Magnetic Anisotropy in an OsIr Dimer Anchored in Defective Graphene. *Nanotechnology* **2021**, *32* (23), 230001.

[24] Beirão da Veiga, L.; Lipnikov, K.; Manzini, G. Maxwell's Equations. *Modeling, Simulation and Applications*. **2014**, 97–219.

[25] Mould, R. F. Pierre Curie, 1859-1906. *Curr. Oncol.* **2007**, *14* (2), 74–82.

[26] Goudsmit, S.; G. Uhlenbeck. Spinning Electrons and the Structure of Spectra. *Nature* **1926**, *117*, 264-265.

[27] Heisenberg, W.. Über Quantentheoretische Umdeutung Kinematischer Und Mechanischer Beziehungen. *Zeitschrift für Physik*, **1925**, *33*, 879–893.

[28] Atalla, M. M.; Tannenbaum, E.; Scheibner, E. J. Stabilization of Silicon Surfaces by Thermally Grown Oxides. *Bell Syst. Tech. J.* **1959**, *38* (3), 749–783.

[29] Zsigmondy, R. Ueber Wässrige Lösungen Metallischen Goldes. *Justus Liebigs Ann. Chem.* **1898**, *301* (1), 29–54.

[30] Hunt, W. H. Nanomaterials : Nomenclature, Novelty, and Necessity. *JOM*, **2004**, *56*, 13–18.

[31] Binnig, G.; Rohrer, H. Scanning Tunneling Microscopy—from Birth to Adolescence (Nobel Lecture). *Angew. Chemie Int. Ed. English* **1987**, *26* (7), 606–614.

[32] Kroto, H. W. C60: Buckminsterfullerene, The Celestial Sphere That Fell to Earth. *Angew. Chemie Int. Ed. English* **1992**, *31* (2), 111–129.

[33] Ilijima. Helical Microtubules of Graphitic Carbon. *Nature* **1991**, *354*, 737–740.

[34] Xu, X.; Ray, R.; Gu, Y.; Ploehn, H. J.; Gearheart, L.; Raker, K.; Scrivens, W. A. Electrophoretic Analysis and Purification of Fluorescent Single-Walled Carbon Nanotube Fragments. *J. Am. Chem. Soc.* **2004**, *126* (40), 12736–12737.

[35] Langer, M.; Paloncýová, M.; Medveď, M.; Pykal, M.; Nachtigallová, D.; Shi, B.; Aquino, A. J. A.; Lischka, H.; Otyepka, M. Progress and Challenges in Understanding of Photoluminescence Properties of Carbon Dots Based on Theoretical Computations. *Appl. Mater. Today*. **2021**, *22*, 100924.

[36] Mak, K. F.; Lee, C.; Hone, J.; Shan, J.; Heinz, T. F. Atomically Thin MoS2: A New Direct-Gap Semiconductor. *Phys. Rev. Lett.* **2010**, *105* (13), 136805.

[37] Manzeli, S.; Ovchinnikov, D.; Pasquier, D.; Yazyev, O. V.; Kis, A. 2D Transition Metal Dichalcogenides. *Nat. Rev. Mater.* **2017**, *2*, 17033.

[38] Naguib, M.; Mochalin, V. N.; Barsoum, M. W.; Gogotsi, Y. 25th Anniversary Article: MXenes: A New Family of Two-Dimensional Materials. *Adv. Mater.* **2014**, *26* (7), 992–1005.

[39] Sun, D.; Wang, M.; Li, Z.; Fan, G.; Fan, L. Z.; Zhou, A. Two-Dimensional Ti3C2 as Anode Material for Li-Ion Batteries. *Electrochem. commun.* **2014**, *47*, 80–83.

[40] Ling, Z.; Ren, C. E.; Zhao, M. Q.; Yang, J.; Giammarco, J. M.; Qiu, J.; Barsoum, M. W.; Gogotsi, Y. Flexible and Conductive MXene Films and Nanocomposites with High Capacitance. *Proc. Natl. Acad. Sci. U. S. A.* **2014**, *111* (47), 16676–16681.

[41] Hantanasirisakul, K.; Alhabeb, M.; Lipatov, A.; Maleski, K.; Anasori, B.; Salles, P.; Ieosakulrat, C.; Pakawatpanurut, P.; Sinitskii, A.; May, S. J.; Gogotsi, Y. Effects of Synthesis and Processing on Optoelectronic Properties of Titanium Carbonitride MXene. *Chem. Mater.* **2019**, *31* (8), 2941–2951.

[42] Dean, C. R.; Young, A. F.; Meric, I.; Lee, C.; Wang, L.; Sorgenfrei, S.; Watanabe, K.; Taniguchi, T.; Kim, P.; Shepard, K. L.; Hone, J. Boron Nitride Substrates for High-Quality Graphene Electronics. *Nat. Nanotechnol.* **2010**, *5* (10), 722–726.

[43] Ares, P.; Cea, T.; Holwill, M.; Wang, Y. B.; Roldán, R.; Guinea, F.; Andreeva, D. V.; Fumagalli, L.; Novoselov, K. S.; Woods, C. R. Piezoelectricity in Monolayer Hexagonal Boron Nitride. *Adv. Mater.* **2020**, *32* (1), 1905504.

[44] Liu, H.; Neal, A. T.; Zhu, Z.; Luo, Z.; Xu, X.; Tománek, D.; Ye, P. D. Phosphorene: An Unexplored 2D Semiconductor with a High Hole Mobility. *ACS Nano* **2014**, *8* (4), 4033–4041.

[45] Lalmi, B.; Oughaddou, H.; Enriquez, H.; Kara, A.; Vizzini, Ś.; Ealet, B.; Aufray, B. Epitaxial Growth of a Silicene Sheet. *Appl. Phys. Lett.* **2010**, *97* (22), 223109.

[46] Cahangirov, S.; Topsakal, M.; Aktürk, E.; Šahin, H.; Ciraci, S. Two- and One-Dimensional Honeycomb Structures of Silicon and Germanium. *Phys. Rev. Lett.* **2009**, *102* (23), 236804.

[47] Zhu, F..; Chen, W.; Xu, Y.; Gao, C.; Guan, D.; Liu, C.; Qian, D.; Zhang, S.; Jia, J. Epitaxial Growth of Two-Dimensional Stanene. *Nature Materials* **2015**, *14*(8), 1020–1025.

[48] Alducin, D.; Myers, B. D.; Liu, X.; Fisher, B. L. Synthesis of Borophenes: Anisotropic, Two-Dimensional Boron Polymorphs. *Science* **2013**, *350* (6267), 1513-1516.

[49] Gonzalez, R. I.; Mella, J.; Diaz, P.; Allende, S.; Vogel, E. E.; Cardenas, C.; Munoz, F. Hematene: A 2D Magnetic Material in van Der Waals or Non-van Der Waals Heterostructures. *2D Mater.* **2019**, *6* (4), 045002.

[50] https://www.sciencealert.com/scientists-have-turned-an-atom-into-the-world-s-smallest-hard-drive, visited 4. 8. 2022.

[51] Coleman, R. V.; Isin, A. Magnetoresistance in Iron Single Crystals. *J. Appl. Phys.* **1966**, *37* (3), 1028–1029.

[52] Baibich, M. N.; Broto, J. M.; Fert, A.; Van Dau, F. N.; Petroff, F.; Eitenne, P.; Creuzet, G.; Friederich, A.; Chazelas, J. Giant Magnetoresistance of (001)Fe/(001)Cr Magnetic Superlattices. *Phys. Rev. Lett.* **1988**, *61* (21), 2472–2475.

[53] Binasch, G.; Grünberg, P.; Saurenbach, F.; Zinn, W. Enhanced Magnetoresistance in Layered Magnetic Structures with Antiferromagnetic Interlayer Exchange. *Phys. Rev. B* **1989**, *39* (7), 4828–4830.

[54] Ando, Y. Spintronics Technology and Device Development. *Jpn. J. Appl. Phys.* **2015**, *54* (7), 070101.

[55] Zoppellaro, G.; Bakandritsos, A.; Błoński, P.; Susi, T.; Lazar, P. Microwave Energy Drives "On – Off – On" Spin-Switch Behavior in Nitrogen-Doped Graphene. *Adv. Mater.* **2019**, *31* (37), 1902587.

[56] Monsma, D. J.; Lodder, J. C.; Popma, T. J. A.; Dieny, B. Perpendicular Hot Electron Spin-Valve Effect in a New Magnetic Field Sensor: The Spin-Valve Transistor. *Phys. Rev. Lett.* **1995**, *74* (26), 5260–5263.

[57] Manipatruni, S.; Nikonov, D. E.; Lin, C. C.; Gosavi, T. A.; Liu, H.; Prasad, B.; Huang, Y. L.; Bonturim, E.; Ramesh, R.; Young, I. A. Scalable Energy-Efficient Magnetoelectric Spin–Orbit Logic. *Nature* **2019**, *565* (7737), 35–42.

[58] Silva, T. J.; Rippard, W. H. Developments in Nano-Oscillators Based upon Spin-Transfer Point-Contact Devices. *J. Magn. Magn. Mater.* **2008**, *320* (7), 1260–1271.

[59] Hirohata, A.; Yamada, K.; Nakatani, Y.; Prejbeanu, L.; Diény, B.; Pirro, P.; Hillebrands, B. Review on Spintronics: Principles and Device Applications. *J. Magn. Magn. Mater.* **2020**, *509*, 166711.

[60] Puebla, J.; Kim, J.; Kondou, K.; Otani, Y. Spintronic Devices for Energy-Efficient Data Storage and Energy Harvesting. *Commun. Mater.* **2020**, *1* (24), 1–9.

[61] Tedrow, P. M.; Meservey, R. Spin-Dependent Tunneling into Ferromagnetic Nickel. *Phys. Rev. Lett.* **1971**, *26* (4), 192–195.

[62] Tedrow, P. M.; Meservey, R. Spin Polarization of Electrons Tunneling from Films of Fe, Co, Ni, and Gd. *Phys. Rev. B* **1973**, *7* (1), 318–326.

[63] Julliere, M. Tunneling between Ferromagnetic Films. *Phys. Lett. A* **1975**, *54* (3), 225–226.

[64] Butler, W. H.; Zhang, X. G.; Schulthess, T. C.; MacLaren, J. M. Spin-Dependent Tunneling Conductance of Fe/MgO/Fe Sandwiches. *Phys. Rev. B - Condens. Matter Mater. Phys.* **2001**, *63* (5), 544161–5441612.

[65] Moodera, J. S.; Kinder, L. R.; Wong, T. M.; Meservey, R. Large Magnetoresistance at Room Temperature in Ferromagnetic Thin Film Tunnel Junctions. *Phys. Rev. Lett.* **1995**, *74* (16), 3273–3276.

[66] Åkerman, J. Toward a Universal Memory. *Science* **2005**, *308* (5721), 508–510.

[67] https://seedscientific.com/how-much-data-is-created-every-day, visited 4. 7. 2022.

[68] Néel, L. Théorie Du Traînage Magnétique Des Ferromagnétiques En Grains Fins Avec Application Aux Terres Cuites. *Ann. Geophys.* **1949**, 5, 99–136.

[69] Li, Y. L.; Lv, P. First-Principles Study on the Electric Field Manipulation of the Magnetic Property and the Electronic Structures for Monolayer Fe2C MXene. *Phys. Lett. Sect. A Gen. At. Solid State Phys.* **2021**, *386*, 126960.

[70] Tanveer, M.; Dorantes-Dávila, J.; Pastor, G. M. Reversible Electric-Field Manipulation of the Adsorption Morphology and Magnetic Anisotropy of Small Fe and Co Clusters on Graphene. *Phys. Rev. B* **2017**, *96* (22), 224413.

[71] Tao, K.; Xue, D.; Polyakov, O. P.; Stepanyuk, V. S. Single-Spin Manipulation by Electric Fields and Adsorption of Molecules. *Phys. Rev. B* **2016**, *94* (1), 014437.

[72] Kikitsu, A.; Kamata, Y.; Sakurai, M.; Naito, K. Recent Progress of Patterned Media. *IEEE Trans. Magn.* **2007**, *43* (9), 3685–3688.

[73] Gambardella, P.; Rusponi, S.; Veronese, M.; Dhesi, S. S.; Grazioli, C.; Dallmeyer, A.; Cabria, I.; Zeller, R.; Dederichs, P. H.; Kern, K.; Carbone, C.; Brune, H. Giant Magnetic Anisotropy of Single Cobalt Atoms and Nanoparticles. *Science* **2003**, *300* (5622), 1130–1133.

[74] Natterer, F. D.; Yang, K.; Paul, W.; Willke, P.; Choi, T.; Greber, T.; Heinrich, A. J.; Lutz, C. P. Reading and Writing Single-Atom Magnets. *Nature* **2017**, *543* (7644), 226–228.

[75] Brune, H.; Gambardella, P. Magnetism of Individual Atoms Adsorbed on Surfaces. *Surf. Sci.* **2009**, *603* (10-12), 1812-1830.

[76] Navrátil, J.; Otyepka, M.; Błoński, P. OsPd Bimetallic Dimer Pushes the Limit of Magnetic Anisotropy in Atom-Sized Magnets for Data Storage. *Nanotechnology* **2022**, *33* (21), 215001.

[77] Lehnert, A.; Dennler, S.; Błoński, P.; Rusponi, S.; Etzkorn, M.; Moulas, G.; Bencok, P.; Gambardella, P.; Brune, H.; Hafner, J. Magnetic Anisotropy of Fe and Co Ultrathin Films Deposited on Rh(111) and Pt(111) Substrates: An Experimental and First-Principles Investigation. *Phys. Rev. B* **2010**, *82* (9), 094409.

[78] Błoński, P.; Lehnert, A.; Dennler, S.; Rusponi, S.; Etzkorn, M.; Moulas, G.; Bencok, P.; Gambardella, P.; Brune, H.; Hafner, J. Magnetocrystalline Anisotropy Energy of Co and Fe Adatoms on the (111) Surfaces of Pd and Rh. *Phys. Rev. B - Condens. Matter Mater. Phys.* **2010**, *81* (10), 104426.

[79] Khajetoorians, A. A.; Schlenk, T.; Schweflinghaus, B.; Dos Santos Dias, M.; Steinbrecher, M.; Bouhassoune, M.; Lounis, S.; Wiebe, J.; Wiesendanger, R. Spin Excitations of Individual Fe Atoms on Pt(111): Impact of the Site-Dependent Giant Substrate Polarization. *Phys. Rev. Lett.* **2013**, *111* (15), 157204.

[80] Krasheninnikov, A. V.; Lehtinen, P. O.; Foster, A. S.; Pyykk??, P.; Nieminen, R. M. Embedding Transition-Metal Atoms in Graphene: Structure, Bonding, and Magnetism. *Phys. Rev. Lett.* **2009**, *102* (12), 126807.

[81] Błoński, P.; Hafner, J. Geometric and Magnetic Properties of Pt Clusters Supported on Graphene: Relativistic Density-Functional Calculations. *J. Chem. Phys.* **2011**, *134* (15), 154705.

[82] Błoński, P.; Hafner, J. On the Interplay between Geometrical Structure and Magnetic Anisotropy: A Relativistic Density-Functional Study of Mixed Pt-Co and Pt-Fe Trimers and Tetramers in the Gas-Phase and Supported on Graphene. *J. Phys. Condens. Matter* **2015**, *27* (4), 046002.

[83] Hu, J.; Wu, R. Giant Magnetic Anisotropy of Transition-Metal Dimers on Defected Graphene. *Nano Lett.* **2014**, *14* (4), 1853–1858.

[84] Błoński, P.; Hafner, J. Cu(1 1 1) Supported Graphene as a Substrate for Magnetic Dimers with a Large Magnetic Anisotropy: Relativistic Density-Functional Calculations. *J. Phys. Condens. Matter* **2014**, *26* (25), 256001.

[85] Xiao, R.; Kuz'Min, M. D.; Koepernik, K.; Richter, M. CoIr-Carbon Complexes with Magnetic Anisotropies Larger than 0.2 EV: A Density-Functional-Theory Prediction. *Appl. Phys. Lett.* **2010**, *97* (23), 111–114.

[86] Błoński, P.; Hafner, J. Pt3 and Pt4 Clusters on Graphene Monolayers Supported on a Ni(111) Substrate: Relativistic Density-Functional Calculations. *J. Chem. Phys.* **2012**, *137* (4), 34107.

[87] Baltic, R.; Pivetta, M.; Donati, F.; Wäckerlin, C.; Singha, A.; Dreiser, J.; Rusponi, S.; Brune, H. Superlattice of Single Atom Magnets on Graphene. *Nano Lett.* **2016**, *16* (12), 7610–7615.

[88] Gan, Y.; Sun, L.; Banhart, F. One- and Two-Dimensional Diffusion of Metal Atoms in Graphene. *Small* **2008**, *4* (5), 587–591.

[89] Cretu, O.; Krasheninnikov, A. V.; Rodríguez-Manzo, J. A.; Sun, L.; Nieminen, R. M.; Banhart, F. Migration and Localization of Metal Atoms on Strained Graphene. *Phys. Rev. Lett.* **2010**, *105* (19), 196102.

[90] Manadé, M.; Viñes, F.; Illas, F. Transition Metal Adatoms on Graphene: A Systematic Density Functional Study. *Carbon N. Y.* **2015**, *95*, 525–534.

[91] Zhang, Y.; Wang, Z.; Cao, J. Prediction of Magnetic Anisotropy of 5d Transition Metal-Doped g-C3N4. *J. Mater. Chem. C* **2014**, *2* (41), 8817–8821.

[92] Zhang, K. C.; Li, Y. F.; Liu, Y.; Zhu, Y. Protecting Quantum Anomalous Hall State from Thermal Fluctuation: Via the Giant Magnetic Anisotropy of Os-Based Dimers. *Phys. Chem. Chem. Phys.* **2018**, *20* (44), 28169–28175.

[93] Khajetoorians, A. A.; Wiebe, J.; Chilian, B.; Wiesendanger, R. Realizing All-Spin-Based Logic Operations Atom by Atom. *Science* **2011**, *332* (6033), 1062–1064.

[94] Ruderman, M. A.; Kittel, C. Indirect Exchange Coupling of Nuclear Magnetic Moments by Conduction Electrons. *Phys. Rev.* **1954**, *96* (1), 99–102.

[95] Kasuya, T. A Theory of Metallic Ferro- and Antiferromagnetism on Zener's Model. *Prog. Theor. Phys.* **1956**, *16* (1), 45–57.

[96] Yosida, K. Magnetic Properties of Cu-Mn Alloys. *Phys. Rev.* **1957**, *106* (5), 893–898.

[97] Tuček, J.; Błoński, P.; Ugolotti, J.; Swain, A. K.; Enoki, T.; Zbořil, R. Emerging Chemical Strategies for Imprinting Magnetism in Graphene and Related 2D Materials for Spintronic and Biomedical Applications. *Chem. Soc. Rev.* **2018**, *47* (11), 3899–3990.

[98] Yazyev, O. V.; Helm, L. Defect-Induced Magnetism in Graphene. *Phys. Rev. B - Condens. Matter Mater. Phys.* **2007**, *75* (12), 125408.

[99] Červenka, J.; Katsnelson, M. I.; Flipse, C. F. J. Room-Temperature Ferromagnetism in Graphite Driven by Two-Dimensional Networks of Point Defects. *Nat. Phys.* **2009**, *5* (11), 840–844.

[100] Nair, R. R.; Sepioni, M.; Tsai, I.-L.; Lehtinen, O.; Keinonen, J.; Krasheninnikov, A. V.; Thomson, T.; Geim, A. K.; Grigorieva, I. V. Spin-Half Paramagnetism in Graphene Induced by Point Defects. *Nat. Phys.* **2012**, *8* (3), 199–202.

[101] Yazyev, O. V. Emergence of Magnetism in Graphene Materials and Nanostructures. *Reports Prog. Phys.* **2010**, *73* (5), 056501.

[102] Carpio, A.; Bonilla, L. L.; De Juan, F.; Vozmediano, M. A. H. Dislocations in Graphene. *New J. Phys.* **2008**, *10*, 053021.

[103] Magda, G. Z.; Jin, X.; Hagymási, I.; Vancsó, P.; Osváth, Z.; Nemes-Incze, P.; Hwang, C.; Biró, L. P.; Tapasztó, L. Room-Temperature Magnetic Order on Zigzag Edges of Narrow Graphene Nanoribbons. *Nature* **2014**, *514* (7524), 608–611.

[104] Kobayashi, Y.; Fukui, K. I.; Enoki, T.; Kusakabe, K.; Kaburagi, Y. Observation of Zigzag and Armchair Edges of Graphite Using Scanning Tunneling Microscopy and Spectroscopy. *Phys. Rev. B - Condens. Matter Mater. Phys.* **2005**, *71* (19), 193406.

[105] Boukhvalov, D. W.; Katsnelson, M. I. Sp-Electron Magnetic Clusters with a Large Spin in Graphene. *ACS Nano* **2011**, *5* (4), 2440–2446.

[106] de la Torre, B.; Švec, M.; Hapala, P.; Redondo, J.; Krejčí, O.; Lo, R.; Manna, D.; Sarmah, A.; Nachtigallová, D.; Tuček, J.; Błoński, P.; Otyepka, M.; Zbořil, R.; Hobza, P.; Jelínek, P. Non-Covalent Control of Spin-State in Metal-Organic Complex by Positioning on N-Doped Graphene. *Nat. Commun.* **2018**, *9* (1), 2831.

[107] Lazar, P.; Zbořil, R.; Pumera, M.; Otyepka, M. Chemical Nature of Boron and Nitrogen Dopant Atoms in Graphene Strongly Influences Its Electronic Properties. *Phys. Chem. Chem. Phys.* **2014**, *16* (27), 14231–14235.

[108] Babar, R.; Kabir, M. Ferromagnetism in Nitrogen-Doped Graphene. *Phys. Rev. B* **2019**, *99* (11), 115442.

[109] Su, C.; Tripathi, M.; Yan, Q.; Wang, Z.; Zhang, Z.; Hofer, C.; Wang, H.; Basile, L.; Su, G.; Dong, M.; Meyer, J. C. Engineering Single-Atom Dynamics with Electron Irradiation. *Sci. Adv.* **2019**, *5*(5) 1–12.

[110] Susi, T.; Hardcastle, T. P.; Hofsäss, H.; Mittelberger, A.; Pennycook, T. J.; Mangler, C.; Drummond-Brydson, R.; Scott, A. J.; Meyer, J. C.; Kotakoski, J. Single-Atom Spectroscopy of Phosphorus Dopants Implanted into Graphene. *2D Mater.* **2017**, *4* (2), 021013.

[111] Lin, L.; Fu, L.; Zhang, K.; Chen, J.; Zhang, W.; Tang, S.; Du, Y.; Tang, N. P - Superdoped Graphene : Synthesis and Magnetic Properties. *ACS Appl. Mater. Interfaces* **2019**, *11* (42), 39062–39067.

[112] Zhang, X.; Lu, Z.; Fu, Z.; Tang, Y.; Ma, D.; Yang, Z. The Mechanisms of Oxygen Reduction Reaction on Phosphorus Doped Graphene : A First-Principles Study. *J. Power Sources* **2015**, *276*, 222–229.

[113] Li, R.; Wei, Z.; Gou, X. Nitrogen and Phosphorus Dual-Doped Graphene/Carbon Nanosheets as Bifunctional Electrocatalysts for Oxygen Reduction and Evolution. *ACS Catal.* **2015**, 5 (7), 4133–4142.

[114] Latorre-Sánchez, M.; Primo, A.; García, H. P-Doped Graphene Obtained by Pyrolysis of Modified Alginate as a Photocatalyst for Hydrogen Generation from

Water – Methanol Mixtures. *Angew. Chem. Int. Ed.* **2013**, *52* (45), 11813–11816.

[115] Song, J.; Yu, Z.; Gordin, M. L.; Hu, S.; Yi, R.; Tang, D.; Walter, T.; Virginia, W.; States, U. Chemically Bonded Phosphorus/Graphene Hybrid as a High Performance Anode for Sodium-Ion Batteries. *Nano Lett.* **2014**, 14(11), 6329–6335.

[116] Niu, F.; Tao, L.; Deng, Y.; Wang, Q.; Song, W. Phosphorus Doped Graphene Nanosheets for Room Temperature NH_3 Sensing. *NJC.* **2014**, *6*, 2269–2272.

[117] Some, S.; Kim, J.; Lee, K.; Kulkarni, A.; Yoon, Y.; Lee, S.; Kim, T.; Lee, H. Highly Air-Stable Phosphorus-Doped n-Type Graphene Field-Effect Transistors. **2012**, *24* (40), 5481–5486.

[118] Base, N. Molecular Magnetism: From Molecular Assemblies to the Devices. *Springer,* **1996**.

[119] Shao, D.; Wang, X. Y. Development of Single-Molecule Magnets. *Chinese J. Chem.* **2020**, *38* (9), 1005–1018.

[120] Wickman, H. H.; Trozzolo, A. M.; Williams, H. J.; Hull, G. W.; Merritt, F. R. Spin-3/2 Iron Ferromagnet: Its Mössbauer and Magnetic Properties. *Phys. Rev.* **1967**, *155* (2), 563–566.

[121] Caneschi, A.; Gatteschi, D.; Sessoli, R.; Barra, A. L.; Brunei, L. C.; Guillot, M. Alternating Current Susceptibility, High Field Magnetization, and Millimeter Band EPR Evidence for a Ground S=10 State in [Mn12O12(CH3COO)16(H2O)4].2CH3COOH.4H2O. *J. Am. Chem. Soc.* **1991**, *113* (15), 5873–5874.

[122] Aubin, S. M. J.; Wemple, M. W.; Adams, D. M.; Tsai, H. L.; Christou, G.; Hendrickson, D. N. Distorted Mn(IV)Mn(III)3 Cubane Complexes as Single-Molecule Magnets. *J. Am. Chem. Soc.* **1996**, *118* (33), 7746–7754.

[123] Friedman, J. R.; Sarachik, M. P.; Tejada, J.; Ziolo, R. Macroscopic Measurement of Resonant Magnetization Tunneling in High-Spin Molecules. *Phys. Rev. Lett.* **1996**, *76* (20), 3830–3833.

[124] Ishikawa, N.; Sugita, M.; Ishikawa, T.; Koshihara, S. Y.; Kaizu, Y. Lanthanide Double-Decker Complexes Functioning as Magnets at the Single-Molecular Level.

J. Am. Chem. Soc. **2003**, *125* (29), 8694–8695.

[125] Rinehart, J. D.; Long, J. R. Slow Magnetic Relaxation in a Trigonal Prismatic Uranium(III) Complex. *J. Am. Chem. Soc.* **2009**, *131* (35), 12558–12559.

[126] Freedman, D. E.; Harman, W. H.; Harris, T. D.; Long, G. J.; Chang, C. J.; Long, J. R. Slow Magnetic Relaxation in a High-Spin Iron(II) Complex. *J. Am. Chem. Soc.* **2010**, *132* (4), 1224–1225.

[127] Zadrozny, J. M.; Xiao, D. J.; Atanasov, M.; Long, G. J.; Grandjean, F.; Neese, F.; Long, J. R. Magnetic Blocking in a Linear Iron(I) Complex. *Nat. Chem.* **2013**, *5* (7), 577–581.

[128] Frost, J. M.; Harriman, K. L. M.; Murugesu, M. The Rise of 3-d Single-Ion Magnets in Molecular Magnetism: Towards Materials from Molecules? *Chem. Sci.* **2016**, *7* (4), 2470–2491.

[129] Sinfelt, J. H. Role of Surface Science in Catalysis. *Surf. Sci.* **2002**, *500* (1–3), 923–946.

[130] Ekerdt, J. G.; Sun, Y. M.; Szabo, A.; Szulczewski, G. J.; White, J. M. Role of Surface Chemistry in Semiconductor Thin Film Processing. *Chem. Rev.* **1996**, *96* (4), 1499–1517.

[131] D'Orazio, P. Biosensors in Clinical Chemistry. *Clin. Chim. Acta* **2003**, *334* (1–2), 41–69.

[132] Zhang, X.; Tian, Z.; Yang, S. W.; Wang, J. Magnetic Manipulation and Half-Metal Prediction of One-Dimensional Bimetallic Organic Sandwich Molecular Wires [CpTM1CpTM 2]∞ (TM1 = Ti, Cr, Fe; TM2 = Sc-Co). *J. Phys. Chem. C* **2011**, *115* (7), 2948–2953.

[133] Xiang, H.; Yang, J.; Hou, J. G.; Zhu, Q. One-Dimensional Transition Metal-Benzene Sandwich Polymers: Possible Ideal Conductors for Spin Transport. *J. Am. Chem. Soc.* **2006**, *128* (7), 2310–2314.

[134] Parida, P.; Kundu, A.; Pati, S. K. One-Dimensional Organometallic V-Anthracene Wire and Its B-N Analogue: Efficient Half-Metallic Spin Filters. *Phys. Chem. Chem. Phys.* **2010**, *12* (26), 6924–6927.

[135] Santhini, V. M.; Stetsovych, O.; Ondráček, M.; Mendieta Moreno, J. I.; Mutombo, P.; de la Torre, B.; Švec, M.; Klívar, J.; Stará, I. G.; Vázquez, H.; Starý, I.; Jelínek, P. On-Surface Synthesis of Polyferrocenylene and Its Single-Chain Conformational and Electrical Transport Properties. *Adv. Funct. Mater.* **2021**, *31* (5), 2006391.

[136] Lindström, B.; Pettersson, L. J. A Brief History of Catalysis. *Cattech* **2003**, *7* (4), 130–138.

[137] Somorjai, G.; Li, Y. Introduction to Surface Chemistry and Catalysis, *Wiley*, **2010**.

[138] Binning, G.; Quate, C. F.; Gerber, Ch. Atomic Force Microscope. *Phys. Rev. Lett.* **1986**, *56*, 930.

[139] https://www.cnet.com/news/ibms-35-atoms-and-the-rise-of-nanotech, visited 4. 8. 2022.

[140] Sen, D.; Błoński, P.; Torre, B. D. La; Jelínek, P.; Otyepka, M. Thermally Induced Intra-Molecular Transformation and Metalation of Free-Base Porphyrin on Au(111) Surface Steered by Surface Confinement and Ad-Atoms. *Nanoscale Adv.* **2020**, *2* (7), 2986–2991.

[141] Medici, S.; Peana, M. F.; Zoroddu, M. A. Noble Metals in Pharmaceuticals: Applications and Limitations. *Springer*, **2018**.

[142] Kummer, J. T. Use of Noble Metals in Automobile Exhaust Catalysts. *J. Phys. Chem.* **1986**, *90* (20), 4747–4752.

[143] Bullock, R. M. Reaction: Earth-Abundant Metal Catalysts for Energy Conversions. *Chem* **2017**, *2* (4), 444–446.

[144] Julkapli, N. M.; Bagheri, S. Graphene Supported Heterogeneous Catalysts: An Overview. *Int. J. Hydrogen Energy* **2015**, *40* (2), 948–979.

[145] Yan, H.; Lin, Y.; Wu, H.; Zhang, W.; Sun, Z.; Cheng, H.; Liu, W.; Wang, C.; Li, J.; Huang, X.; Yao, T.; Yang, J.; Wei, S.; Lu, J. Bottom-up Precise Synthesis of Stable Platinum Dimers on Graphene. *Nat. Commun.* **2017**, *8* (1), 1070.

[146] Deng, D.; Chen, X.; Yu, L.; Wu, X.; Liu, Q.; Liu, Y.; Yang, H.; Tian, H.; Hu, Y.; Du, P.; Si, R.; Wang, J.; Cui, X.; Li, H.; Xiao, J.; Xu, T.; Deng, J.; Yang, F.; Duchesne,

P. N.; Zhang, P.; Zhou, J.; Sun, L.; Li, J.; Pan, X.; Bao, X. A Single Iron Site Confined in a Graphene Matrix for the Catalytic Oxidation of Benzene at Room Temperature. *Sci. Adv.* **2015**, *1* (11), 1500462.

[147] Fei, H.; Dong, J.; Wan, C.; Zhao, Z.; Xu, X.; Lin, Z.; Wang, Y.; Liu, H.; Zang, K.; Luo, J.; Zhao, S.; Hu, W.; Yan, W.; Shakir, I.; Huang, Y.; Duan, X. Microwave-Assisted Rapid Synthesis of Graphene-Supported Single Atomic Metals. *Adv. Mater.* **2018**, *30* (35), 1802146.

[148] Bakandritsos, A.; Kadam, R. G.; Kumar, P.; Zoppellaro, G.; Medved', M.; Tuček, J.; Montini, T.; Tomanec, O.; Andrýsková, P.; Drahoš, B.; Varma, R. S.; Otyepka, M.; Gawande, M. B.; Fornasiero, P.; Zbořil, R. Mixed-Valence Single-Atom Catalyst Derived from Functionalized Graphene. *Adv. Mater.* **2019**, *31* (17), 1900323.

[149] Wang, A.; Li, J.; Zhang, T. Heterogeneous Single-Atom Catalysis. *Nat. Rev. Chem.* **2018**, *2* (6), 65–81.

[150] Liu, L.; Corma, A. Metal Catalysts for Heterogeneous Catalysis: From Single Atoms to Nanoclusters and Nanoparticles. *Chem. Rev.* **2018**, *118* (10), 4981–5079.

[151] Liu, J. Catalysis by Supported Single Metal Atoms. *ACS Catal.* **2017**, *7* (1), 34–59.

[152] Wisniak, J. The History of Catalysis. From the Beginning to Nobel Prizes. *Educ. Quim.* **2010**, *21* (1), 60–69.

[153] Bell, A. T. The Impact of Nanoscience on Heterogeneous Catalysis. *Science* **2003**, *299* (5613), 1688–1691.

[154] Carchini, G.; Almora-Barrios, N.; Revilla-López, G.; Bellarosa, L.; García-Muelas, R.; García-Melchor, M.; Pogodin, S.; Błoński, P.; López, N. How Theoretical Simulations Can Address the Structure and Activity of Nanoparticles. *Top. Catal.* **2013**, *56* (13–14), 1262–1272.

[155] Thomas, J. M. The Enduring Relevance and Academic Fascination of Catalysis. *Nat. Catal.* **2018**, *1*, 2–5.

[156] Monai, M.; Melchionna, M.; Fornasiero, P. From Metal to Metal-Free Catalysts: Routes to Sustainable Chemistry, *Adv. Catal.* **2018**, *63*, 1-73.

[157] Fei, H.; Dong, J.; Feng, Y.; Allen, C. S.; Wan, C.; Volosskiy, B.; Li, M.; Zhao, Z.; Wang, Y.; Sun, H.; An, P.; Chen, W.; Guo, Z.; Lee, C.; Chen, D.; Shakir, I.; Liu, M.; Hu, T.; Li, Y.; Kirkland, A. I.; Duan, X.; Huang, Y. General Synthesis and Definitive Structural Identification of MN4C4 Single-Atom Catalysts with Tunable Electrocatalytic ActivitiesGeneral Synthesis and Definitive Structural Identification of MN4C4 Single-Atom Catalysts with Tunable Electrocatalytic Activ. *Nat. Catal.* **2018**, *1* (1), 63–72.

[158] Zhou, X.; Qiao, J.; Yang, L.; Zhang, J. REVIEW A Review of Graphene-Based Nanostructural Materials for Both Catalyst Supports and Metal-Free Catalysts in PEM Fuel Cell Oxygen Reduction Reactions. *Adv. Energy Mater.* **2014**, *4* (8), 1–25.

[159] Sun, S.; Zhang, G.; Gauquelin, N.; Chen, N.; Zhou, J.; Yang, S.; Chen, W.; Meng, X.; Geng, D.; Banis, M. N.; Li, R.; Ye, S.; Knights, S.; Botton, G. A.; Sham, T.; Sun, X. Single-Atom Catalysis Using Pt/Graphene Achieved through Atomic Layer Deposition. *Sci. Rep.* **2013**, *3* (1), 1775.

[160] Zitolo, A.; Goellner, V.; Armel, V.; Sougrati, M. T.; Mineva, T.; Stievano, L.; Fonda, E.; Jaouen, F. Identification of Catalytic Sites for Oxygen Reduction in Iron- and Nitrogen-Doped Graphene Materials. *Nat. Mater.* **2015**, *14* (9), 937–942.

[161] Blanco, M.; Mosconi, D.; Otyepka, M.; Medveď, M.; Bakandritsos, A.; Agnoli, S.; Granozzi, G. Combined High Degree of Carboxylation and Electronic Conduction in Graphene Acid Sets New Limits for Metal Free Catalysis in Alcohol Oxidation. *Chem. Sci.* **2019**, *10* (41), 9438–9445.

[162] Blanco, M.; Mosconi, D.; Tubaro, C.; Biffis, A.; Badocco, D.; Pastore, P.; Otyepka, M.; Bakandritsos, A.; Liu, Z.; Ren, W.; Agnoli, S.; Granozzi, G. Palladium Nanoparticles Supported on Graphene Acid: A Stable and Eco-Friendly Bifunctional C-C Homo- and Cross-Coupling Catalyst. *Green Chem.* **2019**, *21* (19), 5238–5247.

[163] Lewis, N. S.; Nocera, D. G. Powering the Planet: Chemical Challenges in Solar Energy Utilization. *Proc. Natl. Acad. Sci. U. S. A.* **2007**, *104* (50), 20142.

[164] Dai, L.; Chang, D. W.; Baek, J. B.; Lu, W. Carbon Nanomaterials for Advanced Energy Conversion and Storage. *Small* **2012**, *8* (8), 1130–1166.

[165] Dehghani-Sanij, A. R.; Tharumalingam, E.; Dusseault, M. B.; Fraser, R. Study of

Energy Storage Systems and Environmental Challenges of Batteries. *Renew. Sustain. Energy Rev.* **2019**, *104*, 192–208.

[166] Pomerantseva, E.; Bonaccorso, F.; Feng, X.; Cui, Y.; Gogotsi, Y. Energy Storage: The Future Enabled by Nanomaterials. *Science* **2019**, *366* (6468), eaan8285.

[167] Routledge, B. A Popular History of Science. *Nature*, **1880**.

[168] O'Heir, J. Building Better Batteries. *Mech. Eng.* **2017**, *139* (1), 10–11.

[169] Nitta, N.; Wu, F.; Lee, J. T.; Yushin, G. Li-ion Battery Materials: Present and Future. *Mater. Today* **2015**, *18* (5), 252-264.

[170] Vikström, H.; Davidsson, S.; Höök, M. Lithium Availability and Future Production Outlooks. *Appl. Energy* **2013**, *110*, 252–266.

[171] Zhang, P.; Yuan, T.; Pang, Y.; Peng, C.; Yang, J.; Ma, Z.-F.; Zheng, S. Influence of Current Density on Graphite Anode Failure in Lithium-Ion Batteries. *J. Electrochem. Soc.* **2019**, *166* (3), A5489–A5495.

[172] Cai, W.; Yao, Y.; Zhu, G.; Jiang, L.; He, C.; Huang, J.; Zhang, Q. A Review on Energy Chemistry of Fast-Charging Anodes. *Chem. Soc. Rev.* **2020**, *49* (12), 3806–3833.

[173] Conway, B. E. Electrochemical Supercapacitors: Scientific Fundamentals and Technological Applications. *Springer*, **1999**.

[174] Kelly-Holmes, H. US3288641 Electrical Energy Storage Apparatus Patent. *US Pat.* **1966**.

[175] Conway, B. E. Transition from "supercapacitor" to "Battery" Behavior in Electrochemical Energy Storage. *Proc. Int. Power Sources Symp.* **1991**, *138* (6), 319–327.

[176] Jeena, M. T.; Bok, T.; Kim, S. H.; Park, S.; Kim, J.; Park, S.; Ryu, J. A Siloxane-Incorporated Copolymer as an in situ Cross-Linkable Binder for High Performance Silicon anodes in Li-ion Batteries. *Nanoscale* **2016**, *8* (17), 9245-9253.

[177] E. C. Vermisoglou *et al.*, "Graphene with Covalently Grafted Amino Acid as a Route Vermisoglou, E. C.; Jakubec, P.; Bakandritsos, A.; Kupka, V.; Pykal, M.; Šedajová,

V.; Vlček, J.; Tomanec, O.; Scheibe, M.; Zbořil, R.; Otyepka, M. Graphene with Covalently Grafted Amino Acid as a Route Toward Eco-Friendly and Sustainable Supercapacitors. *ChemSusChem* **2021**, *14* (18), 3904–3914.

[178] Sedajová, V.; Jakubec, P.; Bakandritsos, A.; Ranc, V.; Otyepka, M. New Limits for Stability of Supercapacitor Electrode Material Based on Graphene Derivative. *Nanomaterials* **2020**, *10* (9), 1731.

[179] Gu, W.; Yushin, G. Review of Nanostructured Carbon Materials for Electrochemical Capacitor Applications: Advantages and Limitations of Activated Carbon, Carbide-Derived Carbon, Zeolite-Templated Carbon, Carbon Aerogels, Carbon Nanotubes, Onion-like Carbon, and Graphene. *Wiley Interdiscip. Rev. Energy Environ.* **2014**, *3* (5), 424–473.

[180] Wang, Q.; Yan, J.; Fan, Z. Carbon Materials for High Volumetric Performance Supercapacitors: Design, Progress, Challenges and Opportunities. *Energy Environ. Sci.* **2016**, *9* (3), 729–762.

[181] Gogotsi, Y.; Simon, P. True Performance Metrics in Electrochemical Energy Storage. *Science* **2011**, *334* (6058), 917–918.

[182] Hao, L.; Li, X.; Zhi, L. Carbonaceous Electrode Materials for Supercapacitors. *Adv. Mater.* **2013**, *25* (28), 3899–3904.

[183] Yan, J.; Wang, Q.; Wei, T.; Fan, Z. Recent Advances in Design and Fabrication of Electrochemical Supercapacitors with High Energy Densities. *Adv. Energy Mater.* **2014**, *4* (4), 1300816.

[184] Chronopoulos, D. D.; Bakandritsos, A.; Pykal, M.; Zbořil, R.; Otyepka, M. Chemistry, Properties, and Applications of Fluorographene. *Appl. Mater. Today* **2017**, *9*, 60–70.

[185] Tantis, I.; Bakandritsos, A.; Zaoralová, D.; Medveď, M.; Jakubec, P.; Havláková, J.; Zbořil, R.; Otyepka, M. Covalently Interlinked Graphene Sheets with Sulfur-Chains Enable Superior Lithium–Sulfur Battery Cathodes at Full-Mass Level. *Adv. Funct. Mater.* **2021**, *31* (30), 2101326.

[186] Heng Cheong, Y.; Nasir, M. Z. M.; Bakandritsos, A.; Pykal, M.; Jakubec, P.; Zbořil,

R.; Otyepka, M.; Pumera, M. Cyanographene and Graphene Acid: The Functional Group of Graphene Derivative Determines the Application in Electrochemical Sensing and Capacitors. *ChemElectroChem* **2019**, *6* (1), 229–234.

[187] Reuillard, B.; Blanco, M.; Calvillo, L.; Coutard, N.; Ghedjatti, A.; Chenevier, P.; Agnoli, S.; Otyepka, M.; Granozzi, G.; Artero, V. Noncovalent Integration of a Bioinspired Ni Catalyst to Graphene Acid for Reversible Electrocatalytic Hydrogen Oxidation. *ACS Appl. Mater. Interfaces* **2020**, *12* (5), 5805–5811.

[188] Seelajaroen, H.; Bakandritsos, A.; Otyepka, M.; Zbořil, R.; Sariciftci, N. S. Immobilized Enzymes on Graphene as Nanobiocatalyst. *ACS Appl. Mater. Interfaces* **2020**, *12* (1), 250–259.

[189] Georgakilas, V.; Perman, J. A.; Tucek, J.; Zboril, R. Broad Family of Carbon Nanoallotropes : Classificaation, Chemistry, and Applications of Fullerenes, Carbon Dots, Nanotubes, Graphene, Nanodiamonds, and Combined Superstructures. *Chem. Rev.* **2015**, 115 (11), 4744–4822.

[190] Bae, S.; Kim, H.; Lee, Y.; Xu, X.; Park, J.; Zheng, Y.; Balakrishnan, J.; Lei, T.; Kim, H. R.; Song, Y. Il; Kim, Y.; Kim, K. S. Roll-to-Roll Production of 30-Inch Graphene Films for Transparent Electrodes. *Nat. Nanotechnol.* **2010**, *5*, 574-578.

[191] Liu, B. Z.; Liu, Q.; Huang, Y.; Ma, Y.; Yin, S.; Zhang, X.; Sun, W.; Chen, Y. Organic Photovoltaic Devices Based on a Novel Acceptor Material : Graphene. *Adv. Mater.* **2008**, *20* (20), 3924–3930.

[192] Tan, Z.; Chen, G.; Zhu, Y. Carbon-Based Supercapacitors Produced by Activation of Graphene-Surporting Materials. *Science* **2015**, *1*, 211–225.

[193] Rumyantsev, S.; Liu, G.; Shur, M. S.; Potyrailo, R. A.; Balandin, A. A. Selective Gas Sensing with a Single Pristine Graphene Transistor. *Nano Lett.* **2012**, *12* (5), 2294–2298.

[194] Novoselov, K. S.; Fal, V. I.; Colombo, L.; Gellert, P. R.; Schwab, M. G.; Kim, K. REVIEW A Roadmap for Graphene. *Nature* **2012**, *490* (7419), 192–200.

[195] Min, S. K.; Kim, W. Y.; Cho, Y.; Kim, K. S. Fast DNA Sequencing with a Graphene-Based Nanochannel Device. *Nat. Nanotechnol.* **2011**, *6* (3), 162–165.

[196] Han, Y.; Xu, Z.; Gao, C. Ultrathin Graphene Nanofiltration Membrane for Water Purification. *Adv. Funct. Mater.* **2013**, *23* (29), 3693–3700.

[197] Auwärter, W.; Écija, D.; Klappenberger, F.; Barth, J. V. Porphyrins at Interfaces. *Nat. Chem.* **2015**, *7* (2), 105–120.

[198] Gottfried, J. M. Surface Chemistry of Porphyrins and Phthalocyanines. *Surf. Sci. Rep.* **2015**, *70* (3), 259–379.

[199] Imran, M.; Ramzan, M.; Qureshi, A. K.; Azhar Khan, M.; Tariq, M. Emerging Applications of Porphyrins and Metalloporphyrins in Biomedicine and Diagnostic Magnetic Resonance Imaging. *Biosensors* **2018**, *8* (4), 95.

[200] Wolf, S. A.; Awschalom, D. D.; Buhrman, R. A.; Daughton, J. M.; Von Molnár, S.; Roukes, M. L.; Chtchelkanova, A. Y.; Treger, D. M. Spintronics: A Spin-Based Electronics Vision for the Future. *Science* **2001**, *294* (5546), 1488–1495.

[201] Tsuda, A.; Osuka, A. Fully Conjugated Porphyrin Tapes with Electronic Absorption Bands That Reach into Infrared. *Science* **2001**, *293* (5527), 79–82.

[202] Wallace, P. R. The Band Theory of Graphite. *Phys. Rev.* **1947**, *71*, 622.

[203] oehm, H. P.; Setton, R.; Stumpp, E. Nomenclature and Terminology of Graphite Intercalation Compounds. *Carbon N. Y.* **1986**, *24* (2), 241–245.

[204] Saini, D. Synthesis and Functionalization of Graphene and Application in Electrochemical Biosensing. *Nanotechnol. Rev.* **2011**, *5* (4), 1-49.

[205] Heyrovska, R. The Golden Ratio, Ionic and Atomic Radii and Bond Lengths. *Molecular Physics*. **2005**, *103*, 877–882.

[206] Balandin, A. A.; Ghosh, S.; Bao, W.; Calizo, I.; Teweldebrhan, D.; Miao, F.; Lau, C. N. Superior Thermal Conductivity of Single-Layer Graphene. *Nano Lett.* **2008**, *8* (3), 902-907.

[207] Lee, C.; Wei, X.; Kysar, J. W.; Hone, J. Measurement of the Elastic Properties and Intrinsic Strength of Monolayer Graphene. Science **2008**, *321* (5887), 385–388.

[208] Sur, U. K. Graphene: A Rising Star on the Horizon of Materials Science. *Int. J. Electrochem.* **2012**, *2012*, 1–12.

[209] Sheehy, D. E.; Schmalian, J. Optical Transparency of Graphene as Determined by the Fine-Structure Constant. *Phys. Rev. B - Condens. Matter Mater. Phys.* **2009**, *80* (19), 2–5.

[210] Chen, J. H.; Ishigami, M.; Jang, C.; Hines, D. R.; Fuhrer, M. S.; Williams, E. D. Printed Graphene Circuits. *Adv. Mater.* **2007**, *19* (21), 3623–3627.

[211] Kusmartsev, F. V.; Wu, W. M.; Pierpoint, M. P.; Yung, K. C. Application of Graphene Within Optoelectronic Devices and Transistors. *Springer*, **2015**,.

[212] Kanakia, S.; Toussaint, J. D.; Mullick Chowdhury, S.; Lalwani, G.; Tembulkar, T.; Button, T.; Shroyer, K. R.; Moore, W.; Sitharaman, B. Physicochemical Characterization of a Novel Graphene-Based Magnetic Resonance Imaging Contrast Agent. *Int. J. Nanomedicine* **2013**, *8*, 2821–2833.

[213] Donaldson, L. Graphene: Invisible to Water. *Mater. Today* **2012**, *15* (3), 82.

[214] Liao, L.; Peng, H.; Liu, Z. Chemistry Makes Graphene beyond Graphene. *J. Am. Chem. Soc.* **2014**, *136* (35), 12194–12200.

[215] Elias, D. C.; Nair, R.; Mohiuddin, T. M. G.; Morozov, S. V.; Blake, P.; Halsall, M. P.; Ferrari, A. C.; Boukhvalov, D. W.; Katsnelson, M. I.; Geim, A. K., Novoselov, K. S. Control of Graphene's Properties by Reversible Hydrogenation: Evidence for Graphane. *Science* **2009**, *323* (5914), 610–614.

[216] Sofo, J. O.; Chaudhari, A. S.; Barber, G. D. Graphane: A Two-Dimensional Hydrocarbon. *Phys. Rev. B - Condens. Matter Mater. Phys.* **2007**, *75* (15), 153401.

[217] Zhu, Y.; Murali, S.; Cai, W.; Li, X.; Suk, J. W.; Potts, J. R.; Ruoff, R. S. Graphene and Graphene Oxide: Synthesis, Properties, and Applications. *Adv. Mater.* **2010**, *22* (35), 3906–3924.

[218] Urbanová, V.; Holá, K.; Bourlinos, A. B.; Čépe, K.; Ambrosi, A.; Loo, A. H.; Pumera, M.; Karlický, F.; Otyepka, M.; Zbořil, R. Thiofluorographene-Hydrophilic Graphene Derivative with Semiconducting and Genosensing Properties. *Adv. Mater.* **2015**, *27* (14), 2305–2310.

[219] Shahrezaei, M.; Hejazi, S.; Rambabu, Y.; Vavrecka, M.; Bakandritsos, A.; Oezkan, S.; Zboril, R.; Schmuki, P.; Naldoni, A.; Kment, S. Multi-Leg TiO2 Nanotube

Photoelectrodes Modified by Platinized Cyanographene with Enhanced Photoelectrochemical Performance. *Catalysts* **2020**, *10*(6), 717.

[220] Bakandritsos, A.; Hobza, P.; Zbořil, R.; Kolařík, J.; Bad'ura, Z.; Lo, R.; Zoppellaro, G.; Kment, Š.; Naldoni, A.; Zhang, Y.; Petr, M.; Tomanec, O.; Filip, J.; Otyepka, M. Carboxylated Graphene for Radical-Assisted Ultra-Trace-Level Water Treatment and Noble Metal Recovery. *ACS Nano* **2021**, *15* (2), 3349–3358.

[221] Zbořil, R.; Karlický, F.; Bourlinos, A. B.; Steriotis, T. A.; Stubos, A. K.; Georgakilas, V.; Šafářová, K.; Jančík, D.; Trapalis, C.; Otyepka, M. Graphene Fluoride: A Stable Stoichiometric Graphene Derivative and Its Chemical Conversion to Graphene. *Small* **2010**, *6* (24), 2885–2891.

[222] Leenaerts, O.; Peelaers, H.; Partoens, B.; Peeters, F. M. First-Principles Investigation of Graphene Fluoride and Graphane. *Phys. Rev. B* **2010**, *82*, 195436.

[223] Lei, F.; Yang, M.; Jiang, F.; Zhang, H.; Zhang, Z.; Sun, D. Microwave-Assisted Liquid Phase Exfoliation of Graphite Fluoride into Fluorographene. *Chem. Eng. J.* **2019**, *360*, 673–679.

[224] Robinson, J. T.; Burgess, J. S.; Junkermeier, C. E.; Badescu, S. C.; Reinecke, T. L.; Perkins, F. K.; Zalalutdniov, M. K.; Baldwin, J. W.; Culbertson, J. C.; Sheehan, P. E.; Snow, E. S. Properties of Fluorinated Graphene Films. *Nano Lett.* **2010**, *10* (8), 3001–3005.

[225] Baraket, M.; Walton, S. G.; Lock, E. H.; Robinson, J. T.; Perkins, F. K. The Functionalization of Graphene Using Electron-Beam Generated Plasmas. *Appl. Phys. Lett.* **2010**, *96* (23), 94–97.

[226] Bon, S. B.; Valentini, L.; Verdejo, R.; Fierro, J. L. G.; Peponi, L.; Lopez-Manchado, M. A.; Kenny, J. M. Plasma Fluorination of Chemically Derived Graphene Sheets and Subsequent Modification with Butylamine. *Chem. Mater.* **2009**, *21* (14), 3433–3438.

[227] Tahara, K.; Iwasaki, T.; Matsutani, A.; Hatano, M. Effect of Radical Fluorination on Mono- and Bi-Layer Graphene in Ar/F_2 Plasma. *Appl. Phys. Lett.* **2012**, *101* (16), 163105.

[228] Feng, W.; Long, P.; Feng, Y. Y.; Li, Y. Two-Dimensional Fluorinated Graphene: Synthesis, Structures, Properties and Applications. *Adv. Sci.* **2016**, *3* (7), 1500413.

[229] Banerjee, A. N. Graphene and Its Derivatives as Biomedical Materials: Future Prospects and Challenges. *Interface Focus* **2018**, *8* (3), 1-22.

[230] Jeon, K. J.; Lee, Z.; Pollak, E.; Moreschini, L.; Bostwick, A.; Park, C. M.; Mendelsberg, R.; Radmilovic, V.; Kostecki, R.; Richardson, T. J.; Rotenberg, E. Fluorographene: A Wide Bandgap Semiconductor with Ultraviolet Luminescence. *ACS Nano* **2011**, *5* (2), 1042–1046.

[231] Otyepka, M. Band Gaps and Optical Spectra of Chlorographene, Fluorographene and Graphane from G_0W_0 , GW_0 and GW Calculations on Top of PBE and HSE06 Orbitals. *J. Chem. Theory Comput.* **2013**, *9* (9), 4155–4164.

[232] Dubecký, M.; Karlický, F.; Minárik, S.; Mitas, L. Fundamental Gap of Fluorographene by Many-Body GW and Fixed-Node Diffusion Monte Carlo Methods. *J. Chem. Phys.* **2020**, *153* (18), 184706.

[233] Dubecký, M.; Otyepková, E.; Lazar, P.; Karlický, F.; Petr, M.; Čépe, K.; Banáš, P.; Zbořil, R.; Otyepka, M. Reactivity of Fluorographene: A Facile Way toward Graphene Derivatives. *J. Phys. Chem. Lett.* **2015**, *6* (8), 1430–1434.

[234] Wang, X.; Wang, W.; Liu, Y.; Ren, M.; Xiao, H.; Liu, X. Controllable Defluorination of Fluorinated Graphene and Weakening of C-F Bonding under the Action of Nucleophilic Dipolar Solvent. *Phys. Chem. Chem. Phys.* **2016**, *18* (4), 3285–3293.

[235] Bourlinos, A. B.; Safarova, K.; Siskova, K.; Zbořil, R. The Production of Chemically Converted Graphenes from Graphite Fluoride. *Carbon N. Y.* **2012**, *50* (3), 1425–1428.

[236] Lazar, P.; Chua, C. K.; Holá, K.; Zbořil, R.; Otyepka, M.; Pumera, M. Dichlorocarbene-Functionalized Fluorographene: Synthesis and Reaction Mechanism. *Small* **2015**, *11* (31), 3790–3796.

[237] Whitener, K. E.; Stine, R.; Robinson, J. T.; Sheehan, P. E. Graphene as Electrophile: Reactions of Graphene Fluoride. *J. Phys. Chem. C* **2015**, *119* (19), 10507–10512.

[238] Medveď, M.; Zoppellaro, G.; Ugolotti, J.; Matochová, D.; Lazar, P.; Pospíšil, T.;

Bakandritsos, A.; Tuček, J.; Zbořil, R.; Otyepka, M. Reactivity of Fluorographene Is Triggered by Point Defects: Beyond the Perfect 2D World. *Nanoscale* **2018**, *10* (10), 4696–4707.

[239] Kumar, N.; Sharma, J. D.; Ahluwalia, P. K. First-Principle Study of Nanostructures of Functionalized Graphene. *Pramana - J. Phys.* **2014**, *82* (6), 1103–1117.

[240] Tran, N. T. T.; Nguyen, D. K.; Glukhova, O. E.; Lin, M. F. Coverage-Dependent Essential Properties of Halogenated Graphene: A DFT Study. *Sci. Rep.* **2017**, *7* (1), 17858.

[241] Makarova, T. L.; Shelankov, A. L.; Zyrianova, A. A.; Veinger, A. I.; Tisnek, T. V.; Lähderanta, E.; Shames, A. I.; Okotrub, A. V.; Bulusheva, L. G.; Chekhova, G. N.; Pinakov, D. V.; Asanov, I. P.; Šljivančanin, Ž. Edge State Magnetism in Zigzag-Interfaced Graphene via Spin Susceptibility Measurements. *Sci. Rep.* **2015**, *5* (1), 13382.

[242] Liu, H. Y.; Hou, Z. F.; Hu, C. H.; Yang, Y.; Zhu, Z. Z. Electronic and Magnetic Properties of Fluorinated Graphene with Different Coverage of Fluorine. *J. Phys. Chem. C* **2012**, *116* (34), 18193–18201.

[243] Panáček, D.; Hochvaldová, L.; Bakandritsos, A.; Malina, T.; Langer, M.; Belza, J.; Martincová, J.; Večeřová, R.; Lazar, P.; Poláková, K.; Kolařík, J.; Válková, L.; Kolář, M.; Otyepka, M.; Panáček, A.; Zbořil, R. Silver Covalently Bound to Cyanographene Overcomes Bacterial Resistance to Silver Nanoparticles and Antibiotics. *Adv. Sci.* **2021**, *8* (12), 3–10.

[244] Stankovich, S.; Dikin, D. A.; Piner, R. D.; Kohlhaas, K. A.; Kleinhammes, A.; Jia, Y.; Wu, Y.; Nguyen, S. B. T.; Ruoff, R. S. Synthesis of Graphene-Based Nanosheets via Chemical Reduction of Exfoliated Graphite Oxide. *Carbon N. Y.* **2007**, *45* (7), 1558–1565.

[245] Chua, C. K.; Pumera, M. Chemical Reduction of Graphene Oxide: A Synthetic Chemistry Viewpoint. *Chem. Soc. Rev.* **2014**, *43* (1), 291–312.

[246] Eigler, S.; Hirsch, A. Chemistry with Graphene and Graphene Oxide - Challenges for Synthetic Chemists. *Angew. Chemie - Int. Ed.* **2014**, *53* (30), 7720–7738.

[247] Pumera, M.; Sofer, Z. Towards Stoichiometric Analogues of Graphene: Graphane, Fluorographene, Graphol, Graphene Acid and Others. *Chem. Soc. Rev.* **2017**, *46* (15), 4450–4463.

[248] Chen, Y.; Prociuk, A.; Perrine, T.; Dunietz, B. D. Spin-Dependent Electronic Transport through a Porphyrin Ring Ligating an Fe(II) Atom: An Ab Initio Study. *Phys. Rev. B - Condens. Matter Mater. Phys.* **2006**, *74* (24), 245320.

[249] Abel, M.; Clair, S.; Ourdjini, O.; Mossoyan, M.; Porte, L. Single Layer of Polymeric Fe-Phthalocyanine: An Organometallic Sheet on Metal and Thin Insulating Film. *J. Am. Chem. Soc.* **2011**, 133 (5), 1203–1205.

[250] Zhou, J.; Sun, Q. Magnetism of Phthalocyanine-Based Organometallic Single Porous Sheet. *J. Am. Chem. Soc.* **2011**, *133* (38), 15113–15119.

[251] Getzlaff, M. Fundamentals of Magnetism. *Springer,* **2010**.

[252] Błoński, P.; Hafner, J. Density-Functional Theory of the Magnetic Anisotropy of Nanostructures: An Assessment of Different Approximations. *J. Phys. Condens. Matter* **2009**, *21* (42), 426001.

[253] Błoński, P.; Hafner, J. Magneto-Structural Properties and Magnetic Anisotropy of Small Transition-Metal Clusters: A First-Principles Study. *J. Phys. Condens. Matter* **2011**, *23* (13), 136001.

[254] Arnaut, L. G. Design of Porphyrin-Based Photosensitizers for Photodynamic Therapy. *Adv. Inorg. Chem.* **2011**, *63*, 187-233.

[255] Knör, G. Intramolecular Charge Transfer Excitation of Meso-Tetrakis (1-Pyrenyl) Porphyrinato Gold(III) Acetate. Photosensitized Oxidation of Guanine. *Inorg. Chem. Commun.* **2001**, *4* (3), 160–163.

[256] Zhou, C.; Wai, P.; Chan, H.; Che, C. Gold (III) Porphyrin-Catalyzed Cycloisomerization of Allenones. *Org. Lett.* **2006**, *8* (2), 325–328.

[257] Sun, R. W. Y.; Che, C. M. The Anti-Cancer Properties of Gold(III) Compounds with Dianionic Porphyrin and Tetradentate Ligands. *Coord. Chem. Rev.* **2009**, *253* (11–12), 1682–1691.

[258] Marbach, H. Surface-Mediated in Situ Metalation of Porphyrins at the Solid-Vacuum Interface. *Acc. Chem. Res.* **2015**, *48* (9), 2649–2658.

[259] Shubina, T. E.; Marbach, H.; Flechtner, K.; Kretschmann, A.; Jux, N.; Buchner, F.; Steinru, H.; Clark, T.; Gottfried, J. M. Principle and Mechanism of Direct Porphyrin Metalation: Joint Experimental and Theoretical Investigation. **2007**, *1* (16), 9476–9483.

[260] Buchner, F.; Seufert, K.; Auwa, W.; Heim, D.; Barth, J. V; Flechtner, K.; Gottfried, J. M.; Steinru, H.; Marbach, H. NO-Induced Reorganization of Porphyrin Arrays. **2009**, *3* (7), 1789–1794.

[261] Heim, D.; Écija, D.; Seufert, K.; Auwärter, W.; Aurisicchio, C.; Fabbro, C.; Bonifazi, D.; Barth, J. V. Self-Assembly of Flexible One-Dimensional Coordination Polymers on Metal Surfaces. *J. Am. Chem. Soc.* **2010**, *132* (19), 6783–6790.

[262] Tanaka, T.; Osuka, A. Conjugated Porphyrin Arrays: Synthesis, Properties and Applications for Functional Materials. *Chem. Soc. Rev.* **2015**, *44* (4), 943–969.

[263] Saywell, A.; Browning, A. S.; Rahe, P.; Anderson, H. L.; Beton, P. H. Organisation and Ordering of 1D Porphyrin Polymers Synthesised by On-Surface Glaser Coupling. *Chem. Commun.* **2016**, *52* (68), 10342–10345.

[264] Zheng, J. J.; Li, Q. Z.; Dang, J. S.; Wang, W. W.; Zhao, X. Magnetic and Electronic Properties of Porphyrin-Based Molecular Nanowires. *AIP Adv.* **2016**, *6* (1), 015216.

[265] Rubio-Verdú, C.; Sarasola, A.; Choi, D. J.; Majzik, Z.; Ebeling, R.; Calvo, M. R.; Ugeda, M. M.; Garcia-Lekue, A.; Sánchez-Portal, D.; Pascual, J. I. Orbital-Selective Spin Excitation of a Magnetic Porphyrin. *Commun. Phys.* **2018**, *1* (1), 1–7.

[266] Grill, L.; Hecht, S. Covalent On-Surface Polymerization. *Nat. Chem.*, **2020**, *12*, 115–130.

[267] Cirera, B.; De La Torre, B.; Moreno, D.; Ondráček, M.; Zbořil, R.; Miranda, R.; Jelínek, P.; Écija, D. On-Surface Synthesis of Gold Porphyrin Derivatives via a Cascade of Chemical Interactions: Planarization, Self-Metalation, and Intermolecular Coupling. *Chem. Mater.* **2019**, *31* (9), 3248–3256.

[268] Oszajca, M.; Franke, A.; Brindell, M.; Stochel, G.; van Eldik, R. Redox Cycling in

the Activation of Peroxides by Iron Porphyrin and Manganese Complexes. "Catching" Catalytic Active Intermediates. *Coord. Chem. Rev.* **2016**, *306*, 483–509.

[269] Nakagaki, S.; Ferreira, G. K. B.; Ucoski, G. M.; De Freitas Castro, K. A. D. Chemical Reactions Catalyzed by Metalloporphyrin-Based Metal-Organic Frameworks. *Molecules* **2013**, *18* (6), 7279–7308.

[270] Urbani, M.; Grätzel, M.; Nazeeruddin, M. K.; Torres, T. Meso-Substituted Porphyrins for Dye-Sensitized Solar Cells. *Chem. Rev.* **2014**, *114* (24), 12330–12396.

[271] Wong, W. K.; Zhu, X.; Wong, W. Y. Synthesis, Structure, Reactivity and Photoluminescence of Lanthanide(III) Monoporphyrinate Complexes. *Coord. Chem. Rev.* **2007**, *251* (17–20), 2386–2399.

[272] Bulach, V.; Sguerra, F.; Hosseini, M. W. Porphyrin Lanthanide Complexes for NIR Emission. *Coord. Chem. Rev.* **2012**, *256* (15–16), 1468–1478.

[273] Ladomenou, K.; Natali, M.; Iengo, E.; Charalampidis, G.; Scandola, F.; Coutsolelos, A. G. Photochemical Hydrogen Generation with Porphyrin-Based Systems. *Coord. Chem. Rev.* **2015**, *304–305*, 38–54.

[274] Maaza, M.; Mongwaketsi, N.; Genene, M.; Hailu, G.; Garab, G.; Sahraoui, B.; Hamidi, D. Nonlinear Photonics Properties of Porphyrins Nanocomposites and Self-Assembled Porphyrins. *J. Porphyr. Phthalocyanines* **2012**, *16* (7–8), 985–995.

[275] Takahashi, M.; Tamura, M.; Nozawa, K.; Shiomi, D.; Ishikawa, M.; Kinoshita, M. Discovery of a Quasi-1D Organic Ferromagnet, p-NPNN. *Phys. Rev. Lett.* **1991**, *67* (6), 746-748.

[276] Allemand, P.-M.; Khemani, K. C.; Koch, A.; Wudl, F.; Holczer, K.; Donovan, S.; Gruner, G.; Thompson, J. D. Organic Molecular Soft Ferromagnetism in a Fullerene C60. *Science.* **1991**, *253* (5017), 301–303.

[277] Lieb, E. H. Two Theorems on the Hubbard Model. *Phys. Rev. Lett.* **1989**, *62* (10), 1201–1204.

[278] Blundell, S.; Thoulles, D. Magnetism in Condensed Matter. *Am. J. Phys.* **2003**, *71*, 94.

[279] alacios, J. J.; Fernandez-Rossier, J.; Brey, L. Vacancy Induced Magnetism in Graphene and Graphene Ribbons. *Phys. Rev. B* **2008**, *77* (19), 195428.

[280] Ugeda, M. M.; Brihuega, I.; Guinea, F.; Gómez-Rodríguez, J. M. Missing Atom as a Source of Carbon Magnetism. *Phys. Rev. Lett.* **2010**, *104* (9), 096804.

[281] González-Herrero, H.; Gómez-Rodríguez, J. M.; Mallet, P.; Moaied, M.; Palacios, J. J.; Salgado, C.; Ugeda, M. M.; Veuillen, J.Y.; Yndurain, F.; Brihuega I. Atomic-Scale Control of Graphene Magnetism by Using Hydrogen Atoms. *Science* **2016**, *35*(6284), 437-441.

[282] Susi, T.; Meyer, J. C.; Kotakoski, J. Manipulating Low-Dimensional Materials down to the Level of Single Atoms with Electron Irradiation. *Ultramicroscopy* **2017**, *180*, 163–172.

[283] Enoki, T.; Kobayashi, Y.; Fukui, K. I. Electronic Structures of Graphene Edges and Nanographene. *Int. Rev. Phys. Chem.* **2007**, *26* (4), 609–645.

[284] Son, Y. W.; Cohen, M. L.; Louie, S. G. Energy Gaps in Graphene Nanoribbons. *Phys. Rev. Lett.* **2006**, *97* (21), 216803.

[285] Tucek, J.; Błonski, P.; Malina, O.; Pumera, M.; Chua, C. K.; Otyepka, O.; Zboril, R.. Morphology-Dependent Magnetism in Nanographene- Beyond Nanoribbons. *Adv. Funct. Mater.* **2018**, *28*(22), 1800592.

[286] Ganguly, S.; Kabir, M.; Saha-Dasgupta, T. Magnetic and Electronic Crossovers in Graphene Nanoflakes. *Phys. Rev. B* **2017**, *95* (17), 174419.

[287] Dutta, S.; Wakabayashi, K. Magnetization Due to Localized States on Graphene Grain Boundary. *Sci. Rep.* **2015**, *5*, 11744.

[288] Ruffieux, P.; Wang, S.; Yang, B.; Sanchez-Sanchez, C.; Liu, J.; Dienel, T.; Talirz, L.; Shinde, P.; Pignedoli, C. A.; Passerone, D.; Dumslaff, T.; Feng, X.; Müllen, K.; Fasel, R. On-Surface Synthesis of Graphene Nanoribbons with Zigzag Edge Topology. *Nature* **2016**, *531* (7595), 489–492.

[289] Santos, E. J. G.; Ayuela, A.; Sánchez-Portal, D. Universal Magnetic Properties of Sp 3-Type Defects in Covalently Functionalized Graphene. *New J. Phys.* **2012**, *14*, 043022.

[290] Berashevich, J.; Chakraborty, T. Sustained Ferromagnetism Induced by H-Vacancies in Graphane. *Nanotechnology* **2010**, *21*(35), 355201.

[291] Zhou, J.; Wang, Q.; Sun, Q.; Chen, X. S.; Kawazoe, Y.; Jena, P. Ferromagnetism in Semihydrogenated Graphene Sheet. *Nano Lett.* **2009**, *9* (11), 3867–3870.

[292] Kashtiban, R. J.; Dyson, M. A.; Nair, R. R.; Zan, R.; Wong, S. L.; Ramasse, Q.; Geim, A. K.; Bangert, U.; Sloan, J. Atomically Resolved Imaging of Highly Ordered Alternating Fluorinated Graphene. *Nat. Commun.* **2014**, *5*, 4902.

[293] Mazurenko, V. V; Rudenko, A. N.; Nikolaev, S. A.; Medvedeva, D. S.; Lichtenstein, A. I.; Katsnelson, M. I. Role of Direct Exchange and Dzyaloshinskii-Moriya Interactions in Magnetic Properties of Graphene Derivatives: C2F and C2H. *Phys. Rev. B* **2016**, *94* (21), 214411.

[294] Wang, X.; Li, X.; Zhang, L.; Yoon, Y.; Weber, P. K.; Wang, H.; Guo, J.; Dai, H. N-Doping of Graphene through Electrothermal Reactions with Ammonia. *Science* **2009**, *324* (5928), 768–771.

[295] Zhou, S. Y.; Siegel, D. A.; Fedorov, A. V.; Lanzara, A. Metal to Insulator Transition in Epitaxial Graphene Induced by Molecular Doping. *Phys. Rev. Lett.* **2008**, *101* (8), 086402.

[296] Miao, Q.; Wang, L.; Liu, Z.; Wei, B.; Xu, F.; Fei, W. Magnetic Properties of N-Doped Graphene with High Curie Temperature. *Sci. Rep.* **2016**, *6*, 21832.

[297] Haldar, S.; Pujari, B. S.; Bhandary, S.; Bhandary, S.; Cossu, F.; Eriksson, O.; Kanger, D. G.; Sanyal, B. Fe_n (n = 1–6) Clusters Chemisorbed on Vacancy Defects in Graphene: Stability, Spin-dipole moment, and Magnetic Anisotropy. *Phys. Rev. B* **2014**, *89*, 20541.

[298] Durajski, A. P.; Auguscik, A. E.; Szczȩśniak, R. Tunable Electronic and Magnetic Properties of Substitutionally Doped Graphene. *Phys. E Low-Dimensional Syst. Nanostructures* **2020**, *119*, 113985.

[299] Zarshenas, M.; Gervilla, V.; Sangiovanni, D. G.; Sarakinos, K. Room-Temperature Diffusion of Metal Clusters on Graphene. *Phys. Chem. Chem. Phys.* **2021**, *23*(23), 13087–13094.

[300] Habenicht, B. F.; Teng, D.; Semidey-Flecha, L.; Sholl, D. S.; Xu, Y. Adsorption and Diffusion of 4d and 5d Transition Metal Adatoms on Graphene/Ru(0001) and the Implications for Cluster Nucleation. *Top. Catal.* **2014**, *57* (1–4), 69–79.

[301] Willke, P.; Amani, J. A.; Sinterhauf, A.; Thakur, S.; Kotzott, T.; Druga, T.; Weikert, S.; Maiti, K.; Hofsäss, H.; Wenderoth, M. Doping of Graphene by Low-Energy Ion Beam Implantation: Structural, Electronic, and Transport Properties. *Nano Lett.* **2015**, *15* (8), 5110–5115.

[302] Susi, T.; Hardcastle, T. P.; Hofsäss, H.; Mittelberger, A.; Pennycook, T. J.; Mangler, C.; Drummond-brydson, R.; Andrew, J.; Meyer, J. C.; Kotakoski, J. Single-Atom Spectroscopy of Phosphorus Dopants Implanted into Graphene. *2D Mater.* **2017**, *4* (2), 021013.

[303] Yamamoto, D. Correlated Cluster Mean-Field Theory for Spin Systems. *Phys. Rev. B* **2009**, *79* (14), 144427.

[304] Néda, Z. Mean-Field Approach to Magnetism; Babes-Bolyai University: Cluj, **2011**, 1– 26.

[305] Pisani, L.; Montanari, B.; Harrison, N. M. A Defective Graphene Phase Predicted to Be a Room Temperature Ferromagnetic Semiconductor. *New J. Phys.* **2008**, *10*, 033002.

[306] Ramirez, S.; Chan, K.; Hernandez, R.; Recinos, E.; Hernandez, E.; Salgado, R.; Khitun, A. G.; Garay, J. E.; Balandin, A. A. Thermal and Magnetic pPoperties of Nanostructured Densified Ferrimagnetic Composites with Graphene - Graphite Fillers. *Mater. Des.* **2017**, *118*, 75-80.

[307] Dovesi, R.; Ricart, J. M.; Saunders, V. R.; Orlando, R. Superexchange Interaction in K2NiF 4 : An Ab Initio Hartree-Fock Study. *J. Phys. Condens. Matter* **1995**, *7* (41), 7997–8007.

[308] Ricart, J. M.; Dovesi, R.; Roetti, C.; Saunders, V. R. Electronic and Magnetic Structure of KNiF3 Perovskite. *Phys. Rev. B* **1995**, *52* (4), 2381–2389.

[309] Moreira, D. P. R.; Illas, F. Ab Initio Theoretical Comparative Study of Magnetic Coupling in KNiF3 and K2NiF4. *Phys. Rev. B* **1997**, *55* (7), 4129–4137.

[310] Hu, R.; Zhang, Z. H.; Fan, Z. Q. BN Nanoflake Quantum-Dot Arrays: Structural Stability, and Electronic and Half-Metallic Properties. *Phys. Chem. Chem. Phys.* **2017**, *19* (30), 20137–20146.

[311] Shahjahan, M.; Razzakul, I. M.; Rahman, M. M. First-Principles Calculation of Stable Magnetic State and Curie Temperature in Transition Metal Doped III-V Semiconductors. *Comput. Condens. Matter* **2016**, *9*, 67–71.

[312] Balcerzak, T.; Szałowski, K.; Jaščur, M.; Žukovič, M.; Bobák, A.; Borovský, M. Thermodynamic Description of the Ising Antiferromagnet on a Triangular Lattice with Selective Dilution by a Modified Pair-Approximation Method. *Phys. Rev. E - Stat. Nonlinear, Soft Matter Phys.* **2014**, *89* (6), 062140.

[313] Tuček, J.; Holá, K.; Zoppellaro, G.; Błoński, P.; Langer, R.; Medved, M.; Susi, T.; Otyepka, M.; Zbořil, R. Zigzag Sp2 Carbon Chains Passing through an Sp3 Framework: A Driving Force toward Room-Temperature Ferromagnetic Graphene. *ACS Nano* **2018**, *12* (12), 12847–12859.

[314] Clusel, M.; Fortin, J. Grassmann Techniques Applied to Classical Spin Systems. *Condens. Matter. Phys.* **2009**, *12* (3), 463–478.

[315] Dresselhaus, G. Higher Order Corrections to the Molecular-Field Theory of the Magnetic State *Phys. Rev.* **1965**, *139* (71), A855.

[316] Bethe, H. A. Statistical Theory of Superlattices. **1997**, *145*, 245–270.

[317] Oguchi, T. A Theory of Antiferromagnetism, II. *Prog. Theor. Phys.* **1955**, *13* (2), 148–159.

[318] Domb, C.; Green, M. S.: Editors. Phase Transitions and Critical Phenomena. Academic Press: London and New York, **1974**. *3*, 3-4.

[319] Hartree, D. R. The Wave Mechanics of an Atom with a Non-Coulomb Central Field. *Mathematical Proceedings of the Cambridge Philosophical Society*. **1927**, 89–110.

[320] Hylleraas, E. A. Über Den Grundzustand Des Heliumatoms. *Zeitschrift für Phys.* **1928**, *48* (7–8), 469–494.

[321] Møller, P. Note on an Approximation Treatment for Many-Electron Systems. *Eur. J.*

Cardio-thoracic Surg. **1934**, *53* (6), 1237–1243.

[322] Cizek, J. On the Correlation Problem in Atomic and Molecular Systems. Calculation of Wavefunction Components in Ursell-Type Expansion Using Quantum-Field Theoretical Methods. *J. Chem. Phys.* **1966**, *45* (11), 4256–4266.

[323] Hinze, J.; Clemens, C.; Roothaan, J. Multi-Configuration Self-Consistent-Field Theory. *Prog. Theor. Phys.* **1967**, *40*, 37-51.

[324] Hohenberg, P.; Kohn, W. Inhomogeneous Electron Gas. *Phys. Rev.* **1964**, *136*(3B), B864.

[325] W., K.; Sham, L. J. Self-Consistent Equations Including Exchange and Correlation Effects. *Phys. Rev.* **1965**, *140* (4A), A1133.

[326] Perdew, J. P.; Schmidt, K. Jacob's Ladder of Density Functional Approximations for the Exchange-Correlation Energy. *AIP Conf. Proc.* **2001**, *577*, 1.

[327] Yin, M. T.; Cohen, M. L. Microscopic Theory of the Phase Transformation and Lattice Dynamics of Si. *Neuroscience* **1980**, *45* (1), 1004.

[328] Hafner, J.; Wolverton, C.; Ceder, G. Toward Computational Materials Design: The Impact of Density Functional Theory on Materials Research. *MRS Bull.* **2006**, *31* (9), 659–665.

[329] Szabo, A.; Ostlund, N. L. Modern Quantum Chemistry: Introduction to Advanced Electronic Structure Theory. *Dover Publications, Inc.,* **1996**.

[330] Dubecký, M. Quantum Monte Carlo for Noncovalent Interactions: A Tutorial Review. *Acta Phys. Slovaca* **2014**, *64* (5), 501–574.

[331] Thomas, L. H. The Calculation of Atomic Fields. *Mathematical Proceedings of the Cambridge Philosophical Society* **1927**, *23* (5), 542 - 548.

[332] Fermi, E. Un Metodo Statistico per La Determinazione Di Alcune Prioprietà Dell'Atomo. *Accademia Nazionale dei Lincei.* **1927**, *474*, 602–607.

[333] Slater, J. C. Quantum Theory of Molecules and Solids. *J. Mol. Struct.* **1975**, *24*(2), 447.

[334] Ceperley, D. M.; Alder, B. J. Ground State of the Electron Gas by a Stochastic Method. *Phys. Rev. Lett.* **1980**, *45* (7), 566–569.

[335] Vosko, S. H.; Wilk, L.; Nusair, M. Accurate Spin-Dependent Electron Liquid Correlation Energies for Local Spin Density Calculations: A Critical Analysis. *Can. J. Phys.* **1980**, *58* (8), 1200–1211.

[336] Parr, R. G. Density Functional Theory of Atoms and Molecules. *Horizons of Quantum Chemistry*. **1980**, 5–15.

[337] Von Barth, U.; Hedin, L. A Local Exchange-Correlation Potential for the Spin Polarized Case. I. *J. Phys. C Solid State Phys.* **1972**, *5* (13), 1629–1642.

[338] Becke, A. D. Density-Functional Exchange-Energy Approximation with Correct Asymptotic Behavior. *Phys. Rev. A* **1988**, *38* (6), 3098.

[339] Lee, C.; Yang. W.; Parr, R. G. Development of the Colle-Salvetti Correlation-Energy Formula into a Functional of the Electron Density. *Phys. Rev. B* **1988**, *37* (2), 785.

[340] Perdew, J. P.; Burke, K.; Ernzerhof, M. Generalized Gradient Approximation Made Simple. *Phys. Rev. Lett.* **1996**, *77* (18), 3865–3868.

[341] Perdew, J. P.; Chevary, J. A.; Vosko, S. H.; Jackson, K. A.; Pederson, M. R.; Singh, D. J.; Fiolhais, C. Erratum: Atoms, Molecules, Solids, and Surfaces: Applications of the Generalized Gradient Approximation for Exchange and Correlation. *Phys. Rev. B* **1993**, *48* (7), 4978.

[342] Perdew, J. P.; Wang, Y. Accurate and Simple Analytic Representation of the Electron-Gas Correlation Energy. *Phys. Rev. B* **1992**, *45* (23), 244–249.

[343] Hammer, B.; Hansen, L. B.; Nørskov, J. K. Improved Adsorption Energetics within Density-Functional Theory Using Revised Perdew-Burke-Ernzerhof Functionals. *Phys. Rev. B - Condens. Matter Mater. Phys.* **1999**, *59* (11), 7413–7421.

[344] Armiento, R.; Mattsson, A. E. Functional Designed to Include Surface Effects in Self-Consistent Density Functional Theory. *Phys. Rev. B - Condens. Matter Mater. Phys.* **2005**, *72* (8), 085108.

[345] Perdew, J. P.; Ruzsinszky, A.; Csonka, G. I.; Vydrov, O. A.; Scuseria, G. E.;

Constantin, L. A.; Zhou, X.; Burke, K. Restoring the Density-Gradient Expansion for Exchange in Solids and Surfaces. *Phys. Rev. Lett.* **2008**, *100* (13), 136406.

[346] Hafner. Ab-Initio Simulations of Materials Using VASP: Density-Functional Theory and Beyond. *J. Comput. Chem.* **2012**, *32*, 174–182.

[347] van de Walle, A.; Ceder, G. Correcting Overbinding in Local-Density-Approximation Calculations. *Phys. Rev. B - Condens. Matter Mater. Phys.* **1999**, *59* (23), 14992–15001.

[348] Becke, A. D. Density-Functional Thermochemistry. IV. A New Dynamical Correlation Functional and Implications for Exact-Exchange Mixing. *J. Chem. Phys.* **1996**, *104* (3), 1040–1046.

[349] Tao, J.; Perdew, J. P.; Staroverov, V. N.; Scuseria, G. E. Climbing the Density Functional Ladder: Nonempirical Meta–Generalized Gradient Approximation Designed for Molecules and Solids. *Phys. Rev. Lett.* **2003**, *91* (14), 146401.

[350] Staroverov, V. N.; Scuseria, G. E.; Tao, J.; Perdew, J. P. Tests of a Ladder of Density Functionals for Bulk Solids and Surfaces. *Phys. Rev. B - Condens. Matter Mater. Phys.* **2004**, *69* (7), 075102.

[351] Sun, J.; Ruzsinszky, A.; Perdew, J. P. Strongly Constrained and Appropriately Normed Semilocal Density Functional. *Phys. Rev. Lett.* **2015**, 115(3), 036402.

[352] Sun, J.; Remsing, R. C.; Zhang, Y.; Sun, Z.; Ruzsinszky, A.; Peng, H.; Yang, Z.; Paul, A.; Waghmare, U.; Wu, X.; Klein, M. L.; Perdew, J. P. SCAN: An Efficient Density Functional Yielding Accurate Structures and Energies of Diversely-Bonded Materials. **2015**, 1–19, arXiv:1511.01089.

[353] Perdew, J. P.; Ernzerhof, M.; Burke, K.; Perdew, J. P.; Ernzerhof, M.; Burke, K. Rationale for Mixing Exact Exchange with Density Functional Approximations. *J. Chem. Phys.* **1996**, *105*, 9982.

[354] Adamo, C.; Barone, V. Toward Reliable Density Functional Methods without Adjustable Parameters: The PBE0 Model. *J. Chem. Phys.* **1999**, *110* (13), 6158–6170.

[355] Heyd, J.; Scuseria, G. E.; Ernzerhof, M. Hybrid Functionals Based on a Screened

Coulomb Potential. *J. Chem. Phys.* **2003**, *118* (18), 8207–8215.

[356] Pela, R. R.; Marques, M.; Teles, L. K. Comparing LDA-1/2, HSE03, HSE06 and G0W0 Approaches for Band Gap Calculations of Alloys. *J. Phys. Condens. Matter* **2015**, *27* (50), 505502.

[357] Himmetoglu, B.; Floris, A.; De Gironcoli, S.; Cococcioni, M. Hubbard-Corrected DFT Energy Functionals: The LDA+U Description of Correlated Systems. *Int. J. Quantum Chem.* **2014**, *114* (1), 14–49.

[358] Hubbard, J.; A, P. R. S. L. Electron Correlations in Narrow Energy Bands. *Proc. R. Soc. London. Ser. A. Math. Phys. Sci.* **1963**, *276* (1365), 238–257.

[359] Nemenman, I. Many-Body Quantum Theory in Condensed Matter Physics—An Introduction. *Phys. Biol.* **2012**, *9* (2), 026003.

[360] Tolba, S.; Gameel, K.; Ali, A.; Almossalami, H.; Nageh, K. The DFT+U: Approaches, Accuracy, and Applications. *IntechOpen,* **2017**.

[361] Almbladh, C. O.; Von Barth, U. Exact Results for the Charge and Spin Densities, Exchange-Correlation Potentials, and Density-Functional Eigenvalues. *Phys. Rev. B* **1985**, *31* (6), 3231–3244.

[362] Tsuneda, T.; Hirao, K. Long-Range Correction for Density Functional Theory. *Wiley Interdiscip. Rev. Comput. Mol. Sci.* **2014**, *4* (4), 375–390.

[363] Sekino, H.; Maeda, Y.; Kamiya, M.; Hirao, K. Polarizability and Second Hyperpolarizability Evaluation of Long Molecules by the Density Functional Theory with Long-Range Correction. *J. Chem. Phys.* **2007**, *126* (1), 014107.

[364] Chai, J. Da; Head-Gordon, M. Long-Range Corrected Hybrid Density Functionals with Damped Atom-Atom Dispersion Corrections. *Phys. Chem. Chem. Phys.* **2008**, *10* (44), 6615–6620.

[365] Almora-Barrios, N.; Carchini, G.; Błoński, P.; López, N. Costless Derivation of Dispersion Coefficients for Metal Surfaces. *J. Chem. Theory Comput.* **2014**, *10* (11), 5002–5009.

[366] Zarenba, E.; Kohn, W. Van Der Waals Interaction between an Atom and a Solid

Surface. *Phys. Rev. B* **2014**, *13* (6), 2270.

[367] Nørskov, J. K.; Bligaard, T.; Rossmeisl, J.; Christensen, C. H. Towards the Computational Design of Solid Catalysts. *Nat. Chem.* **2009**, *1* (1), 37–46.

[368] Grimme, S. Semiempirical GGA-Type Density Functional Constructed with a Long-Range Dispersion Correction. *J. Comput. Chem.* **2006**, *27* (15), 1787-1799.

[369] London, F. The General Theory of Molecular Forces. *Trans. Fara. Soc.* **1936**, *8* (8), 8–26.

[370] Gould, T.; Bučko, T. C6 Coefficients and Dipole Polarizabilities for All Atoms and Many Ions in Rows 1-6 of the Periodic Table. *J. Chem. Theory Comput.* **2016**, *12* (8), 3603–3613.

[371] Tysoe, W. T.; Ormerod, R. M.; Lambert, R. M.; Zgrablich, G.; Ramirez-Cuesta, A. Overlayer Structure and Kinetic Behavior of Benzene on Palladium(111). *J. Phys. Chem.* **1993**, *97* (13), 3365–3370.

[372] Grimme, S.; Antony, J.; Ehrlich, S.; Krieg, H.; A Consistent and Accurate Ab Initio Parametrization of Density Functional Dispersion Correction (DFT-D) for the 94 Elements H-Pu *J. Chem. Phys*. **2010**, *132*, 154104.

[373] Tonigold, K.; Gross, A. Dispersive Interactions in Water Bilayers at Metallic Surfaces: A Comparison of the PBE and RPBE Functional Including Semiempirical Dispersion Corrections. *J. Comput. Chem.* **2012**, *33* (6), 695–701.

[374] Tkatchenko, A.; Scheffler, M. Accurate Molecular van Der Waals Interactions from Ground-State Electron Density and Free-Atom Reference Data. *Phys. Rev. Lett.* **2009**, *102* (7), 073005.

[375] Ruiz, V. G.; Liu, W.; Zojer, E.; Scheffler, M.; Tkatchenko, A. Density-Functional Theory with Screened van Der Waals Interactions for the Modeling of Hybrid Inorganic-Organic Systems. *Phys. Rev. Lett.* **2012**, *108* (14), 146103.

[376] Lifshitz, E. M.; Hamermesh, M. The Theory of Molecular Attractive Forces between Solids. *Sov. Phys.* **1956**, *2* (1), 73-83.

[377] Dion, M.; Rydberg, H.; Schröder, E.; Langreth, D. C.; Lundqvist, B. I. Van Der

Waals Density Functional for General Geometries. *Phys. Rev. Lett.* **2004**, *92* (24), 22–25.

[378] Andersson, Y.; Andersson, D. C.; Lundqvist, B. I. Van Der Waals Interactions in Density-Functional Theory. *Phys. Rev. Lett.* **1996**, *76* (1), 102–105.

[379] Hamada, I.; Otani, M. Comparative van Der Waals Density-Functional Study of Graphene on Metal Surfaces. *Phys. Rev. B - Condens. Matter Mater. Phys.* **2010**, *82* (15), 153412.

[380] Langreth, D. C.; Lundqvist, B. I.; Chakarova-Käck, S. D.; Cooper, V. R.; Dion, M.; Hyldgaard, P.; Kelkkanen, A.; Kleis, J.; Kong, L.; Li, S.; Moses, P. G.; Murray, E.; Puzder, A.; Rydberg, H.; Schröder, E.; Thonhauser, T. A Density Functional for Sparse Matter. *J. Phys. Condens. Matter* **2009**, *21* (8), 084203.

[381] Lee, K.; Murray, É. D.; Kong, L.; Lundqvist, B. I.; Langreth, D. C. Higher-Accuracy van Der Waals Density Functional. *Phys. Rev. B - Condens. Matter Mater. Phys.* **2010**, *82* (8), 081101.

[382] Nozières, P.; Pines, D. Correlation Energy of a Free Electron Gas. *Phys. Rev.* **1958**, *111* (2), 442–454.

[383] Dobson, J. F.; Dinte, B. P. Constraint Satisfaction in Local and Gradient Susceptibility Approximations: Application to a van Der Waals Density Functional. *Phys. Rev. Lett.* **1996**, *76* (11), 1780–1783.

[384] Furche, F.; Van Voorhis, T. Fluctuation-Dissipation Theorem Density-Functional Theory. *J. Chem. Phys.* **2005**, *122* (16), 164106.

[385] Pykal, M.; Jurečka, P.; Karlický, F.; Otyepka, M. Modelling of Graphene Functionalization. *Phys. Chem. Chem. Phys.* **2016**, *18* (9), 6351-6372.

[386] Kresse, G.; Hafner, J. Ab Initio Molecular Dynamics for Liquid Metals. *Phys. Rev. B* **1993**, *47* (1), 558–561.

[387] Kresse, G.; Furthmuller, J. Efficient Iterative Schemes for Ab Initio Total-Energy Calculations Using a Plane-wave Basis Set. *Phys. Rev. B* **1996**, *54*, 11169.

[388] Kresse, G.; Furthmuller, J. Efficiency of Ab-initio Total Energy Calculations for

Metals and Semiconductors Using a Plane-Wave Basis Set. *Comput. Mater. Sci.* **1996**, *54* (16), 15-50.

[389] Kittel, C.; Hellwarth, R. W. Introduction to Solid State Physics. *Phys. Today* **1957**, *6*, 43.

[390] Bloch, F. Über Die Quantenmechanik Der Elektronen in Kristallgittern. *Zeitschrift für Phys.* **1929**, *52* (7–8), 555–600.

[391] Gross, A. Theoretical Surface Science. *Springer*, **2009**.

[392] Sholl, D. S.; Steckel, J. A. Density Functional Theory: A Practical Introduction. *Wiley*, **2009**.

[393] Blochl, P. E. Projector Augmented-Wave Method. *Phys. Rev. B Condens. Matter* **1994**, *50* (24), 17953–17979.

[394] Kresse, G. VASP Manual.

[395] Kleinman, L. Relativistic Norm-Conserving Pseudopotential. *Phys. Rev. B* **1980**, *21* (6), 2630–2631.

[396] MacDonald, A. H.; Picket, W. E.; Koelling, D. D. A Linearised Relativistic Augmented-Plane-Wave Method Utilising Approximate Pure Spin Basis Functions. *J. Phys. C Solid State Phys.* **1980**, *13* (14), 2675–2683.

[397] Hobbs, D.; Kresse, G.; Hafner, J. Fully Unconstrained Noncollinear Magnetism within the Projector Augmented-Wave Method. *Phys. Rev. B* **2000**, *62* (17), 11556–11570.

[398] Marsman, M.; Hafner, J. Broken Symmetries in the Crystalline and Magnetic Structures of γ-Iron. *Phys. Rev. B - Condens. Matter Mater. Phys.* **2002**, *66* (22), 224409.

[399] Copeland, C.; Menon, O.; Majumdar, D.; Roszak, S.; Leszczynski, J. Gaussian, Inc., *Wallingford CT*, **2016**.

[400] Sanville, E.; Kenny, D. D.; Smith, R.; Henkelman, G. Improved Grid-Based Algorithm for Bader Charge Allocation. *J. Comput. Chem.* **2007**, *28* (5), 899-908.

[401] Yu, M.; Trinkle, D. R. Accurate and Efficient Algorithm for Bader Charge Integration, *J. Chem. Phys.* **2011** 134, 064111.

[402] Henkelman, G.; Arnaldsson, A.; Jónsson, H. A Fast and Robust Algorithm for Bader Decomposition of Charge Density. *Comput. Mater. Sci.* **2006**, *36* (3), 354–360.

[403] Glendening, E. D.; Badenhoop, J, K.; Reed, A. E.; Carpenter, J. E.; Bohmann, J. A.; Morales, C. M.; Karafiloglou, P.; Landis, C. R.; Weinhold, F. NBO, *Theoretical Chemistry Institute, University Of Wisconsin*, **2018**.

[404] Henkelman, G.; Uberuaga, B. P.; Jónsson, H. A Climbing Image Nudged Elastic Band Method for Finding Saddle Points and Minimum Energy Paths. *J. Chem. Phys.* **2000**, *113*, 9901.

[405] Henkelman, G.; Jónsson, H. Improved Tangent Estimate in the Nudged Elastic Band Method for Finding Minimum Energy Paths and Saddle Points Minimum Energy Paths and Saddle Points. *J. Chem. Phys.* **2000**, *113*, 9978.

[406] Dudarev, S. L.; Botton, G. A.; Savrasov, S. Y.; Humphreys, C. J.; Sutton, A. P. Electron-Energy-Loss Spectra and the Structural Stability of Nickel Oxide: An LSDA+U Study," *Phys. Rev. B* **1998,** *57* (3), 1505–1509.

[407] Meier, F.; Zhou, L.; Wiebe, J.; Wiesendanger, R. Revealing Magnetic Interactions from Single-Atom Magnetization Curves. *Science* **2008**, *320* (5872), 82–86.

[408] Błoński, P.; Hafner, J. Magnetic Anisotropy of Transition-Metal Dimers: Density Functional Calculations. *Phys. Rev. B - Condens. Matter Mater. Phys.* **2009**, *79* (22), 224418.

[409] Heine, V. Electronic Structure from the Point of View of the Local Atomic Environment. *Solid State Phys.* **1980**, *35*, 1-127.

[410] Rani, P.; Jindal, V. K. Designing Band Gap of Graphene by B and N Dopant Atoms. *RSC Adv.* **2013**, *3* (3), 802–812.

[411] Krstic, V.; Ewels, C. P.; Wågberg, T.; Ferreira, M. S.; Janssens, A. M.; Stephan, O.; Glerup, M. Indirect Magnetic Coupling in Light-Element-Doped Single-Walled Carbon Nanotubes. *ACS Nano* **2010**, *4* (9), 5081–5086.

[412] Ronchi, C.; Datteo, M.; Perilli, D.; Ferrighi, L.; Fazio, G.; Selli, D.; Valentin, C. Di. Magnetism of Carbon Monovacancy in Graphene by Hybrid Density Functional Calculations. *J. Phys. Chem. C* **2017**, *121* (15), 8653–8661.

[413] Donati, F.; Rusponi, S.; Stepanow, S.; Wäckerlin, C.; Singha, A.; Persichetti, L.; Baltic, R.; Diller, K.; Patthey, F.; Fernandes, E.; Dreiser, J.; Šljivančanin; Kummer, K.; Nistor, C.; Gambardella, P.; Brune, H. Magnetic Remanence in Single Atoms. *Science* **2016**, *352* (6283), 318–321.

[414] Tripathi, M.; Mittelberger, A.; Pike, N. A.; Mangler, C.; Meyer, J. C.; Verstraete, M. J.; Kotakoski, J.; Susi, T. Electron-Beam Manipulation of Silicon Dopants in Graphene. *Nano Lett.* **2018**, *18* (8), 5319–5323.

[415] Tripathi, M.; Markevich, A.; Böttger, R.; Facsko, S.; Besley, E.; Kotakoski, J.; Susi, T. Implanting Germanium into Graphene. *ACS Nano* **2018**, *12* (5), 4641–4647.

[416] Daalderop, G. H. O.; Kelly, P. J.; Schuurmans, M. F. H. Magnetic Anisotropy of a Free-Standing Co Monolayer and of Multilayers Which Contain Co Monolayers. *Phys. Rev. B* **1994**, *50* (14), 9989–10003.

[417] Whangbo, M. H.; Gordon, E. E.; Xiang, H.; Koo, H. J.; Lee, C. Prediction of Spin Orientations in Terms of HOMO-LUMO Interactions Using Spin-Orbit Coupling as Perturbation. *Acc. Chem. Res.* **2015**, *48* (12), 3080–3087.

[418] Wu, M.; Cao, C.; Jiang, J. Z. Electronic Structure of Substitutionally Mn-Doped Graphene. *New J. Phys.* **2010**, *12*, 063020.

[419] Dyck, O.; Yoon, M.; Zhang, L.; Lupini, A. R.; Swett, J. L.; Jesse, S. Doping of Cr in Graphene Using Electron Beam Manipulation for Functional Defect Engineering. *ACS Appl. Nano Mater.* **2020**, *3* (11), 10855–10863.

[420] Hermenau, J.; Brinker, S.; Marciani, M.; Steinbrecher, M.; dos Santos Dias, M.; Wiesendanger, R.; Lounis, S.; Wiebe, J. Stabilizing Spin Systems via Symmetrically Tailored RKKY Interactions. *Nat. Commun.* **2019**, *10* (1), 2565.

[421] Thakur, J.; Kashyap, M. K.; Taya, A.; Rani, P.; Saini, H. S. Sublattice Dependent Magnetic Response of Dual Cr Doped Graphene Monolayer: A Full Potential Approach. *Indian J. Phys.* **2017**, *91* (1), 43–51.

[422] Błoński, P.; Hafner, J. Magnetic Anisotropy of Heteronuclear Dimers in the Gas Phase and Supported on Graphene: Relativistic Density-Functional Calculations. *J. Phys. Condens. Matter* **2014**, *26* (14), 146002.

[423] Strandberg, T. O.; Canali, C. M.; MacDonald, A. H. Transition-Metal Dimers and Physical Limits on Magnetic Anisotropy. *Nat. Mater.* **2007**, *6* (9), 648–651.

[424] Chen, Z.; Vorobyeva, E.; Mitchell, S.; Fako, E.; Ortuño, M. A.; López, N.; Collins, S. M.; Midgley, P. A.; Richard, S.; Vilé, G.; Pérez-ramírez, J. A Heterogeneous Single-Atom Palladium Catalyst Surpassing Homogeneous Systems for Suzuki Coupling. *Nat. Nanotechnol.* **2018**, *13*, 702-707.

[425] Wei, S.; Li, A.; Liu, J. C.; Li, Z.; Chen, W.; Gong, Y.; Zhang, Q.; Cheong, W. C.; Wang, Y.; Zheng, L.; Xiao, H.; Chen, C.; Wang, D.; Peng, Q.; Gu, L.; Han, X.; Li, J.; Li, Y. Direct Observation of Noble Metal Nanoparticles Transforming to Thermally Stable Single Atoms. *Nat. Nanotechnol.* **2018**, *13* (9), 856–861.

[426] Pašti, I. A.; Jovanović, A.; Dobrota, A. S.; Slavko, V.; Mentus, S. V.; Johansson, B.; Skorodumova, N. V. Atomic Adsorption on Pristine Graphene along the Periodic Table of Elements – From PBE to Non-Local Functionals. *Appl. Surf. Sci.* **2018**, *436*, 433-440.

[427] Pašti, I. A.; Jovanović, A.; Dobrota, A. S.; Mentus, S. V.; Johansson, B.; Skorodumova, N. V. Atomic Adsorption on Graphene with a Single Vacancy: Systematic DFT Study through the Periodic Table of Elements. *Phys. Chem. Chem. Phys.* **2018**, *20* (2), 858–865.

[428] Li, Y.; Gao, W.; Ci, L.; Wang, C. Catalytic Performance of Pt Nanoparticles on Reduced Graphene Oxide for Methanol Electro-Oxidation. *Carbon N. Y.* **2009**, *48* (4), 1124–1130.

[429] Liu, Z.; Duan, X.; Cheng, H.; Zhou, J.; Zhou, X. Synthesis of Platinum / Graphene Composites by a Polyol Method : The Role of Graphite Oxide Precursor Surface Chemistry. *Carbon N. Y.* **2015**, *89*, 93–101.

[430] Armand, M.; Grugeon, S.; Vezin, H.; Laruelle, S.; Ribière, P.; Poizot, P.; Tarascon, J. M. Conjugated Dicarboxylate Anodes for Li-Ion Batteries. *Nat. Mater.* **2009**, *8* (2), 120–125.

[431] Jiao, L. S.; Wu, T.; Li, H. Y.; Li, F.; Niu, L. High Quality Graphitized Graphene as an Anode Material for Lithium Ion Batteries. *Chem. Commun.* **2015**, *51* (88), 15979–15981.

[432] Choi, J. W.; Aurbach, D. Promise and Reality of Post-Lithium-Ion Batteries with High Energy Densities. *Nat. Rev. Mater.* **2016**, *1*, 16013.

[433] Albertus, P.; Babinec, S.; Litzelman, S.; Newman, A. Status and Challenges in Enabling the Lithium Metal Electrode for High-Energy and Low-Cost Rechargeable Batteries. *Nat. Energy* **2018**, *3* (1), 16–21.

[434] Robertson, J. Diamond-like Amorphous Carbon. *Mater. Sci. Eng. R Reports* **2002**, *37* (4–6), 129–281.

[435] Pischedda, V.; Radescu, S.; Dubois, M.; Batisse, N.; Balima, F.; Cavallari, C.; Cardenas, L. Experimental and DFT High Pressure Study of Fluorinated Graphite (C2F)N. *Carbon N. Y.* **2017**, *114*, 690–699.

[436] Touhara, H.; Kadono, K.; Fujii, Y.; Watanabe, N. On the Structure of Graphite Fluoride. *ZAAC - J. Inorg. Gen. Chem.* **1987**, *544* (1), 7–20.

[437] Mazur, A. S.; Vovk, M. A.; Tolstoy, P. M. Solid-State 13C NMR of Carbon Nanostructures (Milled Graphite, Graphene, Carbon Nanotubes, Nanodiamonds, Fullerenes) in 2000–2019: A Mini-Review. *Fullerenes Nanotub. Carbon Nanostructures* **2020**, *28* (3), 202–213.

[438] Bourassa, P. N. Book Reviews: Course Notes on the Interpretation of Infrared and Raman Spectra. *Applied Spectroscopy*. **2004**, 323A-323A.

[439] Wu, X.; Zhao, H.; Pei, J.; Yan, D. Joining of Graphene Flakes by Low Energy N Ion Beam Irradiation. *Appl. Phys. Lett.* **2017**, *110* (13), 133102.

[440] Li, Z.; Gadipelli, S.; Li, H.; Howard, C. A.; Brett, D. J. L.; Shearing, P. R.; Guo, Z.; Parkin, I. P.; Li, F. Tuning the Interlayer Spacing of Graphene Laminate Films for Efficient Pore Utilization towards Compact Capacitive Energy Storage. *Nat. Energy* **2020**, *5* (4), 345.

Appendix

Research Article

Tailoring Electronic and Magnetic Properties of Graphene by Phosphorus Doping

Rostislav Langer, Piotr Błoński,* Christoph Hofer, Petr Lazar, Kimmo Mustonen, Jannik C. Meyer, Toma Susi,* and Michal Otyepka

Cite This: *ACS Appl. Mater. Interfaces* 2020, 12, 34074−34085

Read Online

ACCESS | Metrics & More | Article Recommendations | Supporting Information

ABSTRACT: The electronic and magnetic properties of graphene can be modulated by doping it with other elements, especially those with a different number of valence electrons. In this article, we first provide a three-dimensional reconstruction of the atomic structure of a phosphorus substitution in graphene using aberration-corrected scanning transmission electron microscopy. Turning then to theoretical calculations based on the density functional theory (DFT), we show that doping phosphorus in various bonding configurations can induce magnetism in graphene. Our simulations reveal that the electronic and magnetic properties of P-doped (Gr-P) and/or phosphono-functionalized graphene (Gr-PO$_3$H$_2$) can be controlled by both the phosphorus concentration and configurations, ultimately leading to ferromagnetic (FM) and/or antiferromagnetic (AFM) features with the transition temperature up to room temperature. We also calculate core-level binding energies of variously bonded P to facilitate X-ray photoelectron spectroscopy-based identification of its chemical form present in P-doped graphene-based structures. These results may enable the design of graphene-based organic magnets with tailored properties for future magnetic or spintronic applications.

KEYWORDS: graphene, phosphorus, doping, functionalization, magnetism
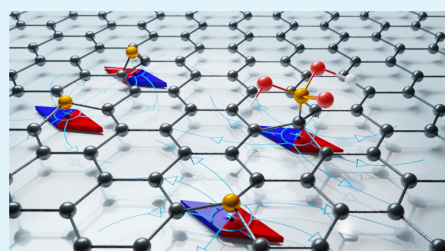
1. INTRODUCTION

Graphene[1] remains one of the most studied materials due to its extraordinary properties such as tensile strength exceeding that of steel,[2] ballistic electron conductivity,[3] huge surface area,[4] and optical transparency.[5] However, the applicability of graphene in current electronics and spintronics is limited due to its zero band gap and the absence of long-range magnetic ordering. Substitutional doping of the lattice by heteroatoms, e.g., sulfur[6] and nitrogen,[7,8] or its sp^3-functionalization,[9−11] has been identified as a viable strategy to modulate the electronic, magnetic, and spintronic properties of graphene.[12] In addition, recent advances in ion implantation and electron-beam manipulation of impurities,[13−15] as well as scanning tunneling microscopy (STM),[16] have started to enable the precise positioning of individual dopants or functional groups in the host lattice, paving the way toward very precise tuning of material properties.

Phosphorus has been introduced as a substitutional dopant into the graphene lattice using either chemical vapor deposition[13] (CVD) or ion implantation,[15] and its single-atom spectroscopic fingerprint[15] and dynamics[13] have been studied using aberration-corrected scanning transmission electron microscopy (STEM) and electron energy loss spectroscopy (EELS). However, the three-dimensional (3D) geometry of the substitutional site has thus far only been inferred by comparison to EEL spectrum simulations.[15] In terms of applications, phosphorus doping has been extensively studied for the oxygen reduction reaction,[17] oxygen evolution reaction,[18] hydrogen generation,[19] batteries,[20] supercapacitors,[21] sensing,[22] field effect transistors,[23] and electrocatalysis.[24,25]

The possibility of imprinting magnetic features into graphene by nitrogen dopants[7] raises the question of whether a heavier element of the same group, e.g., phosphorus, may also allow tailoring the magnetic properties of graphene. Having one additional electron compared to a carbon atom, phosphorus can act as an electron donor when substituted into the graphene lattice, thus affecting its electronic structure and potentially inducing magnetic ordering. However, this heavier element introduces a distortion of the lattice.[15] Recent experimental preparation of Gr-P with P concentration up to

34074

176

6.40 atom % imprinted localized magnetic centers in graphene, which ultimately led to the coexistence of antiferromagnetic (AFM) and ferromagnetic (FM) phases, with the corresponding Neél temperature (T_N) of 125 K and the Curie temperature (T_C) of 300 K. It was presumed that sp^3-type PO_x groups were the major magnetic sources,[26] as oxidation of substitutional P is highly exothermic.[27] However, no theoretical insights into the effects of individual chemical forms of phosphorus on magnetic properties of Gr-P were provided, which would allow a deeper comprehension of the origin of magnetism. To the best of our knowledge, so far only single phosphorus atoms doped into the graphene lattice[28,29] at different concentrations,[30,31] i.e., various sizes of the computational cell, have been theoretically considered.

In this work, we employed density functional theory (DFT) calculations, also going beyond the generalized gradient approximation-Perdew−Burke−Ernzerhof (GGA-PBE) level, to investigate the structural, electronic, and magnetic properties including the theoretical transition temperatures of Gr-P and Gr-PO_3H_2 at various doping concentrations and/or structural arrangements. Our simulation for the single substitution was compared to a three-dimensional reconstruction of the experimental geometry based on atomic-resolution STEM imaging at multiple sample tilts. DFT calculations of simultaneous P doping and −PO_3H_2 functionalization of graphene elucidated the origin of experimentally observed FM ordering up to room temperature,[26] whereas adsorption of P adatoms onto the graphene lattice and substitution of carbon atoms by phosphorus can lead to FM and AFM structures.[26] Organic magnets based on Gr-P, potentially tailored to the level of atomic precision,[13] may stimulate interest in exploiting such a system in spintronics or data-storage applications.

2. METHODS

2.1. Computational Methods. Phosphorus doping into the graphene lattice naturally implies a large variety of possible structural motifs. We used a C_{48} orthorhombic supercell, hereafter denoted the 3 × 3 cell, and considered P atoms embedded in 45 unique configurations reaching concentrations up to 6.67 atom %, to gain a deeper insight into the interplay among the structural, electronic, and magnetic features of these systems. In addition, adsorption of P adatoms on a pristine graphene layer, simultaneous substitution and adsorption of phosphorus, and oxidized Gr-P including oxygen (Gr-P-O_x, x = 1, 2) or hydroxyl (Gr-P-OH) adsorption, −PO_3H_2-functionalized graphene, and P adsorption at vacancy sites were considered by examining additional 100 unique configurations.

All atomistic calculations were carried out using spin-polarized DFT and the projected augmented wave (PAW) scheme as implemented in the Vienna ab initio simulation package (VASP).[32−34] Electronic exchange and correlation effects were treated using the Perdew−Burke−Ernzerhof (PBE)[35] generalized gradient approximation (GGA) with a plane-wave cutoff of 600 eV. The Brillouin zone integrations were performed with a 6 × 6 × 1 Γ point-centered k-point mesh[36] (structure and cell optimization) with the convergence criterion of 10^{-6} eV for each self-consistent field (SCF) cycle. Following convergence tests (Table S1), the final static calculations of which density of states plots (DOS) are based on were performed using the tetrahedron method[37] with a 9 × 9 × 1 k-point mesh and 1800 grid points. It is known that PBE-GGA tends to underestimate the band-gap width;[38] therefore, we further performed single-point calculations using the meta-GGA strongly constrained and appropriately normed semilocal density functional (SCAN),[39] which has been shown to improve band gaps of diversely bonded materials at almost-GGA cost,[40] and with a more demanding hybrid PBE0 functional,[41] which by mixing exact exchange (HF) with PBE exchange may eliminate the—in some sense complementary—

deficiencies of HF and DFT and, thus, provide a better description of band gaps. We used SCAN along with the tetrahedron method[37] and kept the k-point mesh and energy cutoff unchanged, and for PBE0, the k-point mesh was reduced to 3 × 3 × 1 and the energy cutoff to 400 eV. Both SCAN and PBE0 calculations were performed using the structures taken from PBE calculations.

The thermodynamic stability of Gr-P was analyzed in terms of the formation energy $E_f = 1/n(E^d - E^p + n(\mu_C - \mu_P))$, where E^d and E^p denote the total energies of the doped and pristine graphene, respectively, and μ_C and μ_P are, respectively, the chemical potentials of C and P atoms (approximated as the total energies of a C atom in graphene and P in the gas phase and/or a P atom in black phosphorus, BP), and n is the number of substituting atoms. A positive E_f indicates that the doping process is endothermic, although it does not prevent the formation of Gr-P complexes. The adsorption energy of on-surface P adatoms adsorbed on doped graphene was calculated as $E_{ad} = 1/n(E^d - E^{d-X} - nE^X)$, where E^d, E^{d-X}, and E^X denote the total energies of the doped graphene, doped graphene without the P adatom/functional group, and the P adatom/functional group (OH, PO_3H_2, and O_2 molecule) in the gas phase, respectively. To correct the overbinding of O_2 by GGA, we rescaled the adsorption energies of O_2 using an experimental O_2 binding energy.[42] A negative E_{ad} indicates stable structures.

Magnetic transition temperatures were estimated using the Ising model and a mean-field approach.[43,44] We considered a larger C_{96} supercell (hereafter denoted the 6 × 3 cell), which enabled exchange interactions between single spins comprising magnetic moments induced by doping/functionalization in the 3 × 3 cell (Figure S1). Following the convergence test (Table S1), we applied the k-point grid of 3 × 6 × 1 and the energy cutoff of 400 eV for all of the functionals. The magnetic transition temperatures (normalized per 3 × 3 cell) were evaluated using the Ising model on a square lattice[45] as $T_{C(IS)}^{FM-AFM} = \frac{0.567J}{k_B}$ for spin S = 0.5, $T_{C(IS)}^{FM-AFM} = \frac{1.674J}{k_B}$ for S = 1, $T_{C(IS)}^{FM-AFM} = \frac{3.278J}{k_B}$ for S = 1.5, and $T_{C(IS)}^{FM-AFM} = \frac{5.351J}{k_B}$ for S = 2, where k_B stands for the Boltzmann constant and J denotes the magnetic exchange coupling, evaluated[46] as $J = \frac{E_{FM} - E_{AFM}}{2zS^2}$ where E_{FM} and E_{AFM} are total energies of FM and AFM phases, respectively, and z is the coordination number in systems of single spins (Figure S1). For the mean-field estimate of transition temperatures, we used[47] the expression $T_{C(MF)}^{FM-AFM} = \frac{JS(S+1)}{3k_B}$, where $J = \frac{E_{FM} - E_{AFM}}{2}$ per pair of single spins S. Since T_C was hardly dependent on the mutual distance between the single spins (Figure S2) and, further, T_C obtained for FM/AFM phases using the Ising model on a honeycomb lattice[48] $T_{C(IS)}^{FM-AFM} = \frac{0.3797J}{k_B}$ in the 3 × 3 cell led to similar results as the mean-field approach in the 6 × 3 cell (Table S2 and Figure S3), we argue that both approaches can provide reasonable estimates of theoretical T_C.

The X-ray photoelectron spectroscopy (XPS) binding energies were calculated using the final state method as the total energy difference between a system having a core hole in its respective core level (P 2p or C 1s) and the initial state. The final state explicitly included a core hole in the calculation, and the system's electronic structure was relaxed in its presence. Although VASP allows including the core hole and calculating the binding energy shifts,[49] the calculations were performed using the FHI-aims code,[50] which implements an all-electron full-potential approach to the electronic structure. Hence, the absolute value of the binding energy could be calculated. The binding energies were calculated using the static geometries from previous VASP calculations. The Brillouin zone integrations were performed with a 3 × 3 × 1 k-point grid. This grid was found to be fully converged, since core states are not dispersed and, hence, are not sensitive to the k-point mesh. The tier2 tight basis set provided with the code was employed for both P and C atoms. The tight basis provided a converged value of 284.3 eV for the C 1s binding energy of pristine graphene, in excellent agreement with the experiment.[51,52] To test the computational settings further, we
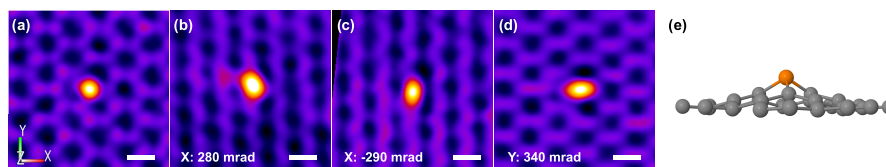
Figure 1. (a−d) Atomically resolved STEM projections of a P substitution in graphene at specimen tilt angles of 0, 280, −290, and 340 mrad along the x-axis (b, c) and the y-axis (d). The scale bars are 2.5 Å. The images were processed by a double-Gaussian filter to enhance the signal-to-noise ratio[55] and colored by the ImageJ lookup table "fire" to enhance contrast. (e) Three-dimensional reconstruction from multiple images recorded at different tilt angles and with threefold averaging.

calculated the reference value for the P 2p binding energy in black phosphorus. We obtained 130.2 eV, which agreed very well with the experimental spin−orbit split values.[53]

2.2. Experimental Methods. P-doped graphene was synthesized by CVD as described previously.[13] STEM images were recorded using a Nion UltraSTEM100 operated at 60 keV with a medium angle annular dark field (MAADF) detector with a semiangular range of 60−200 mrad. The probe current was ∼50 pA, and the beam (semi-)convergence angle was 30 mrad. Multiple frames were averaged to enhance the signal of individual structures, and multiple views of the same P dopant site were acquired by tilting the sample by about 300 mrad along two different axes in a standard double-tilt sample cartridge. The three-dimensional geometry of the site was reconstructed from the tilted images following a procedure established for Si.[54] In short, a structure model was iteratively optimized by minimizing the error between its corresponding image simulation and the experimental images. Due to the greater instability of P under electron irradiation,[13] and therefore the higher noise in the individual images compared to Si, we constrained the reconstruction by assuming threefold symmetry: models rotated by ±120° along the z-axis were averaged, and the z-coordinates of the symmetric neighbors were averaged to reduce the error of the reconstructed model.

3. RESULTS AND DISCUSSION

3.1. Three-Dimensional Reconstruction of a Phosphorus Substitution. Figure 1 shows experimental STEM images of the single P substitution in graphene and a 3D reconstruction of the surrounding geometry. The STEM image evidenced that the substitution of one carbon atom by phosphorus led to a strong geometric distortion of the host graphene lattice. The reconstruction yielded a C−P bond length of 1.61 ± 0.25 Å and a C−P−C angle of $99.6 \pm 11.5°$ (error bounds based on the standard deviation of the reconstructed C atom positions). The main source of uncertainty in these values lies in the z-positions of the P and its three C neighbors, which are the hardest to determine accurately. The experimental observation confirms that the larger atomic radius of P as compared to C (98 vs 67 pm) cannot be accommodated by the lattice, causing a protrusion of phosphorus above the plane, in contrast to a planar geometry when doped with graphitic nitrogen.[7]

3.2. Computational Studies of Phosphorus Doping. *3.2.1. $C_{47}P_1$ (2.13 atom %).* Our DFT calculations indicated that the substitution of carbon by phosphorus led to the same geometric distortion of the graphene lattice as observed experimentally (Figure 2a,b and Table 1). The C−P bond was elongated to 1.76 Å in comparison to the C−C bond length of 1.42 Å in pristine graphene, in good agreement with earlier studies[15] and the experimental estimate of 1.61 ± 0.25 Å. The nearest-neighbor carbon atoms also protruded from the graphene plane with C−C bonds of 1.45 Å. The calculated
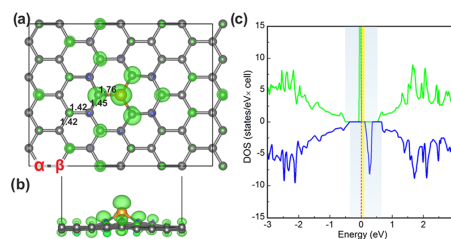
Figure 2. Spin-density distribution plot of Gr-P (2.13 atom %): (a) top view and (b) side view. Isosurface ± 4 meÅ^{-3}. Positive/negative magnetic moments are shown in green/blue. α and β denote the two sublattices of the graphene bipartite lattice. Numbers correspond to the bond length in Ångstrom. Carbon atoms are shown in gray, and phosphorus atoms are in orange. (c) Spin-resolved DOS of Gr-P (2.13 atom %). The Fermi level marked with a vertical red dashed line is set to zero. Blue and yellow bars represent the band gap and the spin-flip gap, respectively. A corresponding atom/orbital decomposed DOS is shown in Figure S4.

Table 1. Formation Energy E_f (eV) Calculated Using the Chemical Potential of P Atoms Approximated by the Total Energy of a Free P Atom (and the Energy of the P Atom in BP), Magnetic Moment μ (μ_B), Spin Number S, C−P Bond Length (Å), C−P−C Angle (°), and Transition Temperature (K) Calculated Using the Ising Model $T_{C(IS)}^{FM-AFM}$ and the Mean-Field Expression $T_{C(MF)}^{FM-AFM}$ for Gr-P (2.13 atom %) Shown in Figure 2a

E_f	μ	S	C−P	C−P−C	$T_{C(IS)}^{FM-AFM}$	$T_{C(MF)}^{FM-AFM}$
−0.41 (3.02)	1.00	0.50	1.76	100.91	79	35

C−P−C angle was 101°, again very close to the experimental estimate of $99.6 \pm 11.5°$. Thus, both experimental and theoretical calculations showed that the graphene lattice cannot house the larger phosphorus atom within its plane, highlighting the difference from substitutional nitrogen with the same valence number.[56]

Pristine graphene is a semimetallic nonmagnetic (NM) material with a Dirac point at the Fermi level. The introduction of a single phosphorus atom into the graphene lattice disturbed its sp^2-delocalized system and opened a band gap of ∼1 eV, with two spin-polarized midgap states at the Fermi energy (E_F) separated in energy by ∼0.12 eV (Figure 2c).

The midgap states reflect an imbalance of the graphene bipartite lattice, $N = N_\alpha - N_\beta$, where N_α and N_β are numbers of atoms belonging to each sublattice, with the total spin of a bipartite lattice given by $2S = |N_\alpha - N_\beta|$[57] and, in this case, $S =$

178

Table 2. Formation Energy E_f (eV) Calculated Using the Chemical Potential of P Atoms Approximated by the Total Energy of a Free P Atom (and the Energy of the P Atom in BP), Magnetic Moment μ (μ_B), Spin Number S, C–P Bond Length (Å), C–P–C Angle (°), and Transition Temperature (K) Calculated Using the Ising Model $T_{C(IS)}^{FM-AFM}$ and the Mean-Field Expression $T_{C(MF)}^{FM-AFM}$ for Gr-P Structures (4.35 atom %) with Various P Atoms' Positions Shown in Figures 3 and S6

structure	E_f	μ	S	C–P	C–P–C	$T_{C(IS)}^{FM-AFM}$	$T_{C(MF)}^{FM-AFM}$
a	−1.63 (1.79)	0.00	0.00	1.78	100.89		
b	−1.37 (2.06)	0.00	0.00	1.77	102.22		
c	−1.33 (2.09)	0.00	0.00	1.77	99.27		
d	−1.25 (2.17)	0.00	0.00	1.78	100.08		
e	−1.21 (2.22)	0.00	0.00	1.77	101.08		
f	−1.18 (2.24)	0.00	0.00	1.77	100.59		
g	−1.16 (2.26)	2.00	1.00	1.76	100.81	162	257
h	−1.11 (2.31)	2.00	1.00	1.76	101.13	192	306
i	−1.06 (2.38)	2.00	1.00	1.76	100.78	169	270
j	−1.04 (2.39)	2.00	1.00	1.76	101.03	150	239
k	−1.04 (2.39)	2.00	1.00	1.76	101.44	150	239

0.5. The quite modest 120 meV energy splitting of the midgap states indicates a large spatial extension of the magnetic state.[19] Indeed, a spin-density distribution plot revealed the spin texture extending over several lattice sites around the doping atom and forming a distinctive $(\sqrt{3} \times \sqrt{3})R30°$ super-structure recognizable in scanning tunneling microscopy (STM) images[58] (Figure 2a,b). Further, atom-/orbital-resolved DOS (Figure S4) revealed a strong contribution from the phosphorus atom and the nearest-neighbor carbon atoms to the midgap states as well as the direct interaction between neighboring C atoms carrying opposite spin moments, in line with the spin-density plot presented in Figure 2a.

The magnetic transition temperature, T_c, is one of the key material parameters to be considered for technological applications. Table 1 reports the theoretically estimated transition temperature between FM and AFM phases whose spin densities are depicted in Figure S5. Using the 6 × 3 cell, we found that the Curie temperature may be as high as 86 K depending on the precise arrangement of two P dopants in the graphene lattice (Figure S2). The synthesis of an FM Gr-P material with T_C of liquid nitrogen (77 K) may inspire an interest in utilizing such a system in magnetic and spintronic applications. FM ordering at 2.13 atom % is in contrast to experimental measurement[26] where such a nominal concentration of P in Gr-P exhibited paramagnetic behavior. This discrepancy might be attributed to the presence of adsorbed P in contamination or as adatoms or even vacancies expected in experimental samples. A larger model of graphene containing more P atoms arranged equally on graphene sublattices can also quench the FM ordering (see below).

3.2.2. $C_{46}P_2$ (4.35 atom %). Upon increasing the concentration of P in the graphene lattice to 4.35 atom %, the average C–P bond length and C–P–C angle changed only slightly (1.76–1.78 Å and 99–102°, respectively) (Table 2). The stability of Gr-P depends on the mutual positions of the phosphorus atoms, as shown in a formation energy map (Figure 3a and Figure S6). In the ground state (GS), 0.26 eV lower in energy than other configurations, phosphorus atoms occupied nearest-neighbor positions in the graphene lattice (Figure 3b). However, experimentally, the spacing of dopants will depend on the local availability of P during the synthesis or implantation process, and thus the system is likely prevented from reaching the energetic GS. Indeed, in our atomic-resolution imaging of P-Gr samples here or reported in earlier studies,[13,15] this configuration has never been observed. We
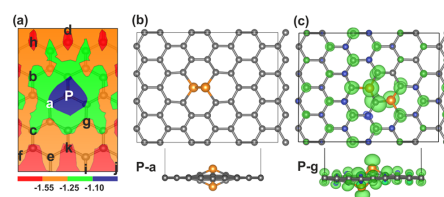
Figure 3. (a) Formation energy map (in eV) of Gr-P (4.35 atom %). Structures and spin textures of Gr-P at 4.35 atom %, (b) GS structure (P-a) and (c) the most stable magnetic arrangement (P-g). The labeling in Table 2 corresponds to the letters in panel (a).

also note that the unavoidable surface contamination present in all samples can be expected to predominantly obstruct the more defective and reactive sites discussed below, making them very challenging to observe using STEM or STM imaging. It is also worth noticing that the relative stabilities of Gr-P structures may depend on the functional used, as M06-L/6-31G* reverted the formation energies of structures P2-a and P2-b.[59] Importantly, relative stabilities of the structures P2-a and P2-b obtained with the PBE functional were not altered using PBE0 and SCAN functionals (Table S3).

The electronic and magnetic properties of Gr-P varied significantly with the configurations of the doping atoms. Incorporation of phosphorus opened a band gap between the valence and conduction bands for some configurations (Figure S7a–f). The gap widths for nonmagnetic Gr-P configurations (Figure S7a–f) were smaller than those for magnetic structures (Figure S7g–k); however, the presence of midgap states effectively lowered the electronic gaps. Experimental samples likely contain various distinct arrangements of P atoms and, thus, their electronic structure reflects a statistical averaging over various configurations. A pronounced density of states near E_F in some of the theoretical structures indicated a possibility of appreciable conductivity (Figures S7).

Due to the bipartite nature of the lattice, the GS of Gr-P was nonmagnetic (Figures 3b and S8). Slightly less stable structures with P atoms evenly substituting C atoms in both sublattices were also nonmagnetic (Figure S6b–f). A long-range FM ordering in Gr-P emerged for P atoms occupying the same sublattice of the graphene sheet, as evident in the spin-density plot (Figures 3c, S6h–k, and S9). As also evident from

Table 3. Formation Energy E_f (eV) Calculated Using the Chemical Potential of P Atoms Approximated by the Total Energy of a Free P Atom (and the Energy of the P Atom in BP), Magnetic Moment μ (μ_B), Spin Number S, C−P Bond Length (Å), C−P−C Angle (°), and Transition Temperature (K) Calculated Using the Ising Model $T_{C(IS)}^{FM\text{-}AFM}$ and the Mean-Field Expression $T_{C(MF)}^{FM\text{-}AFM}$ for Various Gr-P Structures (6.67 atom %) Shown in Figure 4

structure	E_f	μ	S	C−P	C−P−C	$T_{C(IS)}^{FM\text{-}AFM}$	$T_{C(MF)}^{FM\text{-}AFM}$
a	−1.52 (1.90)	1.00	0.50	1.78	102.80	9	4
b	−1.38 (2.04)	1.00	0.50	1.79	99.84	28	12
c	−1.22 (2.20)	1.00	0.50	1.76	102.01	28	13
d	−1.11 (2.31)	3.00	1.50	1.77	102.14	46	157
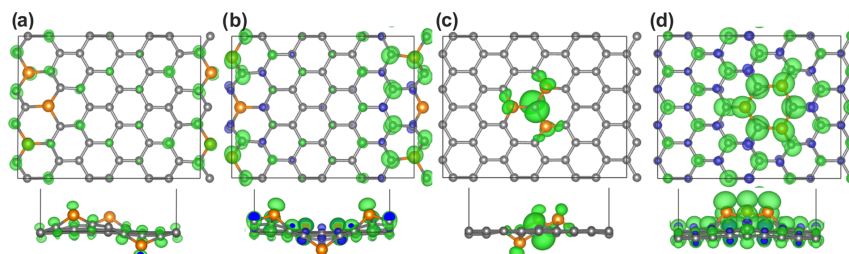
Figure 4. Structures and spin textures of Gr-P (6.67 atom %). The panel labels (a−d) correspond to the structures in Table 3.

the LDOS plots (Figure S10), the p-orbitals of P atoms and the p-orbitals of each C atom are coupled to those of their nearest neighbors, which drive the direct coupling between the magnetic moments over long distances. Spin $S = 1$ was found for magnetic Gr-P, in agreement with the theorem by Lieb[57] (Table 2). The theory thus indicated a role of substitutional doping for the establishment of high-temperature FM ordering in Gr-P (Table 2).

3.2.3. $C_{45}P_3$ (6.67 atom %). Changes in the C−P bond length and the C−P−C angle upon further increase of the doping level were similar to those observed at lower P concentrations: bond lengths remained in the range 1.76−1.78 Å and C−P−C angles within 100−103° (Table 3). In the GS, P atoms occupied *para*-positions in the graphene lattice (Figure 4a).

Electronic DOS of selected structures are shown in Figure S11. Following Lieb's theorem,[57] all structures with an odd number of doping atoms were magnetic either with $S = 0.5$ ($N = 1$, Figure 4a,b) or with $S = 1.5$ ($N = 3$, Figure 4c,d), with the former being more stable than the latter. The direct coupling between the p-orbitals of P and C atoms ensured long-range FM ordering (Figures S12−S14) with a broad distribution of transition temperatures depending on the specific position of P in the host lattice (Table 3). However, this increased concentration of P did not lead to higher T_C.

3.3. Adsorption of Phosphorus Adatom. *3.3.1. $C_{48}P_1$ (2.08 atom %).* To investigate whether magnetism in graphene can also be induced by phosphorus adatoms, we placed P over the high-symmetry sites of the graphene lattice, i.e., on-top (T), bridge (B), and hollow site (H) (Figure 5a). The B site was found to be energetically favorable (Figure 5a,b and Table 4) with an adsorption energy of −0.46 eV, which could be stable at lowered temperatures. The T and H sites were unstable, and the P adatom moved to the B site or desorbed from the graphene lattice upon structural optimization. Thus, the diffusion of P adatoms along B−T−B or B−H−B paths is unlikely, as they would rather desorb from graphene than move
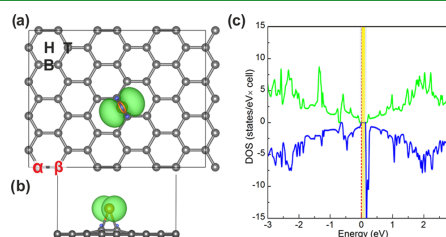
Figure 5. Spin-density distribution plot of Gr-adP (2.08 atom %): (a) top view and (b) side view. Isosurface is ±4 meÅ^{-3}. (c) Density of states of Gr-adP (2.08 atom %). T, B, and H stand for on-top, bridge, and hollow site. The B site corresponds to Table 4.

Table 4. Adsorption Energy E_{ad} (eV), Magnetic Moment μ (μ_B), Spin Number S, C−P Bond Length (Å), C−P−C Angle (°), and Transition Temperature (K) Calculated Using the Ising Model $T_{C(IS)}^{FM\text{-}AFM}$ and the Mean-Field Expression $T_{C(MF)}^{FM\text{-}AFM}$ for Gr-adP (2.08 atom %) Shown in Figure 5

site	E_{ad}	μ	S	C−P	C−P−C	$T_{C(IS)}^{FM\text{-}AFM}$	$T_{C(MF)}^{FM\text{-}AFM}$
B	−0.46	1.00	0.50	1.95	45.14	1	1

on the graphene lattice hopping from one high-symmetry site to another.

The P adatom opened a small gap in the graphene DOS (Figure 5c). The spin value of Gr-P with the adsorbed P adatom was $S = 0.5$, which can be understood by an electron counting consideration: two valence electrons formed covalent bonds with C atoms below, two electrons formed a lone pair, and the fifth valence electron induced a magnetic moment. However, the carbon atoms in the vicinity of P were almost nonmagnetic (0.00−0.01 μ_B; Figure S15), which suggested that long-range FM ordering was not established. Indeed, the

180

magnetic transition temperature did not exceed 2 K. Paramagnetic behavior at a low P concentration[26] was also experimentally observed.

3.3.2. $C_{47}P_2$ (4.26 atom %). We also studied the adsorption of a P adatom onto P-doped graphene. Since the T and H positions were unstable for a single P adatom, we considered only B sites on Gr-P. The adsorption energy strongly depended on the mutual distance between the P adatom and the P dopant site, as can be seen in an adsorption energy map (Figure 6). In general, the P adatoms exhibited a tendency for
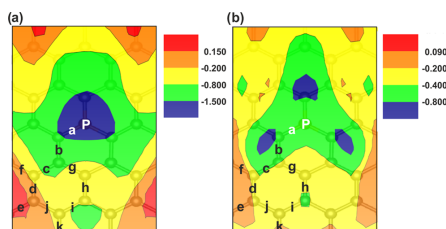
Figure 6. Adsorption energy map (in eV) of Gr-P (4.26 atom %). The adsorbed P adatom is in (a) cis and (b) trans configurations with respect to the substituting P in the graphene lattice. The labels correspond to Table 5.

adsorbing next to the P substituting for C in the graphene lattice. Structures in cis configurations were commonly preferred over those in trans configurations (Table 5).

Electronic DOS of all structures are shown in Figure S16. Depending on the adsorption site, the structures were either FM with $S = 1$ or nonmagnetic (Figure S17). Also, the theoretical magnetic transition temperature strongly depended on the adsorption site (Table 5). Several Gr-P structures were AFM ones (structures e and f in Figure 6a and structures e and f in Figures 6b, and S18). Importantly, the coexistence of FM and AFM structures has been observed in experimental samples.[26]

3.4. Functionalization of Pristine and P-Doped Graphene. *3.4.1. 2.08 atom %.* We considered various oxidized phosphorus groups and functional groups adsorbed onto pristine graphene or onto Gr-P, which were presumably present in experimental samples.[26] Whereas oxygen atoms and hydroxyl groups (Figure S19) adsorbed strongly onto a P dopant, the phosphono $-PO_3H_2$ group (Figure 7) was relatively weakly bound to graphene. Phosphate $-OPO_3H_2$ or $-OPO_2$ groups were unstable and desorbed from the graphene lattice.

The electronic DOS of Gr-P-O$_x$ and Gr-P-OH are shown in Figures S20. Both oxygen and hydroxyl adsorption did not induce magnetism in Gr-P. In contrast, adsorption of the $-PO_3H_2$ group on pristine graphene (Gr-PO$_3$H$_2$, Figure 7) induced localized magnetic moments in the system (Figures S21 and S22), however, with relatively low T_C (Table 6).

3.4.2. 4.17 atom %. Motivated by reported experimental characterization,[26] we further combined the Gr-P, Gr-P-O$_x$, and Gr-PO$_3$H$_2$ structures. Depending on their mutual arrangements, the adsorption energies ranged from -0.06 to -1.99 eV (Table 7). Surprisingly, although the P dopant and the $-PO_3H_2$ group individually induced magnetism in graphene, their combination did not (Figure S23). Only

Table 5. Adsorption Energy E_{ad} (eV), Magnetic Moment μ (μ_B), Spin Number S, P−P Distance (Å), and Transition Temperature (K) Calculated Using the Ising Model $T_{C(IS)}^{FM\text{-}AFM}$ and the Mean-Field Expression $T_{C(MF)}^{FM\text{-}AFM}$ for Gr-P Structures (4.26 atom %) with Various Positions of P Adatoms Shown in Figure 6^a

position	E_{ad}	μ	S	P−P distance	$T_{C(IS)}^{FM\text{-}AFM}$	$T_{C(MF)}^{FM\text{-}AFM}$
				Cis		
a	−1.78	0.00	0.00	2.05		
b	−1.28	0.00	0.00	2.18		
c	−0.95	0.00	0.00	3.06		
d	0.09	2.00	1.00	4.74	68	108
e	0.15	0.00	0.00	5.71	303*	482*
f	0.06	0.00	0.00	4.44	213*	339*
g	−0.60	0.00	0.00	2.92		
h	−0.54	0.00	0.00	4.02		
i	−0.88	0.00	0.00	4.73		
j	−0.06	2.00	1.00	5.26	174	277
k	−0.06	2.00	1.00	6.10	79	127
				Trans		
a	−0.61	2.00	1.00	3.16	18	28
b	−0.86	0.00	0.00	3.33		
c	−0.30	0.00	0.00	4.14		
d	−0.33	2.00	1.00	5.43	123	196
e	−0.09	0.00	0.00	6.43	234*	373*
f	−0.06	0.00	0.00	5.16	230*	367*
g	−0.20	0.00	0.00	3.84		
h	−0.46	0.00	0.00	4.76		
i	−0.30	0.00	0.00	5.55		
j	−0.27	2.00	1.00	5.94	154	245
k	−0.27	2.00	1.00	6.72	74	117

^{a}* denotes AFM structures (Figure S18).
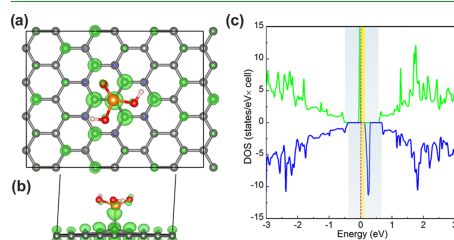
Figure 7. Spin-density distribution plot of Gr-PO$_3$H$_2$: (a) top view and (b) side view. Isosurface is ±4 meÅ^{-3} (see also Table 6). (c) Density of states of Gr-PO$_3$H$_2$.

upon the adsorption of the second $-PO_3H_2$ group into a meta/trans configuration of Gr-PO$_3$H$_2$ did the magnetic alignment emerge (Figure S23h) with quite a high T_C (Table 7). The electronic DOS are displayed in Figure S24.

3.4.3. 6.25 and 8.33 atom %. We also considered simultaneous Gr-P, Gr-P-O$_x$, and Gr-PO$_3$H$_2$ at higher concentrations (Figure S25).[26] Depending on the composition and configurations of the theoretical structures, either NM or FM arrangements were established with adsorption energies ranging from 1.51 to -2.35 eV (Table 8). The electronic DOS are displayed in Figure S26. In line with experimental findings,[26] magnetism with high T_C may thus stem from a

Table 6. Adsorption Energy E_{ad} (eV), Magnetic Moment μ (μ_B), Spin Number S, P−O Bond Length (Å), C−PO$_3$H$_2$ Bond Length (Å), and Transition Temperature (K) Calculated Using the Ising Model $T_{C(IS)}^{FM-AFM}$ and the Mean-Field Expression $T_{C(MF)}^{FM-AFM}$ for Functionalized Gr and Gr-P (2.08 atom %) Shown in Figures 7 and S19

structure	E_a	μ	S	P−O	C−PO$_3$H$_2$	$T_{C(IS)}^{FM-AFM}$	$T_{C(MF)}^{FM-AFM}$
Gr-P-OH	−4.70	0.00	0.00	1.63			
Gr-P-O$_1$	−0.79	0.00	0.00	1.49			
Gr-PO$_3$H$_2$	−0.42	1.00	0.50		1.98	44	19
Gr-P-O$_2$	3.31	0.00	0.00	1.68			

Table 7. Adsorption Energy E_{ad} (eV), Magnetic Moment μ (μ_B), Spin Number S, P−O Bond Length (Å), C−PO$_3$H$_2$ Bond Length (Å), and Transition Temperature (K) Calculated Using the Ising Model $T_{C(IS)}^{FM-AFM}$ and the Mean-Field Expression $T_{C(MF)}^{FM-AFM}$ for Functionalized Gr and Gr-P (4.17 atom %) Shown in Figure S23

structure	E_a	μ	S	P−O	C−PO$_3$H$_2$	$T_{C(IS)}^{FM-AFM}$	$T_{C(MF)}^{FM-AFM}$
a	−1.99	0.00	0.00		1.90		
b	−1.40	0.00	0.00		1.96		
c	−0.91	0.00	0.00	1.49	1.92		
d	−0.72	0.00	0.00		1.93		
e	−0.71	0.00	0.00	1.49	2.00		
f	−0.70	0.00	0.00	1.49	2.04		
g	−0.66	0.00	0.00		1.87		
h	−0.26	2.00	1.00		1.90	148	236
i	−0.08	0.00	0.00	1.49			
j	−0.07	0.00	0.00	1.49			
k	−0.06	0.00	0.00	1.49			

Table 8. Adsorption Energy E_{ad} (eV), Magnetic Moment μ (μ_B), Spin Number S, P−O Bond Length (Å), C−PO$_3$H$_2$ Bond Length (Å), and Transition Temperature (K) Calculated Using the Ising Model $T_{C(IS)}^{FM-AFM}$ and the Mean-Field Expression $T_{C(MF)}^{FM-AFM}$ for Functionalized Gr-P (6.25−8.33 atom %) Shown in Figure S25

structure	E_a	μ	S	P−O	C−PO$_3$H$_2$	$T_{C(IS)}^{FM-AFM}$	$T_{C(MF)}^{FM-AFM}$
				6.25 atom %			
a	−2.35	3.00	1.50		2.71	52	179
b	−1.45	1.00	0.50	1.49	1.90	4	2
c	−1.04	1.00	0.50	1.49	1.97	6	3
d	−0.82	1.00	0.50		1.97	114	50
e	−0.61	3.00	1.50		2.08	218	747
f	−0.60	1.00	0.50	1.49	1.97	65	29
g	−0.54	1.00	0.50		1.98	51	23
h	−0.51	1.50	1.50		2.11	184	630
i	1.51	1.00	0.50	1.49		79	35
				8.33 atom %			
j	−0.38	4.00	2.00		1.97	242	1448
k	−0.21	4.00	2.00		1.97	199	1076

synergistic effect of phosphorus in various bonding configurations (Table 8 and Figure S25).

3.5. Vacancy in Phosphorus-Doped Graphene (2.13−8.70 atom %). Lattice defects, e.g., atomic vacancies, are unavoidable in graphene sheets due to the impact of either growth conditions or irradiation (see refs 60 and 61 and references therein). In the following, we considered P atoms bound in a divacancy defect,[22,23] but also other bonding configurations (Figure 8) that may be encountered. Greater structural changes were observed as compared to the substitutional doping of P into the ideal graphene lattice. Formation energies varied quite widely with C−P bond lengths 1.76−1.80 Å and C−P−C angles 90−99°.

The electronic properties of defective Gr-P varied depending on the types of defects (Figure S27). Gr-P with a tetramerized pyridinic P atom (Figure 8a,d), Gr-P with a dimerized pyridinic P atom (Figure 8e), and Gr-P with P atoms bound in the divacancy defect (Figure 8f) displayed spin-symmetric DOS. More importantly, Gr-P with one pyrrolic and two pyridinic P atoms (Figure 8b) and Gr-P with three pyridinic P atoms (Figure 8c) exhibited magnetic features; however, they were sustainable only at very low temperatures (Table 9), which may explain the paramagnetism of experimental samples at low P concentration.[26] Single pyridinic P atoms (Figure 8g) also induced a magnetic moment in Gr-P with a T_C of 53 K (Table 9).

3.6. Core-Level Binding Energies of P-Doped Graphene. We further calculated core-level binding energies to facilitate the experimental identification of phosphorus incorporated into graphene. The P 2p binding energy was calculated for various phosphorus configurations (Table 10). The binding energy is 130.4 eV for a P substitution and 128.8 eV for a P adatom bonded to two C atoms at the bridge position. The binding energy difference is high enough for adsorptive and substitutional doping to be resolved via X-ray photoelectron spectroscopy (XPS), although adsorption into

182
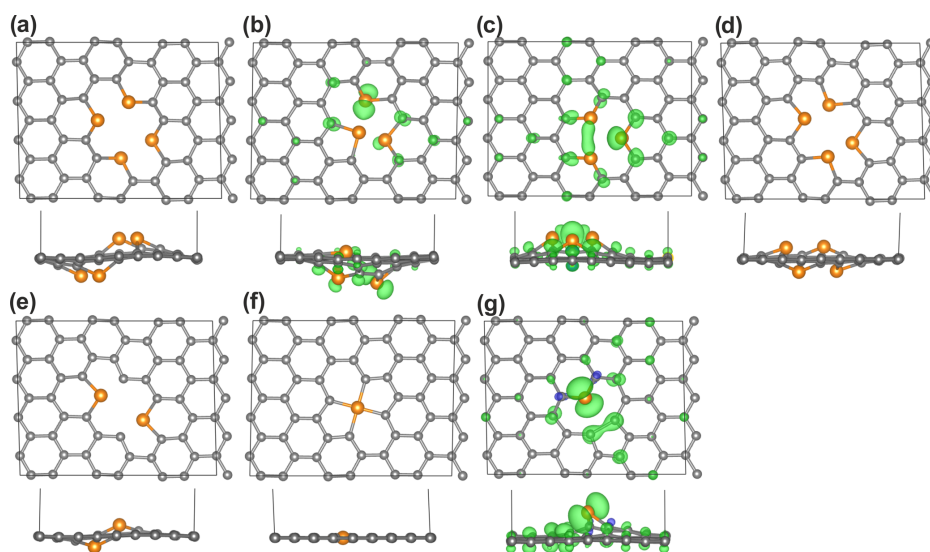
Figure 8. Structures and spin-density textures of defective Gr-P. The panel labels (a–g) correspond to the structures in Table 9.

Table 9. Concentration of P Atoms (atom %), Formation Energy E_f (eV) Calculated Using the Chemical Potential of P Atoms Approximated by the Total Energy of a Free P Atom (and the Energy of the P atom in BP), Magnetic Moment μ (μ_B), Spin Number S, C–P Bond Length (Å), C–P–C Angle (°), and Transition Temperature (K) Calculated Using the Ising Model $T_{C(IS)}^{FM\text{-}AFM}$ and the Mean-Field Expression $T_{C(MF)}^{FM\text{-}AFM}$ for Gr-P (Vacancy) Shown in Figure 8

structure	P atom %	E_f	μ	S	C–P	C–P–C	$T_{C(IS)}^{FM\text{-}AFM}$	$T_{C(MF)}^{FM\text{-}AFM}$
a	8.70	−1.46 (0.82)	0.00	0.00	1.80	97.83		
b	6.40	−1.33 (1.24)	1.00	0.50	1.80	96.54	3	1
c	6.40	−1.18 (1.39)	1.00	0.50	1.77	98.77	7	3
d	8.70	−1.13 (1.15)	0.00	0.00	1.80	98.75		
e	4.35	−0.54 (1.17)	0.00	0.00	1.79	96.46		
f	2.13	−0.18 (1.53)	0.00	0.00	1.86	90.00		
g	2.13	1.28 (2.99)	1.00	0.50	1.76	91.97	53	23

Table 10. P 2p Binding Energies (BEs) of Various Forms of P in Graphene Calculated as the Energy Difference between the Final State (Core-Hole Due to Excited 2p Electron) and the Initial State[a]

type of P	P 2p BE (eV)	C 1s BE (eV)
P1 (Figure 2a)	130.4	283.3
P2a (Figure 3b)	130.5	283.6
P2g (Figure 3c)	130.4	282.5
P1-bridge (Figure 5a)	128.8	283.6
P adatoms-a (Figure 6a)	131.4 (129.7)	283.6
P-O (Figure S19)	130.6	282.6
PO$_3$H$_2$ (Figure 7)	132.8	284.9

[a]The C 1s binding energies are calculated for carbon atoms neighboring P (calculated C 1s of pristine graphene is found at 284.3 eV).

carbonaceous contamination may be impossible to distinguish from lattice adsorption. Nevertheless, when multiple P substitute into the lattice, the P 2p binding energies of various configurations are very uniform near 130.4 eV, and the magnetic and nonmagnetic structures (e.g., Figure 3c,b) cannot be distinguished based on P 2p even in high-resolution XPS. The C 1s binding energy may serve this purpose better because C 1s energies for C atoms bonded to the P dopant are about 1 eV lower than C 1s of other graphitic carbons (Table 10). However, for realistic doping levels, the C 1s response of the bulk will tend to obscure such signals. Notably, the ferromagnetic configuration (Figure 3c) involves a single C between two P dopants, with an even lower C 1s at 282.5 eV. This structure (Figure 3c) is particularly interesting because it had the lowest formation energy of ferromagnetic two-P patterns.

The core-level binding energy of 130.4 eV for a P substitutional dopant embedded into the lattice agrees well with experimental studies.[26] A low-energy peak positioned at 129.5 eV was assigned to C–P bonding in phosphorus-doped carbon nanotubes,[62] with a corresponding peak at 130 eV in XPS spectra of P-doped graphene.[26] Occasionally, a higher value of 131.5 eV was reported for phosphorus-doped

graphene.[19] It should be noted that the P 2p peak is split into the $2p_{1/2}$ and $2p_{3/2}$ components by spin−orbit interaction in experimental spectra. Experimental spectra of P-doped graphitic materials often contain an additional P 2p peak at energies around 133 eV, which is assigned to P−O and P−O−C bonds.[20,21,63,64] Our calculation indicated that oxygen bonded directly to a P dopant in graphene does not shift its P 2p binding energy, yielding a calculated value of 130.6 eV, which is surprisingly similar to 130.4 eV obtained for an unoxidized phosphorus dopant. Instead, we propose that P 2p energies around 133 eV observed in experiments correspond to the PO_3H_2 group (Table 10). Notably, the values of the core-level binding energy for P−O and PO_3H_2 are almost constant regardless of their arrangements in the lattice (Table 8). Therefore, XPS alone is not sufficient for a distinction of specific magnetic configurations but can distinguish among phosphorus doping, adsorption, and the presence of phosphono groups.

3.7. Band-Gap Estimation. Since semilocal GGA functionals tend to underestimate band gaps due to the self-interaction error and overdelocalization of the electronic system,[38,65] we calculated the band gap of several GS structures using the meta-GGA SCAN functional[39] and the demanding hybrid PBE0 functional,[41] which should provide better estimates of gap values. Both SCAN (Figure S28) and PBE0 (Figure S29) led to wider band gaps (Table 11) as compared

Table 11. Band Gap (in eV, Spin-Flip Gap in Parenthesis) of Gr-P Structures with Different Concentrations and/or Topologies of P Calculated using PBE, SCAN, and PBE0 Functionals

structure	PBE	SCAN	PBE0
P1 (a) (Figure 2a)	1.02 (0.12)	1.46 (1.09)	1.40 (1.10)
P2a (b) (Figure 3b)	0.02	0.13	0.69
P2g (c) (Figure 3c)	1.48 (0.14)	1.98 (0.98)	1.74 (1.37)
P3a (d) (Figure 4a)	1.60 (0.00)	2.00 (1.00)	2.37 (1.21)
P adatom-a-cis (e) (Figure 6a)	0.30	0.65 (up), 1.28 (down)	0.90
Pa-vacancy (f) (Figure 8a)	0.14	0.14	0.76

to GGA-PBE. The band gaps of magnetic structures increased by 0.4−0.7 eV and the spin-flip gaps increased even more, i.e., by 0.7−1.2 eV (Table 11a,c,d and Figures S28a,c,d, and S29a,c,d). For nonmagnetic structures, the SCAN functional predicted wider band gaps by about 0.1 eV (Table 11b,f and Figure S28b,f) and for PBE0 by 0.6−0.7 eV (Table 11b,e,f and Figure S29b,e,f). Recently, the variation in band gaps with the size of unit cells of P-doped graphene was studied[66] using VDW-DF/DZP, M06-L/6-31G*, and HSEH1PBE/6-31G* periodic DFT. For the unit cell containing 50 atoms, the band gaps of 0.62/0.59, 0.71/0.61, and 0.94/0.82 eV, respectively, have been predicted. Our PBE and SCAN/PBE0 thus provided, respectively, lower and upper bounds to the band gap of the single P substitution in graphene (Table 11). The deviation between VDW-DF and HSEH1PBE has been shown[66] to become small for large unit cells, and a single P atom in a unit cell of 5000 atoms may still open a gap of 0.05 eV without significantly affecting the carriers' mobilities. Moreover, by opening the electronic gap, P doping may

influence effective masses of carriers. It has been reported[66] that the increased concentration of P atoms results in wider band gaps and, accordingly, contributes to higher effective masses.

Both SCAN and PBE0 functionals did not alter the magnetic structures, except for the one shown in Figure 6a (cis configuration Pa), which became AFM (Table 11e). However, they led to 5−90-fold (SCAN) and 3−50-fold (PBE0) increased T_C (Table S4) and, thus, failed to provide a realistic estimate. This may be attributed to a larger exchange splitting (Figures S30−S35), between 100 and 3450% with respect to the GGA-PBE value.[67] For the sake of completeness, we note that for certain structures, PBE0 provided also lower T_C as compared to the GGA-PBE values (Table S4). Both SCAN and PBE0 showed serious limitations in predicting the magnetic properties of metals.[68,69]

4. CONCLUSIONS

We have theoretically addressed the structural, electronic, and magnetic properties of graphene doped by phosphorus atoms, supported by an experimental reconstruction of the three-dimensional geometry of the single P substitution. The larger atomic radius of P as compared to C atoms could not be accommodated by the graphene lattice and caused a protrusion of phosphorus above the plane of graphene. The experimental geometry showed a good agreement with the theoretical calculations. In addition, we studied graphene containing P in functional groups and in vacancy sites. A synergistic effect of simultaneous P doping and $-PO_3H_2$ functionalization possibly elucidates the origin of experimentally observed FM ordering up to room temperature.[26] Simultaneous substitution of C by P and the adsorption of P adatoms can lead to FM and AFM arrangements in line with experimental findings.[26] The electronic-structure calculations indicated that the magnetic ordering of graphene doped with phosphorus may be attributed to a combined direct coupling in an antiparallel fashion of a spin-polarized electron cloud extending over a long distance from the P dopant between partially filled π-orbitals of neighbor carbon atoms and the RKKY interaction.[70] The electronic and magnetic properties of several GS structures were recalculated using the meta-GGA SCAN functional and the hybrid PBE0 functional. Both functionals in most cases failed to provide a realistic estimate of magnetic transition temperatures. We also provided a catalog of core-level binding energies to facilitate the experimental identification of the phosphorus in various bonding configurations and its incorporation into graphene.

We believe that the presented results will stimulate further research in graphene-based organic magnets with features tunable by varying the level of doping combined with sp^3 functionalization or, ultimately, by the manipulation of P dopants. The unique electronic and magnetic properties of P-doped graphenes, which can be fine-tuned by doping, predispose these materials for various technological applications including electronics, catalysis, electrocatalysis, sensing, energy storage, and spintronics.

■ ASSOCIATED CONTENT

ⓢ Supporting Information

The Supporting Information is available free of charge at https://pubs.acs.org/doi/10.1021/acsami.0c07564.

k-point convergence test, scheme for calculating transition temperatures, $\Delta E_{\text{FM-AFM}}$ and T_{C} vs distance, comparison of T_{C} obtained using the Ising model for the 3×3 cell and the mean-field approach for the 6×3 cell, structures, and spin textures; density of state plots, orbital/atom decomposed density of state plots, and Curie temperatures calculated using PBE, SCAN, and PBE0 functionals (PDF)

■ AUTHOR INFORMATION

Corresponding Authors

Piotr Błoński − *Regional Centre of Advanced Technologies and Materials, Faculty of Science, Palacký University Olomouc, 78371 Olomouc, Czech Republic;* ● orcid.org/0000-0002-7072-232X; Email: piotr.blonski@upol.cz

Toma Susi − *Faculty of Physics, University of Vienna, A-1090 Vienna, Austria;* ● orcid.org/0000-0003-2513-573X; Email: toma.susi@univie.ac.at

Authors

Rostislav Langer − *Department of Physical Chemistry, Faculty of Science, Palacký University Olomouc, 77146 Olomouc, Czech Republic*

Christoph Hofer − *Institute for Applied Physics, Eberhard Karls University of Tübingen, D-72076 Tübingen, Germany; Natural and Medical Sciences Institute at the University of Tübingen, D-72770 Reutlingen, Germany*

Petr Lazar − *Regional Centre of Advanced Technologies and Materials, Faculty of Science, Palacký University Olomouc, 78371 Olomouc, Czech Republic;* ● orcid.org/0000-0002-7312-3656

Kimmo Mustonen − *Faculty of Physics, University of Vienna, A-1090 Vienna, Austria;* ● orcid.org/0000-0002-0953-7299

Jannik C. Meyer − *Institute for Applied Physics, Eberhard Karls University of Tübingen, D-72076 Tübingen, Germany; Natural and Medical Sciences Institute at the University of Tübingen, D-72770 Reutlingen, Germany;* ● orcid.org/0000-0003-4023-0778

Michal Otyepka − *Regional Centre of Advanced Technologies and Materials, Faculty of Science, Palacký University Olomouc, 78371 Olomouc, Czech Republic;* ● orcid.org/0000-0002-1066-5677

Complete contact information is available at:
https://pubs.acs.org/10.1021/acsami.0c07564

Author Contributions

The manuscript was written through contributions of all authors. All authors have given approval to the final version of the manuscript.

Notes

The authors declare no competing financial interest.

■ REFERENCES

(1) Geim, A. K.; Novoselov, K. S. The Rise of Graphene. *Nat. Mater.* **2007**, *6*, 183−191.

(2) Lee, C.; Wei, X.; Kysar, J. W.; Hone, J. Measurement of the Elastic Properties and Intrinsic Strength of Monolayer Graphene. *Science* **2008**, *321*, 385−388.

(3) Novoselov, K. S.; Geim, A. K.; Morozov, S. V.; Jiang, D.; Katsnelson, M. I.; Grigorieva, I. V.; Dubonos, S. V.; Firsov, A. A. Two-Dimensional Gas of Massless Dirac Fermions in Graphene. *Nature* **2005**, *438*, 197−200.

(4) Bonaccorso, F.; Colombo, L.; Yu, G.; Stoller, M.; Tozzini, V.; Ferrari, A. C.; Ruoff, R. S.; Pellegrini, V. Graphene, Related Two-Dimensional Crystals, and Hybrid Systems for Energy Conversion and Storage. *Science* **2015**, *347*, No. 1246501.

(5) Nair, R. R.; Blake, P.; Grigorenko, A. N.; Novoselov, K. S.; Booth, T. J.; Stauber, T.; Peres, N. M. R.; Geim, A. K. Fine Structure Constant Defines Visual Transparency of Graphene. *Science* **2008**, *320*, 1308.

(6) Tuček, J.; Błoński, P.; Sofer, S.; Šimek, P.; Petr, M.; Pumera, M.; Otyepka, O.; Zbořil, R. Sulfur Doping Induces Strong Ferromagnetic Ordering in Graphene: Effect of Concentration and Substitution Mechanism. *Adv. Mater.* **2016**, *28*, 5045−5053.

(7) Błoński, P.; Tuček, J.; Sofer, Z.; Mazánek, V.; Petr, M.; Pumera, M.; Otyepka, M.; Zbořil, R. Doping with Graphitic Nitrogen Triggers Ferromagnetism in Graphene. *J. Am. Chem. Soc.* **2017**, *139*, 3171−3180.

(8) Koch, R. J.; Weser, M.; Zhao, W.; Viñes, F.; Gotterbarm, K.; Kozlov, S. M.; Höfert, O.; Ostler, M.; Papp, C.; Gebhardt, J.; Steinrück, H.-P.; Görling, A.; Seyller, T. Growth and Electronic Structure of Nitrogen-Doped Graphene on Ni(111). *Phys. Rev. B* **2012**, *86*, No. 075401.

(9) Tuček, J.; Holá, K.; Zoppellaro, G.; Błoński, P.; Langer, R.; Medveď, M.; Susi, T.; Otyepka, M.; Zbořil, R. Driving Force toward Room Temperature Ferromagnetic Graphene Zig-Zag sp² Carbon Chains Passing through sp³ Framework − A Driving Force toward Room Temperature Ferromagnetic Graphene. *ACS Nano* **2018**, *12*, 12847−12859.

(10) Langer, R.; Błoński, P.; Otyepka, M. Tuning the Magnetic Properties of Graphene Derivatives by Functional Group Selection. *Phys. Chem. Chem. Phys.* **2019**, *21*, 12697−12703.

(11) Langer, R.; Zaoralová, D.; Medveď, M.; Banáš, P.; Błoński, P.; Otyepka, M. Variability of C−F Bonds Governs the Formation of Specific Structural Motifs in Fluorinated Graphenes. *J. Phys. Chem. C* **2019**, *123*, 27896−27903.

(12) Zoppellaro, G.; Bakandritsos, A.; Tuček, J.; Błoński, P.; Susi, T.; Lazar, P.; Ba'ura, Z.; Steklý, T.; Opletalová, A.; Otyepka, M.; Zbořil, R. Microwave Energy Drives "On−Off−On" Spin-Switch Behavior in Nitrogen-Doped Graphene. *Adv. Mater.* **2019**, *31*, No. 1902587.

(13) Su, C.; Tripathi, M.; Yan, Q.-B.; Wamg, Z.; Zhang, Z.; Hofer, Z.; Wang, H.; Basile, L.; Su, G.; Dong, M.; Meyer, J. C.; Kotakoski, J.; Kong, J.; Idrobo, J.-C.; Susi, T.; Li, J. Engineering Single-Atom Dynamics with Electron Irradiation. *Sci. Adv.* **2019**, *5*, No. eaav2252.

(14) Susi, T.; Meyer, J. C.; Kotakoski, J. Manipulating Low-Dimensional Materials Down to the Level of Single Atoms with Electron Irradiation. *Ultramicroscopy* **2017**, *180*, 163−172.

(15) Susi, T.; Hardcastle, T. P.; Hofsäss, H.; Mittelberger, A.; Pennycook, T. J.; Mangler, C.; Drummond-Brydson, R.; Scott, A. J.; Meyer, J. C.; Kotakoski, J. Single-atom Spectroscopy of Phosphorus Dopants Implanted into Graphene. *2D Mater.* **2017**, *4*, No. 021013.

(16) González-Herrero, H.; Gómez-Rodríguez, J. M.; Mallet, P.; Moaied, M.; Palacios, J. J.; Salgado, C.; Ugeda, M. M.; Veuillen, J. Y.;

185

Yndurain, F.; Brihuega, I. Atomic-scale Control of Graphene Magnetism by Using Hydrogen Atoms. *Science* **2016**, *352*, 437−441.

(17) Zhang, X.; Lu, Z.; Fu, Z.; Tang, Y.; Ma, D.; Yang, Z. The Mechanisms of Oxygen Reduction Reaction on Phosphorus Doped Graphene: A First-principles Study. *J. Power Sources* **2015**, *276*, 222−229.

(18) Li, R.; Wei, Z.; Gou, X. Nitrogen and Phosphorus Dual-Doped Graphene/Carbon Nanosheets as Bifunctional Electrocatalysts for Oxygen Reduction and Evolution. *ACS Catal.* **2015**, *5*, 4133−4142.

(19) Latorre-Sánchez, M.; Primo, A.; García, H. P-Doped Graphene Obtained by Pyrolysis of Modified Alginate as a Photocatalyst for Hydrogen Generation from Water−Methanol Mixtures. *Angew. Chem., Int. Ed.* **2013**, *52*, 11813−11816.

(20) Song, J.; Yu, Z.; Gordin, M. L.; Hu, S.; Yi, R.; Tang, D.; Walter, T.; Regula, M.; Choi, D.; Li, X.; Manivannan, A.; Wang, D. Chemically Bonded Phosphorus/Graphene Hybrid as a High Performance Anode for Sodium-Ion Batteries. *Nano Lett.* **2014**, *14*, 6329−6335.

(21) Wen, Y.; Wang, B.; Huang, C.; Wang, L.; Hulicova-Jurcakova, D. Corrigendum: Synthesis of Phosphorus-Doped Graphene and its Wide Potential Window in Aqueous Supercapacitors. *Chem. - Eur. J.* **2015**, *21*, 3520.

(22) Niu, F.; Tao, L.-M.; Deng, Y.-C.; Wang, Q.-H.; Song, W.-G. Phosphorus Doped Graphene Nanosheets for Room Temperature NH_3 Sensing. *New. J. Chem.* **2014**, *38*, 2269−2272.

(23) Some, S.; Kim, J.; Lee, K.; Kulkarni, A.; Yoon, Y.; Lee, S.; Kim, T.; Lee, H. Highly Air-Stable Phosphorus-Doped n-Type Graphene Field-Effect Transistors. *Adv. Mater.* **2012**, *24*, 5481−5486.

(24) Poh, H. L.; Sofer, Z.; Nováček, M.; Pumera, M. Concurrent Phosphorus Doping and Reduction of Graphene Oxide. *Chem. - Eur. J.* **2014**, *20*, 4284−4291.

(25) Wang, L.; Sofer, Z.; Pumera, M. Will Any Crap We Put into Graphene Increase Its Electrocatalytic Effect? *ACS Nano* **2020**, *14*, 1−25.

(26) Lin, L.; Fu, L.; Zhang, K.; Chen, J.; Zhang, W.; Tang, S.; Du, Y.; Tang, N. P-Superdoped Graphene: Synthesis and Magnetic Properties. *ACS Appl. Mater. Interfaces* **2019**, *11*, 39062−39067.

(27) Krstić, V.; Ewels, C. P.; Wågberg, T.; Ferreira, M. S.; Janssens, A. M.; Stéphan, O.; Glerup, M. Indirect Magnetic Coupling in Light-Element-Doped Single-Walled Carbon Nanotubes. *ACS Nano* **2010**, *4*, 5081−5086.

(28) Wang, H.-m.; Wang, H.-x.; Chen, Y.; Liu, Y.-j.; Zhao, J.-x.; Cai, Q.-h.; Wang, X.-z. Phosphorus-Doped Graphene and (8, 0) Carbon Nanotube: Structural, Electronic, Magnetic Properties, and Chemical Reactivity. *Appl. Surf. Sci.* **2013**, *273*, 302−309.

(29) Dai, J.; Yuan, J. Modulating the Electronic and Magnetic Structures of P-doped Graphene by Molecule Doping. *J. Phys.: Condens. Matter* **2010**, *22*, No. 225501.

(30) Denis, P. A. Band gap Opening of Monolayer and Bilayer Graphene Doped with Aluminium, Silicon, Phosphorus, and Sulfur. *Chem. Phys. Lett.* **2010**, *492*, 251−257.

(31) Denis, P. A. Concentration Dependence of the Band Gaps of Phosphorus and Sulfur Doped Graphene. *Comput. Mater. Sci.* **2013**, *67*, 203−206.

(32) Kresse, G.; Furthmüller, J. Efficient Iterative Schemes for Ab-initio Total-Energy Calculations Using a Plane-wave Basis Set. *Phys. Rev. B* **1996**, *54*, 11169−11186.

(33) Kresse, G.; Joubert, D. From Ultrasoft Pseudopotentials to the Projector Augmented-Wave Method. *Phys. Rev. B* **1999**, *59*, No. 1758.

(34) Blöchl, P. E. Projector Augmented-Wave Method. *Phys. Rev. B* **1994**, *50*, No. 17953.

(35) Perdew, J. P.; Burke, K.; Ernzerhof, M. Generalized Gradient Approximation Made Simple. *Phys. Rev. Lett.* **1996**, *77*, 3865−3868.

(36) Monkhorst, H. J.; Pack, J. D. Special Points for Brillouin-Zone Integrations. *Phys. Rev. B* **1976**, *13*, No. 5188.

(37) Blöchl, P. E.; Jepsen, O.; Andersen, O. K. Improved Tetrahedron Method for Brillouin-Zone Integrations. *Phys. Rev. B* **1994**, *49*, No. 16223.

(38) Karlický, F.; Otyepka, M. Band Gaps and Optical Spectra of Chlorographene, Fluorographene and Graphane from G_0W0, GW_0 and GW Calculations on Top of PBE and HSE06 Orbitals. *J. Chem. Theory Comput.* **2013**, *9*, 4155−4164.

(39) Sun, J.; Ruzsinszky, A.; Perdew, J. P. Strongly Constrained and Appropriately Normed Semilocal Density Functional. *Phys. Rev. Lett.* **2015**, *115*, No. 036402.

(40) Sun, J.; Remsing, R. C.; Zhang, Y.; Sun, Z.; Ruzsinszky, A.; Peng, H.; Yang, Z.; Paul, A.; Waghmare, U.; Wu, X.; Klein, M. L.; Perdew, J. P. SCAN: An Efficient Density Functional Yielding Accurate Structures and Energies of Diversely-Bonded Materials. 2015, arXiv:1511.01089. arXiv.org e-Print archive. https://arxiv.org/abs/1511.01089.

(41) Perdew, J. P.; Ernzerhof, M.; Burke, K. Rationale for Mixing Exact Exchange with Density Functional Approximations. *J. Chem. Phys.* **1996**, *105*, 9982.

(42) Shi, D.; Guo, Z.; Bedford, N. Electro-Optical and Piezoelectric Applications of Zinc Oxide. In *Nanomaterials and Devices*; Elsevier, 2015; pp 175−190.

(43) Blundell, S. *Magnetism in Condensed Matter*; Oxford University Press Inc.: New York, 2001.

(44) Néda, Z. *Mean-Field Approach to Magnetism*; Babes-Bolyai University: Cluj, 2011, pp 1−26.

(45) Clusel, M.; Fortin, J.-Y. Grassmann Technique Applied to Classical Spin Systems. *Condens. Matter Phys.* **2009**, *12*, 463−478.

(46) Dovesi, R.; Ricart, J. M.; Saunders, V. R.; Orlando, R. Superexchange Interaction in K_2NiF_4: an Ab Initio Hartree-Fock Study. *J. Phys.: Condens. Matter* **1995**, *7*, 7997−8007.

(47) Pisani, L.; Montanari, B.; Harrsion, N. M. A Defective Graphene Phase Predicted to be a Room Temperature Ferromagnetic Semiconductor. *New J. Phys.* **2008**, *10*, No. 033002.

(48) Balcerzak, T.; Szałowski, K.; Jaščur, M.; Žukovič, M.; Bobák, A.; Borovský, M. Thermodynamic Description of the Ising Antiferro-magnet on a Triangular Lattice with Selective Dilution by a Modified Pair-Approximation *Method. Phys. Rev. E* **2014**, *89*, No. 062140.

(49) Pueyo Bellafont, N.; Viñes, F.; Hieringer, W.; Illas, F. Predicting Core Level Binding Energies Shifts: Suitability of the Projector Augmented Wave Approach as Implemented in VASP. *J. Comput. Chem.* **2017**, *38*, 518−522.

(50) Blum, V.; Gehrke, R.; Hanke, F.; Havu, P.; Havu, V.; Ren, X.; Reuter, K.; Scheffler, M. Ab Initio Molecular Simulations with Numeric Atom-centered Orbitals. *Comput. Phys. Commun.* **2009**, *180*, 2175−2196.

(51) Lazar, P.; Mach, R.; Otyepka, M. Spectroscopic Fingerprints of Graphitic, Pyrrolic, Pyridinic, and Chemisorbed Nitrogen in N-Doped Graphene. *J. Phys. Chem. C* **2019**, *123*, 10695−10702.

(52) Susi, T.; Scardamaglia, M.; Mustonen, K.; Tripathi, M.; Mittelberger, A.; Al-Hada, M.; Amati, M.; Sezen, H.; Zeller, P.; Larsen, A. H.; Mangler, C.; Meyer, J. C.; Gregoratti, L.; Bittencourt, C.; Kotakoski, J. Intrinsic Core Level Photoemission of Suspended Monolayer Graphene. *Phys. Rev. Materials* **2018**, *2*, No. 074005.

(53) Ambrosi, A.; Sofer, Z.; Pumera, M. Electrochemical Exfoliation of Layered Black Phosphorus into Phosphorene. *Angew. Chem., Int. Ed.* **2017**, *56*, 10443−10445.

(54) Hofer, C.; Skalalova, V.; Monazam, M. R. A.; Mangler, C.; Kotakoski, J.; Susi, T.; Meyer, J. C. Direct Visualization of the 3D Structure of Silicon Impurities in Graphene. *Appl. Phys. Lett.* **2019**, *114*, No. 053102.

(55) Krivanek, O. L.; Chisholm, M. F.; Nicolosi, V.; Pennycook, T. J.; Corbin, G. J.; Dellby, N.; Murfitt, M. F.; Own, C. S.; Szilagyi, Z. S.; Oxley, M. P.; Pantelides, S. T.; Pennycook, S. J. Atom-by-Atom Structural and Chemical Analysis by Annular Dark-Field Electron Microscopy. *Nature* **2010**, *464*, 571−574.

(56) Babar, R.; Kabir, M. Ferromagnetism in Nitrogen Doped Graphene. *Phys. Rev. B* **2019**, *99*, No. 115442.

(57) Lieb, E. H. Two Theorems on the Hubbard Model. *Phys. Rev. Lett.* **1989**, *62*, 1201−1204.

(58) Yazyev, O. V.; Helm, L. Defect-Induced Magnetism in Graphene. *Phys. Rev. B* **2007**, *75*, No. 125408.

186

(59) Denis, P. A. Mono and Dual Doped Monolayer Graphene with Aluminum, Silicon, Phosphorus and Sulfur. *Comput. Theor. Chem.* **2016**, *1097*, 40−47.

(60) Błoński, P.; Otyepka, M. First-principles Study of the Mechanism of Wettability Transition of Defective Graphene. *Nanotechnology* **2017**, *28*, No. 064003.

(61) Błoński, P.; Łodziana, Z. First-principles Study of $LiBH_4$ Nanoclusters Interaction with Models of Porous Carbon and Silica Scaffolds. *Int. J. Hydrogen Energy* **2014**, *39*, 9848−9853.

(62) Larrude, D. G.; da Costa, M. E. H. M.; Monteiro, F. H.; Pinto, A. L.; Freire, F. L., Jr. Characterization of Phosphorus-Doped Multiwalled Carbon Nanotubes. *J. Appl. Phys.* **2012**, *111*, No. 064315.

(63) Hou, H.; Shao, L.; Zhang, Y.; Zou, G.; Chen, J.; Ji, X. Large-Area Carbon Nanosheets Doped with Phosphorus: A High-Performance Anode Material for Sodium-Ion Batteries. *Adv. Sci.* **2017**, *4*, No. 1600243.

(64) Ruiz-Soria, G.; Susi, T.; Sauer, M.; Yanagi, K.; Pichler, T.; Ayala, P. On the Bonding Environment of Phosphorus in Purified Doped Single-Walled Carbon Nanotubes. *Carbon* **2015**, *81*, 91−95.

(65) Ronchi, C.; Datteo, M.; Perilli, D.; Ferrighi, L.; Fazio, G.; Selli, D.; Di Valentin, C. π Magnetism of Carbon Monovacancy in Graphene by Hybrid Density Functional Calculations. *J. Phys. Chem. C* **2017**, *121*, 8653−8661.

(66) Denis, P. A.; Huelmo, C. P.; Iribarne, F. On the Band Gaps and Effective Masses of Mono and Dual Doped Monolayer Graphene. *Comput. Mater. Sci.* **2017**, *137*, 20−29.

(67) Błoński, P.; Hafner, J. Magnetic Anisotropy of Transition-Metal Dimers: Density Functional Calculations. *Phys. Rev. B* **2009**, *79*, No. 224418.

(68) Ekholm, M.; Gambino, D.; Jönsson, H. J. M.; Tasnádi, F.; Alling, B.; Abrikosov, I. A. Assessing the SCAN Functional for Itinerant Electron Ferromagnets. *Phys. Rev. B* **2018**, *98*, No. 094413.

(69) Gao, W.; Abtew, T. A.; Cai, T.; Sun, Y. Y.; Zhang, S. B.; Zhang, P. False Prediction of Fundamental Properties of Metals by Hybrid Functionals. 2015, arXiv:1504.06259. arXiv.org e-Print archive. https://arxiv.org/abs/1504.06259.

(70) Power, S. R.; Ferreira, M. S. Indirect Exchange and Ruderman−Kittel−Kasuya−Yosida (RKKY) Interactions in Magnetically-Doped Graphene. *Crystals* **2013**, *3*, 49−78.

187

Graphene Lattices with Embedded Transition-Metal Atoms and Tunable Magnetic Anisotropy Energy: Implications for Spintronic Devices

Rostislav Langer, Kimmo Mustonen, Alexander Markevich, Michal Otyepka, Toma Susi,* and Piotr Błoński*

Read Online

ACCESS | Metrics & More | Article Recommendations | Supporting Information

ABSTRACT: Doping of the graphene lattice with transition-metal atoms resulting in a high magnetic anisotropy energy (MAE) is an important goal of materials research owing to its potential application in spintronics. In this article, using spin-polarized density functional theory including spin−orbit coupling, we examined the magnetic properties of graphene with vacancy defects, both bare and nitrogen-decorated, and doped by Cr, Mn, and Fe transition-metal single atom (TM-SA) and two different TM atoms simultaneously. The adsorption of a second TM atom on an already embedded TM atom, i.e., the formation of upright TM dimers, was also considered. It is found that the graphene-mediated coupling between TM dopants can significantly increase MAE compared to that of SA impurities. While the MAE of TM-SA did not exceed 2 meV, it was enhanced to −23 meV for Cr and Fe simultaneously embedded into two separated double-vacancy (DV) defects and to a remarkably high value of 119.7 meV for two upright Fe−Mn dimers bound to two separate DVs, considerably exceeding the sum for individual TM-SAs. The latter MAE corresponds to a blocking temperature of 34 K assuming a relaxation time of 10 years. The origin of the enhanced MAE is discussed in relation to the spin excitations at the Fermi level and changes in d-derived states accompanying the rotation of the magnetization between in-plane and out-of-plane directions. We demonstrate that the presence of partially occupied degenerate states at the Fermi level favors its formation. The stability of the systems is also discussed. The computational findings are supplemented by an atomic-resolution characterization of an incidental Mn impurity bonded to four carbon atoms, whose localized spin matches expectations as measured using core-level electron energy-loss spectroscopy. Conducting TM-doped graphene with robust magnetic features offers prospects for the design of graphene-based spintronic devices.

KEYWORDS: doped graphene, defective graphene, magnetism, magnetic anisotropy energy, blocking temperature
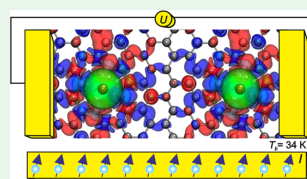
■ INTRODUCTION

Since the isolation of graphene in 2004,[1] a great deal of research effort has been devoted to endowing it with robust magnetic features that are lacking in its pristine form to enhance its potential in spintronic applications[2] ranging from quantum computing[3] to storing data in magnets with the size of single atoms.[4] One of the great challenges in this field is preventing thermally induced reorientation of the magnetic moments between the easy and hard magnetization axis or, in other words, increasing the blocking temperatures (T_b), which is enforced by MAE, i.e., the energy barrier for magnetic moments to flip their directions. A high MAE necessitates large spin and orbital magnetic moments per atom and a large spin−orbit coupling (SOC). Further, magnetic anisotropy is highly dependent on symmetry, dimensionality, and atomic composition and is often found to be much larger in low-symmetry nanostructures than in highly symmetric bulk materials.[5−8] Surface-supported nanoparticles offer additional degrees of freedom to tune the MAE by the particle shape and size—down to single atoms and coupling with the substrate.[9−11]

To this end, transition-metal (TM) atoms and their nanoclusters adsorbed onto graphene have been extensively studied.[7,12,13] While they can be mobile over structurally perfect regions of the graphene sheet, lattice imperfections create spots that can firmly anchor TM atoms or clusters, preventing their diffusion and conserving their size, symmetry, and, accordingly, the desired properties.[12,14−16]

As revealed by density functional theory calculations (DFT), Fe clusters can promote vacancy formation, i.e., it becomes easier to remove C atoms from the graphene lattice in the presence of Fe.[17] A high diffusion barrier of 6.8 eV has been calculated for a Fe atom in a single vacancy (SV) defect in the graphene lattice using the Perdew−Burke−Ernzerhof (PBE)
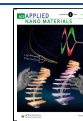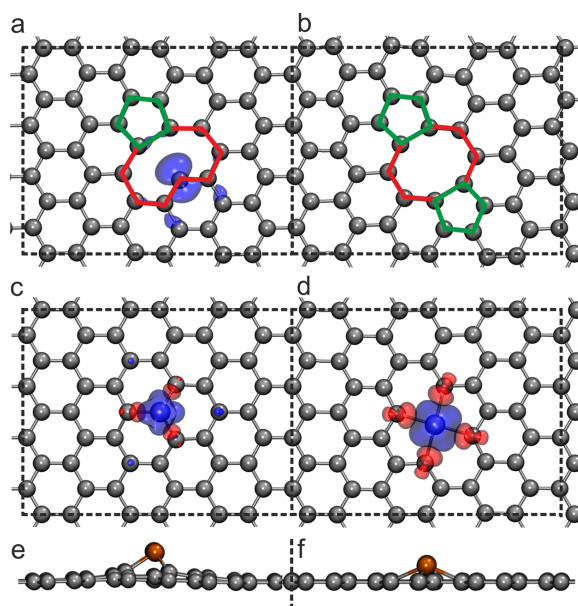
Figure 1. Top view of (a) single-vacancy defect in graphene, (b) double-vacancy defect in graphene, (c) TM@SV, and (d) TM@DV (where TM stands for Cr, Mn, and Fe). Side view of (e) TM@SV and (f) TM@DV. Carbon atoms are depicted in gray, and TM atoms in ocher. Five-membered rings are highlighted in green, and eight- and nine-membered rings are highlighted in red (*cf.* text). Spin densities corresponding to positive/negative magnetic moments are displayed in blue/red at isosurface values of ± 0.035 e$^-$ Å^{-3}. Supercells are marked by dashed lines. After the cell was doubled in the x-direction, a second defect was introduced into the lattice.

functional, sufficient to prevent the migration of Fe at room temperature.[18] The strong adsorption of Fe in vacancy defects in graphene was found to give rise to a large anisotropy in geometries and MAE, which, however, did not exceed 1 meV.[17] Although theory predicted ferromagnetic (FM) alignment for four Fe atoms substituting C atoms in a 6 × 6 supercell of graphene that initially contains 72 C atoms (corresponding to 5.55 atom % dopant concentration),[19] a single Fe atom embedded in SV was found to be nonmagnetic. In contrast, a single Fe atom in a double-vacancy (DV) defect in graphene acquired a high magnetic moment of 3.5 μ_B.[14] The high spin state of Fe@DV was further experimentally verified via core-level electron energy-loss spectroscopy of its L edge white-line intensity ratio.[20]

Theoretical calculations based on DFT have also revealed strong binding of Sc-Zn, Pt, and Au atoms in vacancy defects in graphene due to the strong interaction between sp^2 carbon and spd orbitals of a metal, with migration barriers around 2−4 eV for metals at SV and slightly higher for DV. The total magnetic moments of Cr and Mn were 2 and 3 μ_B, respectively, for both types of defects.[18] The nonbonding d-orbitals were partially occupied for Cr and Mn, while the antibonding states were filled for Fe.[21] Further, the Curie temperature of Cr@SV was theoretically estimated to be 498.2 K.[19]

DFT calculations have revealed that graphene doped by a single Mn atom undergoes a transition from nonmagnetic semimetal into an FM half-metal.[22] A second Mn atom binds preferentially in the immediate vicinity of the Mn already

present in the graphene lattice, and they interact antiferro-magnetically (AFM) in the ground state (GS).[19,22] The magnetic moments of Mn@SV vary with the Mn concentration and originate from the p−d exchange mechanism.[23]

Such calculations have also indicated that doping a Cr atom into the SV defect in graphene tuned its Fermi level (E_F) from semimetal to half-metal. The p−d exchange mechanism between the C-p and Cr-d states was responsible for the induced magnetism in the otherwise nonmagnetic graphene.[24] The doping of two Cr atoms into the graphene monolayer generated a magnetic moment of ~4 μ_B. Depending on the distance between the Cr dopants, the GS was found to be FM, AFM, or paramagnetic (PM). The origin of the particular magnetic state was described on the basis of RKKY indirect exchange interactions.[25] Experimentally, a Cr atom was inserted into e-beam-induced vacancies in a graphene lattice *in situ* in STEM, although unfortunately its electron energy-loss spectrum was not reported.[26]

Despite the abundant computational literature on the structural, electronic, and magnetic properties of graphene doped with Cr, Mn, and Fe, calculations of their MAEs are more elusive[14,17] and, to the best of our knowledge, MAE of Cr- and Mn-doped graphene has not been calculated until now. This is surprising because the estimation of the magnetic anisotropy caused by SOC is of fundamental importance for assessing the material's applicability for spintronic applications. Further, information can be stored and processed in the atomic scale, if the atomic spins are coupled.[3,27,28] Thus, for the

Table 1. Binding Energy E_{bind} (eV), TM−C Bond Length (Å), Total Magnetic Moment μ_{tot} (μ_B), Magnetic Moment of TM μ_{TM} (μ_B), Magnetic Moment of Nearest Carbon Atoms μ_C (μ_B), Bader Charges q_{Bader} of TM (e^-), $MAE_{(TE)}$, and $MAE_{(FT)}$ (Both in meV) of TM@SV and TM@DV

system	E_{bind}	TM−C	μ_{tot}	μ_{TM}	μ_C	q_{Bader}	$MAE_{(TE)}$	$MAE_{(FT)}$
Cr@SV	−6.47	1.88	2.00	2.44	−0.12	1.04	−0.15	−0.11
Mn@SV	−6.39	1.85	3.00	2.75	−0.09	0.91	−0.26	−0.25
Fe@SV	−7.13	1.81	1.95	1.81	−0.03	0.74	0.83	0.25
Cr@DV	−7.24	2.07	2.00	2.44	−0.10	1.18	0.05	0.02
Mn@DV	−7.21	1.98	3.25	3.42	−0.08	1.17	0.64	0.49
Fe@DV	−6.48	1.90	3.16	2.98	−0.03	1.17	1.11	0.21

questionable, and if moderate values of the on-site Coulomb repulsion are admitted, they introduce only modest changes with respect to conventional DFT calculations,[27] whereas large values of the on-site repulsion led to unrealistic eigenvalue spectra of TM dimers,[48] we used DFT + U method with U−J of 2 eV.

In addition to fully self-consistent calculations of MAE, the magnetic force theorem,[49] $MAE_{(FT)}$, was applied. The FT allows us to approximate the MAE by the difference in the band energies from non-self-consistent calculations, thus significantly reducing the computational efforts, although it can also lead to errors that are difficult to control.[14]

The energy barrier against thermal agitations can be represented by the MAE via a simple equation, $MAE = k_B T$. Thus, an MAE of 32 meV would be sufficient to allow the system withstand a single thermal excitation up to 373 K. However, given the stochastic nature of the thermally induced reversal of the magnetization direction, the MAE corresponds to the blocking temperature T_b by an equation based on Néel's theory[50]

$$MAE = k_B T_b \left(\ln \frac{\tau_N}{\tau_0} \right)$$

where τ_N represents the aimed relaxation time (10 years) and τ_0 is the attempt period specific for every magnetic material (usually in the order of 10^{-10} s, which is also assumed here).

■ EXPERIMENTAL DETAILS

Scanning transmission electron microscopy images were recorded using an aberration-corrected Nion UltraSTEM100 instrument operated at 60 kV in near-ultrahigh vacuum using the MAADF (medium-angle annular dark-field) detector with an angular range of 80−200 mrad. As a sample, we used chemically synthesized commercial monolayer graphene (Graphenea), which occasionally contains incidental lattice imperfections. Localized magnetic moment analysis was further conducted via electron energy-loss spectroscopy using a Gatan PEELS 666 spectrometer retrofitted with an Andor iXon 897 electron-multiplying charge-coupled device camera, with an energy spread of approximately 0.35 eV and a dispersion of 0.5 eV px^{-1}. The Mn L edge fine structure white-line ratio L_3/L_2, which represents dipole transitions from the Mn $2p_{3/2}$ and Mn $2p_{1/2}$ to unoccupied 3d levels,[20] was calculated after smoothing the spectrum with a 3.5 eV moving average, and then subtracting the pre-edge background to estimate the L_3 peak area, followed by subtracting the background from the tail of that peak to determine the L_2 peak area.

■ RESULTS

Single-Atom Doped Graphene. First, we focused on the binding energies and structural properties of TM@SV and TM@DV (Figure 1). All TM atoms were strongly bound to defective graphene in line with previous reports.[14,18,21] Binding in the DV defect was more favored than in the SV defect in line

with a larger charge transfer from TM atoms to graphene lattice in TM@DV (Table 1). TM atoms were lifted out of the graphene plane during optimization due to the steric effect of their larger size. For the TM@SV, the length of the TM−C bond varied between 1.81 and 1.88 Å. The bonds of TM@DV were longer, in the range 1.90−2.07 Å (Table 1). Generally, the length of the TM−C bond decreased in the order from Cr to Fe as the size of the atoms decreases. TM@SV caused buckling of the graphene layer, which was more pronounced in the vicinity to the TM atom, while for TM@DV, almost no buckling was observed (Figure S2).

Bader analysis showed charge transfer from TM atoms to their carbon neighbors (0.7−1.2 e^-, cf. Table 1) consistent with the higher electronegativity of C than the TM atoms. We also considered the charge states of TM (common oxidation states II and III) in SV and DV defects using the finite model of ovalene (Figure S3), B3LYP[51,52] functional, and def2SVP basis set as implemented in Gaussian 09.[53] The natural bond orbital (NBO) analysis[54] was employed to evaluate TM's partial charges. The analysis revealed a charge transfer mainly from the s and p orbitals of TM atoms, while the C atoms of graphene lattice back-donate charge to the d-orbitals of TM atoms (Tables S1 and S2).

All TM atoms studied here induced magnetic moments in graphene (Figure 1c,d). In TM@SV, three metal valence electrons participate in the formation of TM−C σ-bonds, one electron in a TM−C π-bond, and remaining unpaired valence electrons (two of Cr and three of Mn) induce magnetic moments of 2.0 and 3.0 μ_B, respectively (Table 1). In TM@DV, metal valence electrons are involved in the formation of four TM−C σ-bonds and one to create the π-bond. The π-electrons on the atoms in the immediate vicinity to the DV defect have opposite spins canceling each other out; the remaining valence electrons of TM atoms induce magnetic moment in graphene (Table 1). The magnetic moments on Fe were 1.8 μ_B and 3.0 μ_B for Fe@SV and Fe@DV, respectively. An earlier study at the GGA-PBE level revealed a zero magnetic moment for Fe@SV because the Fe impurity has doubly occupied states and an even number of electrons;[18] however, the on-site Coulomb correction led to the non-magnetic solution higher in energy than the magnetic one by 0.03 eV in agreement with the study by Santos et al.[21]

Doping with TM atoms induced changes in the electronic structure of graphene from semimetal to metal (Mn@DV and Fe@DV), half-metal (Fe@SV[17,19]), and/or semiconductor (Cr@SV,[19,26] Mn@SV,[22,55] and Cr@DV[26]), in good agreement with the literature, as depicted in Figure S1 and Table S3. However, the atom- and orbital-decomposed partial densities of states (PDOS) revealed an even more complex picture of changes in the electronic structure of graphene upon doping. Although the C_{3v} symmetry of TM@SV broke the degeneracy

190

application of graphene in spintronic devices, the graphene lattice will contain multiple TM atoms rather than a single-atom dopant. In addition, the easy axis must be oriented perpendicular to the surface of the substrate to reduce the dipolar magnetic interactions between neighboring magnetic moments. Hence, examining the interaction of magnetic atoms in the graphene lattice is of both fundamental and practical interest.

In this work, systematic spin-polarized (SP) DFT calculations including SOC were carried out to investigate structural, electronic, and magnetic properties of defective graphene containing SV and DV defects, optionally also N-decorated,[29] doped with Cr, Fe, and Mn. In light of recent advances in the experimental manipulation of foreign atoms in the graphene lattice[30,31] and the theoretical prediction for manipulation of a Fe atom,[32] these elements were selected as examples from Groups VI–VIII.B to elucidate changes in electronic and magnetic properties of doped graphene, including the MAE, with respect to the distances between TM atoms, both of the same element and two different TM atoms. The formation of upright TM dimers was further considered. Our main finding is that doping graphene with two different TM atoms and the formation of TM dimers leads to a tremendous increase in MAE compared to SA-doped graphene.

■ COMPUTATIONAL DETAILS

First-principles calculations were performed using SP-DFT as implemented in the Vienna Ab initio Simulation Package (VASP).[33–35] The electron−ion interactions were treated by the projector-augmented wave (PAW) method.[36,37] The basis set contained plane waves with a maximum kinetic energy of 500 eV. The electronic exchange and correlation effects were treated by the Perdew−Burke−Ernzerhof (PBE)[38] functional in the generalized gradient approximation (GGA).

The graphene monolayer was represented by 3×3 and 6×3 orthorhombic cells containing 48 and 96 atoms, respectively, and a vacuum layer of 15 Å deployed along the z-direction to avoid spurious interactions between the images of the graphene layers due to the periodic boundary conditions. To construct the SV and DV defects, one and two carbon atoms were removed from the graphene lattice, respectively, which resulted in the reconstruction of carbon bonds after optimization[39] (Figure 1a,b). In the SV, five- and nine-membered rings were formed, and due to the unsaturated C center (2-fold-coordinated C atom) a local magnetic moment of about 1.2 μ_B was observed.[39] In the DV five- and eight-membered rings were formed and remained nonmagnetic as the reconstruction of the atomic positions facilitates an overlap of unpaired sp^2 electron clouds. The density of states (DOS) of SV showed spin-polarized metallic behavior (Figure S1a), while DV exhibited nonmagnetic DOS with a band gap of 0.1 eV (Figure S1e). Nitrogen-containing vacancy defects were also considered; the quadruple-N-decorated double vacancy (NDV) was nonmagnetic, while the corresponding triple-N-decorated single vacancy (NSV) possessed a magnetic moment of 0.3 μ_B.[40] To include TM atoms, we initially placed the Cr, Mn, and Fe atoms ∼1 Å above the center of the optimized vacancy because it is the most preferred binding site[14] and reoptimized the structures.

We further introduced two defects in the 6×3 cell to examine possible changes in the structural, electronic, and magnetic properties of graphene doped with two TM atoms of the same/different elements. We also considered changes in the distance between TM atoms and their effect on the properties of the doped graphene. Finally, we adsorbed another TM atom on top of TM@(N)SV and TM@(N)DV to study the properties of dimers TM2@TM1@(N)SV and TM2@TM1@(N)DV.

All structures were optimized until forces acting on all atoms were reduced to less than 10 meV/Å and the electronic and magnetic degrees of freedom were relaxed until the change in total energy between successive iteration steps was smaller than 10^{-6} eV. A Gaussian smearing of width 0.02 eV was used for partial occupancies of orbitals. For sampling of the Brillouin zone, convergence tests demonstrated the sufficiency of a Γ-centered $6 \times 6 \times 1$ k-point mesh ($3 \times 6 \times 1$ mesh for the 6×3 cell). Static calculations were performed with the tetrahedron method with Blöchl correction,[41] while keeping the remaining computational parameters unchanged.

The binding energies, E_{bind}, of TM atoms to defective graphene were evaluated as

$$E_{bind} = E_{DG+TM} - E_{DF} - E_{TM}$$

where E_{DG+TM}, E_{DF}, and E_{TM} are energies of defective graphene doped with TM, defective graphene, and a single TM atom in the gas phase, respectively. The binding energy of a second (upper) TM atom with the lower TM atom already embedded into the graphene lattice to form an upright TM dimer was evaluated as

$$E_{bind} = E_{DG+TM1+TM2} - E_{DF+TM1} - E_{TM2}$$

To further assess the stability of TM atoms and dimers in their ground-state configurations, we evaluated their migration barriers from imperfect regions of the graphene lattice. In addition, the Hessian matrix was determined to exclude the presence of imaginary modes in the spectrum of phonon frequencies. The finite difference method was used, i.e., each ion was displaced in the direction of each Cartesian coordinate, and from the forces, the Hessian matrix was determined. Only symmetry-inequivalent displacements were considered with a step size of 0.02 Å and the self-consistency cycle converged until the energy difference reached 10^{-7} eV.

Bader charge analysis[42,43] was performed to evaluate the charge located on each atom (q_{Bader})

$$q_{Bader} = V_{val} - N_{Bader}$$

where V_{val} and N_{Bader} denote the number of valence electrons in a free atom and the computed number of valence electrons in the atom in the system, respectively.

Spin−orbit coupling has been implemented in VASP by Kresse and Lebacq following the approach of Kleinman[44] and MacDonald et al.[45] Calculations including SOC were performed in the noncollinear mode as implemented in VASP by Hobbs et al.[46] The magnetic anisotropy energy (MAE) per computational cell was evaluated as the difference in total energies (TE) between different orientations of the magnetization

$$MAE = E_x - E_z$$

In this convention, a positive MAE corresponds to an easy axis perpendicular to the graphene plane. For selected systems and the denser $11 \times 11 \times 1$ k-point mesh, the MAE changes were about 1 meV.[14]
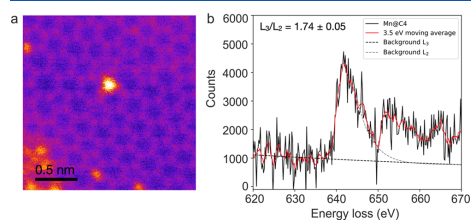
Since DFT + U methods depend on semiempirical values of $U−J$[47] whose transferability between different systems is

191

of d-orbitals into d_{z^2}, $d_{xy}/d_{x^2-y^2}$ and d_{xz}/d_{yz} that coupled with the p-orbitals of the carbon atoms, the coupling of states with energies above and below the Fermi level (E_F) through spin–orbit interaction promotes either perpendicular or in-plane magnetization, depending on the spins and symmetries of the interacting states,[56,57] as schematically shown in Figure S4. PDOS of Cr@SV demonstrated predominant contribution of the occupied d_δ (and in a smaller extent d_{z^2}) orbitals and empty d_{z^2} orbital to the intragap states (Figure S5) favoring in-plane MAE, which is, however, dominated by the large energy denominator and, thus, very small. PDOS of Mn@SV and Fe@SV (Figures S6 and S7) showed that the TM d_{z^2} orbital contributes to the spin-up valence band (VB) edge and the TM d_δ and d_π orbitals to the spin-down conduction band (CB) edge that provides competitive negative/positive contributions to the MAE. The spin-up VB(CB) edge of Cr@DV (Figure S8) exhibited sharp peaks of $d_{xy}/d_{x^2-x^2}$ (d_{xz}/d_{yz}); thus, the electron hopping between the nearest occupied and unoccupied states favors the in-plane anisotropy, which is counterbalanced by another mechanism, i.e., lowering of the total energy by a downshift of $d_{x^2-y^2}$-derived bands. Since the degenerate $d_{xy}/d_{x^2-y^2}$ states are far from E_F, the effect is small, and altogether, the MAE for Cr@DV does not exceed 0.05 meV (Table 1). Both Mn@DV (Figure S9) and Fe@DV (Figure S10) showed half-metallic DOS originating, respectively, from spin-up and spin-down of d_{xz}/d_{yz}, which provides the primary contribution to the positive MAE.

SP-DFT calculations including SOC revealed quite small MAEs ranging between ±0.1 and 1.1 meV and increasing within the Cr–Mn–Fe order (Table 1) in line with the low orbital moment anisotropy at isotropic spin moments (Table S4). The magnetic force theorem provided even lower values of MAE (Table 1).

In our scanning transmission electron microscopy observations of chemically synthesized monolayer graphene, we were able to find an incidental Mn impurity bonded to four carbon neighbors in a defected area of the lattice (Figure 2a). The identity of the impurity was confirmed by electron energy-loss spectroscopy, which also allowed us to determine its Mn L_3/L_2 white-line ratio as 1.74 ± 0.05 (Figure 2b). This value contrasts with the almost twice as high value of 3.38 ± 0.05 reported by Lin et al. for Fe@DV.[20] While it is difficult to precisely quantify the values of their magnetic moment based

on these ratios,[58] such a large difference is surprising considering that our simulation results shown in Table 1 would lead to expect that both Fe and Mn exhibit similar localized magnetic moments.

The reason for this discrepancy could be the local disorder here: while the Mn is bonded to four carbon neighbors, the nearby lattice contains pentagonal and heptagonal rings. Furthermore, other impurities that are presumably silicon are bound to vacancies in the nearby lattice, which might further disturb the localized properties of the Mn site. Indeed, simulations with simultaneous Mn and Si dopants in the 6×3 cell indicated the reduction of the magnetic moment on Mn because of nearby Si (Tables S5 and S6). Bader charge analysis revealed a charge transfer of 2.2−2.5 e− from Si to the graphene lattice, and the DOS plots of $Mn_1Si@SV$ and $Mn_1Si@DV$ shown in Figure S11 exhibit small electronic gaps, overlap of p_z^- and d_{z^2}-derived states, and, thus, the reduced Mn magnetic moment. There are multiple Si atoms in the experimental sample, which further reduces the Mn magnetic moment. These findings highlight the sensitivity of the experimental magnetic moment to sample quality and the need for further systematic studies.

Very recently, the incorporation of substitutional Mn atoms into SV defects in graphene on Cu(111) has been reported.[59] While the L_3/L_2 Mn white-line ratio has not been studied, the reported magnetic moment on Mn from DFT calculations is ∼3 μ_B, which agrees with our results (Table 1).

Graphene Simultaneously Doped by Two TM Atoms. Recent experimental manipulation of impurity atoms in monolayer graphene[30,31,60] has raised our interest in studying the influence of the mutual arrangement and distance of TM atoms (thereafter denoted as $TM_1TM_2@SV$ and $TM_1TM_2@DV$) on the electronic and magnetic properties of graphene. We used a larger 6×3 orthorhombic cell containing 96-carbon atoms to introduce a second SV or DV defect in the graphene lattice as shown in Figure 1, and by changing the distance between the vacancy defects (Figures S12 and S13), we simulated the mutual interaction of TM atoms at different separations within the graphene lattice. Both cis/trans position of TM atoms in graphene lattice (i.e., both TM were above the graphene lattice vs one TM above and one below the lattice) were considered, but only the most energetically stable structures are discussed in the following.

While virtually no differences in the structural features of $TM_1TM_2@SV$ and $TM_1TM_2@DV$ were observed compared to TM@SV and TM@DV, the magnetic moments significantly differed from those of single TM-atom-doped graphene (Tables S7 and S8). One could expect that the magnetic moments of the larger 6×3 cells should correspond to the sum of the magnetic moments of TM-SAs (this is indeed true for CrCr@SV and MnMn@SV); however, CrCr@DV and MnMn@DV exhibited even higher magnetic moments indicating a synergistic effect between the TM atoms, i.e., a maximum value of 8.0 μ_B per computational cell vs the expected 4.0 μ_B for Cr and 6.0 μ_B for Mn. At the same time, the values of magnetic moments varied between 6.1 and 8.0 μ_B (CrCr@DV) and between 7.3 and 8.0 μ_B (MnMn@DV) depending on the mutual TM−TM distance, and between 2.5 and 6.0 μ_B and between 5.6 and 6.9 μ_B, respectively, for FeFe@SV and FeFe@DV (Tables S7 and S8). No systematic change of magnetic moments with the TM−TM distance was however observed. In agreement with the previous reports[19,22,25,61] depending on the distribution of the TM atoms in the

Figure 2. Experimental observation of an Mn@DV impurity. (a) STEM/MAADF image of the Mn atom (bright contrast) bonded to four carbon atoms in a disordered patch of graphene. The slight irregular variation in the contrast of some scan lines before the impurity is likely due to mechanical or electronic scan noise. (b) EEL spectrum of the Mn L core edge, confirming the identity of the impurity and allowing us to determine its localized magnetic moment via the L_3/L_2 white-line ratio.

Table 2. Binding Energy E_{bind} (eV), TM_1–TM_2 Distance (Å), Total Magnetic Moment μ_{tot} (μ_B), Magnetic Moments of TM_1 and TM_2 μ_{TM1}, μ_{TM2} (μ_B), and MAE$_{(TE)}$ and MAE$_{(FT)}$ (Per Computational Cell, Both in meV) of TM_1TM_2@SV and TM_1TM_2@ DV Depicted in Figures S32–S38

structure	E_{bind}	TM_1–TM_2	μ_{tot}	μ_{TM1}, μ_{TM2}	MAE$_{(TE)}$	MAE$_{(FT)}$
CrFe@SV	−12.16	13.24	4.00	2.49, 1.55	8.80	0.15
CrMn@SV	−11.73	12.86	5.00	2.48, 2.73	0.40	−0.34
FeMn@SV	−11.25	13.04	4.89	1.58, 2.84	2.90	−0.16
CrFe@DV (AFM)	−5.53	12.95	0.00	0.23, −0.04	−23.20	0.61
CrFe@DV	−5.52	12.95	6.00	2.43, 3.12	−23.00	0.49
CrMn@DV	−5.17	13.00	5.09	2.45, 3.42	16.00	0.59
FeMn@DV	−3.97	12.87	6.70	3.02, 3.48	−15.80	1.08

graphene lattice, the AFM order was more energetically preferred than the FM one; for instance, MnMn@SV (Figures S12-20) and CrCr@DV (Figure S13-4) were AFM in the GS and lower in energy by 69.8 and 30.4 meV, respectively, compared to the FM order.

Compared to TM@SV and TM@DV, DOS of TM_1TM_2@SV and TM_1TM_2@DV (Figures S14–S23 and S24–S31) changed significantly due to the introduction of a second TM atom into the graphene lattice. For the CrCr@SV GS structure (Figure S14; see also Figure S15), the degeneracy of the d_δ-derived states was broken, and they were broadened due to the largely increased binding energy of the second Cr atom. Further, an upshift toward lower binding energies was observed for occupied d_{xz}/d_{yz}, which were also broadened. Importantly, while the bandgap value (Table S9) for the GS structure was 0.5 (0.3) eV for the spin-up (down) channel, the less stable FM structure (Figure S12-4) exhibited metallic DOS (Figure S16), while in the AFM alignment (more stable than the FM one by 99.1 meV), it exhibited an electronic gap of 0.3 eV (Figure S17).

For MnMn@SV, a broadening and upshift of the occupied d states brought about the metallic character to the DOS of the GS structure (Figure S18, Table S9) with FM alignment of the magnetic moments. For the GS structure ordered AFM (Figure S19), and for the less stable system (Figure S20), the electronic gap was shrunk by 0.1–0.2 eV compared to the SA counterpart. Similarly, the electronic gap of FeFe@SV GS was as low as 0.1 eV (Table S9, Figure S21), or even disappeared for the GS−1 FM structure (Figure S22). The band gap of the GS-1 AFM structure (more stable than the FM one by 98.4 meV) was 0.2 eV (Figure S23).

For TM_1TM_2@DV, we observed the half-metallic (metallic) character of CrCr@DV in the GS (GS−1) (Figures S24–S26) and a small band gap (up to 0.3 eV) opening for MnMn@DV (Figures S27 and S28) and FeFe@DV in the spin-up channel (Figures S29 and S30) (Table S9). The AFM FeFe@DV (Figure S31) was lower in energy than the FM analogue by 29.7 meV and exhibited a tiny band gap of 0.1 eV.

Although the MAE changed within the range of 0.4 meV (calculated per computational cell) for the TM pairs, no systematic dependence of the MAE on the TM–TM distance was observed. While the MAE of both MnMn@SV and MnMn@DV roughly reached twice the MAE value of Mn@SV and Mn@DV, the MAE of CrCr@SV and CrCr@DV increased and the MAE of FeFe@SV and FeFe@DV decreased compared to the SA counterparts (Tables S7 and S8). It should be noted, however, that for the graphene-doping homoatomic pairs, the MAEs are in the sub-meV range, and the highest MAE found for CrCr@DV is only 1.6 meV. We also note that the sign of the MAE changed in some cases.

Since the value of MAE for homoatomic doped graphene did not significantly change with the mutual distance between TM atoms, for graphene doped with two different atoms, we only examined MAE for a fixed distance of 12.87–13.24 Å between TM_1 and TM_2. The total magnetic moment of such a system increased to approximately the sum of the magnetic moments of the individual TM atoms (Tables 2 and S10). The electronic band gaps reached roughly intermediate values obtained for the SA counterpart (Table S11 and Figures S32–S38). FeMn@SV and FeMn@DV exhibited metallic DOS. Apart from CrFe@DV, whose GS was AFM and higher in energy than the FM one by 15.4 meV, all other systems were FM in the GS.

Noticeably, the MAE (calculated per computational cell) significantly increased compared to the single TM atoms, reaching −23.0 meV for FM CrFe@DV, 16.0 meV for CrMn@DV, and −15.8 meV for FeMn@DV. The character of spin excitations near E_F remains similar for Cr in Cr@DV (Figure S8) and in mixed systems CrTM@DV (Figures S35, S36, and S39), i.e., the electron hopping between the nearest occupied and unoccupied states, d_{xy} and d_{yz}, favors the in-plane anisotropy. For the Mn atom in CrMn@DV, spin excitations involving spin-up occupied/empty $d_{xz/yz}$ and spin-up occupied d_{xz} and spin-down empty d_{z^2} favors positive MAE (Figures S37 and S40). For Mn in FeMn@DV (Figures S38 and S41), spin excitations in the immediate vicinity to E_F involving $d_{yz/xz}$ favor positive MAE, which is counterbalanced by the negative contribution from the coupling between majority-spin occupied d_{xy} and empty $d_{xz/yz}$. Similarly, the coupling between spin-majority occupied d_{yz} and spin-minority empty d_{xz}, and between spin-majority occupied d_{xy} and spin-minority unoccupied d_{xz} favors, respectively, negative and positive MAE.

While the occupation scheme of Fe in FeMn@DV is like in Fe@DV—the negative contribution to MAE is due to the coupling of majority-spin and minority-spin $d_{yz/xz}$, which compete with the positive contribution as described above for Fe@DV—it changed in CrFe@DV (Figure S35) so that now easy-plane is also favored due to the net negative contribution from the coupling between majority-spin/minority-spin occupied/unoccupied $d_{xz/yz}$, and between minority-spin d_{z^2} and unoccupied $d_{xz/yz}$; however, the coupling between majority-spin occupied $d_{xz/yz}$ and minority-spin unoccupied d_{z^2} provides a positive contribution to the MAE. One shall also note that the energy denominators in the mixed systems and thus the corresponding contributions to the MAE can be different from that in SA-doped graphene.

The visible effect of the enhanced MAE in DV-graphene doped with two different TM atoms, which contrasts with SA-doped graphene, is a changed splitting of energy bands that were degenerate in the absence of spin−orbit interaction,

specifically the $d_{xz/yz}$ states, and the downshift in binding energies of the d_{z^2} states, both leading to a lowering of the total energy (Figures S39−S44) upon the reorientation of the magnetization direction: The easy-plane of the CrFe@DV and FeMn@DV systems seems associated with the downshift in binding energies, respectively, d_{yz}, d_{xz}, and d_{z^2} states (Figures S39 and S40) and the d_{xz} and d_{yz} states (Figures S43 and S44). As for CrMn@DV, the changes in d-DOS of Cr at about −1.5 to −1.0 eV and of Mn at about −1.5 eV brought about the positive MAE (Figures S41 and S42). Surprisingly, the spin and orbit anisotropy for both CrFe@DV and CrMn@DV was ~0.0 μ_B, while for FeMn@DV, a substantial spin anisotropy at almost isotropic orbital moments was found (Table S10). Interestingly, when Cr and Mn atoms of CrMn@DV were separated by 6.55 Å, the MAE increased up to 47.5 meV due to a strong anisotropy of the spin moments (−0.55 μ_B).

Note that the MAE obtained using the magnetic force theorem, $MAE_{(FT)}$, was much lower than $MAE_{(TE)}$. In principle, FT calculations can be used to decipher the atomic and orbital partial contribution to MAE; however, this was not possible for the systems studied here due to the negligible $MAE_{(FT)}$.

The presence of TM atoms induces magnetic moments in the surrounding carbon atoms, as revealed by the asymmetry in electronic DOS (Figures S32−S44), i.e., the sharing of electrons between the magnetic atoms and the lattice leads to a net magnetic moment on the carbon sites (Figures S45−S47). Further, a (half)metallic DOS at E_F (CrMn@DV) and FeMn@DV can enable the conduction electrons to couple to the magnetic moments indicating the presence of an RKKY (Rudermann−Kittel−Kasuya−Yoshida)[62−64] exchange through the graphene lattice (Figure S48). For the CrFe@DV system with small energy gaps at E_F, the RKKY interaction is suppressed and the coupling between TM atoms is due to a superexchange network of interactions throughout the carbon atoms. Thus, the origin of the greatly enhanced MAE up to −23 meV for DV-graphene doped simultaneously by two different TM atoms can be sought in graphene-mediated coupling due to the RKKY-like superexchange interactions between TM atoms. Electrons predominantly hop between the occupied and unoccupied states in the immediate vicinity to E_F, which leads to the switch of magnetic anisotropy from the easy-plane direction for CrFe@DV (Figure S35) and FeMn@DV (Figure S38) to the out-of-plane direction for CrMn@DV (Figure S37). Although the RKKY-like superexchange interactions between Cr and Mn pairs and trimers doping the graphene lattice[65,66] have also been reported, only pairs of different TM atoms in DV appear to influence their electronic structures in favor of large MAEs.

Notably, the graphene-doping heteroatomic TM pairs should exhibit high stability in the vacancy defects (Table S12 and Figure S49). This contrasts the behavior of 3p/2p or 4p/2p co-doping elements, which in almost all cases prefer to replace a C−C bond.[67,68]

For the sake of completeness, the simultaneous adsorption of two TM atoms in the centers of two different defect types separated by about 7.8 and 9.5 Å was considered: Cr_1Cr_2@SVDV and CrFe@SVDV (Table S13 and Figure S50). The magnetic moments were close to the sum of the individual Cr@SV and Cr@DV systems; only the magnetic moment on Fe was lower as in Fe@DV. The MAEs were low, about 1 meV. However, it was significantly enhanced from 0.1 to 8.1 meV in Cr_1Cr_2@SVDV when the intervacancy distance

changed from 7.8 to 9.4 Å, indicating that in experimental samples, the precise implementation of TM atoms may play a significant role in achieving a large MAE.

Adsorption of a TM Atom onto TM-Doped Graphene. Theoretical calculations revealed that transition-metal dimers can exhibit an enhanced MAE than the SA-doped graphene.[7,14,48] Therefore, we considered TM−TM dimers embedded into defective graphene as shown in Figures S51−S62. The binding energy of a second TM atom on top of TM@DV and TM@SV was exothermic in energy ranging from −4.05 to −0.04 eV with a TM_1−TM_2 bond length of 1.98−2.85 Å (Table 3). It must be noted that while more stable

Table 3. Binding Energy E_{bind} (eV), TM_1−TM_2 Distance (Å), Total Magnetic Moment μ_{tot} (μ_B), Magnetic Moments of TM_1 and TM_2 μ_{TM1}, μ_{TM2} (μ_B), and $MAE_{(TE)}$ and $MAE_{(FT)}$ (Per Computational Cell, Both in meV) of TM_2@TM_1@SV and Dimers TM_2@TM_1@DV Depicted in Figures S51−S62

structure	E_{bind}	TM_1−TM_2	μ_{tot}	μ_{TM1}, μ_{TM2}	$MAE_{(TE)}$	$MAE_{(FT)}$
Cr@Cr@SV	−0.39	2.85	3.72	2.32, 1.28	−0.73	−0.43
Fe@Cr@SV	−1.66	2.19	2.97	1.89, 1.80	−6.85	−1.26
Mn@Cr@SV	−2.70	2.19	6.86	1.90, 4.38	−1.13	−0.22
Fe@Fe@SV	−0.09	2.27	1.42	−0.03, 1.37	−12.40	0.77
Fe@Mn@SV	−3.61	2.31	5.00	1.65, 3.44	−5.05	−1.79
Mn@Mn@SV	−0.19	2.47	7.98	2.48, 4.61	14.90	−1.96
Cr@Cr@DV	−0.04	2.48	6.00	0.75, 4.56	−0.42	−0.20
Fe@Cr@DV	−3.39	2.19	4.00	0.76, 3.09	−2.31	−1.39
Mn@Cr@DV	−4.05	2.19	3.00	−1.60, 3.84	0.35	0.27
Fe@Fe@DV	−1.58	2.13	3.96	−0.96, 3.75	−0.86	1.29
Fe@Mn@DV	−1.25	1.98	3.03	0.46, 2.52	9.79	0.61
Mn@Mn@DV	−2.64	2.37	8.04	3.30, 4.28	0.16	0.11

configurations may be obtained by binding TM atoms to graphene on both sides, the resulting MAEs are low, in the sub-meV range (cf. Table S14 and Figure S63), as are the MAEs of the graphene-doping TM-SAs.

The interaction between the TM atoms in a dimer led to lower or higher total (1.4−8.0 μ_B) and local magnetic moments compared to the SA-doped defective graphene (Tables 3 and S15). The magnetic moment of the lower TM atom was quenched by the adsorption of a second TM atom.
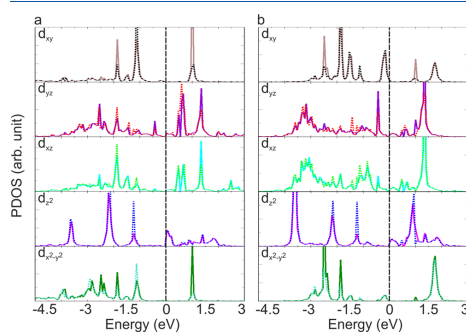
The relatively strong binding of a second TM_2 atom above the TM_1 in TM_2@TM_1@SV and TM_2@TM_1@DV significantly altered the electronic structure of the TM_1-doped graphene (Figures S51−S62, Table S16). Particularly, broadening and/or upshift of the states led to the metallic DOS for several systems (Cr@Cr@SV, Fe@Cr@SV, Fe@Fe@SV; cf. Figures S51, S52, S54, and S64−S67). For the metallic Fe@Cr@DV and Fe@Mn@DV, the reordering of states in the vicinity to E_F was observed (Figures S58, S61, and S67). In the remaining systems, the band gap in the range of 0.1−0.5 eV was calculated (Table S16).

Among the TM dimers considered, a large positive MAE was calculated for Fe@Mn@DV (9.8 meV) and Mn@Mn@SV (14.9 meV), and a large negative MAE for Fe@Fe@SV (−12.4 meV) (Table 3). The systems with the largest MAE exhibited the largest anisotropies of the magnetic moments (Table S15). The shape anisotropy contribution[69] to MAE is negligible, below 1 meV, increasing from 0.04 meV for the mixed-atom system CrFe@DV to 0.91 meV for Fe@Mn@DV. Since only Fe@Mn@DV has a big E_{bind} among dimers with a large MAE, we will focus only on it in the following.

Figure S61 shows the change of occupation of the Mn atom in the Fe@Mn@DV system compared to SA Mn@DV (Figure S9). The d_{xy/x^2-y^2} states of the lower atom are pushed down to −0.75 eV, the $d_{xz/yz}$ states above E_F, and d_{z^2} split into two components, one below occupied d_{xy/x^2-y^2} and another just above E_F. The states of Fe lie in the immediate vicinity to E_F. The d_{z^2} states of both TM atoms split and coincide indicating σ bonding between two metal atoms. The $d_{xz/yz}$ states of both TM atoms are broadened and overlap, indicating π bonding.

The spin excitations near E_F for the Mn atoms (Figure S61) favor a negative MAE. This, however, due to the large energy denominator is very small. Previous reports[13,14,16] have demonstrated that the leading contribution to the MAE is imposed by the upper TM atom despite the opposite sign of MAE of the lower TM atom. For the upper Fe atom, the coupling between minority-spin occupied d_{xy} and majority-spin empty $d_{xz/yz}$ favors the positive MAE. Further positive contribution to the MAE is associated with the downshift of the peaks in the d_{yz} spectra to about −1.4 to −1.2 eV for the perpendicular magnetization, which was located just below E_F for the in-plane direction. Altogether, the downshift in binding energies of the d-states of the upper TM atom favoring the positive MAE can be seen in the relativistic PDOS (Figures 3 and S67).

Figure 4. (a) Top view and (b) side view of spin densities plotted at ±0.01 e⁻ Å⁻³ isovalues for Fe@Mn (displayed in green/cyan for spin densities corresponding to positive/negative magnetic moments) and ±0.001 e⁻ Å⁻³ (shown in blue/red) for DV-graphene for the system of two Fe—Mn dimers bound to separate DV defects. (c) Side view of the corresponding structure. Gray, purple, and ocher colors represent carbon, manganese, and iron atoms, respectively.

excitations near E_F. However, the gapless PDOS facilitates graphene-mediated coupling between the dimers due to the RKKY exchange interactions (see above and Figure S69), and furthermore, the quasi-degeneracy of partially occupied states at E_F for in-plane magnetization is lifted for axial magnetization, as shown in Figure 5, bringing about the dominant

Figure 3. Relativistic partial atom/orbital-resolved densities of states for Fe@Mn@DV (Figure S61h) for in-plane (solid lines) and perpendicular magnetization (dashed lines): (a) Mn atom and (b) Fe atom (cf. Figure S67).
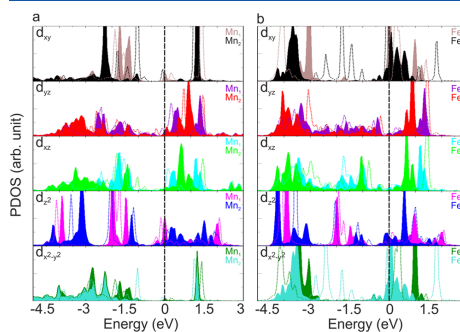
Figure 5. Relativistic partial atom/orbital-resolved densities of states for two Fe—Mn dimers bound to separate DV defects (Figure 4) for in-plane (solid lines) and perpendicular magnetization (dashed lines): (a) Mn atoms and (b) Fe atoms.

Interestingly, the introduction of the second dimer separated by 12.9 Å (6 × 3 cell, Figure 4) caused the increase of MAE up to 119.7 meV in Fe@Mn@DV due to the spin transition as indicated in spin anisotropy of −1.6 μ_B and orbital anisotropy of 0.1 μ_B. The scalar-relativistic PDOS (Figure S68) for the two Fe—Mn dimers bound to separate DV defects indicates competing contributions to positive/negative MAE due to

positive contribution to the enormous MAE of ~120 meV. Similarly, the existence of a partially occupied quasi-degenerate state at E_F has been shown to favor the formation of a large magnetic anisotropy in an Ir—Co dimer supported on an ideal graphene layer.[13]

The giant MAE of ~120 meV corresponds to the blocking temperature of 34 K based on Néel's theory.[50]

195

It is noteworthy that the Fe−Mn dimers with the high MAE are expected to be stable in their GS configurations in the vacancy defects (Table S17 and Figure S70), as also shown by the phonon frequency calculations (Table S18) and the calculated Gibbs energy[70] of −1.36 eV at 373 K.

TM Doping of N-Decorated Defective Graphene. The presence of N atoms at the edges of the defects in the graphene layer (Figure S71) led to higher binding energies of TM@NSV and TM@NDV, smaller TM−C/N distances, and higher charge transfers in comparison with TM@SV and TM@DV (Table S19). Magnetic moments of TM atoms in TM@NSV and TM@NDV can either increase or decrease depending on the system, and they varied in the range of 0.3−1.9 μ_B (Tables S19 and S20). The lower spin state of Fe@NDV compared to Fe@DV is in line with experimental observations.[20] In general, N-impurities act as n-dopants and shift the density of states toward lower energies (Figures S72−S77). This also led to the semiconductor (Cr@SV and Mn@SV) to metal transition (Cr@NSV and Mn@NSV), half-metal (Fe@SV) to semiconductor transition (Fe@NSV), and metal (Mn@DV and Fe@DV) to semiconductor transition (Mn@NDV and Fe@NDV) (Table S21). No significant changes of MAE (by 0.1−1.8 meV) were observed compared to TM@DV and TM@SV. The magnetic force theorem revealed much higher MAE than the fully self-consistent calculations (Table S19), which indicates that MAE of atom-sized magnets calculated as the difference in the band energies at a fixed potential and charge density should be validated against MAE calculated as the difference in the total energies from self-consistent calculations for different orientations of the magnetic moments.

The mixed element dopants, TM_1TM_2@NSV and TM_1TM_2@NDV, showed a reversed stability trend compared with pristine analogues, $i.e.$, TM_1TM_2@NDV possessed lower binding energies than TM_1TM_2@NSV (Table S22). Their magnetic moments increased due to the combination of individual TM atoms ranging between 2.6 and 8.7 μ_B (Table S22). The lowest-in-energy structures of single and double vacancies demonstrated half-metallic DOS (Figures S78 and S79, Table S21).

The FeMn@NSV system, with the largest magnetic moment of 8.7 μ_B, exhibited the biggest MAE (5.2 meV) among the TM_1TM_2@NSV and TM_1TM_2@NDV systems (with the MAE in the sub-meV range or about 1 meV) with an 8-fold increase of MAE in comparison to TM@NSV and TM@NDV (Table S22 and S23), due to the favorable graphene-mediated coupling between TM atoms doping graphene (see above). However, the presence of nitrogen led to the significantly smaller values of MAE compared to TM_1TM_2@SV and TM_1TM_2@DV, $i.e.$, 5.2 vs 16.0 meV.

Finally, the formation of upright dimers TM_2@TM_1@NSV and TM_2@TM_1@NDV were energetically favorable (Table S24). The lowest-in-energy structure of single and double vacancies showed metallic and half-metallic states (Figures S80 and S81, Table S21), differing from the pristine analogues. The MAE was lower than that for the corresponding dimers bound to the pristine vacancy defects, except Cr@Cr@NSV, which possesses an MAE of −17.6 meV (Table S24 and S25).

CONCLUSIONS

In this work, we theoretically examined the stability as well as the electronic and magnetic properties of TM atoms and dimers of the elements Cr, Mn, and Fe bound to graphene single or double vacancies. We studied the dependence of magnetic anisotropy energy (MAE) on (i) the distances between the TM atoms within the monolayer graphene; (ii) co-doping of graphene with two atoms of the same and different elements; (iii) formation of upright TM dimers, both homo- and heteroatomic; and, finally, (iv) the presence of nitrogen atoms within the vacancy defects.

While the MAE of TM single atoms in defective graphene did not exceed 2 meV, the binding of a second TM atom to another defect in the graphene lattice led to a significant increase of MAE to −23 meV for CrFe@DV and a remarkably high value of 119.7 meV for two upright Fe−Mn dimers bound to two separate DVs, with the easy-plane and perpendicular easy axis, respectively. This giant MAE corresponds to the blocking temperature of 34 K. The origin of the greatly enhanced MAE can be sought in graphene-mediated coupling due to the RKKY-like superexchange interactions between TM dopants that modifies the occupations of states near E_F such that a changed splitting of energy bands that were degenerate in the absence of spin−orbit interaction lowers the total energy. Specifically, the presence of partially occupied degenerate states at E_F favors the formation of a giant MAE, which appears to be a general feature of the mechanism favoring the large MAE formation.[5] It is worth noticing that the value and even the sign of MAE as well as the electronic DOS are sensitive to both the distribution of TM atoms in the graphene lattice and composition of the graphene-doping atoms.

Finally, we provided the atomic-scale observation of a Mn substitution in graphene, including a spectroscopic measurement of its L edge core energy-loss white-line intensity ratio. Mn dopants bonded to four carbon atoms may create spots for the Fe−Mn dimer formation.

The conductive TM-doped graphene with robust magnetic features offers a new vista to the design of graphene-based spintronic devices. For practical applications of TM-doped graphene, the carbon sheet must be deposited on a solid substrate. The effect of substrates on the MAE of TM atoms and dimers anchored by the defects in graphene remains to be studied.

ASSOCIATED CONTENT

Ⓢ Supporting Information

The Supporting Information is available free of charge at https://pubs.acs.org/doi/10.1021/acsanm.1c04309.

Density of states of TM@SV and TM@DV; finite model calculations of defective graphene; scheme showing the coupling of eigenstates; atom/orbital-decomposed DOS of TM@SV and TM@DV; properties of Mn_1Si@SV and Mn_1Si@DV; properties and density of states of TM_1TM_2@SV and TM_1TM_2@DV with variable TM_1−TM_2 distance; relativistic partial atom/orbital-resolved densities of states of TM_1TM_2@SV and TM_1TM_2@DV; spin density distribution plots of TM_1TM_2@SV and TM_1TM_2@DV; variation in the properties of CrFe@DV with the distance between TM atoms; barrier for diffusion of TM_1TM_2@SV and TM_1TM_2@DV; structure and density of states for a system of two TM atoms, one embedded into SV and the other into DV defect; atom/orbital-decomposed DOS of TM_2@TM_1@SV and TM_2@TM_1@DV; relativistic partial atom/orbital-resolved densities of states of TM_2@TM_1@SV and TM_2@TM_1@DV; variation in the properties of Fe@

196

Mn@DV with the distance between TM atoms; barrier for the diffusion of TM$_2$@TM$_1$@SV and TM$_2$@TM$_1$@DV; and structures, properties, and density of states of TM@NSV, TM@NDV, TM$_1$TM$_2$@NSV, TM$_1$TM$_2$@NDV, TM$_2$@TM$_1$@NSV, and TM$_2$@TM$_1$@NDV (PDF)

■ AUTHOR INFORMATION

Corresponding Authors

Toma Susi − *Faculty of Physics, University of Vienna, A-1090 Vienna, Austria;* ● orcid.org/0000-0003-2513-573X; Email: toma.susi@univie.ac.at

Piotr Błoński − *Regional Centre of Advanced Technologies and Materials, Czech Advanced Technology and Research Institute (CATRIN), Palacký University Olomouc, 779 00 Olomouc, Czech Republic;* ● orcid.org/0000-0002-7072-232X; Email: piotr.blonski@upol.cz

Authors

Rostislav Langer − *Regional Centre of Advanced Technologies and Materials, Czech Advanced Technology and Research Institute (CATRIN), Palacký University Olomouc, 779 00 Olomouc, Czech Republic; Department of Physical Chemistry, Faculty of Science, Palacký University Olomouc, 779 00 Olomouc, Czech Republic*

Kimmo Mustonen − *Faculty of Physics, University of Vienna, A-1090 Vienna, Austria;* ● orcid.org/0000-0002-0953-7299

Alexander Markevich − *Faculty of Physics, University of Vienna, A-1090 Vienna, Austria*

Michal Otyepka − *Regional Centre of Advanced Technologies and Materials, Czech Advanced Technology and Research Institute (CATRIN), Palacký University Olomouc, 779 00 Olomouc, Czech Republic; IT4Innovations, Technical University of Ostrava, 708 00 Ostrava-Poruba, Czech Republic;* ● orcid.org/0000-0002-1066-5677

Complete contact information is available at:
https://pubs.acs.org/10.1021/acsanm.1c04309

Notes

The authors declare no competing financial interest.

■ REFERENCES

(1) Novoselov, K. S.; Geim, A. K.; Morozov, S. V.; Jiang, D.; Zhang, Y.; Dubonos, S. V.; Grigorieva, I. V.; Firsov, A. A. Electric Field Effect in Atomically Thin Carbon Films. *Science* **2004**, *306*, 666−669.

(2) Tuček, J.; Błoński, P.; Ugolotti, J.; Swain, A. K.; Enoki, T.; Zbořil, R. Emerging Chemical Strategies for Imprinting Magnetism in Graphene and Related 2D Materials for Spintronic and Biomedical Applications. *Chem. Soc. Rev.* **2018**, *47*, 3899−3990.

(3) Khajetoorians, A. A.; Wiebe, J.; Chilian, B.; Wiesendanger, R. Realizing All-Spin-Based Logic Operations Atom by Atom. *Science* **2011**, *332*, 1062−1064.

(4) Natterer, F. D.; Yang, K.; Paul, W.; Willke, P.; Choi, T.; Greber, T.; Heinrich, A. J.; Lutz, C. P. Reading and Writing single-Atom Magnets. *Nature* **2017**, *543*, 226−228.

(5) Strandberg, T. O.; Canali, C. M.; MacDonald, A. H. Transition-Metal Dimers and Physical Limits on Magnetic Anisotropy. *Nat. Mater.* **2007**, *6*, 648−51.

(6) Błoński, P.; Lehnert, A.; Dennler, S.; Rusponi, S.; Etzkorn, M.; Moulas, G.; Bencok, P.; Gambardella, P.; Brune, H.; Hafner, H. Magnetocrystalline Anisotropy Energy of Co and Fe Adatoms on the (111) Surfaces of Pd and Rh. *Phys. Rev. B* **2010**, *81*, No. 104426.

(7) Błoński, P.; Hafner, J. Magnetic Anisotropy of Heteronuclear Dimers in the Gas Phase and Supported on Graphene: Relativistic Density-Functional Calculations. *J. Phys.: Condens. Matter* **2014**, *26*, No. 146002.

(8) Lehnert, A.; Dennler, S.; Błoński, P.; Rusponi, S.; Etzkorn, M.; Moulas, G.; Bencok, P.; Gambardella, P.; Brune, H.; Hafner, J. Magnetic Anisotropy of Fe and Co Ultrathin Films Deposited on Rh(111) and Pt(111) Substrates: An Experimental and First-Principles Investigation. *Phys. Rev. B* **2010**, *82*, No. 094409.

(9) Sun, S.; Murray, C. B.; Weller, D.; Folks, L.; Moser, A. Monodisperse FePt Nanoparticles and Ferromagnetic FePt Nano-crystal Superlattices. *Science* **2000**, *287*, 1989−1992.

(10) Gambardella, P.; Rusponi, S.; Veronese, M.; Dhesi, S.; Grazioli, C.; Dallmeyer, A.; Cabria, I.; Zeller, R.; Dederichs, P.; Kern, K.; Carbone, C.; Brune, H. Giant Magnetic Anisotropy of Single Cobalt Atoms and Nanoparticles. *Science* **2003**, *300*, 1130−1133.

(11) Błoński, P.; Hafner, J. Density-Functional Theory of the Magnetic Anisotropy of Nanostructures: An Assessment of Different Approximations. *J. Phys.: Condens. Matter* **2009**, *21*, No. 426001.

(12) Hu, J.; Wu, R. Giant Magnetic Anisotropy of Transition-Metal Dimers on Defected Graphene. *Nano Lett.* **2014**, *14*, 1853−1858.

(13) Błoński, P.; Hafner, J. Cu(1 1 1) Supported Graphene as a Substrate for Magnetic Dimers with a Large Magnetic Anisotropy: Relativistic Density-Functional Calculations. *J. Phys.: Condens. Matter* **2014**, *26*, No. 256001.

(14) Navrátil, J.; Błoński, P.; Otyepka, M. Large Magnetic Anisotropy in an OsIr Dimer Anchored in Defective Graphene. *Nanotechnology* **2021**, *32*, No. 230001.

(15) Zhang, Y.; Wang, Z.; Cao, J. Prediction of Magnetic Anisotropy of 5d Transition Metal-Doped g-C$_3$N$_4$. *J. Mater. Chem. C* **2014**, *2*, 8817−8821.

(16) Zhang, K. C.; Li, Y. F.; Liu, Y.; Zhu, Y. Protecting Quantum Anomalous Hall State from Thermal Fluctuation: Via the Giant Magnetic Anisotropy of Os-based Dimers. *Phys. Chem. Chem. Phys.* **2018**, *20*, 28169−28175.

(17) Haldar, S.; Pujari, B. S.; Bhandary, S.; Sanyal, B.; et al. Fe$_n$ (n = 1−6) Clusters Chemisorbed on Vacancy Defects in Graphene: Stability, Spin-dipole moment, and Magnetic Anisotropy. *Phys. Rev. B* **2014**, *89*, No. 20541.

(18) Krasheninnikov, A.; Lehtinen, P.; Foster, A.; Pyykkö, P.; Nieminen, R. Embedding Transition-Metal atoms in Graphene: Structure, Bonding, and Magnetism. *Phys. Rev. Lett.* **2009**, *102*, No. 126807.
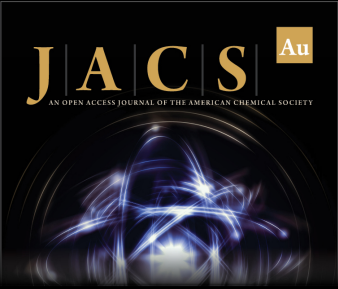
(19) Durajski, A.; Auguscik, A.; Szczęśniak, R. Tunable Electronic and Magnetic Properties of Substitutionally Doped Graphene. *Phys. E* **2020**, *119*, No. 113985.

(20) Lin, Y.-C.; Teng, P.; Chiu, P.; Suenaga, K. Exploring the Single Atom Spin State by Electron Spectroscopy. *Phys. Rev. Lett.* **2015**, *115*, No. 206803.

(21) Santos, E. J. G.; Ayuela, A.; Sánchez-Portal, D. First-Principles Study of Substitutional Metal Impurities in Graphene: Structural,

197

Electronic and Magnetic Properties. *New J. Phys.* **2010**, *12*, No. 053012.

(22) Wu, M.; Cao, C.; Jiang, J. Electronic Structure of Substitutionally Mn-Doped Graphene. *New J. Phys.* **2010**, *12*, No. 063020.

(23) Liu, J.; Lei, T.; Zhang, Y.; Ma, P.; Zhang, Z. First-Principle Calculations for Magnetism of Mn-Doped Graphene. *Adv. Mater. Res.* **2013**, *709*, 184−187.

(24) Thakur, J.; Saini, H.; Kashyap, M. Electronic and Magnetic Properties of Cr Doped Graphene; Full Potential Approach. *AIP Conf. Proc.* **2015**, *1675*, No. 030032.

(25) Thakur, J.; Kashyap, M.; Taya, A.; Rani, P.; Saini, H. Sublattice Dependent Magnetic Response of Dual Cr Doped Graphene Monolayer: A Full Potential Approach. *Indian J. Phys.* **2017**, *91*, 43−51.

(26) Dyck, O.; Yoon, M.; Zhang, L.; Lupini, A.; Swett, J.; Jesse, S. Doping of Cr in Graphene Using Electron Beam Manipulation for Functional Defect Engineering. *ACS Appl. Nano Mater.* **2020**, *3*, 10855−10863.

(27) Meier, F.; Zhou, L.; Wiebe, J.; Wiesendanger, R. Revealing Magnetic Interactions from Single-Atom Magnetization Curves. *Science* **2008**, *320*, 82−86.

(28) Hermenau, J.; Brinker, S.; Marciani, M.; Steinbrecher, M.; dos Santos Dias, M.; Wiesendanger, R.; Lounis, S.; Wiebe, J. Stabilizing Spin Systems via Symmetrically Tailored RKKY Interactions. *Nat. Commun.* **2019**, *10*, No. 2565.

(29) Lin, Y.; Teng, P.; Yeh, C.; Koshino, M.; Chiu, O.; Suenaga, K. Structural and Chemical Dynamics of Pyridinic-Nitrogen Defects in Graphene. *Nano Lett.* **2015**, *15*, 7408−7413.

(30) Susi, T.; Meyer, J.; Kotakoski, J. Manipulating Low-Dimensional Materials Down to The Level of Single Atoms with Electron Irradiation. *Ultramicroscopy* **2017**, *180*, 163−172.

(31) Tripathi, M.; Mittelberger, A.; Pike, N. A.; Mangler, C.; Meyer, J. C.; Verstraete, M. J.; Kotakoski, J.; Susi, T. Electron-Beam Manipulation of Silicon Dopants in Graphene. *Nano Lett.* **2018**, *18*, 5319−5323.

(32) Markevich, A. V.; Baldoni, M.; Warner, J. H.; Kirkland, A. I.; Besley, E. Dynamic Behavior of Single Fe Atoms Embedded in Graphene. *J. Phys. Chem. C* **2016**, *120*, 21998−22003.

(33) Kresse, G.; Hafner, J. Ab Initio Molecular Dynamics for Liquid Metals. *Phys. Rev. B* **1993**, *47*, 558.

(34) Kresse, G.; Furthmüller, J. Efficient Iterative Schemes for Ab Initio Total-Energy Calculations Using a Plane-Wave Basis Set. *Phys. Rev. B* **1996**, *54*, No. 11169.

(35) Kresse, G.; Furthmüller, J. Efficiency of Ab-Initio Total Energy Calculations for Metals and Semiconductors Using a Plane-Wave Basis Set. *Comput. Mater. Sci.* **1996**, *6*, 15−50.

(36) Blöchl, P. E. Projector Augmented-Wave Method. *Phys. Rev. B* **1994**, *50*, No. 17953.

(37) Kresse, G.; Joubert, D. From Ultrasoft Pseudopotentials to the Projector Augmented-Wave Method. *Phys. Rev. B* **1999**, *59*, No. 1758.

(38) Perdew, J. P.; Burke, K.; Ernzerhof, M. Generalized Gradient Approximation Made Simple. *Phys. Rev. Lett.* **1996**, *77*, No. 3865.

(39) Robertson, A.; Montanari, B.; He, K.; Allen, C.; Wu, Y.; Harrison, N.; Kirkland, A.; Warner, J. Structural Reconstruction of the Graphene Monovacancy. *ACS Nano* **2013**, *7*, 4495−4502.

(40) Babar, R.; Kabir, M. Ferromagnetism in Nitrogen-Doped Graphene. *Phys. Rev. B* **2018**, *99*, No. 115422.

(41) Blöchl, P. E.; Jepsen, O.; Andersen, O. Improved Tetrahedron Method for Brillouin-Zone Integrations. *Phys. Rev. B* **1994**, *49*, No. 16223.

(42) Bader, R. F. W. Atoms in Molecules. *Acc. Chem. Res.* **1985**, *18*, 9−15.

(43) Henkelman, G.; Arnaldsson, A.; Jónsson, H. A Fast and Robust Algorithm for Bader Decomposition of Charge Density. *Comput. Mater. Sci.* **2006**, *36*, 354−360.

(44) Kleinman, L. Relativistic Norm-Conserving Pseudopotential. *Phys. Rev. B* **1980**, *21*, No. 2630.

(45) MacDonald, A.; Picket, W.; Koelling, D. A Linearised Relativistic Augmented-Plane-Wave Method Utilising Approximate Pure Spin Basis Functions. *J. Phys. C: Solid State Phys.* **1980**, *13*, 2675.

(46) Hobbs, D.; Kresse, G.; Hafner, J. Fully Unconstrained Noncollinear Magnetism within the Projector Augmented-Wave Method. *Phys. Rev. B* **2000**, *62*, No. 11556.

(47) Dudarev, S.; Botton, G.; Savrasov, S.; Humphreys, C.; Sutton, A. Electron-Energy-Loss Spectra and the Structural Stability of Nickel Oxide: An LSDA+U Study. *Phys. Rev. B* **1998**, *57*, No. 1505.

(48) Błoński, P.; Hafner, J. Magnetic Anisotropy of Transition-Metal Dimers: Density Functional Calculations. *Phys. Rev. B* **2009**, *79*, No. 224418.

(49) Heine, V. Electronic Structure from the Point of View of the Local Atomic Environment. *Solid States Phys.* **1980**, *35*, 1−127.

(50) Néel, L. Théorie du Traînage Magnétique des Ferromagnétiques en Grains Fins avec Application aux Terres Cuites. *Ann. Géophys.* **1949**, *5*, 99−136.

(51) Becke, A. Density-Functional Thermochemistry. III. The Role of Exact Exchange. *J. Chem. Phys.* **1993**, *98*, 5648−5652.

(52) Lee, C.; Hill, C.; Carolina, N. Development of the Colle-Salvetti Correlation-Energy Formula into a Functional of the Electron Density. *Phys. Rev. B* **1988**, *37*, No. 785.

(53) Frisch, M. J.; Trucks, G. W.; Schlegel, H. B.; Scuseria, G. E.; Robb, M. A.; Cheeseman, J. R.; Scalmani, G.; Barone, V.; Petersson, G. A.; Nakatsuji, H.; Li, X.; Caricato, M.; Marenich, A. V.; Bloino, J.; Janesko, B. G.; Gomperts, R.; Mennucci, B.; Hratchian, H. P.; Ortiz, J. V.; Izmaylov, A. F.; Sonnenberg, J. L.; Williams-Young, D.; Ding, F.; Lipparini, F.; Egidi, F.; Goings, J.; Peng, B.; Petrone, A.; Henderson, T.; Ranasinghe, D.; Zakrzewski, V. G.; Gao, J.; Rega, N.; Zheng, G.; Liang, W.; Hada, M.; Ehara, M.; Toyota, K.; Fukuda, R.; Hasegawa, J.; Ishida, M.; Nakajima, T.; Honda, Y.; Kitao, O.; Nakai, H.; Vreven, T.; Throssell, K.; Montgomery, J. A., Jr.; Peralta, J. E.; Ogliaro, F.; Bearpark, M. J.; Heyd, J. J.; Brothers, E. N.; Kudin, K. N.; Staroverov, V. N.; Keith, T. A.; Kobayashi, R.; Normand, J.; Raghavachari, K.; Rendell, A. P.; Burant, J. C.; Iyengar, S. S.; Tomasi, J.; Cossi, M.; Millam, J. M.; Klene, M.; Adamo, C.; Cammi, R.; Ochterski, J. W.; Martin, R. L.; Morokuma, K.; Farkas, O.; Foresman, J. B.; Fox, D. J. *Gaussian 09*; Gaussian, Inc.: Wallingford CT, 2016.

(54) Glendening, E. D.; Badenhoop, J. K.; Reed, A. E.; Carpenter, J. E.; Bohmann, J. A.; Morales, C. M.; Weinhol, F. *NBO*; Theoretical Chemistry Institute, University Of Wisconsin: Madison, WI, 2001.

(55) Ma, H.; Ma, L.; Ma, L.-C. Tuning the Electronic and Magnetic Properties of Mn-Doped Graphene by Gas Adsorption and Effect of External Electric Field: First-Principles Study. *Int. J. Mod. Phys. B* **2019**, *33*, No. 1950166.

(56) Daalderop, G. H. O.; Kelly, P. J.; Schuurmans, M. F. H. Magnetic Anisotropy of a Free-Standing Co Monolayer and of Multilayers which Contain Co Monolayers. *Phys. Rev. B* **1994**, *50*, No. 9989.

(57) Whangbo, M. H.; Gordon, E. E.; Xiang, H.; Koo, H. J.; Lee, C. Prediction of Spin Orientations in Terms of HOMO−LUMO Interactions Using Spin−Orbit Coupling as Perturbation. *Acc. Chem. Res.* **2015**, *48*, 3080−3087.

(58) Pease, D.; Fasihuddin, A.; Daniel, M.; Budnick, J. Method of Linearizing the 3d L_3/L_2 White Line Ratio as a Function of Magnetic Moment. *Ultramicroscopy* **2001**, *88*, 1−16.

(59) Lin, P. C.; Villarreal, R.; Achilli, S.; Bana, H.; Nair, M. N.; Tejeda, A.; Verguts, K.; De Gendt, S.; Auge, M.; Hofsäss, H.; De Feyter, S.; Di Santo, G.; Petaccia, L.; Brems, S.; Fratesi, G.; Pereira, L. M. C. Doping Graphene with Substitutional Mn. *ACS Nano* **2021**, *15*, 5449−5458.

(60) Tripathi, M.; Markevich, A.; Böttger, R.; Facsko, S.; Besley, E.; Kotakovski, J.; Susi, T. Implanting Germanium into Graphene. *ACS Nano* **2018**, *12*, 4641−4647.

(61) Anagaw, M.; Mekonnen, S. The Effect of Manganese(Mn) Substitutional Doping on Structural, Electronic and Magnetic Properties of Pristine Hexagonal Graphene: Using Spin Polarized Density Functional Theory. *J. At., Mol., Condens. Matter Nano Phys.* **2020**, *7*, 95.

198

(62) Ruderman, M. A.; Kittel, C. Indirect Exchange Coupling of Nuclear Magnetic Moments by Conduction Electrons. *Phys. Rev.* **1954**, *96*, 99−102.

(63) Kasuya, T. A Theory of Metallic Ferro- and Antiferromagnetism on Zener's Model. *Prog. Theor. Phys.* **1956**, *16*, 45−57.

(64) Yosida, K. Magnetic Properties of Cu-Mn Alloys. *Phys. Rev.* **1957**, *106*, 893−898.

(65) Crook, C. B.; Constatntin, C.; Ahmed, T.; Zhu, J. X.; Balatsky, A. V.; Haraldsen, J. T. Proximity-Induced Magnetism in Transition-Metal Substituted Graphene. *Sci. Rep.* **2015**, *5*, No. 12322.

(66) Crook, C. B.; Houchins, G.; Zhu, J. X.; Balatsky, A. V.; Constantin, C.; Haraldsen, J. T. Spatial Dependence of the Super-Exchange Interactions for Transition-Metal Trimers in Graphene. *J. Appl. Phys.* **2018**, *123*, No. 013903.

(67) Denis, P. A.; Pereyra Huelmo, C. Structural characterization and chemical reactivity of dual doped graphene. *Carbon* **2015**, *87*, 106−115.

(68) Denis, P. A.; Iribarne, F. Dual doped monolayer and bilayer graphene: The case of 4p and 2p elements. *Chem. Phys. Lett.* **2016**, *658*, 152−157.

(69) Tejedor, M.; García, J. A.; Carrizo, J.; Elbaile, L.; Santos, J. D.; Mira, J.; Rivas, J. In-Plane Magnetic Anisotropy along the Width in Amorphous Magnetic Ribbons. *J. Magn. Magn. Mater.* **2004**, *227−276*, 1362−1364.

(70) Cramer, C. J. *Essentials of Computational Chemistry: Theories and Models*, 2nd ed.; Wiley, 2004; ISBN 978-0-470-09182-1.

199

On-Surface Synthesis of One-Dimensional Coordination Polymers with Tailored Magnetic Anisotropy

Benjamin Mallada, Piotr Błoński,* Rostislav Langer, Pavel Jelínek, Michal Otyepka, and Bruno de la Torre*

ACCESS | Metrics & More | Article Recommendations | Supporting Information

ABSTRACT: One-dimensional (1D) metalloporphyrin polymers can exhibit magnetism, depending on the central metal ion and the surrounding ligand field. The possibility of tailoring the magnetic signal in such nanostructures is highly desirable for potential spintronic devices. We present low-temperature (4.2 K) scanning tunneling microscopy and spectroscopy (LT-STM/STS) in combination with high-resolution atomic force microscopy (AFM) and a density functional theory (DFT) study of a two-step synthetic protocol to grow a robust Fe-porphyrin-based 1D polymer on-surface and to tune its magnetic properties. A thermally assisted Ullmann-like coupling reaction of Fe(III)diphenyl-bromine-porphyrin (2BrFeDPP-Cl) on Au(111) in ultra-high vacuum results in long (up to 50 nm) 1D metal−organic wires with regularly distributed magnetic and (electronically) independent porphyrins units, as confirmed by STM images. Thermally controlled C−H bond activation leads to conformational changes in the porphyrin units, which results in molecular planarization steered by 2D surface confinement, as confirmed by high-resolution AFM images. Spin-flip STS images in combination with DFT self-consistent spin−orbit coupling calculations of porphyrin units with different structural conformations reveal that the magnetic anisotropy of the triplet ground state of the central Fe ion units drops down substantially upon intramolecular rearrangements. These results point out to new opportunities for realizing and studying well-defined 1D organic magnets on surfaces and demonstrate the feasibility of tailoring their magnetic properties.

KEYWORDS: coordination-polymer, on-surface chemistry, metal-porphyrin, magnetic anisotropy, scanning probe microscopy
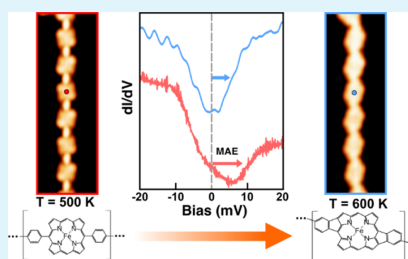
1. INTRODUCTION

The synthesis and functionalization of molecular spintronic nanostructures have attracted considerable interest due to their great potential for being beneficial to the next generation of electronic devices.[1−5] Among others, organic nanostructures enabling to tailor the spin-polarized signal is a burgeoning area of spintronic research.[5] One-dimensional (1D) polymeric organic magnets with regularly distributed magnetic centers are desirable networks, thanks to their long spin coherence length and mechanical flexibility.[6] Till date, several 1D molecular wires with transition-metal (TM) atoms have been proposed, including 1D TM-cyclopentadienyl,[7] TM-benzene,[8] TM-anthracene,[9] TM-phthalocyanine,[10] TM-metallocene,[11] TM-benzoquinonediimines,[12] and TM-naphthalene.[13] However, despite significant efforts, the experimental realization of such 1D polymeric molecular spintronics still remains a significant challenge. Nevertheless, the fabrication of novel frameworks that could be fashioned by a simple synthetic method is urgently required. To make progress in this field, it is important to choose a suitable functional molecule for making a large 1D polymeric framework.

Porphyrin molecules with coordinated TM atoms emerge as a promising candidate for constructing molecular spintronics because they combine inherent optical, redox, and magnetic properties of the intervening metal centers with those of the purely organic materials.[14−22] In such coordination polymer complexes, the ligand field coordinated with the central metal atom governs its magnetic anisotropy due to spin−orbit coupling (SOC).[23,24] Additionally, porphyrins exhibit high thermal stability and propensity to form well-ordered assemblies on a variety of solid surfaces.[25−27] Commonly, peripheral ligands are attached to the porphyrin macrocycle in specific positions in order to steer the intermolecular bonding.[28] Thus, arrays of conjugated porphyrin with delocalized electronic networks have been intensively explored

200

Chart 1. Thermal Reaction Sequence of 2BrFeDPP-Cl on Au(111) Obtained in the First Step of Annealing: Dehalogenation and Subsequent On-Surface Homocoupling Polymerization upon Annealing up to 500 K, and Furthermore, Cyclohydrogenation into cis- and trans-Polymers upon Annealing up to 600 K
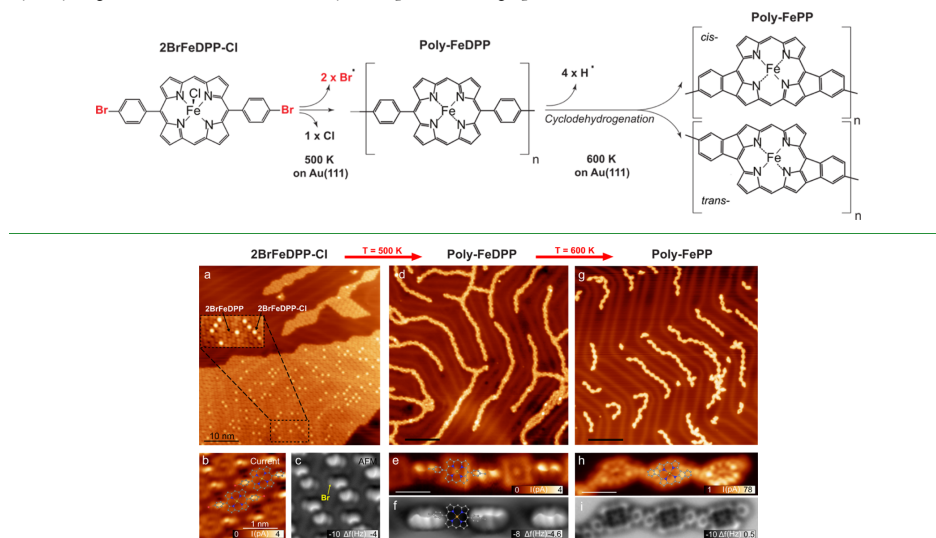
Figure 1. (a) STM topography upon deposition of 2BrFeDPP-Cl on Au(111) at RT ($V_{bias} = -200$ mV, $I_{set} = 20$ pA). (b,c) Detailed STM/nc-AFM constant height images with CO-tip. (d) STM topography upon sample annealing to 500 K ($V_{bias} = 100$ mV, $I_{set} = 20$ pA). (e,f) Corresponding detailed STM/nc-AFM constant height images with CO-tip of FeDPP molecular wires. (g) STM topography upon sample annealing to 600 K ($V_{bias} = -500$ mV, $I_{set} = 50$ pA). (h,i) Corresponding detailed STM/nc-AFM constant height images with CO-tip of the FePP molecular wires. The scale bar corresponds to 10 nm in (a,d,g) and to 1 nm in (b,c,e,f,h,i).

over the last two decades.[29−32] For example, the 1D Zn-porphyrin arrays have been already obtained experimentally, and they may find promising applications as a conducting molecule.[33]

However, such large structures are difficult to form by traditional chemical synthesis and to deposit on surfaces for further characterization and application onto devices; therefore, only oligomers formed by a few porphyrin units have been investigated so far. Recently, the emerging field of on-surface synthesis has enabled to overcome the limitation of both solubility and reactivity found in the solution synthesis, along with allowing in situ atomic-scale characterization by means of scanning tunneling microscopy/non-contact atomic force microscopy (STM/nc-AFM).[34] Furthermore, the 2D confinement imposed by the substrate during the polymerization process may result in molecular structure rearrangements, which would be otherwise difficult to induce as molecular planarization.

Here, we report a thorough investigation into the on-surface synthesis of large (up to 50 nm) metal-porphyrin based 1D molecular wires with regularly distributed magnetic and thermally adjustable anisotropy signals by means of low-temperature STM and high-resolution nc-AFM with CO-tip[35] complemented with theoretical calculations. Importantly, the formation of such long 1D chains have not been observed so far. Porphyrin building blocks are functionalized by bromine atoms in both phenyls at the para position, which steer an

thermally induced intermolecular Ullman-like coupling reaction of aryl-halides, giving rise to 1D molecular wires, and further intramolecular transformations (planarization) at higher temperatures, allowing stepwise thermal control of chemical reactions.

We show that the adsorption of iron(III) 5,15-(di-4-bromophenyl)porphyrin-chloride molecules on Au(111) leads to the dechlorination of a large portion of molecules, which reduces the total spin of the molecule. Subsequent annealing to 500 K induces debromination, which gives rise to 1D molecular structures of covalently linked iron porphyrin molecules driven by aryl−aryl intermolecular coupling. A second step of annealing to 600 K affords intramolecular dehydrogenation and ring closure reactions as a consequence of activation at such a temperature of both C−H bonds of the aryl and porphyrin moieties, which results in molecular wires formed by iron-metaled planarized porphyrin molecules. Inelastic spin excitation experiments in combination with DFT calculations reveal a substantial modification of the magnetic anisotropy energy (MAE) at the iron atom upon porphyrin planarization due to the adjustment of the electron density at d and π orbitals.

We envision that our investigation into the magnetic anisotropy dependence and the spin−spin coupling in porphyrin-based molecular wires can provide insights into the magnetism, spin delocalization, metal−ligand d-π mixing,

and pathways for transmitting spin effects in 1D molecular nanostructures.[36−40]

2. RESULTS

2.1. Structural Characterization. Chart 1 shows the chemical structure of the iron(III)-chlorine biphenyl porphyrin archetype [iron(III) 5,15-(di-4-bromophenyl)porphyrin chloride, hereafter referred to as 2BrFeDPP-Cl], we used as a molecular precursor in this study. This porphyrin species possesses phenyl moieties functionalized with C−Br groups at the para position to facilitate the linearity of the intermolecular coupling reaction product upon dehalogenation on the Au(111)substrate. Initial step-by-step structural characterization of the on-surface reaction was conducted by scanning probe microscopy (SPM) measurements to identify the distinct molecular structures present on the sample. Subsequently, after each sample annealing step, the sample is transferred and cooled to 5 K in ultra-high vacuum (UHV) conditions for SPM inspection.

2.1.1. Structure at 300 K. Upon adsorption at room temperature, 2BrFeDPP-Cl porphyrins were arranged into spatially extended close-packed islands with a majority of molecules appearing with a dim center, as depicted by STM images (cf. Figure 1). They correspond to the dechlorinated (loss of the Cl ligand) species 2BrFeDPP, which adopt a saddle conformation with twisted aryl moieties.[25,41] 2BrFeDPP molecules can be controllably realized by removing the Cl ligand from the 2BrFeDPP-Cl molecules using tunneling electrons over the Cl position[41] or by gently annealing the substrate ($T < 500$ K). The nc-AFM constant high images with CO-tip of assembled 2BrFeDPP molecules displayed a bonded Br atom as bright features (see Figure 1c), which correspond to strong repulsive force contributions, corroborating the preservation of bromine at the termini of both twisted phenyl moieties (cf. Figure 1b,c). According to the 2BrFeDPP optimized structure on Au(111) from DFT calculations (see Figure S1), the single molecule adsorbed preferentially on the Au(111) surface in a way that the Fe ion was directly above the Au atom of the top-most layer, with the adsorption energy of −77.4 kcal/mol at the Fe−Au distance of 3.53 Å. The in-plane rotation of the molecule, which decreased the Br−Br distance, increased the adsorption energy by at most 7.7 kcal/mol.

2.1.2. Structure at 500 K. A first step of the sample annealing to $T \sim 500$ K for 30 min led to the development of large 1D molecular wires extended over the surface (cf. Figure 1d). As illustrated by high-resolution STM/nc-AFM images, the molecular wires were composed of covalently bonded iron-porphyrin molecules that lost their coordinated chlorine atoms (cf. Figure 1e,f). Thus, we denote the subunits within the 1D structure as FeDPP, indicating the structural relationship with the precursor molecule. The annealing resulted in the cleavage of the C−Br bonds and the subsequent formation of 1D supramolecular structures upon surface-assisted aryl−aryl cross-coupling of adjacent porphyrin molecules. A wise choice of molecular functionalization in para positions at the porphyrin precursor allowed linearity during the intermolecular coupling process, which led to molecular wires with lengths that extend up to ∼40 monomers with no appreciable structural defects.

Importantly, the connecting aryl−aryl pairs were twisted owing to the steric hindrance, similar to unreacted 2BrFeTPP molecules on Au(111). Moieties at the same monomer were twisted differently; thus, consecutive bridges with opposite twist angle were observed within the 1D structures (cf. Figure 1e,f). In consequence, the non-planar configuration of the monomers hindered the submolecular resolution of the porphyrin centers by means of constant height nc-AFM imaging; therefore, only the linker moieties, which protruded further out of the surface, are featured in nc-AFM images (cf. Figures 1f and S2).

Finally, the loose end of the molecular wires was passivated by bromine or residual hydrogen atoms, precluding further polymerization. Interestingly, FeDPP molecular wires were easily manipulated with the SPM tip both vertically and laterally over the surface, which demonstrates the robustness of the nanostructure (see Figure S3).

2.1.3. Structure at 600 K. Following the thermal annealing of the molecule-decorated sample to $T \sim 600$ K for 30 min, molecular units within the wires underwent an intramolecular reaction through dehydrogenation and electrocyclic ring closure of their aryl termini and the macrocyclic pyrroles. This process led to the formation of isoindole motifs, which induced planarization of the porphyrin monomers on the surface (hereafter referred to as FePP units, Figure 1g), as unambiguously corroborated by high-resolution STM and nc-AFM images shown in Figure 1h,i. Therefore, the Fe atom at the center of the porphyrin unit is displayed as a cross-like feature in nc-AFM images, similar to the nc-AFM contrast observed on other metal phthalocyanines and porphyrin complexes.[42−44]

The ring closure of aryl moieties toward the macrocycle gave rise either to trans- or cis-configurations of the molecular repeating units (Chart 1). Statistically (over hundreds of monomer units counted on several samples), we observed equivalent abundance of the intramolecular cis (52%) and trans (48%) motifs, pointing out that both configurations are equally favorable. Interestingly, we found two effects regarding the substrate reconstruction: (1) the FePP molecular chains aligned along the herringbone, and, (2) frequently, the molecular chains terminated at the elbow sites. Thus, the segments that showed repeated cis or trans motifs were found with a maximum length of five units.

The intramolecular- versus intermolecular-induced reaction observed at different temperatures is rationalized by theoretical calculations of the dissociation energy (BDE) for various C−H and C−Br bonds of a single porphyrin specie on the Au(111) surface. Our theoretical calculations revealed that the activation energy for bromine abstraction was lower than that of hydrogen abstraction (C−H₁ and C−H₂, see bond labeling shown in Figure 2) by at least 30 kcal/mol (see Table 1). Upon adsorption, this value dropped up to 15 kcal/mol due to surface-assisted molecular structure stabilization. The initial removal of the Br atom further reduced the bond dissociation energies of the C−H₁, which favored H abstraction at higher temperatures, resulting in the ring closure of aryl moieties
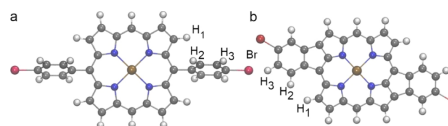
Figure 2. Stick-ball model for 2BrFeDPP (a) and 2BrFePP (b). BDEs of the labeled bonds are gathered in Table 1. C atoms are shown in gray, H in white, N in blue, Fe in orange, and Br in red.

202

Table 1. BDEs (in kcal/mol) of C−Br and C−H Bonds Labeled in Figure 2a

	2BrFeDPP		2BrFePP	
bond	freestanding	on Au(111)	freestanding	on Au(111)
C−Br	99.3	102.1	85.3	102.8
C−H$_1$	133.2 (104.1)	117.9 (116.5)		118.5
C−H$_2$	129.5 (101.7)	128.2	128.1	117.8
C−H$_3$	129.8		116.2	115.8

^{a}BDEs of selected C−H bonds after the removal of the Br atom are shown in brackets. See also note 1 in SOM on the calculated adsorption of 2BrFeDPP and 2BrFePP on Au(111).

steered by the 2D confinement of the surface. Thus, the stepwise annealing of 2BrFeDPP first allowed the formation of poly-FeDPP structures through Ullmann-like coupling of aryl-halides and, subsequently, the emergence of poly-FePP planar structures at higher temperatures. Interestingly, we found shorter molecular chains upon the planarization process (annealing at 600 K) in average (4−11 monomers). This may be due to thermally induced polymer breaking. However, molecular chains containing up to 50 nm can be found on the sample (see Figure S4).

Accordingly, annealing the sample at intermediate temperatures in the range of $T \sim 500-600$ K, that is, at 550 K, for 30 min, partially activated the ring closure reaction, thus yielding molecular wires with a mixture of FeDPP and FePP units (see Figure S5). Notably, no trace of intramolecular dehydrogenation was observed at temperatures below 550 K. Indeed, no dehydrogenation reaction was identified prior to the polymerization process of the molecular precursor.

On the other hand, annealing to elevated temperatures ($T >$ 600 K) resulted in molecular wires fused together, which reduced the 1D character of the nanostructures. These structures were formed by the dissociation of the C−H bonds at the periphery of the porphyrin units and by the subsequent fusion of the nearby polymer, as depicted in STM/nc-AFM images (see Figure S6).

2.2. Experimental Spin Features. Next, we focused on spin characteristics of 2BrFeDPP-Cl molecules upon adsorption, dechlorination, polymerization (poly-FeDPP), and intramolecular planarization (poly-FePP) by means of inelastic spin excitation spectroscopy with STM.[45−47] Figure 3 plots specific site spectra of the differential conductance (dI/dV) around the Fermi level with the STM tip placed on the Fe center (red) for both single 2BrFeDPP-Cl (Figure 3a) and 2BrFeDPP (Figure 3b) and on FeDPP (Figure 3c) and FePP (Figure 3d) units in a molecular wire as well. Reference spectroscopy on the bare Au(111) surface (featureless) is plotted with black lines, as shown in Figure 3.

In the case of 2BrFeDPP-Cl molecules, we identified a prominent dip feature at the Fermi level (cf. Figure 3a). In similar FeTPP-Cl molecules, step-like features at ±1.7 meV associated with spin-flip excitations have been reported.[48] However, due to the thermal broadening at the temperature at which we conducted our experiments (4.2 K), we cannot unequivocally distinguish weather the observed feature represents a spin-flip excitation or a Kondo resonance. The change in contrast between 2BrFeDPP-Cl and 2BrFeDPP (see Figure S7) is consistent with the same process in FeTPPCl (see, e.g., ref 41). In contrast, the spectra acquired on the Fe center of the dechlorinated 2BrFeDPP (cf. Figure 3b),
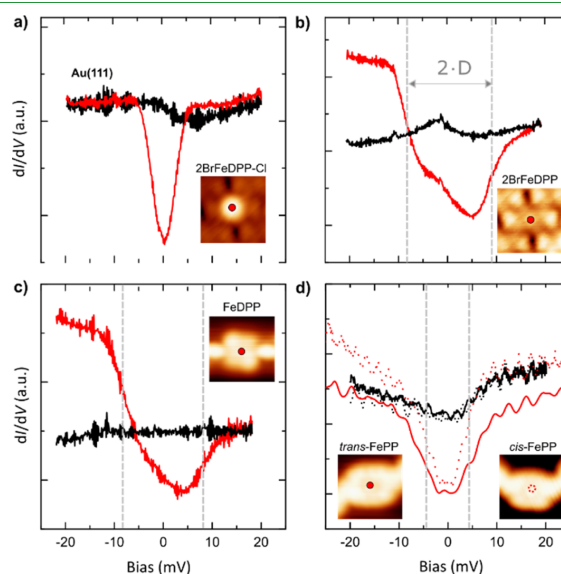
Figure 3. dI/dV spectra recorded on the center (red) of single 2BrFeDPP-Cl (a), on 2BrFeDPP (b), on monomer in poly-FeDPP wire, (c) on cis- (dash-shaped) and trans- (line-shaped) monomer in poly-FePP wire, and (d) corresponding reference spectra on the bare substrate (black).

203

polymerized FeDPP (cf. Figure 3c), and FePP (cf. Figure 3d) molecules revealed stepwise stepwise increments in conductance at symmetric bias values. Consistent with previous studies on similar Fe-TPP on Au(111), we ascribed this feature to the spin-flip inelastic excitation process.[48,49]

Notably, the removal of the coordinated chlorine atom from the 2BrFeDPP-Cl molecules reduced the Fe-oxidation state from Fe^{3+} to Fe^{2+} and consequently lowered the total spin from $S = 3/2$ to $S = 1$.[41] The spin reduction was confirmed by the current SP-DFT calculations. Furthermore, the calculations predicted MAE of −4.1 meV for 2BrFeDPP-Cl, where the negative MAE represented the easy-axis system, which was in contrast with the MAE of dechlorinated 2BrFeDPP (cf. Section 3). Upon dechlorination, the degenerated triplet state splits into the ground spin state $m_s = 0$ and the doubly degenerated $m_s = ±1$ excited states due to the spin−orbit interaction. This splitting is referred to as zero-field splitting and occurs even in the absence of a magnetic field.[50] In the first approximation, the spin excitation is determined by the magnetic anisotropy of the molecule on the surface, which is well described by a spin Hamiltonian $HS_O = DS_z^2 + E(S_x^2 − S_y^2)$, where D is vertical magnetic anisotropy (origin of the zero-field splitting) and E is in-plane magnetic anisotropy, which typically vanishes for planar molecules. Therefore, we attributed the inelastic spin excitation spectra to the triplet $S = 1$, and the excitation energy corresponded to the axial anisotropy constant. It should be noted that very similar spectra were also obtained for an Fe-tetraphenyl-porphyrin molecule,[49] which was attributed to inelastic spin excitation of the $S = 1$ spin state as well.

The spectra acquired on the 2BrFeDPP molecules and FeDPP monomers showed excitation voltage onsets at $V_s = ±8.5$ mV and $V_s = ±7.5$ mV (see Figure S8), respectively (similar to previously reported values of D for FeDPP complexes[49]). It is worth noting that the difference in the excitation onset observed for 2BrFeDPP and FeDPP was lower than that in our experimental resolution (2 mV). Interestingly, the excitation spectra on both the 2BrFeDPP molecule and the FeDPP unit showed similar steps with asymmetric line shapes. Such asymmetries have been previously attributed to the characteristic particle-hole excitation symmetry in Fe-tetra-phenyl porphyrin complexes.[48]

Based on this data and in accordance with our theoretical calculations (see below), we conclude that the polymerization process (aryl−aryl coupling) hardly affects the magnetic anisotropy of the FeDPP molecule (similar energy onset and line shape of the spin excitation). This result can be attributed to the lack of large distortions of the molecular ligand field upon the formation of poly-FeDPP chains, as confirmed by our calculations.

On the other hand, although the planarization process from poly-FeDPP toward poly-FePP did not change the overall character of the stepped spectrum (step-like shape), it decreased the onset of the excitation energy to $V_s = ±3.5$ mV ($D = 3.5$ meV). Additionally, the excitation in the FePP features had a more symmetric line shape than that in FeDPP. All together hint toward a change in the magnetic polarization of the spin state upon molecular planarization, as will be discussed below.

For comparison, we analyzed isolated FePP molecules, which were often found on the surface after annealing the sample to 600 K. They displayed identical characteristics to the corresponding FePP units in molecular wires (see Figure S9),

confirming that the observed change in the MAE from FeDPP ($D = 7.5$ meV) to FePP ($D = 3.5$ meV) units was induced by planarization and the subsequent ligand field variation. Thus, we assume that the structure of the ligand field ruled the magnetic anisotropy of the wire units rather than that of the polymer bridges. This observation was further corroborated by measurements on a molecular chain composed of a mixture of FeDPP and FePP (see Figure S5), where we observed that the magnetic anisotropy of every molecular unit was not affected by being connected to either a planar or a non-planar unit. This result was expected due to the low degree of electronic delocalization of the single C−C bond connecting the monomers.

3. DISCUSSION

To gain a deeper insight into the origin of the reduction of MAE of the planarized FePP molecules observed experimentally, we performed spin-polarized DFT calculations including a self-consistent treatment of SOC. While the theoretical calculations of the MAE hinge on several inevitable approximations including the choice of an exchange−correlation functional, the degree of optimization of the geometry of the adsorbate/substrate complex, and the MAE calculated either self-consistently or via the magnetic force theorem, leading to a lower bound of the actual MAE, the theory still provides a sound physical picture of the MAE.[51] We examined the magnetic properties of the single molecules of 2BrFeDPP and 2BrFePP and polymers of FeDPP and FePP, both freestanding and supported on Au(111).

Scalar relativistic (SR) calculations predict the spin-triplet ground state for both the freestanding and Au(111)-supported molecules and chains, while the spin-singlet is at least ∼0.4 eV higher in energy. The total magnetic moment is localized mostly on the Fe ion and, to a much lesser extent, on the four coordinating N atoms (see Figure S10).

Table 2 gathers the theoretical MAE of all the systems considered. While the theoretical MAE of 2BrFeDPP and

Table 2. MAE (in meV) of Freestanding and Au(111)-Supported 2BrFeDPP and 2BrFePP

	2BrFeDPP		2BrFePP	
	freestanding	on Au(111)	freestanding	on Au(111)
single molecule	6.2	2.0	1.0	0.3
dimer	4.8		1.1	
wire	1.5	3.7	0.4	1.7

[a]Positive MAE corresponds to an easy-plane system. The in-plane MAE of all systems was negligible.

2BrFePP is reduced by polymerization, the trend is reversed for the Au(111)-supported counterparts, due to the interaction with the substrate. The relative reduction of the MAE of the Au(111)-supported molecules and chains due to planarization is, however, similar and amounts to 1.7 and 2.0 meV, respectively. Thus, the reduction of MAE for the planarized molecules is in semi-quantitative agreement with the experimental observation, regardless of whether they were deposited on the Au(111) surface or/and polymerized. This indicates that the origin of the MAE reduction must be viewed in the differences in the symmetry of the Fe environment, which may lead to a different occupation scheme of the central Fe atom.

Indeed, in the 2BrFeDPP molecule, all Fe−N distances were equal to 2.01 Å. Occupations of the Fe 3d levels were similar for the SR limit and for the axial (hard) direction of magnetization after adding SOC (Figure S11). The rotation of magnetic moments in the in-plane (easy) direction led to the lifting of the degeneracy of the dπ states and the reordering and change in the occupation of the 3d levels.

In the 2BrFePP molecule, the square-planar symmetry was broken with two short and two long Fe−N bonds in the length of 1.94 and 2.04 Å, respectively, and the lifting of the degeneracy of the dπ states was already observed in the SR limit (see Figure S11). With SOC, no significant changes occurred in the occupation of the Fe 3d levels upon the rotation in the direction of magnetization between the axial (hard) and in-plane (easy) direction. This explains the reduced MAE in planarized 2BrFePP.

For a single molecule of 2BrFeDPP supported on Au(111), an in-plane magnetic direction is favored; as for a free-standing molecule (Table 2), with the spin/orbital moment of 2.361/0.113 μ_B. The perpendicular hard magnetic direction is disfavored by 2.0 meV with the spin/orbital moments reduced to 2.358/0.009 μ_B. The internal cyclization (planarization) reduced the MAE only to 0.3 meV, which is in line with the experimental observation. We identified the spin/orbital moments for 2.005/0.119 μ_B for the easy magnetic direction and 2.002/0.025 μ_B for the hard magnetic axis. It should be in line with the reduced anisotropy of the orbital moments, compared to the 2BrFeTPP/Au(111) system.

Densities of states of 2BrFeDPP/Au(111) and 2BrFePP/Au(111) projected on the Fe-d orbitals are shown in Figure 4a,b (see also Figures S12 and S13), and the corresponding occupation schemes of the Fe 3d levels are shown in Figure 4c,d. The $d_{x^2-y^2}$ and d_{xy}-derived states, which were localized and narrow due to their weak interaction with the Au substrate, were fully occupied and empty, respectively. While the spin-down d_{z^2} and dπ-derived states were occupied in both systems, for 2BrFeDPP/Au(111), the spin-up counterparts were partially occupied and empty, respectively. For planarized 2BrFePP/Au(111), the spin-up d_{z^2} and d_{xz}-derived states were both partially occupied, and, moreover, the d_{z^2} and dπ-derived states were slightly broadened because of their larger hybridization with the substrate. Accordingly, projected density of states (PDOS) indicates that the spin polarization originated predominantly from the contribution of d_{z^2} and dπ. As for the freestanding molecules, the degeneracy of dπ was largely broken for planarized 2BrFePP/Au(111) (Figures S12 and S13). In addition, the effect of SOC on the occupations of the 3d electronic states for the supported molecules was lower than that of the freestanding molecules (cf. Figure S11) as a consequence of the hybridization with the substrate and according to lower MAE[S1] (cf. Table 2).

The occupation scheme of the 3d electronic states of the infinite chain of FeDPP and FePP supported on Au(111) corresponds well to those for the supported molecules (as shown in Figure 4c,d) and, accordingly, the MAE is in semi-qualitative agreement with the experimental findings. A slightly larger MAE, compared to the single-molecule counterparts, may be due to the intrachain interactions; this being at the expense of the interaction with the substrate.

4. CONCLUSIONS

In conclusion, we have synthesized large 1D metal-porphyrin wires on-surface and have investigated their conformational
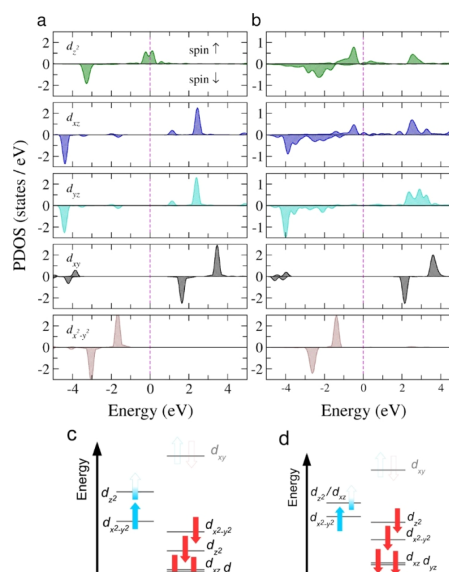
Figure 4. PDOS of the d orbitals of Fe for the Au(111)-supported 2BrFeDPP (a) and 2BrFePP (b). The corresponding PDOS-derived occupation schemes of Fe 3d levels are shown in (c,d). Due to two unpaired Fe-d electrons, the systems have S = 1 ground state (cf. Figures S12 and S13).

and intrinsic magnetic characteristics. High-resolution AFM images confirmed that annealing the 2BrFeDPP-Cl-decorated Au(111) sample to $T \approx 500$ K led to 1D polymers with regular Fe-porphyrins and surface-assisted intramolecular planarization upon sample annealing to $T \approx 600$ K. Such intramolecular planarization resulted in substantial adjustment of the magnetic properties of porphyrin's metal atom, as confirmed by spin-flip STS measurements and DFT-SOC calculations. Upon planarization, the MAE from the triplet ground state of the Fe ion dropped down due to a reduction of the ligand field symmetry and subsequent charge redistribution. We anticipate that the large flexibility of porphyrin compounds to incorporate different TM atoms and linkers into the macro-cycle, together with the synthetic protocols presented here to control inter- and intramolecular on-surface reactions, may open new opportunities for designing π-d 1D nanostructures with desirable magnetic properties.

5. METHODS

5.1. Experimental Section. Experiments were performed in a custom-designed LT-STM/AFM UHV system (Createc GmbH) at 4.2 K with a base pressure below 5×10^{-10} mbar. STM/nc-AFM images were taken with sharpened focus ion beam Pt/Ir tips. STM images were acquired in the constant current mode with a bias voltage applied to the sample. For the spectroscopic measurements, specific site dI/dV were taken by a conventional lock-in technique with a modulation of 0.5 mV at 937 Hz. For nc-AFM imaging, the tip was functionalized with a single CO molecule picked up from the bare metal substrate and operated in the frequency-modulation mode

(oscillated with a constant amplitude of 50 pm; resonant frequency ≈30 kHz; stiffness ≈1800 N/m). All nc-AFM images were acquired in a constant height mode with a bias voltage of 1 mV. All images were subject to a standard process using WSxM software.[52]

The Au(111) substrate was prepared by repeated cycles of Ar⁺ sputtering (1 keV) and subsequent annealing. A molecular precursor (commercial from PorphyChem) was deposited by organic molecular-beam epitaxy from a tantalum pocket maintained at 625 K onto a clean Au(111) held at room temperature. When annealed to the desired temperature, the samples were transferred to the STM stage, which was maintained at 4.2 K.

5.2. Theoretical Calculations. DFT calculations[53,54] were performed with the Perdew−Burke−Ernzerhof exchange and correlation functional,[55] projected augmented wave potentials representing atomic cores,[56,57] and zero-damping DFT-D3 method of Grimme[58] to account for the dispersion corrections. The Hubbard $U - J$ = 4 eV parameter[59] was applied for Fe. Occupations of the Fe 3d levels of freestanding molecules were re-examined by using non-local correlation functional optB86b + U.[60] The plane-wave basis set contained waves with kinetic energy lower than 500 eV. The Brillouin zone samplings were restricted to Γ point as the supercell dimensions were sufficiently large. Bond dissociation energies were computed by employing PBE0 hybrid functional[54,55,61] (see also Sen et al.[62]). The Au(111) surface was modeled using 7 × 7 supercells consisting of four Au layers, the bottom two layers of which were kept constrained in all structural relaxations. The vacuum layer of ∼15 Å was applied along the off-planar direction to ward off spurious interactions with the periodic images. Structural optimizations were performed employing a quasi-Newton algorithm until the residual atomic forces were below 25 meV Å⁻¹. Simultaneously, the electronic and magnetic degrees of freedom were converged to an energy of less than 10⁻⁶ eV. MAEs were computed in the noncollinear mode following implementations of Hobbs et al.[61] and Marsman and Hafner.[63] The adsorption energy E_{ad} of the BrFeDPP and 2BrFePP molecules on the Au(111) surface was calculated using the formula

$$E_{ad} = E_{tot} - E_{slab} - E_{molecule}$$

where E_{tot} represents the total energy of the entire surface-adsorbed system, E_{slab} is the total energy of the Au(111) slab, and $E_{molecule}$ is the total energy of the gas-phase 2BrFeDPP or 2BrFePP. In this convention, negative adsorption energy means that the adsorption is energetically favorable, and lower adsorption energy denotes higher energetic stability of the surface-adsorbed system.

■ ASSOCIATED CONTENT

ⓢ Supporting Information

The Supporting Information is available free of charge at https://pubs.acs.org/doi/10.1021/acsami.1c04693.

> Optimized structures of 2BrFeTPP [and 2BrFePP on Au(111)]; nc-AFM constant height images simulated using a DFT-calculated FeDPP dimer structure; lateral manipulation of FeDPP molecular chains; statistical distribution of chain lengths upon annealing the sample up to 600 K; overview after annealing the molecule decorated sample to 550 K; overview upon sample annealing to temperatures higher than 600 K; dechlorination of 2BrFeDPP-Cl molecule; measurements of the onset of magnetic anisotropy using the first derivative of the dI/dV spectra; characterization of single FePP molecule; isosurface of the spin density calculated for the 2BrFeDPP/Au(111) system; simplified scheme of the occupation of Fe 3d levels of the freestanding 2BrFeDPP and 2BrFePP; and spin- and orbital-resolved PDOS on Fe and N of 2BrFeDPP supported on Au(111) (PDF)

■ AUTHOR INFORMATION

Corresponding Authors

Piotr Błoński − Regional Centre of Advanced Technologies and Material, Czech Advanced Technology and Research Institute (CATRIN), Palacký University Olomouc, 783 71 Olomouc, Czech Republic; ⓞ orcid.org/0000-0002-7072-232X; Email: piotr.blonski@upol.cz

Bruno de la Torre − Regional Centre of Advanced Technologies and Material, Czech Advanced Technology and Research Institute (CATRIN), Palacký University Olomouc, 783 71 Olomouc, Czech Republic; Institute of Physics, The Czech Academy of Sciences, 162 00 Prague, Czech Republic; ⓞ orcid.org/0000-0002-6462-6833; Email: bdelatorre@fzu.cz

Authors

Benjamin Mallada − Regional Centre of Advanced Technologies and Material, Czech Advanced Technology and Research Institute (CATRIN), Palacký University Olomouc, 783 71 Olomouc, Czech Republic; Institute of Physics, The Czech Academy of Sciences, 162 00 Prague, Czech Republic; ⓞ orcid.org/0000-0002-8209-9977

Rostislav Langer − Regional Centre of Advanced Technologies and Material, Czech Advanced Technology and Research Institute (CATRIN), Palacký University Olomouc, 783 71 Olomouc, Czech Republic; Department of Physical Chemistry, Faculty of Science, Palacký University Olomouc, 78371 Olomouc, Czech Republic; ⓞ orcid.org/0000-0003-1703-6707

Pavel Jelínek − Regional Centre of Advanced Technologies and Material, Czech Advanced Technology and Research Institute (CATRIN), Palacký University Olomouc, 783 71 Olomouc, Czech Republic; Institute of Physics, The Czech Academy of Sciences, 162 00 Prague, Czech Republic; ⓞ orcid.org/0000-0002-5645-8542

Michal Otyepka − Regional Centre of Advanced Technologies and Material, Czech Advanced Technology and Research Institute (CATRIN), Palacký University Olomouc, 783 71 Olomouc, Czech Republic; IT4Innovations, Technical University of Ostrava, 708 00 Ostrava-Poruba, Czech Republic; ⓞ orcid.org/0000-0002-1066-5677

Complete contact information is available at:
https://pubs.acs.org/10.1021/acsami.1c04693

Notes

The authors declare no competing financial interest.

206

■ REFERENCES

(1) Wolf, S. A. Spintronics: A Spin-Based Electronics Vision for the Future. *Science* **2001**, *294*, 1488−1495.

(2) Žutić, I.; Fabian, J.; Das Sarma, S. Spintronics: Fundamentals and Applications. *Rev. Mod. Phys.* **2004**, *76*, 323−410.

(3) Maslyuk, V. V.; Bagrets, A.; Meded, V.; Arnold, A.; Evers, F.; Brandbyge, M.; Bredow, T.; Mertig, I. Organometallic Benzene-Vanadium Wire: A One-Dimensional Half-Metallic Ferromagnet. *Phys. Rev. Lett.* **2006**, *97*, 097201.

(4) Wang, L.; Cai, Z.; Wang, J.; Lu, J.; Luo, G.; Lai, L.; Zhou, J.; Qin, R.; Gao, Z.; Yu, D.; Li, G.; Mei, W. N.; Sanvito, S. Novel One-Dimensional Organometallic Half Metals: Vanadium-Cyclopentadienyl, Vanadium-Cyclopentadienyl-Benzene, and Vanadium-Anthracene Wires. *Nano Lett.* **2008**, *8*, 3640−3644.

(5) Xiong, Z. H.; Wu, D.; Valy Vardeny, Z.; Shi, J. Giant Magnetoresistance in Organic Spin-Valves. *Nature* **2004**, *427*, 821−824.

(6) Tsukagoshi, K.; Alphenaar, B. W.; Ago, H. Coherent Transport of Electron Spin in a Ferromagnetically Contacted Carbon Nanotube. *Nature* **1999**, *401*, 572−574.

(7) Zhang, X.; Tian, Z.; Yang, S.-W.; Wang, J. Magnetic Manipulation and Half-Metal Prediction of One-Dimensional Bimetallic Organic Sandwich Molecular Wires [CpTM 1 CpTM 2] ∞ (TM 1 = Ti, Cr, Fe; TM 2 = Sc−Co). *J. Phys. Chem. C* **2011**, *115*, 2948−2953.

(8) Xiang, H.; Yang, J.; Hou, J. G.; Zhu, Q. One-Dimensional Transition Metal−Benzene Sandwich Polymers: Possible Ideal Conductors for Spin Transport. *J. Am. Chem. Soc.* **2006**, *128*, 2310−2314.

(9) Parida, P.; Kundu, A.; Pati, S. K. One-Dimensional Organometallic V−Anthracene Wire and Its B−N Analogue: Efficient Half-Metallic Spin Filters. *Phys. Chem. Chem. Phys.* **2010**, *12*, 6924.

(10) Ma, Y.; Dai, Y.; Zhang, Z.; Yu, L.; Huang, B. Magnetic Properties of Phthalocyanine-Based Organometallic Nanowire. *Appl. Phys. Lett.* **2012**, *101*, 062405.

(11) Santhini, V. M.; Stetsovych, O.; Ondráček, M.; Mendieta Moreno, J. I.; Mutombo, P.; Torre, B.; Švec, M.; Klívar, J.; Stará, I. G.; Vázquez, H.; Starý, I.; Jelínek, P. On-Surface Synthesis of Polyferrocenylene and its Single-Chain Conformational and Electrical Transport Properties. *Adv. Funct. Mater.* **2020**, *31*, 2006391.

(12) Santhini, V. M.; Wäckerlin, C.; Cahlík, A.; Ondráček, M.; Pascal, S.; Matěj, A.; Stetsovych, O.; Mutombo, P.; Lazar, P.; Siri, O.; Jelínek, P. 1D Coordination π−d Conjugated Polymers with Distinct Structures Defined by the Choice of the Transition Metal: Towards a New Class of Antiaromatic Macrocycles. *Angew. Chem., Int. Ed.* **2021**, *60*, 439−445.

(13) Telychko, M.; Su, J.; Gallardo, A.; Gu, Y.; Mendieta-Moreno, J. I.; Qi, D.; Tadich, A.; Song, S.; Lyu, P.; Qiu, Z.; Fang, H.; Koh, M. J.; Wu, J.; Jelínek, P.; Lu, J. Strain-Induced Isomerization in One-Dimensional Metal−Organic Chains. *Angew. Chem., Int. Ed.* **2019**, *58*, 18591−18597.

(14) Kang, B. K.; Aratani, N.; Lim, J. K.; Kim, D.; Osuka, A.; Yoo, K.-H. Length and Temperature Dependence of Electrical Conduction through Dithiolated Porphyrin Arrays. *Chem. Phys. Lett.* **2005**, *412*, 303.

(15) Tagami, K.; Tsukada, M.; Matsumoto, T.; Kawai, T. Electronic Transport Properties of Free-Base Tape-Porphyrin Molecular Wires Studied by Self-Consistent Tight-Binding Calculations. *Phys. Rev. B: Condens. Matter Mater. Phys.* **2003**, *67*, 245324.

(16) Long, M.-Q.; Chen, K.-Q.; Wang, L.; Qing, W.; Zou, B. S.; Shuai, Z. Negative Differential Resistance Behaviors in Porphyrin Molecular Junctions Modulated with Side Groups. *Appl. Phys. Lett.* **2008**, *92*, 243303.

(17) Ribeiro, F. J.; Lu, W.; Bernholc, J. Doping-Dependent Negative Differential Resistance in Hybrid Organic/Inorganic Si−Porphyrin−Si Junctions. *ACS Nano* **2008**, *2*, 1517−1522.

(18) Holten, D.; Bocian, D. F.; Lindsey, J. S. Probing Electronic Communication in Covalently Linked Multiporphyrin Arrays. A Guide to the Rational Design of Molecular Photonic Devices. *Acc. Chem. Res.* **2002**, *35*, 57−69.

(19) Yamaguchi, Y. Time-Dependent Density Functional Calculations of Fully π-Conjugated Zinc Oligoporphyrins. *J. Chem. Phys.* **2002**, *117*, 9688−9694.

(20) Chen, Y.; Prociuk, A.; Perrine, T.; Dunietz, B. D. Spin-Dependent Electronic Transport through a Porphyrin Ring Ligating an Fe(II) Atom: An Ab Initio Study. *Phys. Rev. B: Condens. Matter Mater. Phys.* **2006**, *74*, 245320.

(21) Abel, M.; Clair, S.; Ourdjini, O.; Mossoyan, M.; Porte, L. Single Layer of Polymeric Fe-Phthalocyanine: An Organometallic Sheet on Metal and Thin Insulating Film. *J. Am. Chem. Soc.* **2011**, *133*, 1203−1205.

(22) Zhou, J.; Sun, Q. Magnetism of Phthalocyanine-Based Organometallic Single Porous Sheet. *J. Am. Chem. Soc.* **2011**, *133*, 15113−15119.

(23) Carlin, R. L. Paramagnetism: Zero-Field Splittings. *Magnetochemistry*; Springer-Verlag: Berlin, 1986.

(24) Getzlaff, M. Magnetic Anisotropy Effects. *Fundamentals of Magnetism*; Springer-Verlag: Berlin, 2008.

(25) Auwärter, W.; Écija, D.; Klappenberger, F.; Barth, J. V. Porphyrins at Interfaces. *Nat. Chem.* **2015**, *7*, 105.

(26) Marbach, H. Surface-Mediated in Situ Metalation of Porphyrins at the Solid−Vacuum Interface. *Acc. Chem. Res.* **2015**, *48*, 2649−2658.

(27) Gottfried, J. M. Surface Chemistry of Porphyrins and Phthalocyanines. *Surf. Sci. Rep.* **2015**, *70*, 259−379.

(28) Jurow, M.; Schuckman, A. E.; Batteas, J. D.; Drain, C. M. Porphyrins as Molecular Electronic Components of Functional Devices. *Coord. Chem. Rev.* **2010**, *254*, 2297−2310.

(29) Tanaka, T.; Osuka, A. Conjugated Porphyrin Arrays: Synthesis, Properties and Applications for Functional Materials. *Chem. Soc. Rev.* **2015**, *44*, 943−969.

(30) Judd, C. J.; Nizovtsev, A. S.; Plougmann, R.; Kondratuk, D. V.; Anderson, H. L.; Besley, E.; Saywell, A. Molecular Quantum Rings Formed from a π -Conjugated Macrocycle. *Phys. Rev. Lett.* **2020**, *125*, 206803.

(31) Svatek, S. A.; Perdigão, L. M. A.; Stannard, A.; Wieland, M. B.; Kondratuk, D. V.; Anderson, H. L.; O'Shea, J. N.; Beton, P. H. Mechanical Stiffening of Porphyrin Nanorings through Supramolecular Columnar Stacking. *Nano Lett.* **2013**, *13*, 3391−3395.

(32) Saywell, A.; Browning, A. S.; Rahe, P.; Anderson, H. L.; Beton, P. H. Organisation and Ordering of 1D Porphyrin Polymers Synthesised by On-Surface Glaser Coupling. *Chem. Commun.* **2016**, *52*, 10342−10345.

(33) Tsuda, A. Fully Conjugated Porphyrin Tapes with Electronic Absorption Bands That Reach into Infrared. *Science* **2001**, *293*, 79−82.

(34) Grill, L.; Hecht, S. Covalent On-Surface Polymerization. *Nat. Chem.* **2020**, *12*, 115−130.

(35) Jelínek, P. High Resolution SPM Imaging of Organic Molecules with Functionalized Tips. *J. Phys.: Condens. Matter* **2017**, *29*, 343002.

(36) Iwamura, H.; Koga, N. Studies of Organic Di-, Oligo-, and Polyradicals by Means of Their Bulk Magnetic Properties. *Acc. Chem. Res.* **1993**, *26*, 346−351.

(37) Ung, V. Ã.; Cargill Thompson, A. M. W.; Bardwell, D. A.; Gatteschi, D.; Jeffery, J. C.; McCleverty, J. A.; Totti, F.; Ward, M. D. Roles of Bridging Ligand Topology and Conformation in Controlling Exchange Interactions between Paramagnetic Molybdenum Fragments in Dinuclear and Trinuclear Complexes. *Inorg. Chem.* **1997**, *36*, 3447−3454.

(38) Pardo, E.; Carrasco, R.; Ruiz-García, R.; Julve, M.; Lloret, F.; Muñoz, M. C.; Journaux, Y.; Ruiz, E.; Cano, J. Structure and Magnetism of Dinuclear Copper(II) Metallacyclophanes with Oligoacenebis(Oxamate) Bridging Ligands: Theoretical Predictions on Wirelike Magnetic Coupling. *J. Am. Chem. Soc.* **2008**, *130*, 576−585.

(39) Ferrando-Soria, J.; Castellano, M.; Yuste, C.; Lloret, F.; Julve, M.; Fabelo, O.; Ruiz-Pérez, C.; Stiriba, S.-E.; Ruiz-García, R.; Cano, J. Long-Distance Magnetic Coupling in Dinuclear Copper(II) Com-

207

plexes with Oligo-Para-Phenylenediamine Bridging Ligands. *Inorg. Chim. Acta* **2010**, *363*, 1666−1678.

(40) Castellano, M.; Fortea-Pérez, F. R.; Stiriba, S.-E.; Julve, M.; Lloret, F.; Armentano, D.; De Munno, G.; Ruiz-Garcı, R.; Cano, J. Very Long-Distance Magnetic Coupling in a Dicopper(II) Metallacyclophane with Extended π-Conjugated Diphenylethyne Bridges. *Inorg. Chem.* **2011**, *50*, 11279−11281.

(41) Gopakumar, T. G.; Tang, H.; Morillo, J.; Berndt, R. Transfer of Cl Ligands between Adsorbed Iron Tetraphenylporphyrin Molecules. *J. Am. Chem. Soc.* **2012**, *134*, 11844.

(42) Kaiser, K.; Gross, L.; Schulz, F. A Single-Molecule Chemical Reaction Studied by High-Resolution Atomic Force Microscopy and Scanning Tunneling Microscopy Induced Light Emission. *ACS Nano* **2019**, *13*, 6947−6954.

(43) Chutora, T.; de la Torre, B.; Mutombo, P.; Hellerstedt, J.; Kopeček, J.; Jelínek, P.; Švec, M. Nitrous Oxide as an Effective AFM Tip Functionalization: A Comparative Study. *Beilstein J. Nanotechnol.* **2019**, *10*, 315−321.

(44) Doležal, J.; Merino, P.; Redondo, J.; Ondič, L.; Cahlík, A.; Švec, M. Charge Carrier Injection Electroluminescence with CO-Functionalized Tips on Single Molecular Emitters. *Nano Lett.* **2019**, *19*, 8605−8611.

(45) Heinrich, A. J.; Gupta, J. A.; Lutz, C. P.; Eigler, D. M. Single-Atom Spin-Flip Spectroscopy. *Science* **2004**, *306*, 466.

(46) Madhavan, V. Tunneling into a Single Magnetic Atom: Spectroscopic Evidence of the Kondo Resonance. *Science* **1998**, *280*, 567−569.

(47) Ternes, M. Spin Excitations and Correlations in Scanning Tunneling Spectroscopy. *New J. Phys.* **2015**, *17*, 063016.

(48) Rubio-Verdú, C.; Sarasola, A.; Choi, D.-J.; Majzik, Z.; Ebeling, R.; Calvo, M. R.; Ugeda, M. M.; Garcia-Lekue, A.; Sánchez-Portal, D.; Pascual, J. I. Orbital-Selective Spin Excitation of a Magnetic Porphyrin. *Commun. Phys.* **2018**, *1*, 15.

(49) Li, J.; Merino-Díez, N.; Carbonell-Sanromà, E.; Vilas-Varela, M.; De Oteyza, D. G.; Peña, D.; Corso, M.; Pascual, J. I. Survival of Spin State in Magnetic Porphyrins Contacted by Graphene Nanoribbons. *Sci. Adv.* **2018**, *4*, No. eaaq0582.

(50) Tsukahara, N.; Noto, K.-i.; Ohara, M.; Shiraki, S.; Takagi, N.; Takata, Y.; Miyawaki, J.; Taguchi, M.; Chainani, A.; Shin, S.; Kawai, M. Adsorption-Induced Switching of Magnetic Anisotropy in a Single Iron(II) Phthalocyanine Molecule on an Oxidized Cu(110) Surface. *Phys. Rev. Lett.* **2009**, *102*, 167203.

(51) Błoński, P.; Hafner, J. Density-Functional Theory of the Magnetic Anisotropy of Nanostructures: An Assessment of Different Approximations. *J. Phys.: Condens. Matter* **2009**, *21*, 426001.

(52) Horcas, I.; Fernández, R.; Gómez-Rodríguez, J. M.; Colchero, J.; Gómez-Herrero, J.; Baro, A. M. WSXM: A Software for Scanning Probe Microscopy and a Tool for Nanotechnology. *Rev. Sci. Instrum.* **2007**, *78*, 013705.

(53) Kresse, G.; Hafner, J. Ab Initio Molecular Dynamics for Liquid Metals. *Phys. Rev. B: Condens. Matter Mater. Phys.* **1993**, *47*, 558−561.

(54) Kresse, G.; Furthmüller, J. Efficiency of Ab-Initio Total Energy Calculations for Metals and Semiconductors Using a Plane-Wave Basis Set. *Comput. Mater. Sci.* **1996**, *6*, 15−50.

(55) Perdew, J. P.; Burke, K.; Ernzerhof, M. Generalized Gradient Approximation Made Simple. *Phys. Rev. Lett.* **1996**, *77*, 3865−3868.

(56) Blöchl, P. E. Projector Augmented-Wave Method. *Phys. Rev. B: Condens. Matter Mater. Phys.* **1994**, *50*, 17953.

(57) Kresse, G.; Joubert, D. From Ultrasoft Pseudopotentials to the Projector Augmented-Wave Method. *Phys. Rev. B: Condens. Matter Mater. Phys.* **1999**, *59*, 1758−1775.

(58) Grimme, S.; Antony, J.; Ehrlich, S.; Krieg, H. A Consistent and Accurate Ab Initio Parametrization of Density Functional Dispersion Correction (DFT-D) for the 94 Elements H-Pu. *J. Chem. Phys.* **2010**, *132*, 154104.

(59) Dudarev, S. L.; Botton, G. A.; Savrasov, S. Y.; Humphreys, C. J.; Sutton, A. P. Electron-Energy-Loss Spectra and the Structural Stability of Nickel Oxide: An LSDA+U Study. *Phys. Rev. B: Condens. Matter Mater. Phys.* **1998**, *57*, 1505−1509.

(60) Klimeš, J.; Bowler, D. R.; Michaelides, A. Van Der Waals Density Functionals Applied to Solids. *Phys. Rev. B: Condens. Matter Mater. Phys.* **2011**, *83*, 195131.

(61) Hobbs, D.; Kresse, G.; Hafner, J. Fully Unconstrained Noncollinear Magnetism within the Projector Augmented-Wave Method. *Phys. Rev. B: Condens. Matter Mater. Phys.* **2000**, *62*, 11556−11570.

(62) Sen, D.; Błoński, P.; Torre, B. d. l.; Jelínek, P.; Otyepka, M. Thermally Induced Intra-Molecular Transformation and Metalation of Free-Base Porphyrin on Au(111) Surface Steered by Surface Confinement and Ad-Atoms. *Nanoscale Adv.* **2020**, *2*, 2986.

(63) Marsman, M.; Hafner, J. Broken Symmetries in the Crystalline and Magnetic Structures of γ-Iron. *Phys. Rev. B: Condens. Matter Mater. Phys.* **2002**, *66*, 224409.
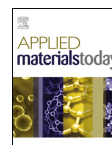
208

Anchoring of single-platinum-adatoms on cyanographene: Experiment and theory

Rostislav Langer [a],[1], Edvin Fako [c],[1], Piotr Błoński [b],[*], Miroslav Vavrečka [a],[b], Aristides Bakandritsos [b], Michal Otyepka [a],[b], Núria López [c],[*]

[a] Department of Physical Chemistry, Faculty of Science, Palacký University, Olomouc, Czech Republic
[b] Regional Centre of Advanced Technologies and Materials, Faculty of Science, Palacký University, Olomouc, Czech Republic
[c] Institute of Chemical Research of Catalonia (ICIQ), The Barcelona Institute of Science and Technology, Tarragona, Spain

ARTICLE INFO

ABSTRACT

Graphene decorated with isolated single atoms (SAs) offers new vista to magnetic and spintronic devices up to single-atom catalysts. While sp atoms can be efficiently bound to graphene, d-block atoms require anchoring groups to prevent nanoparticle formation. Identification of suitable binding sites is a challenging task because the interaction among graphene, anchoring groups and adatoms is very complex. Using density functional theory (DFT) we explored strength and nature of interactions of graphene covalently functionalized by −OH, −CN, −F, and −H groups as anchors for Pt SAs. Both theory and experiment showed that −CN groups acted as suitable ligand enabling immobilization of 3.7 wt % single Pt adatoms. The findings imply that CN functionalized graphene, i.e., cyanographene, is a perspective material for anchoring metal adatoms with potential implications as single-atom-catalysts.

© 2019 Elsevier Ltd. All rights reserved.

1. Introduction

Since the discovery of graphene [1–3], its vast application potential has driven research in many fields [4–6]. Graphene is one of the most studied materials of recent decades making it a popular model system for graphitic materials [7]. Many of the fascinating properties of pristine graphene can be tuned by functionalization [8–11] and put to use in diverse applications, including electrical devices, sensors, spintronics and other [12–17].

High specific surface and affordable price make graphene an attractive support for heterogeneous catalysis. Atomistic design of the active phase is vital for unlocking the full potential of heterogeneously catalyzed industrial (and other) chemical reactions [18]. These catalytic reactions take place on (typically) metal surfaces and therefore bulk metal atoms that are not accessible by the reactants are not involved in the catalysis. There are clear benefits to be had from reducing the amount of such inactive atoms. The downsizing of heterogeneous metal catalysts is a prominent way of improving their catalytic properties, and single atom catalysts (SACs) are at the border of what is possible in terms of advanc-

ing this trend [19–21]. The benefit of SACs lies not only in that they provide the highest possible surface to volume ratio of any heterogeneous catalyst, but they also give rise to several specific interactions enhancing selectivity. SACs are at the ultimate frontier in atom economy with nearly 100% metal loading being utilized to form accessible active sites. Moreover, the well-defined structure and strong interaction between the support and SAC suggest easy reusability and recycling of the catalytic material [22,23].

Particularly, carbon supported SACs have recently been successfully employed for several processes traditionally considered to be difficult to perform utilizing a heterogeneous catalyst, e.g. Pd-catalyzed coupling reactions or Pd-SAs enhanced catalytic reactivity in the semi-hydrogenation of acetylene to ethylene [24–27]. Despite the successful application of SACs for an increasing number of applications, only a few highly stable coordination environments [28–32] have yet been experimentally characterized. Graphene derivatives were identified as promising supports for single adatoms [33,34], however, stabilizing the individual metal atoms on the support remains a significant challenge in further development of efficient and stable SACs. The doping of graphene with sp elements (particularly sp^3 doping) unlocked the means of adjusting the electronic structure of graphene [16], however, the relatively low interaction of the pristine graphene layer with the d-block adatoms [35], implies that a different approach must be utilized when trying to stabilize these isolated atoms on graphene

* Corresponding authors.
  E-mail addresses: piotr.blonski@upol.cz (P. Błoński), nlopez@iciq.es (N. López).
[1] These authors are contributed equally to this work.

[36–38]. Binding isolated metal atoms to already functionalized graphene, provides additional interaction between the metal and functional group with respect to pristine graphene and may represent an efficient way for synthesis of new branch of graphene-based derivatives applicable in electronics and single atom catalysis. To advance this field, it is necessary to identify suitable anchoring groups for metal single atoms and deeply understand the nature of metal-linker-graphene interaction and influence of the adatom on the electronic structure of the graphene-derivative.

Here, we discuss the possibility of attaching single platinum adatoms to diluted graphene derivatives, because platinum is often used as the active center in various important catalytic processes [25,32,39,40]. We considered existing graphene derivatives, i.e., fluorinated graphene [41], graphene oxide [42], cyanographene [43] and graphane [44], i.e., derivatives containing functional groups (X = −F, −OH, −CN, and −H), which can potentially anchor the platinum single atoms (Fig. S1 and Table S1). Using theoretical calculations we identified the nitrile group as the most efficient anchor for the Pt adatoms (in Pt^0 and Pt^{II} oxidation states, Fig. S2) which otherwise easily diffuse along the pristine graphene surface (Fig. S3 and Table S2). We also successfully grafted the Pt single atoms to cyanographene with high content, 3.7 wt %. It should be noted, that the cyanographene was very recently used for anchoring the Cu atoms and applied as SAC for oxidative amine coupling and alcohol oxidation reactions [21]. All these results show that the nitrile groups are well suited for anchoring of metal single atoms to graphene and identify cyanographene an ideal platform for synthesis of a wide portfolio of SACs.

2. Materials and methods

2.1. Computational details

The first-principle spin-polarized density functional theory (DFT) calculations were performed using the Vienna Ab initio Simulation Package (VASP) code [45,46]. The Perdew-Burke-Ernzerhof functional (PBE) [47] was employed with inner electrons represented as projector augmented waves (PAW) [48,49]. Dispersion contributions were introduced through the D3 approach [50,51]. The valence monoelectronic states expanded in plane waves with a cut-off kinetic energy of 500 eV. The Brillouin zone was sampled with a $6 \times 6 \times 1$ (structure and cell optimization) and $15 \times 15 \times 1$ (DOS and energy calculations) Γ–centered grid. Graphene was modelled as a (3×3) and (6×6) supercell containing 18 and 72 carbon atoms. The molecules were placed in a triclinic box with 18 Å sides. We considered diluted systems containing one functional group attached on-top of the graphene lattice and systems with two functional groups in the *ortho/trans* position (Fig. S1). In all cases the ionic and electronic convergence criteria were 10^{-3} eV and 10^{-6} eV, respectively, in the self-consistent field (SCF) cycle. A dipole correction was employed along the z-direction [52]. Transition states were located following the climbing image nudged elastic band procedure (CI-NEB) [53,54]. Analysis of the charges was performed using the Bader approach [55]. Total magnetic moments were calculated as the difference between the numbers of electrons in occupied majority- and minority-spin states.

The stability of g-X structures (X: fluorine –F, hydroxyl –OH, nitrile –CN, hydrogen –H or platinum Pt) shown in Fig. S1 was assessed in terms of the binding energy per group

$$E_{bind} = (E_{g-X} - E_g - n \cdot E_X)/n \tag{1}$$

where E_{g-X}, E_g, and E_X denote the total energy of the functionalized graphene, pristine graphene, and functional groups, n stands for number of functional groups. The average C—C bond distance in pristine graphene (1.43 Å) agrees well with experimental results

[56]. A functional group has been placed onto three high symmetry sites of graphene lattice, i.e. top (t), bridge (b) and six-fold hollow (h) position. The thermodynamic stability of all reported g-X-Pt configurations was analysed in terms of the binding energy per platinum adatom

$$E_{bind/Pt} = E_{g-X-Pt} - E_{g-X} - E_{Pt} \tag{2}$$

where E_{g-X-Pt}, E_{g-X}, and E_{Pt} and denote the total energy of functionalized graphene doped by Pt adatom, functionalized graphene and Pt adatom, respectively.

The finite model calculations of g-$(CN)_2$-Pt (Fig. S2) were performed using Gaussian software [57] employing PBE exchange-correlation functional [47,58] and empirical dispersions D3 [51]. All structures can be retrieved from the ioChem-BD database [59] following the link [https://doi.org/10.19061/iochem-bd-1-101].

2.2. Materials

Cyanographene (g-CN) was synthesized according to the previously reported procedure [43], $K_2[PtCl_4]$ was purchased from Sigma-Aldrich, ethanol absolute from Penta, ultrapure water (18 MΩ cm^{-1}) was used in all cases, produced from a Puris Esse-UP Ultra Pure Water System.

2.3. Synthesis of the cyanographene/Pt(II) hybrid (g-CN/Pt)

g-CN (120 mg in 12 mL H_2O) and $K_2[PtCl_4]$ (162 mg in 12 mL H_2O) were mixed and microwave-heated at 60 °C for 15 min. (850 W, 300 Anthon par microwave synthesizer). Then, the mixture was centrifuged and washed three times with water and once with ethanol.

2.4. Experimental techniques

The samples were dispersed in water, sonicated for 5 min and one drop put on copper grid with Holey carbon film. After drying on the air at room temperature, the samples were measured by High Resolution Transmission Electron Microscope (HR-TEM) Titan G2 (FEI) with Image corrector on accelerating voltage 80 kV. Images were taken with BM UltraScan CCD camera (Gatan). Energy Dispersive Spectrometry (EDS) was performed in Scanning TEM (STEM) mode by Super-X system with four silicon drift detectors (Bruker). STEM images were taken with HAADF detector 3000 (Fishione).

The concentration of metals was determined by the atomic absorption spectroscopy (AAS) technique, using a graphite furnace (ContrAA 600; Analytik Jena AG, Germany) equipped with a high-resolution Echelle double monochromator (spectral band width, 2 pm at 200 nm). A xenon lamp was used as a continuum radiation source.

High-resolution X-ray photoelectron spectroscopy (HR-XPS) was performed using a PHI VersaProbe II spectrometer (Physical Electronics) equipped with an Al Kα source (15 kV, 50 W). All spectra were acquired at room temperature (22 °C), under vacuum (1.4×10^{-7} Pa). High-resolution spectra were acquired by setting the pass energy to 23.500 eV and the step size to 0.200 eV. These spectra were analyzed using the MultiPak (Ulvac-PHI, Inc.) program. The binding energy values were reported with respect to the C1s lowest peak energy at 284.70 eV.

3. Results and discussions

The bond strengths of functional groups to graphene depend on the hybrid state of the neighboring carbon atoms. Generally, the bonds are weak if the sp^3 carbon bearing the functional group is attached to three sp^2 carbon atoms, however, their strength
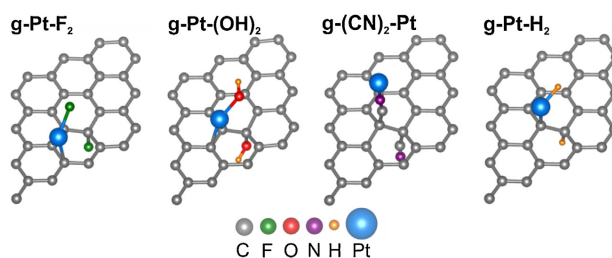
Fig. 1. The most stable structures of g-X-Pt complexes: two-sided fluorinated g-Pt-F$_2$, hydroxylated g-Pt-(OH)$_2$, nitrilated g-(CN)$_2$-Pt and hydrogenated g-Pt-H$_2$.
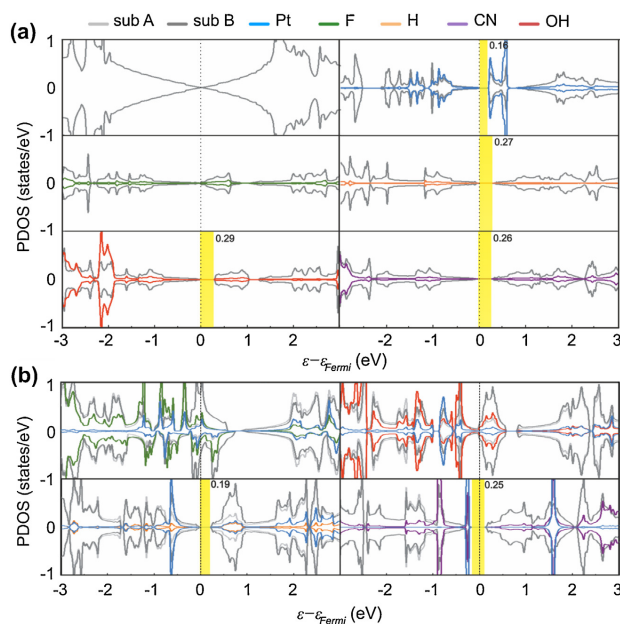

Fig. 2. Spin-polarized PDOS plots of two-sided functionalized graphene (a) g-X$_2$, (b) g-X$_2$-Pt. The Fermi level is set to zero. Band-gaps are depicted by vertical bars; numbers correspond to the width of the band-gap (in eV).

increase if the sp^3 carbon is attached to another sp^3 (bearing an attached group in *trans*-position) and just two sp^2 carbon atoms (see Section 2.1 in Supporting Information for details). Therefore, we have focused on the double-sided functionalized graphene g-X$_2$ with functional groups in *ortho/trans* positions (see Section 2.2 in Supporting Information for details) and the results concerning one-sided functionalized graphene g-X are shown in Section 2.3 and 2.4 in the Supporting Information.

We considered all unique positions of Pt atoms relative to the functional groups (Fig. S4). Surprisingly, the Pt adatom cleaved the bonds of −F, −OH, and −H to graphene and they released fluorine, hydroxyl, and hydrogen groups attached on-top of the Pt adatom, forming graphene–Pt–F (−OH, or −H) complexes (Fig. 1). This process was exothermic with binding energies per platinum adatom from −2.79 to −4.05 eV (Eq. 2, Table S3, and Fig. S5). An easy diffusion of −Pt–X moiety following a top-bridge path was enabled by

low diffusion barriers (0.13-0.44 eV, Table S4) similar to the diffusion barrier of isolated platinum adatom (0.15 eV, Table S2). This finding agrees with the experimental observation that −OH groups were released from graphene after the Pt deposition [60,61]. On the other hand, Pt adatom did not cause the release of −CN from the graphene surface and is instead coordinated on top of the −CN group, forming a linear g−CN−Pt complex (Fig. 1). The anchoring of Pt adatom above or in the vicinity of the −CN group (Fig. S5c1-4) prevented any potential detrimental processes, e.g. agglomeration, diffusion or leaching, with a high top-bridge diffusion barrier of 1.34 eV (Table S4). Such high diffusion barriers reveal that thermal effects do not compromise the long term stability of this material. The g-CN based catalysts remained highly stable even upon recycling [21,62]. Additionally, when a Pt adatom is bound on top of a −CN group, this leaves the coordination sphere of Pt accessible which is desirable for catalytic activity. One shall note that both the release of −F, −OH, and −H from the graphene lattice to
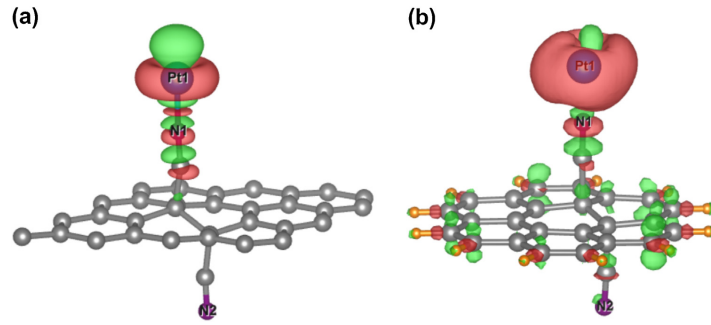
Fig. 3. (a) Charge density difference plot of periodic model g-CN_2-Pt (isovalue 5 meÅ^{-3}) and (b) charge density difference plot of finite model g-CN_2-Pt^{II} in gas phase (isovalue 5 meÅ^{-3}).
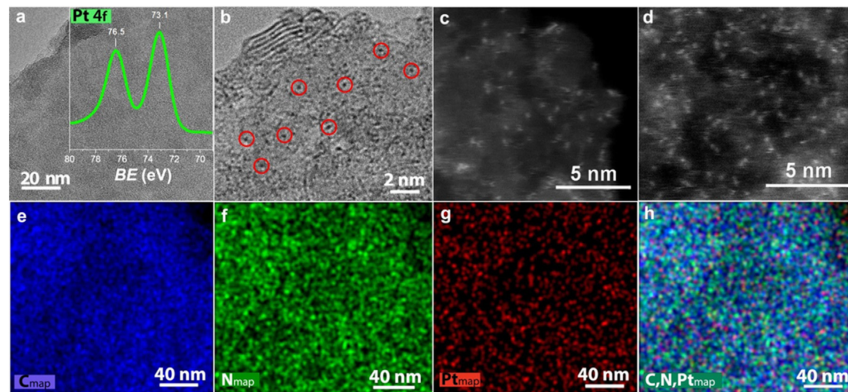
Fig. 4. Representative HR-TEM image of a flake from the g-CN/Pt hybrid and HR-XPS of the Pt 4f region (a), higher magnification HR-TEM image showing high-contrast spots probably originating from embedded Pt(II) ions (b), HAADF-STEM images showing the heavier (and thus brighter) single metal ions embedded in the g - CN support (c,d) and EDS elemental mapping performed on g-CN/Pt for carbon (e), nitrogen (f), platinum (g), and combined C, N and Pt (h).

form g–Pt–F(F_2), g–Pt–OH(OH_2), and g–Pt–H(H_2) complexes and the formation of g–CN(CN_2)–Pt was predicted for one-sided and two-sided functionalized graphene (Tables S5-S16).

The chemical functionalization of graphene, which is a non-magnetic zero bandgap semi-metal [2] with its valence and conductive bands crossing at the Dirac point at the Fermi level (E_F), significantly changes its electronic structure. The covalent bonding of –H, –OH, and –CN to the graphene lattice in *trans*-positions opened the graphene's zero-band-gap, while fluorinated graphene is a p-type metal (Fig. 2a and Fig. S6-S9, Table S3 and Tables S5-S8) [63–65]. All g–X_2 systems are non-magnetic. The deposition of Pt adatom onto the fluorinated graphene leading to the formation of graphene–Pt–F_2 complex, further strengthen the metallic character of the system (Fig. 2b, Fig. S10). Also, the electronic gap at E_F for the graphene–(OH_2) system was closed by the formation of the g-Pt-(OH_2) complex (Fig. 2b and Fig. S11) although with a much lower DOS at E_F. Accordingly, the DOS of the latter system is spin symmetric, whereas the g-Pt-F_2 complex is spin-polarized. The formation of graphene-Pt-H_2 complex lower the electronic gap of the hydrogenated graphene from 0.27 to 0.19 eV, while the electronic gap of cyanographene (0.26 eV) was hardly modified (0.25 eV) due to the presence of Pt bound on top of the –CN group

(Fig. 2b and Fig. S12-S13). The conductive character of the material can be highly advantageous in electrochemical sensing, capacitors, (photo)redox and (photo)electrocatalytic applications due to the possibility of storing and shuttling electrons [17,21,43,62,66]. Both g-Pt-H_2 and g-(CN_2)-Pt are non-magnetic with spin symmetric DOSs. Whereas for the metallic g–Pt–F_2 and g-Pt-(OH_2) complexes the charge depletion on Pt was the greatest (respectively 0.47 *e* and 0.34 *e*), the charge lost on Pt atom bound on-top of –CN was only 0.06 *e*, and in the g-Pt-H_2 complex there was hardly any charge-transfer from/to Pt observed (Table S3). Fig. 3 and Fig. S14 show the difference-electron densities calculated for the g–CN–Pt complex with platinum in both oxidation Pt^0 and Pt^{II}. The picture demonstrates a polar-covalent bond formation between Pt and N ($E_{bind/Pt}$ = −2.29 eV) associated with the electron transfer to antibonding σ_d^* state of the Pt atom, which is accompanied with the accumulation of electrons in bonding states between Pt, N, and C atoms, shown as a charge depletion both on the Pt site within the donut-shaped ring parallel to the graphene plane, and on the N site.

Both platinum atom Pt^0 and Pt^{II} ion which represents a common oxidation state of platinum were considered in the gas phase and water environment using an implicit solvent model. As expected, the calculations (Eq. 2) identified that Pt^{II} binds to g-CN more

strongly (13.92 eV) than Pt^0 (2.35 eV) in vacuum. In water, the interaction of Pt^{II} to g-CN significantly dropped to 3.98 eV, while the interaction of Pt^0 remained less affected amounting to 2.63 eV. These calculations suggest that the nitrile group is well suited for anchoring platinum in both Pt^0 and Pt^{II} states (Table S17 and S18).

The ability of g-CN to bind Pt atoms was evaluated experimentally by mixing of aqueous dispersions of the cyanographene with the Pt^{II} salt. The obtained g-CN/Pt hybrid was analyzed with HR-TEM, revealing the absence of any inorganic crystalline phases, i.e. nanoparticles (Fig. 4a, Fig. S29), but unveiled atomic sized high-contrast spots, suggesting the presence of heavy metal atoms (Fig. 4b). This was confirmed by the abundant bright spots from metal atoms, revealed via the sub-Ångstrom resolution aberration corrected high-angle annular dark-field (HAADF) STEM in Fig. 4c,d. Furthermore, Pt atoms appear to populate densely and homogeneously the nitrogen rich graphene sheets, as verified with EDS mapping (Fig. 4b-e). HR-XPS further confirmed the presence and oxidation state of the Pt^{II} ions, with the two spin-orbit split 4f components appearing at electron binding energies (*EBE*) of 73.1 and 76.5 eV. According to AAS analysis, the Pt content on g-CN/Pt was particularly high (3.7 wt %), surpassing the recently reported SAC where 3 wt % Pt loading on ceria was achieved [67]. No Pt was detectable in a control analysis of the as synthesized g-CN. Therefore, g-CN acted as a very effective 2D-ligand for trapping and sustaining single Pt ions over the out-of-plane functionalized graphene.

4. Conclusions

In conclusion, we addressed the anchoring of single-platinum-adatom on functionalized graphene. Since Pt adatoms easily diffuse on pristine graphene, which may lead to undesirable aggregation and nanoparticles formation, we explored graphene derivatives bearing –F, –OH, –CN and –H functional groups as possible means of anchoring single Pt atoms and preventing their diffusion. Whereas the Pt adatom cleaved the bonds of –F, –OH, and –H to graphene leading to the formation of graphene–Pt-F (–OH, or –H) complexes, the –CN group remained bound to graphene lattice and anchored the single-platinum-adatom with high energy barrier against –CN-Pt migration. The anchoring of Pt adatoms on g–CN provide a scaffold for SACs which are considered as one of the holy grails in catalysis as they enable the best use of rare and rather expensive noble metals. As cyanographene was experimentally prepared in 2017, the g–CN material seems to be very promising as an anchor for metals, as recently experimentally demonstrated with the synthesis of SACs based on Cu and Fe ions [21], but also in the present work with the effective immobilization of Pt ions enabling plethora of catalytic reactions which could be examined in future.

Declaration of Competing Interest

The authors declare no competing financial interests.

Appendix A. Supplementary data

Supplementary material related to this article can be found, in the online version, at doi:https://doi.org/10.1016/j.apmt.2019.100462.

References

[1] K.S. Novoselov, A.K. Geim, S.V. Morozov, D. Jiang, Y. Zhang, S.V. Dubonos, I.V. Grigorieva, A.A. Firsov, Electric field effect in atomically thin carbon films, Science 306 (2004) 666–669, http://dx.doi.org/10.1126/science.1102896.
[2] K.S. Novoselov, A.K. Geim, S.V. Morozov, D. Jiang, M.I. Katsnelson, S.V. Grigorieva, S.V. Dubonos, A.A. Firsov, Two-dimensional gas of massless dirac fermions in graphene, Nature 438 (2005) 197–200, http://dx.doi.org/10.1038/nature04233.
[3] K. Novoselov, Mind the gap, Nat. Mater. 6 (2007) 720–721, http://dx.doi.org/10.1038/nmat2006.
[4] A.K. Geim, K.S. Novoselov, The rise of graphene, Nat. Mater. 6 (2007) 183–191, http://dx.doi.org/10.1038/nmat1849.
[5] V. Georgakilas, J.A. Perman, J. Tuček, R. Zbořil, Broad family of carbon nanoallotropes: classification, chemistry, and applications of fullerenes, carbon dots, nanotubes, graphene, Nanodiamonds, and combined superstructures, Chem. Rev. 115 (2015) 4744–4822, http://dx.doi.org/10.1021/cr500304f.
[6] A.H. Castro-Neto, F. Guinea, N.M.R. Peres, K.S. Novoselov, A.K. Geim, The electronic properties of graphene, Rev. Mod. Phys. 81 (2009) 109–162, http://dx.doi.org/10.1103/RevModPhys.81.109.
[7] P. Błoński, Z. Łodziana, First-principles study of $LiBH_4$ nanoclusters interaction with models of porous carbon and silica scaffolds, Int. J. Hydrogen. Energ. 39 (2014) 9848–9853, http://dx.doi.org/10.1016/j.ijhydene.2014.03.264.
[8] H. Wang, T. Maiyalagan, X. Wang, Review on recent progress in nitrogen-doped graphene: synthesis, characterization, and its potential applications, ACS Catal. 2 (2012) 781–794, http://dx.doi.org/10.1021/cs200652y.
[9] P. Błoński, J. Tuček, Z. Sofer, V. Mazánek, M. Petr, M. Pumera, M. Otyepka, R. Zbořil, Doping with graphitic nitrogen triggers ferromagnetism in graphene, J. Am. Chem. Soc. 139 (2017) 3171–3180, http://dx.doi.org/10.1021/jacs.6b12934.
[10] C. Lee, X. Wei, J.W. Kysar, J. Hone, Measurement of the Elastic Properties and Intrinsic Strength of Monolayer Graphene, Science 321 (2008) 385–388, http://dx.doi.org/10.1126/science.1157996.
[11] M.J. Allen, V.C. Tung, R.B. Kaner, Honeycomb carbon: a review of graphene, Chem. Rev. 110 (2010) 132–145, http://dx.doi.org/10.1021/cr900070d.
[12] W. Han, R.K. Kawakami, M. Gmitra, J. Fabian, Graphene spintronics, Nat. Nanotechnol. 9 (2014) 794–807, http://dx.doi.org/10.1038/nnano.2014.214.
[13] Z. Liu, Q. Liu, Y. Huang, Y. Ma, S. Yin, X. Zhang, W. Sun, Y. Chen, Organic photovoltaic devices based on a novel acceptor material, Graphene Adv. Mater. 20 (2008) 3924–3930, http://dx.doi.org/10.1002/adma.200800366.
[14] M.D. Stoller, S. Park, Y. Zhu, J. An, R.S. Ruoff, Graphene-based ultracapacitors, Nano Lett. 8 (2008) 3498–3502, http://dx.doi.org/10.1021/nl802558y.
[15] V. Urbanová, K. Holá, A.B. Bourlinos, K. Čépe, A. Ambrosi, A.H. Loo, M. Pumera, F. Karlický, M. Otyepka, R. Zbořil, Thiofluorographene-hydrophilic graphene derivative with semiconducting and genosensing properties, Adv. Mater. 27 (2015) 2305–2310, http://dx.doi.org/10.1002/adma.201500094.
[16] J. Tuček, K. Holá, B. Bourlinos, P. Błoński, A. Bakandritsos, J. Ugoloti, M. Dubecký, F. Karlický, V. Ranc, K. Čépe, M. Otyepka, R. Zbořil, Room temperature organic magnets derived from sp3 functionalized graphene, Nat. Commun. 8 (1–12) (2017) 14525, http://dx.doi.org/10.1038/ncomms14525.
[17] A. Bakandritsos, P. Jakubec, M. Pykal, M. Otyepka, Covalently functionalized graphene as a supercapacitor electrode material, FlatChem 13 (2019) 25–33, http://dx.doi.org/10.1016/j.flatc.2018.12.004.
[18] G. Carchini, N. Almora-Barrios, G. Revilla-López, L. Bellarosa, R. García-Muelas, M. García-Melchor, S. Pogodin, P. Błoński, N. López, How theoretical simulations can address the structure and activity of nanoparticles, Top. Catal. 56 (2013) 1262–1272, http://dx.doi.org/10.1007/s11244-013-0093-3.
[19] J.M. Thomas, The enduring relevance and academic fascination of catalysis, Nat. Catal. 1 (2018) 2–5, http://dx.doi.org/10.1038/s41929-017-0014-0.
[20] J.M. Thomas, W.J. Thomas, Principles and Practice of Heterogeneous Catalysis, Wiley – VCH, Weinheim, Germany, 2015.
[21] A. Bakandritsos, R.G. Kadam, P. Kumar, G. Zoppellaro, M. Medveď, J. Tuček, T. Montini, O. Tomanec, P. Andrýsková, B. Drahoš, R.S. Varma, M. Otyepka, M.B. Gawande, P. Fornasiero, R. Zbořil, Mixed-Valence Single-Atom Catalyst

Derived from Functionalized Graphene, Adv. Mater. 31 (1–9) (2019) 1900323, http://dx.doi.org/10.1002/adma.201900323.

[22] M. Monai, M. Melchionna, P. Fornasiero, From metal to metal-free catalysts: route to sustainable chemistry, J. Adv. Catal. Sci. Technol. 63 (2018) 1–73, http://dx.doi.org/10.1016/bs.acat.2018.10.001.

[23] H. Fei, J. Dong, Y. Feng, C.S. Allen, C. Wan, B. Volosskiy, M. Li, Z. Zhao, Y. Wang, H. Sun, P. An, W. Chen, Z. Guo, C. Lee, D. Chen, I. Shakir, M. Liu, T. Hu, Y. Li, A.I. Kirkland, X. Duan, Y. Huang, General synthesis and definitive structural identification of MN4C4 single-atom catalysts with tunable electrocatalytic activities, Nat. Catal. 1 (2018) 63–72, http://dx.doi.org/10.1038/s41929-017-0008-y.

[24] L. Yin, J. Liebscher, Carbon–Carbon coupling reactions catalyzed by heterogeneous palladium catalysts, Chem. Rev. 107 (2007) 133–173, http://dx.doi.org/10.1021/cr0505674.

[25] J. Liu, Catalysis by supported single metal atoms, ACS Catal. 7 (2017) 34–59, http://dx.doi.org/10.1021/acscatal.6b01534.

[26] S. Wei, A. Li, J.C. Liu, Z. Li, W. Chen, Y. Gong, Q. Zhang, W.C. Cheong, Y. Wang, L. Zheng, H. Xiao, C. Chen, D. Wang, Q. Peng, L. Gu, X. Han, J. Li, Y. Li, Direct observation of noble metal nanoparticles transforming to thermally stable single atoms, Nat. Nanotechnol. 13 (2018) 856–861, http://dx.doi.org/10.1038/s41565-018-0197-9.

[27] Z. Chen, E. Vorobyeva, S. Mitchell, E. Fako, M.A. Ortuño, N. López, S.M. Collins, P.A. Midgley, S. Richard, G. Vilé, J. Pérez-Ramírez, A heterogeneous single-atom palladium catalyst surpassing homogeneous systems for suzuki coupling, Nat. Nanotechnol. 13 (2018) 702–707, http://dx.doi.org/10.1038/s41565-018-0167-2.

[28] Z. Chen, S. Mitchell, E. Vorobyeva, R.K. Leary, R. Hauert, T. Furnival, Q.M. Ramasse, J.M. Thomas, P.A. Midgley, D. Dontsova, M. Antonietti, S. Pogodin, N. López, J.A. Pérez- Ramírez, Stabilization of single metal atoms on graphitic carbon nitride, Adv. Funct. Mater. 27 (2017) 1–12, http://dx.doi.org/10.1002/adfm.201605785.

[29] G. Vilé, D. Albani, M. Nachtegaal, Z. Chen, D. Dontsova, M. Antonietti, N. López, J.A. Pérez-Ramírez, Stable single-site palladium catalyst for hydrogenations, Angew. Chem. 54 (2015) 11265–11269, http://dx.doi.org/10.1002/anie.201505073.

[30] A. Zitolo, V. Goellner, V. Armel, M. Sougrati, T. Mineva, L. Stievano, E. Fonda, F. Jaouen, Identification of catalytic sites for oxygen reduction in Iron- and nitrogen-doped graphene materials, Nat. Mater. 14 (2015) 937–942, http://dx.doi.org/10.1038/nmat4367.

[31] S. Vajda, M.J. Pellin, J.P. Greeley, C.L. Marshall, L.A. Curtiss, G.A. Ballentine, J.W. Elam, S. Catillon-Mucherie, P.C. Redfern, F. Mehmood, P. Zapol, Subnanometre platinum clusters as highly active and selective catalysts for the oxidative dehydrogenation of propane, Nat. Mater. 8 (2009) 213–216, http://dx.doi.org/10.1038/nmat2384.

[32] E. Fako, Z. Lodziana, N. López, Comparative single atom heterogeneous catalysts (SAHCs) on different platforms: a theoretical approach, Catal. Sci. Technol. 7 (2017) 4285–4293, http://dx.doi.org/10.1039/C7CY01136A.

[33] X. Zhou, J. Qiao, L. Yang, J.A. Zhang, Review of graphene-based nanostructural materials for both catalyst supports and metal-free catalysts in PEM fuel cell oxygen reduction reactions, Adv. Energy Mater. 4 (1–25) (2014) 1301523, http://dx.doi.org/10.1002/aenm.201301523.

[34] S. Sun, G. Zhang, N. Gauquelin, N. Chen, J. Zhou, S. Yang, W. Chen, D. Geng, M.N. Banis, R. Li, S. Ye, S. Knights, G.A. Botton, T.-K. Sham, X. Sun, Single-atom catalysis using Pt/Graphene achieved through atomic layer deposition, Sci. Rep. 3 (1–9) (2013) 1775, http://dx.doi.org/10.1038/srep01775.

[35] I.A. Pasti, A. Jovanovič, A.S. Dobrota, S.V. Mentus, B. Johansson, N.V. Skorodumova, Atomic adsorption on pristine graphene along the periodic table of elements - from PBE to non-local functionals, Appl. Surf. Sci. 436 (2017) 433–440, http://dx.doi.org/10.1016/j.apsusc.2017.12.046.

[36] I.A. Pasti, A. Jovanovič, A.S. Dobrota, S.V. Mentus, N.V. Skorodumova, Atomic adsorption on graphene with a single vacancy: systematic DFT study through the periodic table of elements, Phys. Chem. Chem. Phys. 20 (2017) 858–865, http://dx.doi.org/10.1039/C7CP07542A.

[37] B. de la Torre, M. Švec, P. Hapala, J. Redondo, O. Krejčí, R. Lo, D. Manna, A. Sarmah, D. Nachtigallová, J. Tuček, P. Błoński, M. Otyepka, R. Zbořil, P. Hobza, P. Jelínek, Non-covalent control of spin-state in metal-organic complex by positioning on N-doped graphene, Nat. Commun. 9 (1–9) (2018) 2831, http://dx.doi.org/10.1038/s41467-018-05163-y.

[38] M. Lefèvre, E. Proietti, F. Jaouen, J.-P. Dodelet, Iron-based catalysts with improved oxygen reduction activity in polymer electrolyte fuel cells, Science 324 (2009) 71–74, http://dx.doi.org/10.1126/science.1170051.

[39] N. Cheng, S. Stambula, D. Wang, M.N. Banis, J. Liu, A. Riese, B. Xiao, R. Li, T.K. Sham, L.M. Liu, G.A. Botton, X. Sun, Platinum single-atom and cluster catalysis of the hydrogen evolution reaction, Nat. Commun. 7 (1-9) (2016) 13638, http://dx.doi.org/10.1038/ncomms13638.

[40] X. Li, P. Cui, W. Zhong, J. Li, X. Wang, Z. Wang, J. Jiang, Graphitic carbon nitride supported single-atom catalysts for efficient oxygen evolution reaction, ChemComm. 52 (2016) 13233–13236, http://dx.doi.org/10.1039/C6CC07049C.

[41] R. Zbořil, F. Karlický, A.B. Bourlinos, T.A. Steriotis, A.K. Stubos, V. Georgakilas, K. Safarova, D. Jancik, C. Trapalis, M. Otyepka, Graphene fluoride: a stable stoichiometric graphene derivative and its chemical conversion to graphene, Small 6 (2010) 2885–2891, http://dx.doi.org/10.1002/smll.201001401.

[42] Y. Zhu, S. Murali, W. Cai, X. Li, J.W. Suk, J.R. Potts, R.S. Ruoff, Graphene and graphene oxide: synthesis, properties, and applications, Adv. Mater. 22 (2010) 3906–3924, http://dx.doi.org/10.1002/adma.201001068.

[43] A. Bakandritsos, M. Pykal, P. Błoński, P. Jakubec, D.D. Chronopoulos, K. Poláková, V. Georgakilas, K. Čépe, O. Tomanec, V. Ranc, A.B. Bourlinos, R. Zbořil, M. Otyepka, Cyanographene and graphene acid: emerging derivatives enabling high-yield and selective functionalization of graphene, ACS Nano 11 (2017) 2982–2991, http://dx.doi.org/10.1021/acsnano.6b08449.

[44] J.O. Sofo, A.S. Chaudhari, G.D. Barber, Graphane: a two-dimensional hydrocarbon, Phys. Rev. B 75 (1–4) (2007) 153401, http://dx.doi.org/10.1103/PhysRevB.75.153401.

[45] G. Kresse, J. Furthmüller, Efficiency of ab-initio total energy calculations for metals and semiconductors using a plane-wave basis set, Comp. Mater. Sci. 6 (1996) 15–50, http://dx.doi.org/10.1016/0927-0256(96)00008-0.

[46] G. Kresse, J. Furthmüller, Efficient iterative schemes for ab initio total-energy calculations using a plane-wave basis set, Phys. Rev. B 54 (1996) 11169–11186, http://dx.doi.org/10.1103/PhysRevB.54.11169.

[47] J.P. Perdew, K. Burke, M. Ernzerhof, Generalized gradient approximation made simple, Phys. Rev. Lett. 77 (1996) 3865–3868, http://dx.doi.org/10.1103/PhysRevLett.77.3865.

[48] P.E. Blöchl, Projector augmented-wave method, Phys. Rev. B 50 (1994) 17953–17979, http://dx.doi.org/10.1103/physrevb.50.17953.

[49] G. Kresse, D. Joubert, From Ultrasoft Pseudopotentials to the Projector Augmented-Wave Method, Phys. Rev. B 59 (1999) 11–19, http://dx.doi.org/10.1103/PhysRevB.59.1758.

[50] S. Grimme, S. Ehrlich, L. Goerigk, Effect of the damping function in dispersion corrected density functional theory, J. Comput. Chem. 32 (2011) 1456–1465, http://dx.doi.org/10.1002/jcc.21759.

[51] S. Grimme, J. Antony, S. Ehrlich, H. Krieg, Consistent and accurate ab initio parametrization of density functional dispersion correction (DFT-D) for the 94 elements H-Pu, J. Chem. Phys. 132 (1-19) (2010) 154104, http://dx.doi.org/10.1063/1.3382344.

[52] G. Makov, M.C. Payne, Periodic boundary consitions in ab initio calculations, Phys. Rev. B 51 (1994) 4014–4022, http://dx.doi.org/10.1103/physrevb.51.4014.

[53] G.A. Henkelman, B.P. Uberuaga, H. Jónsson, Climbing image nudged elastic band method for finding saddle points and minimum energy paths and minimum energy paths, J. Chem. Phys. 113 (2010) 9901–9904, http://dx.doi.org/10.1063/1.1329672.

[54] G. Henkelman, H. Jónsson, Improved tangent estimate in the nudged elastic band method for finding minimum energy paths and saddle points minimum energy paths and saddle points, J. Chem. Phys. 113 (2000) 9978–9985, http://dx.doi.org/10.1063/1.1323224.

[55] E. Sanville, S.D. Kenny, R. Smith, G. Henkelman, Improved grid-based algorithm for bader charge allocation, J. Comput. Chem. 28 (2007) 899–908, http://dx.doi.org/10.1002/jcc.20575.

[56] R. Heyrovska, The golden ratio, ionic and atomic radii and bond lengths, Mol. Phys. 103 (2007) 877–882, http://dx.doi.org/10.1080/00268970412331333591.

[57] M.J. Frisch, G.W. Trucks, H.B. Schlegel, G.E. Scuseria, M.A. Robb, J.R. Cheeseman, G. Scalmani, V. Barone, B. Mennucci, G.A. Petersson, H. Nakatsuji, M. Caricato, X. Li, H.P. Hratchian, A.F. Izmaylov, J. Bloino, G. Zheng, J.L. Sonnenberg, M. Hada, M. Ehara, K. Toyota, R. Fukuda, J. Hasegawa, M. Ishida, T. Nakajima, Y. Honda, O. Kitao, H. Nakai, T. Vreven, J.A. Montgomery, J.E. Peralta, F. Ogliaro, M. Bearpark, J.J. Heyd, E. Brothers, K.N. Kudin, V.N. Staroverov, R. Kobayashi, J. Normand, K. Raghavachari, A. Rendell, J.C. Burant, S.S. Iyengar, J. Tomasi, M. Cossi, N. Rega, J.M. Millam, M. Klene, J.E. Knox, J.B. Cross, V. Bakken, C. Adamo, J. Jaramillo, R. Gomperts, R.E. Stratmann, O. Yazyev, A.J. Austin, R. Cammi, C. Pomelli, J.W. Ochterski, R.L. Martin, K. Morokuma, V.G. Zakrzewski, G.A. Voth, P. Salvador, J.J. Dannenberg, S. Dapprich, A.D. Daniels, O. Farkas, J.B. Foresman, J.V. Ortiz, J. Cioslowski, D.J. Fox, Gaussian 09, Revision D.01, Wallingford CT, 2009.

[58] J.P. Perdew, K. Burke, M. Ernzerhof, Errata: generalized gradient approximation made simple, Phys. Rev. Lett. 78 (1997) 1396.

[59] M. Álvarez-Moreno, C. de Graaf, N. López, F. Maseras, J.M. Poblet, C. Bo, Managing the computational chemistry big data problem: the ioChem-BD platform, J. Chem. Inf. Model. 55 (2015) 95–103, http://dx.doi.org/10.1021/ci500593j.

[60] Y. Li, W. Gao, L. Ci, C. Wang, P.M. Ajayan, Catalytic performance of Pt nanoparticles on reduced graphene oxide for methanol electro-oxidation, Carbon 48 (2009) 1124–1130, http://dx.doi.org/10.1016/j.carbon.2009.11.034.

[61] Z. Liu, X. Duan, H. Cheng, Z. Zhou, X. Zhou, Synthesis of Platinum/Graphene composites by a polyol method: the role of graphite oxide precursor surface chemistry, Carbon 89 (2015) 93–101, http://dx.doi.org/10.1016/j.carbon.2015.03.022.

[62] Y.H. Cheong, M.Z.M. Nasir, A. Bakandritsos, M. Pykal, P. Jakubec, R. Zbořil, M. Otyepka, M. Pumera, Cyanographene and Graphene Acid: The Functional Group of Graphene Derivative Determines the Application in Electrochemical Sensing and Capacitors, ChemElectroChem. 6 (2019) 229–234, http://dx.doi.org/10.1002/celc.201800675.

[63] O.V. Yazyev, L. Helm, Defect-induced magnetism in graphene, Phys. Rev. B 75 (1–5) (2007) 125408, http://dx.doi.org/10.1103/PhysRevB.75.125408.

[64] M. Wu, E.-Z. Liu, J.Z. Jiang, Magnetic behavior of graphene absorbed with N, O, and F atoms: a first-principles study, Appl. Phys. Lett. 93 (1–3) (2008) 082504, http://dx.doi.org/10.1063/1.2973209.

[65] T.-T. Jia, B.-Z. Sun, H.-X. Lin, Y. Li, W.-K. Chen, Bonding of hydroxyl and epoxy groups on graphene: insights from density functional calculations, Chinese J. Struct. Chem. 32 (2013) 1475–1484.

[66] I.V. Lightcap, T.H. Kosel, P.V. Kamat, Anchoring semiconductor and metal nanoparticles on a two-dimensional catalyst mat. Storing and shuttling electrons with reduced graphene oxide, Nano Lett. 10 (2010) 577–583, http://dx.doi.org/10.1021/nl9035109.

[67] D. Kunwar, S. Zhou, A. DeLaRiva, E.J. Peterson, H. Xiong, X.I. Pereira-Hernández, S.C. Purdy, R. ter Veen, H.H. Brongersma, J.T. Miller, H. Hashiguchi, L. Kovarik, S. Lin, H. Guo, Y. Wang, A.K. Datye, Stabilizing high metal loadings of thermally stable platinum single atoms on an industrial catalyst support, ACS Catal. 9 (2019) 3978–3990, http://dx.doi.org/10.1021/acscatal.8b04885.

ADVANCED
ENERGY
MATERIALS

Graphene Acid for Lithium-Ion Batteries—Carboxylation Boosts Storage Capacity in Graphene

Ievgen Obraztsov, Aristides Bakandritsos,* Veronika Šedajová, Rostislav Langer, Petr Jakubec, Giorgio Zoppellaro, Martin Pykal, Volker Presser, Michal Otyepka,* and Radek Zbořil*

Environmentally sustainable, low-cost, flexible, and lightweight energy storage technologies require advancement in materials design in order to obtain more efficient organic metal-ion batteries. Synthetically tailored organic molecules, which react reversibly with lithium, may address the need for cost-effective and eco-friendly anodes used for organic/lithium battery technologies. Among them, carboxylic group-bearing molecules act as high-energy content anodes. Although organic molecules offer rich chemistry, allowing a high content of carboxyl groups to be installed on aromatic rings, they suffer from low conductivity and leakage to the electrolytes, which restricts their actual capacity, the charging/discharging rate, and eventually their application potential. Here, a densely carboxylated but conducting graphene derivative (graphene acid (GA)) is designed to circumvent these critical limitations, enabling effective operation without compromising the mechanical or chemical stability of the electrode. Experiments including operando Raman measurements and theoretical calculations reveal the excellent charge transport, redox activity, and lithium intercalation properties of the GA anode at the single-layer level, outperforming all reported organic anodes, including commercial monolayer graphene and graphene nanoplatelets. The practical capacity and rate capability of 800 mAh g^{-1} at 0.05 A g^{-1} and 174 mAh g^{-1} at 2.0 A g^{-1} demonstrate the true potential of GA anodes in advanced lithium-ion batteries.

1. Introduction

The rapidly growing need for electric vehicles and grid electric energy storage, alongside powering portable electronics, calls for energy storage materials that are synthesized from earth-abundant elements, are sustainable and safe, have minimal environmental impact, and give higher performance.[1,2] In this context, lithium-ion batteries (LIBs)[3,4] have transformed the contemporary energy storage landscape, currently dominating it. The next generation of electrochemical energy storage devices requires removing LIBs' bottlenecks; the cathode materials dictate the capacity of LIBs, with many cathodes being based on non-sustainable Co or Ni elements. Simultaneously, the graphite anodes limit the rate performance and safety due to the slow Li-ion diffusion and operation potential window that is very close to the voltage of Li metal plating. These factors result in rapid graphite anode aging, particularly in power-demanding applications, such as electric

I. Obraztsov, A. Bakandritsos, V. Šedajová, R. Langer, P. Jakubec,
G. Zoppellaro, M. Pykal, M. Otyepka, R. Zbořil
Regional Centre of Advanced Technologies and Materials
Czech Advanced Technology and Research Institute (CATRIN)
Palacký University Olomouc
Šlechtitelů 27, Olomouc 77 900, Czech Republic
E-mail: a.bakandritsos@upol.cz; michal.otyepka@upol.cz;
radek.zboril@upol.cz
A. Bakandritsos, R. Zbořil
Nanotechnology Centre
Centre of Energy and Environmental Technologies
VŠB-Technical University of Ostrava
17. listopadu 2172/15, Ostrava-Poruba 708 00, Czech Republic

V. Šedajová, R. Langer
Department of Physical Chemistry
Faculty of Science
Palacký University Olomouc
17. Listopadu 12, Olomouc 77 900, Czech Republic
V. Presser
INM – Leibniz Institute for New Materials
Campus D2 2, 66123 Saarbrücken, Germany
V. Presser
Department of Materials Science and Engineering
Saarland University
Campus D2 2, 66123 Saarbrücken, Germany
V. Presser
Saarene – Saarland Center for Energy Materials and Sustainability
Campus C4 2, 66123 Saarbrücken, Germany
M. Otyepka
IT4Innovations
VŠB-Technical University of Ostrava
17. listopadu 2172/15, Ostrava-Poruba 708 00, Czech Republic

vehicles, and impose the risk of catastrophic battery failure due to Li metal dendrites growth.[5,6]

Organic materials undergoing reversible electrochemical redox processes and coordinating lithium, are attractive anode candidates in organic/LIBs thanks to their cost-effective and eco-friendly nature, abundance, processability, and design versatility.[7,8] Moreover, customized functional groups and heteroatoms in these materials may tune the redox potential, the system's capacity, and the mechanism of charge storage.[9,10] Several organic materials have been proposed, embracing conjugated polymers[11] and systems bearing carbonyl,[12,13] nitrile,[14] organosulfur,[15] imine,[16] azo compounds,[17,18] or organic radicals.[19,20] Such electrode materials are not restricted by the dimensions of a charge-carrying ion, thus allowing the use of alternatives more sustainable than lithium, such as sodium,[21,22] potassium,[23,24] zinc,[25] magnesium,[26] or aluminum.[27,28]

Carboxylic acids have emerged as stable and high-energy organic LIB anode materials owing to their low reduction potential and their coordination proclivity toward Li. Di-lithium salts of terephthalic and muconic acids were initially reported as LIB anode active materials.[29] Terephthalate could bind 2.3 Li ions per molecule with a reduction potential plateau near 0.8 V, delivering 300 mAh g^{-1}. Muconate's performance was about half of that, with its potential plateau being at 1.4 V. Aromatic conjugated carboxyl derivatives demonstrate intramolecular charge delocalization superior to that of non-conjugated derivatives. Consequently, they provide more efficient utilization of carboxyl groups for the storage of lithium ions.[29–34]

The capacity of active organic materials can be expressed as the ratio between the number of coordinated Li-ions over the molecular mass of the organic molecule. Therefore, an organic anode active material containing a high percentage of carboxyl groups is extremely desirable for enhancing the capacity. However, the trade-off between imprinting a high content of carboxylic moieties and preserving high conductivity poses a problem, which limits the further development of LIB anode materials. The capacity of most carboxylate active materials known in literature lies below 300 mAh g^{-1}.[29,31–34] Furthermore, large contents (as high as 50%) of conductive carbon additives in the electrodes are usually required for bypassing the limited conductivity of organic molecules, which however further restrains the practical capacity and commercialization feasibility.[31,35]

One way to improve carboxylic acid anodes' performance could be covalent, dense, and spacer-free grafting carboxyls on a highly conductive backbone, such as graphene. In this context, graphene oxide (GO) stands out as a versatile material, bearing a very high amount of various oxygen-containing functionalities[36,37] in a complex mixture of tertiary alcohols, epoxides, carboxyl, and carbonyl groups.[38] The carboxylic groups in GO represent only a small fraction of the oxygen functionalities (e.g., 1.3 at% by Hummers method)[39] located at the edges and around defects.[39,40] Unfortunately, the dense functionalization of GO turns it into an insulator, while its reduction enhancing the conductivity leads to a significant loss of the functional groups.[41] Another synthetic approach based on graphene functionalization that uses noncovalent interactions[42] (e.g., π–π) is not robust enough for such electrochemical applications because it affords materials with low stability due to leakage of the functionalities into the electrolyte.

Herein, we examine graphene acid (GA, **Figure 1**a), a selectively and densely functionalized carboxylic graphene derivative,

which was thoroughly characterized in previous works,[43–48] as a LIB anode. Therefore, we leveraged GA's outstanding functionalization degree of 13 at% (corresponding to more than 30 mass% in carboxylic groups[48]), with a sheet resistance of 6800 Ω sq^{-1}, which is five orders of magnitude lower than that of GO.[43] GA was prepared from fluorographene by reproducible and up-scalable protocol,[43,47] and currently represents the most conductive graphene derivative with such a high content of carboxyl groups. The titration profile of GA closely resembles that of molecular organic acids, with pK_a of 5.2, reflecting its well-defined structure.[43] Thus, GA can be regarded as the first 2D acid. Owing to these features, we can demonstrate that GA, as an organic LIB anode, brings the advantage of i) high redox capacity stemming from its carboxyl groups; ii) high conductivity, boosting the rate capability; iii) high capacity considering the total electrode mass since only 5 mass% of conductive carbon black (CB) additive was used; and iv) extra charge storage due to the co-presence of significant content of sp^2 moieties serving as Li intercalation sites (Figure 1a). These results indicate that the covalent grafting of carboxyl groups on the conductive skeleton of graphene paves the way for efficient and stable organic anodes for LIBs.

2. Results and Discussion

GA was synthesized according to the reported procedure[43] described in details in the Experimental, and in the Supporting Information. Briefly, GA was obtained via the selective acidic hydrolysis of cyanographene (G-CN), which was produced from the nucleophilic reaction between [CN]$^-$ anions and fluorographene,[43] a large band-gap 2D sp^3 carbon sheet with covalently bonded fluorine atoms. The reaction proceeded replacing of fluorine atoms by −CN groups, accompanied by reductive defluorination, re-establishing the aromatic network and thus the conductivity.[43] More details on the chemistry of fluorographene can also be found in other works.[49–51] In the following step, a relatively mild acidic hydrolysis selectively transformed the −CN covalent functionalities to −COOH, yielding GA.[43] This particular methodology bypasses the harsh oxidation conditions used to introduce diverse oxygen-containing functional groups to graphene during a GO synthesis, and contributed to GA's conductivity, as revealed by conductivity measurements, cyclic voltammetry (CV), electrochemical impendance spectroscopy (EIS), and density functional theory (DFT) calculations.[43]

GA electrodes (mixed with Ketjenblack EC-600JD as a conductive additive and polymer binder at a 90:5:5 mass ratio and cast onto a copper current collector) were evaluated in coin cells versus Li metal (Experimental Section). The polymer binder (polyvinylidene fluoride, PVDF) created bridges between the GA microflakes (indicated with arrows in Figure S1a,b, Supporting Information, see pure GA in Figure S1c,d, Supporting Information), forming a compact electrode architecture with good adhesion between GA's sheets.[52] The final electrodes revealed the desirable space filling by conductive nanoparticles of CB (Figure S2a,b, Supporting Information), fully preserved even after the electrode's electrochemical operation (Figure S2c,d, Supporting Information).

The shapes of the galvanostatic charge-discharge curves (Figure 1b) and CV curves (Figure 1c) were characteristic for an extended conjugated system with combined redox and
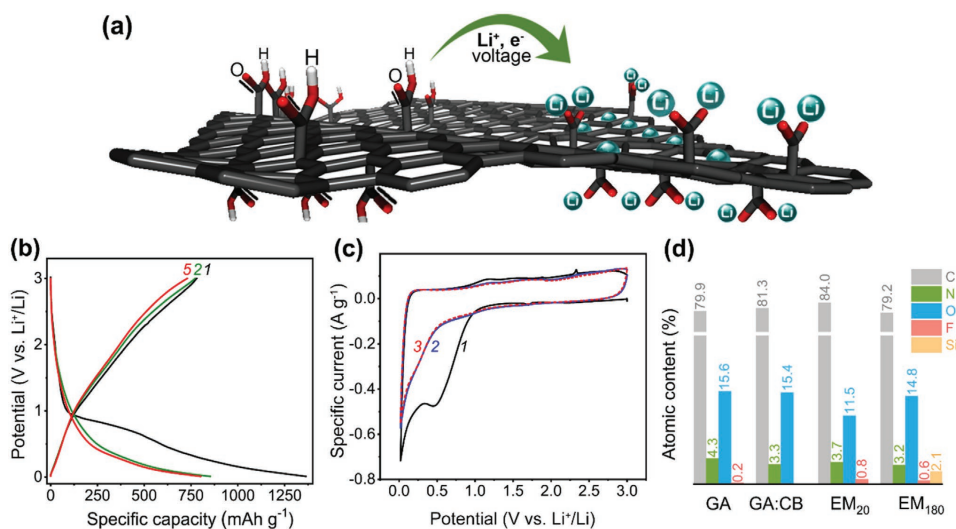
Figure 1. a) Schematic representation of GA and its interaction with lithium ions; b) the first, second, and fifth charge–discharge cycle of GA anode in a GA ∥ Li half-cell at 0.05 A g^{-1} specific current; c) the three first CV curves for GA anode at a 0.1 mV s^{-1} sweep rate (composition GA:CB:PVDF, 90:5:5; cycle number 3 appears as a red-dotted line); and d) relative atomic contents, as obtained from X-ray photoelectron spectroscopy, for pure GA, GA:CB mixture (95:5 by mass), and purified electrode materials after 20 (EM$_{20}$) and 180 (EM$_{180}$) charge-discharge cycles. Si (as SiO$_2$) contamination of 2.1 at% after 180 cycles originates from the glass fiber separator; it contributes ≈4% to the oxygen signal.

intercalation energy storage mechanisms.[53] Conjugated small molecule carboxylates have sharp reversible redox peaks and distinct plateau during charging and discharging.[29,54] However, in GA, a distribution of redox potentials was observed over a wide potential window, as reflected by the smooth redox bands in the range of 1.0–2.0 V versus Li$^+$/Li (Figure 1c). This effect was ascribed to the diverse surrounding local environment of the carboxyl groups[55,56] bonded on the reconstructed graphene plane after its functionalization, leading to differences in the respective redox potentials (discussed later, in the kinetic redox analysis).

The GA anode (mass loading: 1.0–1.5 mg cm^{-2}; thickness: ≈20 μm) delivered a high specific capacity of 747 mAh g^{-1} after the first delithiation at 0.05 A g^{-1}. The capacity difference between lithiation (1300 mAh g^{-1}) and delithiation of the initial cycle (Figure 1b) was due to the proton[57,58] and electrolyte reduction with the formation of a solid electrolyte interface (SEI) on the electrode surface.[59,60] Therefore, the Coulombic efficiency of the first charge-discharge cycle was 57%, exceeding 90% in the second cycle and finally improving significantly in the successive cycles (>99.4%). The SEI formation was inferred from the voltammogram as an irreversible peak in the first cycle at ≈0.5 V (Figure 1c). Reversible peaks below 0.5 V versus Li$^+$/Li in the successive cycles correspond to lithium-ion insertion into graphene.

The composition-based capacity of GA was calculated for a better understanding and interpretation of the experimentally obtained values. For that, the elemental analysis of GA was obtained by X-ray photoelectron spectroscopy, showing 79.9 at%, 4.3 at%, and 15.6 at% of C, N, and O atoms, respectively, along with a trace amount of fluorine atoms (Figure 1d and Figure S3, Supporting Information). The determined atomic content of carboxylic carbons according to C 1s deconvolution was 8 at% (Figure S4 and Table S1, Supporting Information), which translates into 16 at% in oxygen content, because every carboxylic carbon has two oxygen atoms. Since the oxygen content according to the elemental XPS analysis is 15.6 at% (Figure S3b, Supporting Information), the carboxylic carbons alone represent all the oxygen in GA. The 4.3 at% of nitrogen incorporated into graphene, mostly in pyridinic and pyrrolic configurations, originated from the solvent dimethylformamide reactivity.[43] Considering the C(sp^3)-COOH moieties and the surrounding carbon sp^2 area as a single Li-host ensemble, the composition-based capacity of GA was calculated (Figure S4e and Table S1, Supporting Information) for different numbers of coordinated and intercalated Li atoms. The composition-based capacity was 706 mAh g^{-1} for reversible binding of four Li atoms per one carboxylic-sp^2 area (Note S1, Supporting Information). These values strongly corroborate (discussed later) the experimentally determined capacity in the rate test (800 or 700 mAh g^{-1} at 0.05 A g^{-1} for the 5th and 10th cycle, respectively), as well as the computation results on the lithium-ion storage mechanism.

The current–rate performance of the GA electrode was tested at current densities ranging from 0.05 to 2.0 A g^{-1} (**Figure 2**a,b) with capacity ranging from 700 to 174 mAh g^{-1}, respectively (10th cycle of each rate). These values correspond to the binding of four and one Li$^+$ per carboxylic-sp^2 area, respectively

2103010 (3 of 11)

**ADVANCED
SCIENCE NEWS**
www.advancedsciencenews.com

**ADVANCED
ENERGY
MATERIALS**
www.advenergymat.de
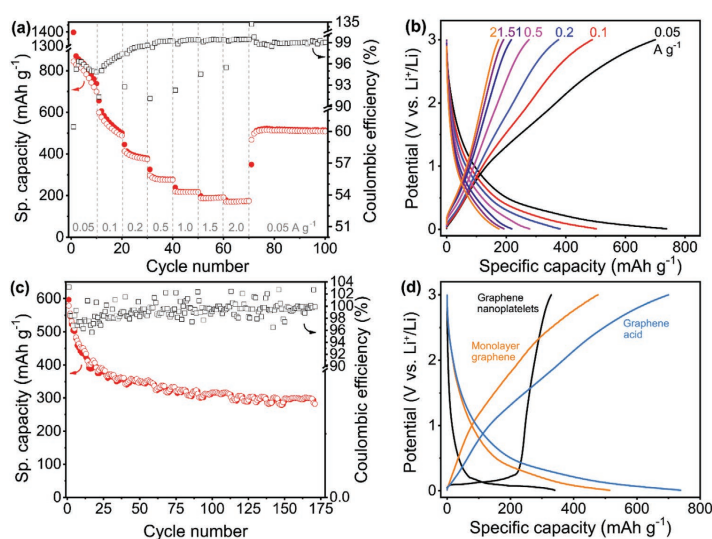
Figure 2. Electrochemical testing of GA in half-cell versus Li: a) rate capability test; b) 10th charge-discharge curve for each current density, from the rate test of panel (a); c) cycling performance at 0.2 A g^{-1} after one-cycle at 0.05 A g^{-1} at 24 ± 2 °C, and d) the comparison of GA with anodes consisting of monolayer graphene and graphene nanoplatelets at 0.05 A g^{-1} (5th cycle), measured under identical conditions. In panels (a) and (c) open symbols represent lithiation and filled symbols represent delithiation.

(Note S1 and Table S5, Supporting Information). Then, the electrode was cycled again at 0.05 A g^{-1}, recovering a capacity of 510 mAh g^{-1}. The recovered capacity remained stable for 30 consecutive cycles with the Coulombic efficiency exceeding 99% (Figure 2a). Comparatively, polymeric carboxylic anodes severely suffered from slow Li-ion diffusion at higher current rates, exhibiting 500 mAh g^{-1} and 50 mAh g^{-1} at 0.05 A g^{-1} and 2 A g^{-1}, respectively.[61] The advantage of GA is also clearly observed comparing its operation with a (carboxylic acid)-modified reduced GO anode (rGO-poly(methyl methacrylate)), which delivered ≈170 mAh g^{-1} at 0.1 A g^{-1}.[62] The specific capacity and the Coulombic efficiency of GA anodes were reproducible in the subsequent electrode material preparations, even under different mass loadings (Figure S5a,b, Supporting Information). The average delithiation voltage advantageously decreased from 1.83 to 1.47 V at higher current rates (Figure S6, Supporting Information) because of a change in the ratio of diffusion- to surface-controlled capacity components.

After the initial 20 cycles of the stability test at 0.2 A g^{-1}, the GA anode's specific capacity was 400 mAh g^{-1} and then gradually reduced to 300 mAh g^{-1} during the consecutive 150 cycles (Figure 2c). After 180 galvanostatic charge/discharge cycles (stability testing) and CV at different rates, the GA electrode recovered a specific capacity of 475 mAh g^{-1} when cycled back at 0.05 A g^{-1}. This behavior demonstrates the high repeatability and stability of its electrochemical properties (Figure S7, Supporting Information).

Examination via X-ray photoelectron spectroscopy was also performed in order to better understand the electrochemical

behavior of GA during cycling. The GA material was collected from the electrodes after 20 and 180 cycles of the stability test at 0.2 A g^{-1} and was purified from the electrolyte and the polymer binder. The oxygen content after 20 cycles decreased from 15.4 to 11.5 at% (Figure S1d, Supporting Information), corroborating the similar decrease in carboxyl groups from 8 to 5.2 at% (Figure S4, Supporting Information). The decline in the oxygen content occurred during the first 20 cycles. The structure remained practically unchanged for the following 180 cycles; this may be attributed to the reduction of some carboxyl groups during SEI formation.

The performance of the GA anode was compared to anodes made of graphene from commercial suppliers: i) graphene nanoplatelets dispersed in 1-methyl-2-pyrrolidinone (ACS Materials) containing flakes of 1–3 μm in diameter and 3–5 nm in thickness, and ii) monolayer (99.8%) graphene powder (Ossila) containing flakes of ≈2 μm in diameter and 0.7–1.2 nm in thickness. The specific capacity of graphene anodes after the fifth cycle at 0.05 A g^{-1} was 476 and 330 mAh g^{-1} for monolayer graphene and graphene nanoplatelets, respectively. These values were significantly lower than that of GA (800 mAh g^{-1}, Figure 2d). The charging/discharging of graphene nanoplatelets was found similar to that expressed by small-crystal graphite[63] (indicating its multilayered nature) and suffered from severe capacity decay to ≈50 mAh g^{-1} at 1.5 A g^{-1} (Figure S8a, Supporting Information). The monolayer graphene performed better, keeping 250 mAh g^{-1} at 1.5 A g^{-1} (Figure S8b, Supporting Information). The GA anode at comparable electrode material loading delivered higher capacity than monolayer graphene at

2103010 (4 of 11)
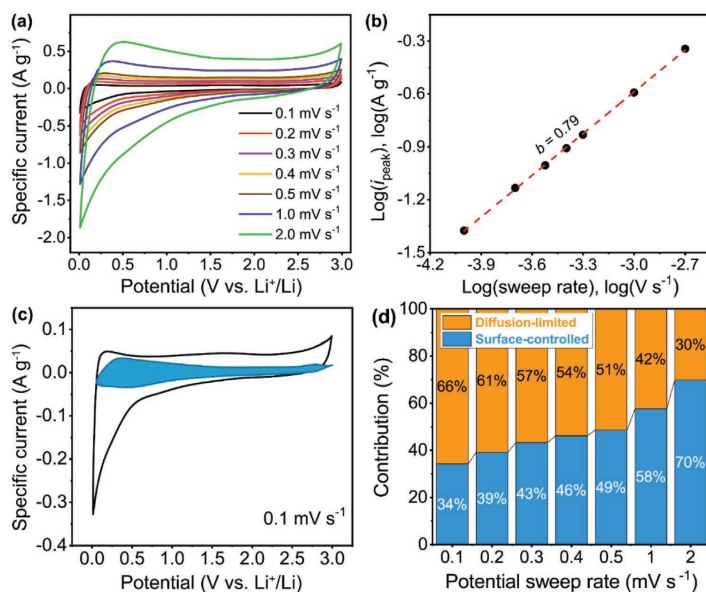
Figure 3. a) CV curves for GA at different scan rates performed after the life-cycle test, b) The linear curve from Equation (1) for the determination of the b-value at 1.27 V and at the potential sweep rate range of 0.1–2.0 mV s^{-1}, c) CV curve for GA anode showing the fractions corresponding to surface capacity (shaded region) and redox processes, at 0.1 mV s^{-1}, d) Contribution of diffusion- and surface-controlled processes on the capacity of the GA anode at different potential sweep rates.

all current rates (Figure S8c, Supporting Information), which is particularly interesting considering the much higher conductivity of pristine graphene. The performance of GA was also compared against maleic acid[64–66] anodes (Figure S9, Supporting Information), which were prepared following the published protocols and using a range of different carbon additives, further highlighting the superior performance of GA.

To experimentally determine the contribution of the diffusion-limited and surface-controlled charge storage mechanisms arising from the carboxylic groups and graphene moieties, respectively, an electrochemical kinetic analysis was performed.[67] The CV curves were recorded at different scan rates (**Figure 3**a) after the 180-cycle stability test. Using equation $i_p = a v^b$ and plotting the logarithm of the peak current (i_p, for the 1.27 oxidation peak) versus the logarithm of the scan rate v (Figure 3b), the b value was calculated from the slope. Many advanced materials show a mixed behavior with intermediate values. In the present case, a b-value of 0.79 was obtained. Such a value reflects the excellent rate handling ability of GA anodes owing to the high conductivity of GA and the surface-exposed -COOH groups where the diffusion-controlled processes mostly operate.

When the k_1-k_2 model is employed, the purely diffusion-limited and purely surface-controlled contributions to the overall current response can be separated. Equation (1) separates the total current, which can be presented as the sum of surface capacitive ($k_1 v$) and of diffusion-limited ($k_2 v^{1/2}$) processes components:

$$i = k_1 v + k_2 v^{1/2} \ or \ i(v) / v^{1/2} = k_1 v^{1/2} + k_2 \quad (1)$$

where, k_1 and k_2 are potential sweep rate-independent values. These values for fixed potentials were determined from the slope and y-axis intercept point from the $i/v^{1/2}$ versus $v^{1/2}$ plot, respectively (Figure S10a,b, Supporting Information).

The total currents during CV at each potential sweep rate were deconvoluted accordingly (Figure S11, Supporting Information), showing that the diffusion-limited current fraction (66% at 0.1 mV s^{-1}) of the electrode was substantially higher than the one estimated from the stoichiometry of GA (24%). This suggests significant redox contribution from the GA radical sites[48] and N-doped centers.[68]

The fraction of the diffusion-limited current, most likely linked to the redox process from GA surfaces, decreased to 30% when the scan rate increased to 2.0 mV s^{-1} (Figure 3d). The same analysis performed for a freshly assembled half-cell (Figure S12a–c, Supporting Information) showed similar electrochemical performance but with a higher fraction of diffusion-limited processes at each potential sweep rate. The b-value was 0.72 in this case, in line with the larger contribution of diffusion-limited processes, reaching 75% at 0.1 mV s^{-1} and 37% at 2 mV s^{-1}.

The charge–discharge transient at 0.05 A g^{-1} in the form of differential capacity versus voltage plot allowed the delineation of the different electrochemical processes at the whole potential

220

**ADVANCED
SCIENCE NEWS**
www.advancedsciencenews.com
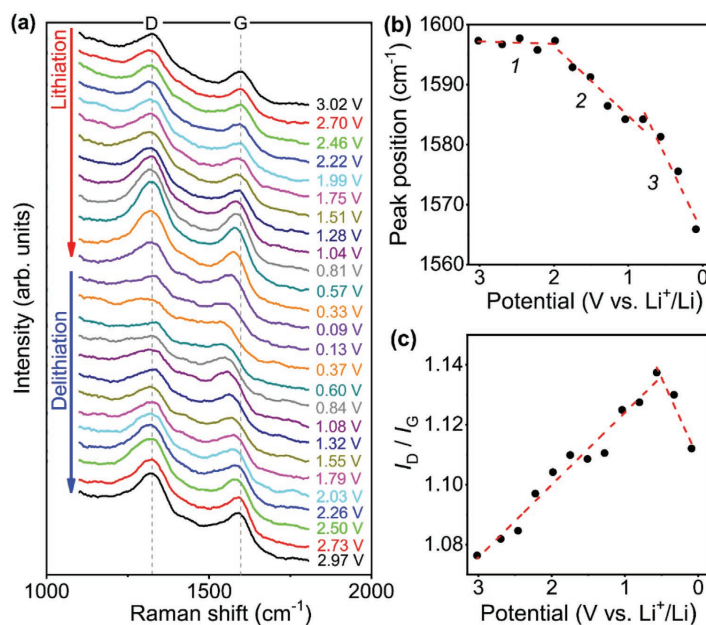
**ADVANCED
ENERGY
MATERIALS**
www.advenergymat.de
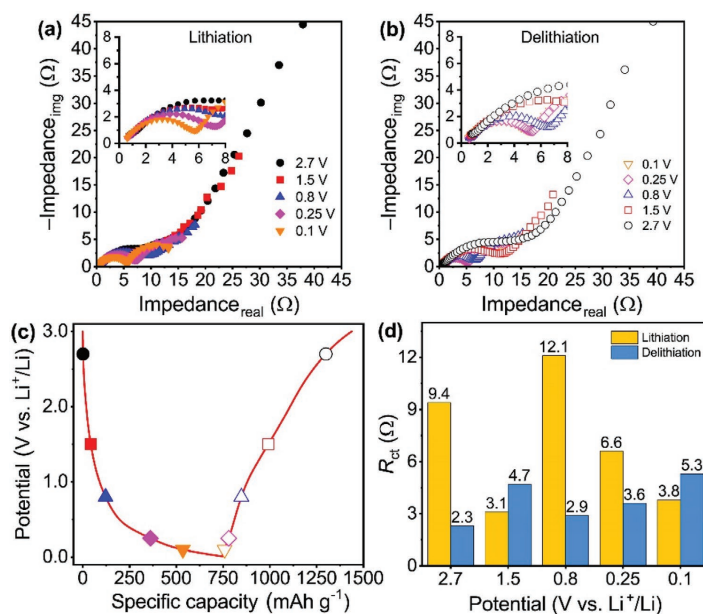
Figure 4. EIS spectra for the GA anode against Li, galvanostatically recorded at specific voltages during a) lithiation and b) delithiation, c) charge–discharge curve with indicated voltages where EIS is performed, and d) R_{ct} dependence on state of charge and discharge of the cell.

region (Figure S13, Supporting Information). Three broad redox peaks were distinguishable: below 0.5, between 1.0 and 2.0 V, and above 2.5 V versus Li^+/Li. The first one corresponds to lithiation-delithiation of the sp^2 graphene moieties of GA. The second is a typical region for carboxylate redox reactions;[9] the third could be regarded as redox-processes involving nitrogen-containing graphene moieties[68] introduced during the synthesis (Figures S3 and S4, Supporting Information).

As previously identified, GA showed a very high rate capability. To better understand this property, Nyquist plots were obtained from electrochemical impedance spectroscopy (EIS) measurements at different discharge states of the GA electrode (**Figure 4**a–c). Fitting Nyquist plots with a modified Randles circuit (Figure S14, Supporting Information) showed very low charge transfer resistance (R_{ct}) values in the entire voltage (Figure 4d). These values were significantly lower in comparison with dozens or hundreds of ohms typically observed for previously reported carboxyl-based organic anodes (Table S3, Supporting Information).[54,55,62] The low R_{ct} value verifies and highlights the fast kinetics of the carboxyls' group redox process and the high electronic charge transfer offered from the conductive graphenic backbone corroborating the initial hypothesis. Specifically, the lowest R_{ct} values for GA were 3.1 and 2.9 Ω on lithiation (discharge) and lithiation (charge) of the half-cell at 1.5 and 0.8 V versus Li^+/Li, respectively, unveiling GA's beneficial properties.

Operando Raman spectra were recorded every ≈250 mV during CV at 0.05 mV s⁻¹ potential sweep rate (**Figure 5**a) to

shed more light on the Li storage processes in the GA anode. Raman spectra revealed that the G-band position was red-shifting during the charging of the GA anode due to the biaxial tensile strain in GA. It is known that the red-shift in the G-band below 0.5 V is more pronounced as the number of graphene layers in a stack decreases.[69] For example, a G-band position shift of 3, 5, and 11 cm⁻¹ was found for 100 nm graphite particles, 20 nm graphite flakes, and 3-layer graphene nanoplatelets, respectively. The G-band of GA was shifted by ≈18 cm⁻¹ in the 0.5–0.09 V region (Figure 5b), which is larger than that of a few-layer graphene material. This indicates that extensive interactions of Li atoms with GA take place at the single-layer level. In the plot of the G-band position versus potential, three slopes were observed during lithiation (≈ in the 3.0–2.0, 2.0–0.75, and 0.75–0.09 V range, Figure 5b) instead of two slopes observed for graphene.[69] In particular, the additional slope between ≈2.0–0.75 V probably reflects the mechanism of Li storage involving the carboxyl groups of GA. This is strongly corroborated by the voltage ranges very similar to those observed in the CV kinetic analysis (Figure 3) and the differential capacity analysis (Figure S13, Supporting Information), which was ascribed to a lithium-ion interaction with the graphene moieties (3.0–2.0 V), as well as to carboxylate redox reactions with Li (2.0–0.5 V) and Li interactions with nitrogen-containing sp^2 areas (0.5–0.01 V). Finally, Raman results also showed that the I_D/I_G ratio grew during the lithiation of GA to ≈0.5 V, where a knee was observed (Figure 5c). The increase of the I_D/I_G ratio is

ADVANCED
SCIENCE NEWS
www.advancedsciencenews.com
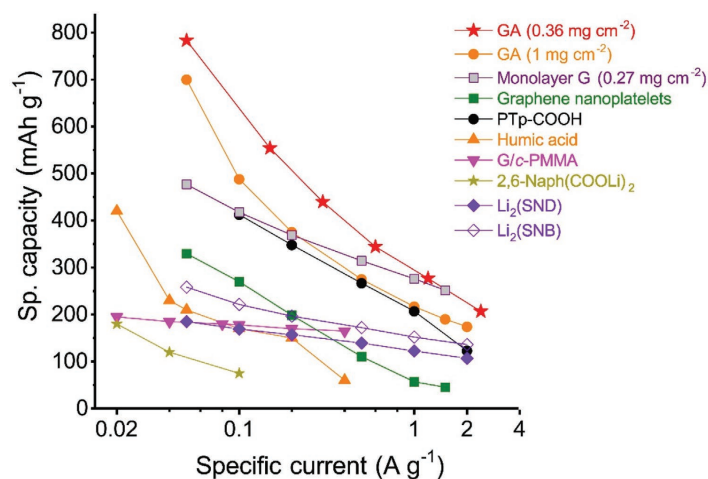
ADVANCED
ENERGY
MATERIALS
www.advenergymat.de

Figure 5. a) Operando Raman spectra of GA anode recorded at different potentials during CV at potential sweep rate of 0.05 mV s^{-1}, b) G-band position at different potentials, and c) D-to-G peak intensity ratio during lithiation.

associated with lowering the Fermi level[70] caused by n-doping during the negative polarization of the GA electrode followed by the reduction of Li$^+$ to Li^0 and a free carrier concentration decrease in the GA, causing an abrupt change (the knee) in this potential (Figure 5c).

Theoretical calculations using both finite (functionalized ovalene) and infinite (periodic) models were carried out for a better understanding of the energy storage mechanism in GA. The calculations show that up to 4 Li^0 atoms per one carboxyl group (**Figure 6**) can be bound to GA (with adsorption energy
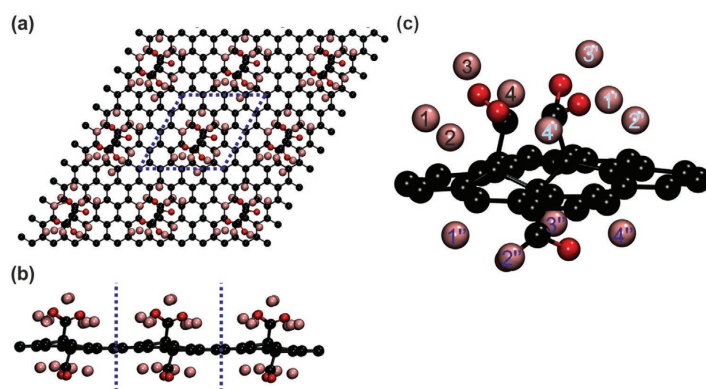
Figure 6. A model of lithiated GA according to DFT calculations; a) top and b) side views (the dashed line dictates the super-cell used in calculations). The zoom view c) shows two binding modes of Li atoms close to one (bottom) and two (up) carboxyl groups (C, O, and Li atoms are shown as black, red, and pink, respectively, balls). The atom numbering is arbitrary to highlight up to four Li atoms close to the nearest carboxyl group.

2103010 (7 of 11)

**ADVANCED
SCIENCE NEWS**
www.advancedsciencenews.com

**ADVANCED
ENERGY
MATERIALS**
www.advenergymat.de

Figure 7. Performance comparison of organic materials from Table S4, Supporting Information: PTp-COOH,[61] humic acid,[71] G/c-PMMA,[62] 2,6-Naph(COOLi)$_2$,[72] Li$_2$(SND), Li$_2$(SNB),[55] and electrodes prepared using commercial graphene (monolayer, and nanoplatelets). Capacity values are normalized to the total mass of electrode materials and refer to the stabilized capacity in the current rate tests.

of −57.6 kcal mol^{-1} per Li^0 atom) without significant structural changes. The Li^0 atoms prefer to bind close to carboxyl group adopting two binding modes: the Li atom is either in contact both with the sp^2 carbon area and the carboxyl oxygens or, the Li atom binds between the carboxyl oxygens (Figure 6). These findings are in line with the composition-based GA capacity calculation (Note S1 and Table S5, Supporting Information) and with the experimentally determined capacity of GA (Figure 2a), suggesting the same ratio of four Li atoms per carboxyl with its respective sp^2-hybridized carbon lattice area. Such excellent agreement of the theoretical results (based on single sheet model of GA) with the experiments supports the operation of GA on the single-layer level, as Raman investigations also unveiled. According to calculations, the addition of a fifth Li atom per carboxyl is not favored, because it has positive adsorption energy. Also, Li$^+$ ions have weaker bonding to GA than Li^0, thus allowing their easy migration to the cathode (Note S2, Supporting Information), as required during the discharging. Finally, in both oxidized/reduced states, the partial charge on Li is ≈0.94–0.99 e (see S2, Supporting Information), which indicates strong charge transfer processes between the Li species and the GA skeleton and is attributed to the linker-free installation of the carboxyl groups on the sp^2 backbone.

The performance of GA anode is found superior to most of the polymer, oligomer, composite and small-molecule, and carboxyl anodes, both at low and higher specific currents (**Figure 7** and Table S4, Supporting Information). For example, the capacity of a carboxyl modified polythiophene (PTp-COOH) electrode material was ≈500 mAh g^{-1} at 0.05 A g^{-1}; however, at high rates, the film gave only 50 mAh g^{-1} at 2 A g^{-1}.[61] A humic acid anode showed a capacity of ≈420 mAh g^{-1} and 20 mAh g^{-1} at 0.06 A g^{-1} and 0.4 A g^{-1}, respectively.[71] An electrode made

from graphene chemically cross-linked with poly(methyl methacrylate) (Gr/c-PMMA composite) delivered 250 mAh g^{-1} and 167 mAh g^{-1} at 0.02 A g^{-1} and 0.4 A g^{-1}, respectively.[62] Small-molecule carboxylic anodes, such as terephthalate, muconate,[29] 2,5-dihydroxyterephthalic acid,[32] 2,6-naphthalene dicarboxylate,[33] 4,4′-(phenazine-5,10-diyl)dibenzoate,[34] demonstrated only moderate capacities (≤300 mAh g^{-1}) because of the low ratio between stored lithium ions and molar mass (Table S4, Supporting Information).

Although graphene anode was reported to possess a 650 mAh g^{-1} capacity after the 1st delithiation,[73] this value was reached under undefined mass loading and temperature conditions. Accordingly, we tested two commercial graphene samples under conditions identical to GA. As described earlier, of these two materials, one had a very high content of monolayer sheets and the other showed multilayered nature. As demonstrated by our data, the GA anode outperformed these reference materials. The advantage of GA lies in its conductivity combined with a high content in carboxyl groups, delivering a capacity and rate performance that is unmatched by any value expressed by the wide gamut of carboxyl-based organic LIB electrodes, as highlighted in the comparative graph in Figure 7 and Table S4, Supporting Information.

3. Conclusions

Graphene-acid (GA, a densely functionalized carboxylated graphene) is a very effective LIB anode material by combining redox and intercalation properties, originating from the conductive and selectively carboxylated 2D graphene backbone. Due to the spacer-free carboxyl groups attached to graphene's

2103010 (8 of 11)

223

**ADVANCED
SCIENCE NEWS**

www.advancedsciencenews.com

**ADVANCED
ENERGY
MATERIALS**

www.advenergymat.de

lattice, which allowed their direct communication with the graphene backbone, the anode was endowed with particularly low charge transfer resistance, and effective interactions and intercalation of lithium-ions. Operando Raman, as well as theoretical results, indeed verified that GA behaved as a high-quality monolayer graphene. Further, calculations confirmed a direct charge communication pathway between the Li atoms/ions and the GA host, with the experimental and composition-based capacities being in agreement with the theoretically calculated capacities. The carboxylic groups of GA coordinated the lithium ions upon the electroreduction in a broad potential range (in contrast to small molecule materials). Simultaneously, the graphene skeleton served concurrently as a highly conducting backbone, redox, and intercalation electrode material. Therefore, overall, the GA anode worked better than polymeric, oligomeric, and molecular carboxylated anodes and few-layered and monolayer graphene in terms of the capacity as well as the rate performance. The particularly competitive performance of GA, alongside its highly reproducible and scalable synthesis, predisposes this material for efficient application as a LIB anode.

4. Experimental Section

Chemicals: Fluorographite, DMF, 1-methyl-2-pyrrolidinone, bulk solvents, PVDF, battery-grade 1.0 M LiPF$_6$ ethylene carbonate: dimethyl carbonate (EC:DMC, 1:1 by volume) electrolyte solution, and Whatman GF/A glass microfiber filters were purchased from Sigma-Aldrich. The 0.75 mm-thick lithium metal foil (99.9%) was from Alfa Aesar; CB (Ketjenblack EC-600JD) was supplied by AkzoNobel Functional Chemicals BV. Monolayer graphene powder (M901, 99.8% single layer ratio, >99% purity) was from Ossila Ltd.; graphene nanoplatelets NMP dispersion of 98.9% purity was from ACS Material. All reagents were used as received.

GA was synthesized according to the literature procedure.[43] In brief: commercial fluorographene powder was dispersed in DMF followed by adding NaCN and stirring at 130 °C. The resulting cyanographene was separated, washed, and deionized by dialysis. Next, cyanographene was hydrolyzed with a nitric acid solution to form GA water dispersion. The GA was washed in successive separation-dispersion cycles and freeze-dried. Detailed synthesis is provided in the Supporting Information, along with transmission electron microscopy and atomic force microscopy (AFM) results (Figure S15, Supporting Information).

Materials Characterizations: XPS post-mortem analysis of electrodes was performed by PHI VersaProbe II (Physical Electronics) spectrometer using an Al-Kα source (15 kV, 50 W). The obtained data were evaluated with the MultiPak (Ulvac-PHI) software package. The electrode materials were washed in several consecutive redispersion-separation cycles in NMP, hot DMF, 1 mM HCl, and ethanol (twice in each solvent) in order to remove the electrolyte, polymer binder, and residual SEI components. Raman spectra were recorded by using DXR Raman Microscope (Thermo Fisher Scientific) using 633 nm excitation line diode laser with an aperture of 50 μm, 5 cm^{-1} resolution and MTI electrochemical cell with a quartz window for Raman analysis, a GA:PVDF (90:10 by mass) film was cast onto a Ni foam. Transmission electron microscopy images were obtained with a JEOL 2100 system. For these analyses, a droplet of GA dispersion in ultrapure water (concentration approximately 0.1 mg mL^{-1}) was placed on a holey carbon-coated copper grid and left to dry, before the analysis. AFM images were obtained in the amplitude-modulated semi-contact mode on an NT-MDT NTegra system equipped with a VIT-P AFM probe using freshly cleaved muscovite mica as a substrate.

Electrode Preparation and Cell Assembling: The active material, the carbon additive, and the binder were mixed in the 90:5:5 (GA:carbon black:polymer binder) weight ratio. The composition of the reference commercial graphene electrodes was ACS Materials graphene nanoplatelets:PVDF (95:5 by mass) and Ossila monolayer graphene:PVDF (80:20 by mass). A higher binder content in a monolayer graphene anode was required for preparing physically stable film on the current collector foil. Individual components were dispersed separately by ultrasonication in a suitable amount of NMP and then mixed in a Thinky ARV-310 planetary mixer (Thinky Co.) for 5 min at 1100 rpm under pressure decreased to 30 kPa. The slurry was cast onto a 10-μm thick copper foil (Cambridge Energy Solutions) with a doctor blade using 100-μm slot. The film was dried with an infrared lamp for 10 min, left overnight in a vacuum oven at 120 °C, and then cut into 15-mm disks, which were used for CR2032 and research-grade coin cells (PAT-cell of EL-Cell GmbH) assembling in a dry Ar-filled glove box ([O$_2$] < 0.6, [H$_2$O] < 0.8 ppm). Lithium metal coin (15.5 mm diameter, 0.75 mm thickness), glass microfiber separator, and 1.0 M LiPF$_6$ EC:DMC (1:1 vol.) were used as the counter electrode, the separator, and the electrolyte (100 μL), respectively. The lithium metal surface was mechanically refreshed before cell assembling. The electrode material loading was 1.0–1.5 mg cm^{-2} unless otherwise specified.

Electrochemical Measurements: CV experiments were performed using a BCS-810 system under BT-lab software control of BioLogic Science Instruments; charge-discharge rate and stability tests were performed using Novonix HPC setup with a dedicated thermostatic chamber (Novonix) at 25 °C. The cells were tested at 3.0–0.01 V versus Li$^+$/Li. The mass of all electrode material components was used for specific capacity calculations. All cells were discharged to 3.0 V by a CC-CV (constant current-constant voltage) procedure after assembling in order to prevent Cu collector oxidation, followed by a 6-h rest at OCP and charging back to 3.0 V (Figure S16a, Supporting Information). One charge–discharge cycle at 0.05 A g^{-1} was performed (Figure S16b, Supporting Information) before the stability test reported in Figure 3c. EIS measurements were performed in a three-electrode PAT-Cells (EL-Cell GmbH) with a Li reference ring electrode using Metrohm Autolab PGSTAT128N potentiostat equipped with FRA32M extension card under Nova 1.11.2 control and analysis software (Metrohm Autolab BV). The GA electrode material was aged for 10 cycles at 0.05 A g^{-1}, followed by two cycles with a fresh Li metal coin (Figure S17, Supporting Information). The EIS was performed at different states of charge of the cell in a galvanostatic mode; 50 μA AC oscillation amplitude over the frequency range of 0.3 Hz to 100 kHz was used.

Computational Methods: The infinite (periodic) calculations were performed by using spin-polarized DFT as implemented in a Vienna Ab-initio Simulation Package.[74–76] The electron-ion interactions were treated by a projector-augmented wave (PAW) method,[77,78] and the Perdew, Burke, and Ernzerhof functional[79] in the generalized gradient approximation and Grimme D2 dispersion.[80]

The basis set contained plane waves with a maximum kinetic energy of 500 eV and a Γ-centered 6 × 6 × 1 k-point mesh. All structures were optimized until the forces acting on all atoms were reduced to less than 10 meV Å^{-1} and the electronic and magnetic degrees of freedom were relaxed until the change in total energy between the successive iteration steps was smaller than 10^{-6} eV.

The adsorption energy, E_{ad}, per lithium atom was evaluated as

$$E_{ad} = 1/n(E_{GA+nLi} - E_{GA-nLi} - nE_{Li}) \qquad (2)$$

where E_{GA+nLi}, E_{GA-nLi} and E_{Li} stands for total energies of whole GA-lithium system, system without lithium atom and lithium atom, respectively. n denotes the number of lithium atoms (Figures S18 and S19, Supporting Information).

Supporting Information

Supporting Information is available from the Wiley Online Library or from the author.

Conflict of Interest

The authors declare no conflict of interest.

Data Availability Statement

The data that support the findings of this study are available from the corresponding author upon reasonable request.

[1] A. R. Dehghani-Sanij, E. Tharumalingam, M. B. Dusseault, R. Fraser, *Renewable Sustainable Energy Rev.* **2019**, *104*, 192.
[2] Y. Yang, E. G. Okonkwo, G. Huang, S. Xu, W. Sun, Y. He, *Energy Storage Mater.* **2021**, *36*, 186.
[3] G. E. Blomgren, *J. Electrochem. Soc.* **2017**, *164*, A5019.
[4] M. Li, J. Lu, Z. Chen, K. Amine, *Adv. Mater.* **2018**, *30*, 1800561.
[5] Q. Zhang, W. Cai, Y. X. Yao, G. L. Zhu, C. Yan, L. L. Jiang, C. He, J. Q. Huang, *Chem. Soc. Rev.* **2020**, *49*, 3806.
[6] P. Zhang, T. Yuan, Y. Pang, C. Peng, J. Yang, Z.-F. Ma, S. Zheng, *J. Electrochem. Soc.* **2019**, *166*, A5489.
[7] Y. Lu, J. Chen, *Nat. Rev. Chem.* **2020**, *4*, 127.
[8] P. Poizot, J. Gaubicher, S. Renault, L. Dubois, Y. Liang, Y. Yao, *Chem. Rev.* **2020**, *120*, 6490.
[9] S. Lee, G. Kwon, K. Ku, K. Yoon, S. K. Jung, H. D. Lim, K. Kang, *Adv. Mater.* **2018**, *30*, 1704682.
[10] S. Lee, J. Hong, K. Kang, *Adv. Energy Mater.* **2020**, *10*, 2001445.
[11] D. MacInnes, M. A. Druy, P. J. Nigrey, D. P. Nairns, A. G. MacDiarmid, A. J. Heeger, *J. Chem. Soc. – Ser. Chem. Commun.* **1981**, 317.
[12] D. L. Williams, J. J. Byrne, J. S. Driscoll, *J. Electrochem. Soc.* **1969**, *116*, 2.
[13] H. G. Rasheev, R. B. Araujo, A. Tadjer, P. Johansson, *J. Mater. Chem. A* **2020**, *8*, 14152.
[14] S. Tobishima, *J. Electrochem. Soc.* **1984**, *131*, 57.
[15] S. J. Visco, L. C. DeJonghe, *J. Electrochem. Soc.* **1988**, *135*, 2905.
[16] T. Matsunaga, T. Kubota, T. Sugimoto, M. Satoh, *Chem. Lett.* **2011**, *40*, 750.
[17] C. Luo, O. Borodin, X. Ji, S. Hou, K. J. Gaskell, X. Fan, J. Chen, T. Deng, R. Wang, J. Jiang, C. Wang, *Proc. Natl. Acad. Sci. U.S.A.* **2018**, *115*, 2004.
[18] C. Luo, X. Ji, S. Hou, N. Eidson, X. Fan, Y. Liang, T. Deng, J. Jiang, C. Wang, *Adv. Mater.* **2018**, *30*, 1706498.
[19] K. Nakahara, S. Iwasa, M. Satoh, Y. Morioka, J. Iriyama, M. Suguro, E. Hasegawa, *Chem. Phys. Lett.* **2002**, *359*, 351.
[20] Y. Morita, S. Suzuki, K. Sato, T. Takui, *Nat. Chem.* **2011**, *3*, 197.
[21] Q. Zhao, Y. Lu, J. Chen, *Adv. Energy Mater.* **2017**, *7*, 1601792.
[22] Y. Xu, M. Zhou, Y. Lei, *Mater. Today* **2018**, *21*, 60.
[23] J. Y. Hwang, S. T. Myung, Y. K. Sun, *Adv. Funct. Mater.* **2018**, *28*, 1802938.
[24] H. Kim, J. C. Kim, M. Bianchini, D. H. Seo, J. Rodriguez-Garcia, G. Ceder, *Adv. Energy Mater.* **2018**, *8*, 1702384.
[25] D. Bin, W. Huo, Y. Yuan, J. Huang, Y. Liu, Y. Zhang, F. Dong, Y. Wang, Y. Xia, *Chem* **2020**, *6*, 968.
[26] B. T. McAllister, L. T. Kyne, T. B. Schon, D. S. Seferos, *Joule* **2019**, *3*, 620.
[27] D. J. Kim, D. J. Yoo, M. T. Otley, A. Prokofjevs, C. Pezzato, M. Owczarek, S. J. Lee, J. W. Choi, J. F. Stoddart, *Nat. Energy* **2019**, *4*, 51.
[28] Y. Zhang, S. Liu, Y. Ji, J. Ma, H. Yu, *Adv. Mater.* **2018**, *30*, 1706310.
[29] M. Armand, S. Grugeon, H. Vezin, S. Laruelle, P. Ribière, P. Poizot, J. M. Tarascon, *Nat. Mater.* **2009**, *8*, 120.
[30] Q. Zhao, J. Wang, Y. Lu, Y. Li, G. Liang, J. Chen, *Angew. Chem., Int. Ed.* **2016**, *55*, 12528.
[31] B. Häupler, A. Wild, U. S. Schubert, *Adv. Energy Mater.* **2015**, *5*, 1402034.
[32] S. Wang, L. Wang, K. Zhang, Z. Zhu, Z. Tao, J. Chen, *Nano Lett.* **2013**, *13*, 4404.
[33] N. Ogihara, T. Yasuda, Y. Kishida, T. Ohsuna, K. Miyamoto, N. Ohba, *Angew. Chem., Int. Ed.* **2014**, *53*, 11467.
[34] G. Dai, Y. He, Z. Niu, P. He, C. Zhang, Y. Zhao, X. Zhang, H. Zhou, *Angew. Chem., Int. Ed.* **2019**, *58*, 9902.
[35] X. Judez, L. Qiao, M. Armand, H. Zhang, *ACS Appl. Energy Mater.* **2019**, *2*, 4008.
[36] S. Eigler, A. Hirsch, *Angew. Chem., Int. Ed.* **2014**, *53*, 7720.
[37] D. R. Dreyer, A. D. Todd, C. W. Bielawski, *Chem. Soc. Rev.* **2014**, *43*, 5288.
[38] D. C. Marcano, D. V. Kosynkin, J. M. Berlin, A. Sinitskii, Z. Sun, A. Slesarev, L. B. Alemany, W. Lu, J. M. Tour, *ACS Nano* **2010**, *4*, 4806.
[39] A. Y. S. Eng, C. K. Chua, M. Pumera, *Nanoscale* **2015**, *7*, 20256.
[40] A. Lerf, H. He, M. Forster, J. Klinowski, *J. Phys. Chem. B* **1998**, *102*, 4477.
[41] V. Georgakilas, M. Otyepka, A. B. Bourlinos, V. Chandra, N. Kim, K. C. Kemp, P. Hobza, R. Zboril, K. S. Kim, *Chem. Rev.* **2012**, *112*, 6156.
[42] X. Li, L. Zhi, *Chem. Soc. Rev.* **2018**, *47*, 3189.
[43] A. Bakandritsos, M. Pykal, P. Bořski, P. Jakubec, D. D. Chronopoulos, K. Poláková, V. Georgakilas, K. Čépe, O. Tomanec, V. Ranc, A. B. Bourlinos, R. Zbořil, M. Otyepka, *ACS Nano* **2017**, *11*, 2982.
[44] M. Blanco, D. Mosconi, M. Otyepka, M. Medveď, A. Bakandritsos, S. Agnoli, G. Granozzi, *Chem. Sci.* **2019**, *10*, 9438.
[45] Y. Heng Cheong, M. Z. M. Nasir, A. Bakandritsos, M. Pykal, P. Jakubec, R. Zbořil, M. Otyepka, M. Pumera, *ChemElectroChem* **2019**, *6*, 229.
[46] A. Lenarda, A. Bakandritsos, M. Bevilacqua, C. Tavagnacco, M. Melchionna, A. Naldoni, T. Steklý, M. Otyepka, R. Zbořil, P. Fornasiero, *ACS Omega* **2019**, *4*, 19944.
[47] V. Šedajová, P. Jakubec, A. Bakandritsos, V. Ranc, M. Otyepka, *Nanomaterials* **2020**, *10*, 1731.
[48] J. Kolařík, A. Bakandritsos, Z. Bad'ura, R. Lo, G. Zoppellaro, Š. Kment, A. Naldoni, Y. Zhang, M. Petr, O. Tomanec, J. Filip, M. Otyepka, P. Hobza, R. Zbořil, *ACS Nano* **2021**, *15*, 3349.
[49] M. Medveď, G. Zoppellaro, J. Ugolotti, D. Matochová, P. Lazar, T. Pospíšil, A. Bakandritsos, J. Tuček, R. Zbořil, M. Otyepka, *Nanoscale* **2018**, *10*, 4696.

**ADVANCED
SCIENCE NEWS**
www.advancedsciencenews.com

**ADVANCED
ENERGY
MATERIALS**
www.advenergymat.de

[50] B. Pan, C.-M. Hu, L. Bai, F.-G. Zhao, L. Dong, B. Zuo, W. Zhang, X. Wang, W.-S. Li, *Adv. Funct. Mater.* **2019**, *29*, 1906076.

[51] F.-G. Zhao, Y.-T. Kong, B. Pan, C.-M. Hu, B. Zuo, X. Dong, B. Li, W.-S. Li, *J. Mater. Chem. A* **2019**, *7*, 3353.

[52] M. Shaibani, M. S. Mirshekarloo, R. Singh, C. D. Easton, M. C. D. Cooray, N. Eshraghi, T. Abendroth, S. Dörfler, H. Althues, S. Kaskel, A. F. Hollenkamp, M. R. Hill, M. Majumder, *Sci. Adv.* **2020**, *6*, eaay2757.

[53] Y. Gogotsi, R. M. Penner, *ACS Nano* **2018**, *12*, 2081.

[54] L. Fédèle, F. Sauvage, S. Gottis, C. Davoisne, E. Salager, J. N. Chotard, M. Becuwe, *Chem. Mater.* **2017**, *29*, 546.

[55] J. Wang, H. Zhao, L. Xu, Y. Yang, G. He, Y. Du, *ACS Appl. Mater. Interfaces* **2018**, *10*, 35469.

[56] Y. Wang, L. Lv, R. Guo, W. Huang, W. Wang, H. Chen, H. Zheng, *J. Power Sources* **2020**, *473*, 228515.

[57] C. L. Bentley, A. M. Bond, A. F. Hollenkamp, P. J. Mahon, J. Zhang, *J. Phys. Chem. C* **2015**, *119*, 21840.

[58] L. Fédèle, F. Sauvage, F. Lepoivre, S. Gottis, C. Davoisne, M. Courty, J.-M. M. Tarascon, M. Becuwe, *Chem. Mater.* **2019**, *31*, 6224.

[59] E. Peled, S. Menkin, *J. Electrochem. Soc.* **2017**, *164*, A1703.

[60] P. Verma, P. Maire, P. Novák, *Electrochim. Acta* **2010**, *55*, 6332.

[61] H. Numazawa, K. Sato, H. Imai, Y. Oaki, *NPG Asia Mater* **2018**, *10*, 397.

[62] Z. Sha, S. Qiu, Q. Zhang, Z. Huang, X. Cui, X. Yang, Z. Lin, *J. Mater. Chem. A* **2019**, *7*, 23019.

[63] L. S. Jiao, T. Wu, H. Y. Li, F. Li, L. Niu, *Chem. Commun.* **2015**, *51*, 15979.

[64] Y. Wang, Y. Deng, Q. Qu, X. Zheng, J. Zhang, G. Liu, V. S. Battaglia, H. Zheng, *ACS Energy Lett.* **2017**, *2*, 2140.

[65] Y. Wang, X. Zheng, Q. Qu, G. Liu, V. S. Battglia, H. Zheng, *Carbon* **2018**, *132*, 420.

[66] Z. Hu, S. Sayed, T. Jiang, X. Zhu, C. Lu, G. Wang, J. Sun, A. Rashid, C. Yan, L. Zhang, Z. Liu, *Adv. Energy Mater.* **2018**, *8*, 1802273.

[67] M. Forghani, S. W. Donne, *J. Electrochem. Soc.* **2018**, *165*, A664.

[68] Y. Huang, D. Wu, A. Dianat, M. Bobeth, T. Huang, Y. Mai, F. Zhang, G. Cuniberti, X. Feng, *J. Mater. Chem. A* **2017**, *5*, 1588.

[69] J. Zou, C. Sole, N. E. Drewett, M. Velický, L. J. Hardwick, *J. Phys. Chem. Lett.* **2016**, *7*, 4291.

[70] W. Su, N. Kumar, A. Krayev, M. Chaigneau, *Nat. Commun.* **2018**, *9*, 2891.

[71] H. Zhu, J. Yin, X. Zhao, C. Wang, X. Yang, *Chem. Commun.* **2015**, *51*, 14708.

[72] T. Yasuda, N. Ogihara, *Chem. Commun.* **2014**, *50*, 11565.

[73] G. Wang, X. Shen, J. Yao, J. Park, *Carbon* **2009**, *47*, 2049.

[74] G. Kresse, J. Hafner, *Phys. Rev. B* **1993**, *47*, 558.

[75] G. Kresse, J. Furthmüller, *Phys. Rev. B* **1996**, *54*, 11169.

[76] G. Kresse, J. Furthmüller, *Comput. Mater. Sci.* **1996**, *6*, 15.

[77] P. E. Blöchl, *Phys. Rev. B* **1994**, *50*, 17953.

[78] G. Kresse, D. Joubert, *Phys. Rev. B* **1999**, *59*, 1758.

[79] J. P. Perdew, K. Burke, M. Ernzerhof, *Phys. Rev. Lett.* **1996**, *77*, 3865.

[80] S. Grimme, *J. Comput. Chem.* **2006**, *27*, 1787.

PAPER

Check for updates

Nitrogen doped graphene with diamond-like bonds achieves unprecedented energy density at high power in a symmetric sustainable supercapacitor†

Veronika Šedajová, [ab] Aristides Bakandritsos, *[ac] Piotr Błoński, [a] Miroslav Medveď, [a] Rostislav Langer, [ab] Dagmar Zaoralová, [ab] Juri Ugolotti, [a] Jana Dzíbelová, [ad] Petr Jakubec, [a] Vojtěch Kupka[a] and Michal Otyepka *[ae]

Supercapacitors have attracted great interest because of their fast, reversible operation and sustainability. However, their energy densities remain lower than those of batteries. In the last decade, supercapacitors with an energy content of ~110 W h L^{-1} at a power of ~1 kW L^{-1} were developed by leveraging the open framework structure of graphene-related architectures. Here, we report that the reaction of fluorographene with azide anions enables the preparation of a material combining graphene-type sp^2 layers with tetrahedral carbon–carbon bonds and nitrogen (pyridinic and pyrrolic) superdoping (16%). Theoretical investigations showed that the C–C bonds develop between carbon-centered radicals, which emerge in the vicinity of the nitrogen dopants. This material, with diamond-like bonds and an ultra-high mass density of 2.8 g cm^{-3}, is an excellent host for the ions, delivering unprecedented energy densities of 200 W h L^{-1} at a power of 2.6 kW L^{-1} and 143 W h L^{-1} at 52 kW L^{-1}. These findings open a route to materials whose properties may enable a transformative improvement in the performance of supercapacitor components.

Broader context

Modern society relies on electricity. The demand is bound to grow due to the increasing electromobility, the number of mobile devices, and extending the networks for the internet of things. The depleting reserves of fossil-based energy resulted in efforts to support renewable resources, which are, however, intermittent in their production. These facts call for the development of electrochemical energy storage devices with improved performance, safety, eco-friendliness, and lower cost in order to contribute to the goal of the United Nations for affordable, reliable, and sustainable energy. Lithium-ion batteries have matured and currently dominate the field. Nevertheless, carbon-based supercapacitors offer independence of critical elements, alongside safety, long life-cycle, and ultrafast charging–discharging. Here, we present a nitrogen superdoped graphene material with diamond-like interlayer bonds that dramatically increases the energy content, which can be stored per volumetric unit of the electrode—the Achilles heel of contemporary supercapacitors. The electrode displays an ultrahigh mass density compared to porous carbons, keeping intact its ability to host the electrolyte ions—the energy carriers. Consequently, a supercapacitor device made from this electrode delivers energy density twice as high as that of top-rated materials and several-fold higher than commercial supercapacitor carbons, thus enhancing the performance of supercapacitor components.

[a] *Regional Centre of Advanced Technologies and Materials, Czech Advanced Technology and Research Institute (CATRIN), Palacký University, Šlechtitelů 27, 783 71, Olomouc, Czech Republic. E-mail: michal.otyepka@upol.cz, a.bakandritsos@upol.cz*

[b] *Department of Physical Chemistry, Faculty of Science, Palacký University, 17. listopadu 1192/12, 779 00 Olomouc, Czech Republic*

[c] *Nanotechnology Centre, Centre of Energy and Environmental Technologies, VŠB–Technical University of Ostrava, 17. listopadu 2172/15, Poruba, 708 00 Ostrava, Czech Republic*

[d] *Department of Experimental Physics, Faculty of Science, Palacký University Olomouc, 17. listopadu 1192/12, Olomouc, 77900, Czech Republic*

[e] *IT4Innovations, VŠB–Technical University of Ostrava, 17. listopadu 2172/15, 708 00 Ostrava-Poruba, Czech Republic*

† Electronic supplementary information (ESI) available. See DOI: 10.1039/d1ee02234b

1. Introduction

Supercapacitors are energy storage devices with remarkable qualities including fast charging/discharging (*i.e.* high power) and extralong cycle-life.[1] Unfortunately, the energy density of the best existing supercapacitors (*i.e.* their ability to store charge/energy) is low. Commercial supercapacitors have cell-level specific energies (and energy densities) of 10 W h kg^{-1} (5–8 W h L^{-1}),[2,3] while lead–acid batteries offer 20–35 W h kg^{-1} (40–80 W h L^{-1})[4] and state-of-the-art Li-ion batteries achieve ~150 W h kg^{-1} (~250 W h L^{-1}).[5,6] However, Li-ion batteries

740 | *Energy Environ. Sci.*, 2022, **15**, 740–748

This journal is © The Royal Society of Chemistry 2022

Paper

suffer from long charging times and, unlike supercapacitors, undergo irreversible processes during cycling that gradually reduce their energy density and thus their cycle-life. To exploit the benefits of supercapacitors in a broader range of applications, it will be necessary to identify electrode materials that have substantially improved energy densities combined with long life and high power. In addition, replacing metal atoms in electrode materials with non-metal and earth-abundant elements, such as carbon, would have significant environmental advantages, reducing our reliance on critical natural resources and increasing sustainability.

Due to the importance of the electrode material/electrolyte interface for charge storage,[7] intense efforts have been focused on lightweight materials with high surface areas such as nitrogen-doped mesoporous carbon[8] (2000 $m^2 g^{-1}$), carbon nanosheets[9] (2500 $m^2 g^{-1}$), activated graphene[10] (3100 $m^2 g^{-1}$), and carbon nanotubes[11] (1300 $m^2 g^{-1}$). The specific energies of these materials range from *ca.* 10 to 90 W h kg^{-1}, with the highest values being reported for activated graphene,[10] carbon nanosheets,[9] and nanotubes[11] in ionic liquid (IL)-based electrolytes. Unfortunately, like most commercial electrodes,[12] these carbon materials have very low mass densities (*ca.* 0.3–0.7 g cm^{-3}).[8,10] Consequently, the energy densities achieved with mesoporous carbon,[8] activated graphene,[10] and carbon nanosheets[9] (or single wall carbon nanotubes[11]) are only 22, 26, and 45 W L^{-1}, respectively.

To achieve higher energy densities, which is a key performance parameter,[2–4,13–16] efforts have been made to increase the mass density of electrode materials. Compressing a graphene electrode increased its mass density from 0.34 to 0.75 g cm^{-3} and its energy density from 26[10] to 48 W h L^{-1} (ref. 17) without adversely affecting the interactions between the electrolyte ions and the carbon surface. Capillary densification of a chemically reduced graphene gel in the presence of an IL led to an even higher density of 1.3 g cm^{-3}, resulting in a material that delivered 90 W h L^{-1} at a power density of 1.1 kW L^{-1} (1 A g^{-1}).[18] It was deduced that densification in the presence of the non-evaporating IL prevented the restacking of the graphene sheets and helped preserve the material's charge transport properties. Mechanical compression of a H_2O_2-treated reduced graphene oxide[19] yielded a material with a density of 0.7 g cm^{-3} and a holey structure (beneficial for ion diffusion) that very effectively promoted three-dimensional ionic transport, delivering 85 W h L^{-1} at 1.75 kW L^{-1} (1 A g^{-1}). In 2016, capillary drying was combined with a different pore-forming agent ($ZnCl_2$), to afford a monolithic dense (0.9 g cm^{-3}) graphene electrode[14] exhibiting 60 W h L^{-1} at 0.4 kW L^{-1} (0.6 A g^{-1}). Further attempts to increase the energy density by heteroatom tri-doping[20] and densification[21] were not more effective, resulting in energy densities of 40 and 65 W h L^{-1}, respectively. Even high mass density inorganic phases such as 1T-MoS_2 did not exceed 80 W h L^{-1} at 1.12 kW L^{-1} (0.5 A g^{-1}).[22] The highest energy density reported to date was obtained using electrodes consisting of interdigitated bilayers of exfoliated graphene-mediated hydrogen iodide-reduced graphene oxide (EGM-GO)[23] with a mass density of *ca.* 1 g cm^{-3} and a capacitance of 203 F cm^{-3}. These

electrodes offered an energy density of 113 W h L^{-1} at 0.9 kW L^{-1} (1 A g^{-1}) (see the experimental section for information on the metrics used). Thus, over the last decade there have been small improvements in materials design for higher energy contents, and power densities have remained relatively low.

Here we report a carbon-based electrode material, GN3, with an unprecedented density of 2.8 g cm^{-3} and an N_2 sorption-based surface area of 128 $m^2 g^{-1}$ that can host ions even more efficiently than carbon materials with surface areas exceeding 2000 $m^2 g^{-1}$. GN3, which is prepared by reacting graphite fluoride with sodium azide, has tetrahedral (sp^3) C–C bonds, which were identified by solid-state nuclear magnetic resonance in the same region as the C–C bonds in diamond. However, it retains a 2-D structure with a very high content of aromatic (and thus conductive) regions, together with nitrogen superdoping in the vacancies and holes of the aromatic lattice. The ultrahigh mass density of GN3 combined with its polar nitrogen moieties and vacancies facilitated an energy density of 200 W h L^{-1} at a power density of 2.6 kW L^{-1}, corresponding to improvements of 74% and 190%, respectively, over the previous record.[23]

2. Results and discussion

Motivated by the importance of fluorine and radical chemistry[24,25] in the synthesis of sp^3-rich carbon materials,[26–28] and by the high density of such materials,[29] we hypothesized that fluorographene chemistry could produce carbon derivatives with high mass densities. This hypothesis was strengthened by the fact that in $(C_2F)_n$, whereby fluorine atoms occupy one side of every other carbon sheet in an FCCF manner, the carbon atoms in between adopt a diamond-like structure,[30,31] ascribing high mass density.[31] The formation of similar sp^3-rich structures was also verified theoretically and experimentally for bilayer graphene.[32,33] Despite their high mass density, fluorocarbons are large band-gap insulators[34] and lack sites capable of interacting strongly with ionic species and facilitating their transport. However, because the defluorination and functionalization of fluorographene is known to occur *via* radical reactions propagated by fluorine elimination,[35,36] these processes could potentially be exploited to drive sp^3 C–C bond formation and create graphene-based materials with high mass density.

To investigate this hypothesis, we experimentally and theoretically probed the reaction of few-layered fluorographene with sodium azide as a defluorinating agent that could at the same time introduce nitrogen atoms in the formed structure. This would increase the polarity of the carbon surface and create vacancies, as previously observed following reactions of fluorographene with various nitrogen-containing nucleophiles.[36–38] Sonicated bulk graphite fluoride reacted very efficiently with NaN_3 in dimethylformamide at 130 °C, resulting in nitrogen superdoping (Fig. 1a). X-ray photoelectron spectroscopy (XPS) revealed a decrease in the material's content of F atoms after a reaction time of 4 h and almost complete elimination of F after 72 h, at which point the material's N content reached 16.1 at% (Fig. 1b and c). This change was reflected in the C 1s regions of the materials' XPS spectra (Fig. 1c): the initially

This journal is © The Royal Society of Chemistry 2022

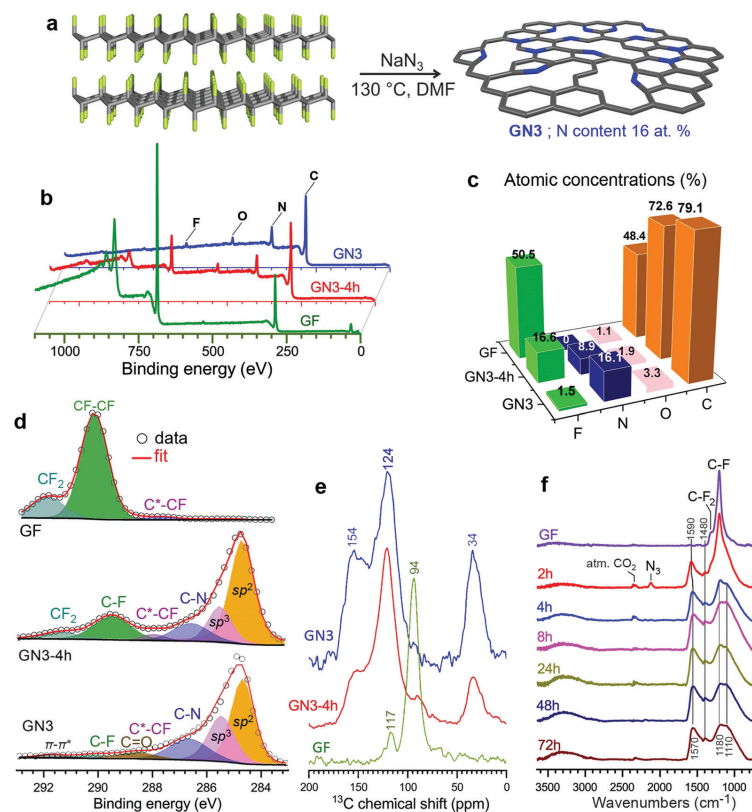*Energy Environ. Sci.*, 2022, **15**, 740–748 | **741**

Fig. 1 Synthesis and characterization of the GN3 material. (a) Schematic depiction of the synthesis of GN3 from sonicated graphite fluoride (GF). (b) XPS survey spectra of the starting GF and the N-doped derivative after reaction times of 4 h and 72 h (GN3). (c) Elemental compositions of the same materials determined by XPS. (d) Deconvoluted HR-XPS spectra for the C 1s regions. (e) CP MAS ^{13}C solid state NMR spectra and (f) IR spectra of GF, reaction intermediates at various time points, and the final GN3 product.

F-bonded carbon atoms of fluorographene, with binding energies above 289.5 eV, were transformed into (i) aromatic sp^2 carbons (284.7 eV, 45%), (ii) non-functionalized sp^3 carbons (285.5 eV, 25%), and (iii) nitrogen bonded carbons (286.6 eV, 19%). The other components in this spectral region were attributed to small amounts of residual fluorine and oxygen from the environment. The HR-XPS spectra of the N 1s envelope (Fig. S1, ESI†) revealed the presence of nitrogen atoms in pyridinic and pyrrolic configurations (or protonated and non-protonated N centres), as well as a very small number of graphitic nitrogens (44, 49, and 7 at%, respectively). The dominance of pyridinic and pyrrolic nitrogens is consistent with the vacancies present in the parent material[36] and with the extensive development of such vacancies during defluorination.[36–38]

The ^{1}H → ^{13}C CP MAS solid-state NMR spectra of the GN3-4 h intermediate and GN3 show peaks at 34 ppm (Fig. 1e).

Chemical shifts in this range are typical for non-functionalized and non-nitrogen bonded sp^3 carbons in diamond and diamond-like carbon materials.[39] This peak was stronger in the spectrum of GN3 than the GN3-4 h intermediate, indicating that these sp^3 carbons formed gradually as the reaction progressed. Furthermore, the peaks centred at 124 and 154 ppm indicate the presence of a π-conjugated aromatic network and aromatic >C=N moieties (pyridinic and pyrrolic),[39,40] respectively. ^{19}F → ^{13}C CP MAS of the starting GF revealed peaks corresponding to CF_2 (117 ppm) and CF (94 ppm) groups, typical for FG.[41] Such non-functionalized tetrahedral carbons at 34 ppm are not detected in graphene oxide, reduced graphene oxide, or graphene.[42,43] The reaction's progress was also verified by infra-red spectroscopy (Fig. 1f). Specifically, the bands of the CF and CF_2 groups of GF (1200 and 1305 cm^{-1}, respectively) were progressively replaced with

742 | Energy Environ. Sci., 2022, 15, 740–748

This journal is © The Royal Society of Chemistry 2022

229

Paper

bands at 1580 and 1210 cm^{-1} (characteristic of aromatic carbon rings[44]), indicating the formation of an sp^2 network. Additional aromatic-ring vibrations, appearing at 1400 cm^{-1}, could be ascribed to heteroatom substitution (*e.g.* with pyridinic nitrogens[44,45]), as suggested by theoretical calculations.[46,47] The Raman spectrum of GN3 featured broad D and G bands at 1300 and 1590 cm^{-1}, respectively, and an I_D/I_G ratio of 1.3, which remained unchanged even after heating at 1000 °C in an argon atmosphere (Fig. S2, ESI†), indicating the presence of a large number of non heat-susceptible sp^3 carbons and non-healable defects (*i.e.* vacancies). Raman bands and X-ray diffraction peaks (XRD) deconvolution performed on GN3, and on the commercial porous carbon for comparison (Fig. S3 and S4, ESI†), showed that the GN3 displays a disordered structure with randomly developed tetrahedral C–C bonds. Results also highlighted the very small planarity of the aromatic areas, with a lateral size (L_a) of *ca.* 4 nm (Fig. S3 and S4 (ESI†), and comments in the caption). Further insights into the N-doping of fluorographene with NaN$_3$ were obtained through density functional theory (DFT) calculations. The N$_3^-$ anion initiated the reaction by nucleophilic attack on carbon radical defects, leading to N$_2$ release and fluorine elimination (Fig. S5, ESI†). The attachment of azide groups in the initial stages of the reaction was confirmed by the infra-red spectrum of the 2 h intermediate (Fig. 1f). High-resolution transmission electron microscopy (HR-TEM, Fig. 2a and b) revealed that GN3 indeed exists as sheets with patches and holes.

Energy dispersive X-ray spectroscopy (EDXS) elemental mapping with high-angle annular dark-field scanning transmission electron microscopy (HAADF-STEM, Fig. 2c) showed that the GN3 sheets (Fig. 2d) are densely and homogeneously covered with nitrogen (Fig. 2e). Thermogravimetric and evolved gas analyses in air (Fig. S6, ESI†) indicated that these nitrogen atoms were embedded in the lattice rather than being out-of-plane functionalities, because emission of NO gas (m/z = 30) peaked at very high temperature (675 °C), at which CO$_2$ emission also took place due to carbon lattice decomposition.

To better understand the formation of the tetrahedral C–C bonds, theoretical models of GN3 sheet fragments were studied using spin-polarized DFT (Fig. 3), consistent with the experimental findings (*i.e.* containing vacancies and nitrogen dopants mainly in pyridinic and pyrrolic configurations, Fig. 3). Remarkably, the system relaxed into a thermodynamically stable structure with spontaneously formed tetrahedral sp^3 C–C bonds, verifying the experimental NMR findings. The bonds were formed between the carbons in the pyridinic vacancies, where radicals were centred (highlighted by spheres in Fig. 3). Similar sp^3 bonding was suggested to form after the introduction of atomic vacancies and pyrrolic N atoms by N-ion beam irradiation of graphene sheets, which creates carbon atoms with dangling bonds (radicals) around the vacancies.[48]

Films of GN3 or GN3 with additives (polymer binder 10%; conductive additive 5%) were formed by pasting slurries onto 15 μm-thick Al foils for density measurements and preparation
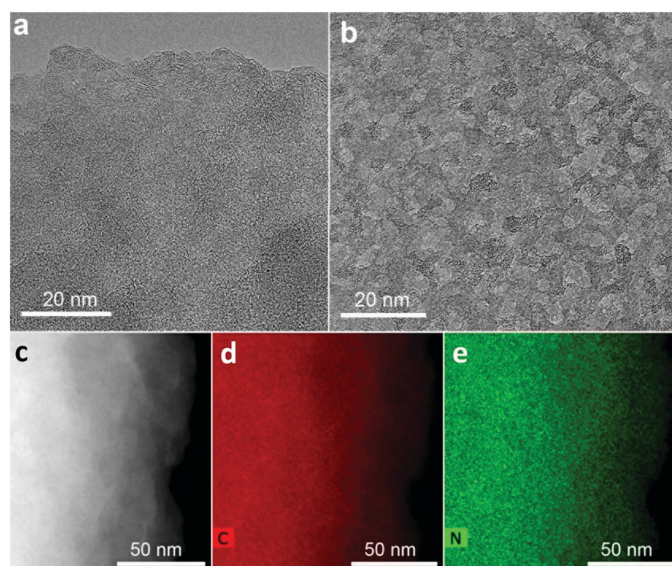

Fig. 2 (a) and (b) High-resolution transmission electron microscopy images of GN3 flakes; several areas had extensively holey structure, as shown in (b), and in Fig. S1b (ESI†). (c) HAADF image of a GN3 flake used for EDXS mapping, along with the corresponding (d) carbon and (e) nitrogen map.
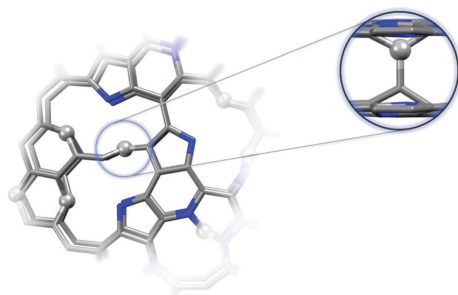
Fig. 3 Theoretical model of GN3 structural fragment (C : N atomic ratio of *ca.* 84 : 16) optimized by first-principles spin-polarized DFT calculations. Top view of this structure with the carbons bearing radicals and forming interlayer bonds highlighted as spheres (zoomed side-view). The model simulates the structure locally (few-atom level) and does not (and cannot) provide macroscopic structural information.

of supercapacitor electrodes (ESI,† Methods). Scanning electron microscopy (SEM, Fig. 4a–c) showed that compression at 80 kN for 1 minute ($\sim$65 MPa) reduced a *ca.* 10 μm thick film of GN3 to a thickness of 2 μm (Fig. 4d–f). From thickness measurements performed using SEM and a digital micrometer (Fig. S7c and d, ESI†), the density of these films consistently reached values of 2.7–2.8 g cm^{-3}, compared to $\sim$0.5 g cm^{-3} before pressing. The same mass density was also attained for a high-mass loading electrode (8.3 mg cm^{-2}, Fig. S7i and j, ESI†). The NMR spectrum of the pressed material was identical to that before pressing, indicating that pressing caused only bed consolidation, and not formation of bonds. Five GN3 batches

from different reactions were measured to determine the mass density; it should be noted that densities were only measured after dialysis of GN3. Control tests were performed using the same procedure with Al foil alone (Fig. S7a and b, ESI†) and with commercial carbons of high surface area (Fig. S7e–h, ESI†), namely porous carbon (PC) from ACS Material (0.3 g cm^{-3}, 2000 m^2 g^{-1} according to N$_2$ BET) and YP-80F Kuraray carbon (KC) (0.6 g cm^{-3}, 2363 m^2 g^{-1} according to N$_2$ BET; also measured in-house, Fig. S8b and d, ESI†). The thickness measurements for the PC carbon were cross-checked by SEM (Fig. S9, ESI†). Results verified that no compression took place for Al foil, and that all mass density calculations for the commercial carbons after their pressing matched those given by the provider. Moreover, we performed elemental analysis for Na showing that 0.02 mass% of sodium remained in GN3, and therefore, the respective contribution in mass density of the material is negligible. The surface area of GN3 determined from the N$_2$ sorption isotherm using BET equation was only 128 m^2 g^{-1}, (Fig. S8a and c, ESI†). The surface area determined by methylene blue sorption was 300 m^2 g^{-1} (Fig. S10, ESI†), suggesting that under solvated conditions (as in an electrolytic supercapacitor cell), charged species/molecules, like methylene blue in this case, may penetrate into the structure of GN3. Interestingly, preliminary electrochemical testing of GN3 showed that pressing did not affect its charge storage properties; in fact, pressing increased the capacitance relative to the non-pressed electrode (Fig. S11, ESI†).

The electrochemical properties of GN3 were studied in a symmetric full cell using as the electrolyte the IL 1-ethyl-3-methylimidazolium tetrafluoroborate (EMIM-BF$_4$) with 1,1,2,2-tetrafluoroethyl-2,2,3,3-tetrafluoropropyl ether (TTE) in a 9 : 1
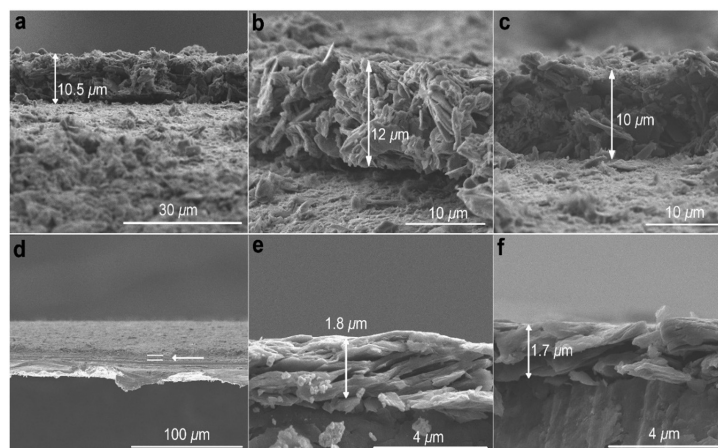

Fig. 4 SEM images of GN3 with 10 mass% additives pasted on Al foil. (a)–(c) Before pressing and (d)–(f) after pressing. Pressing the Al foil itself did not affect its thickness (Fig. S7a and b, ESI†).
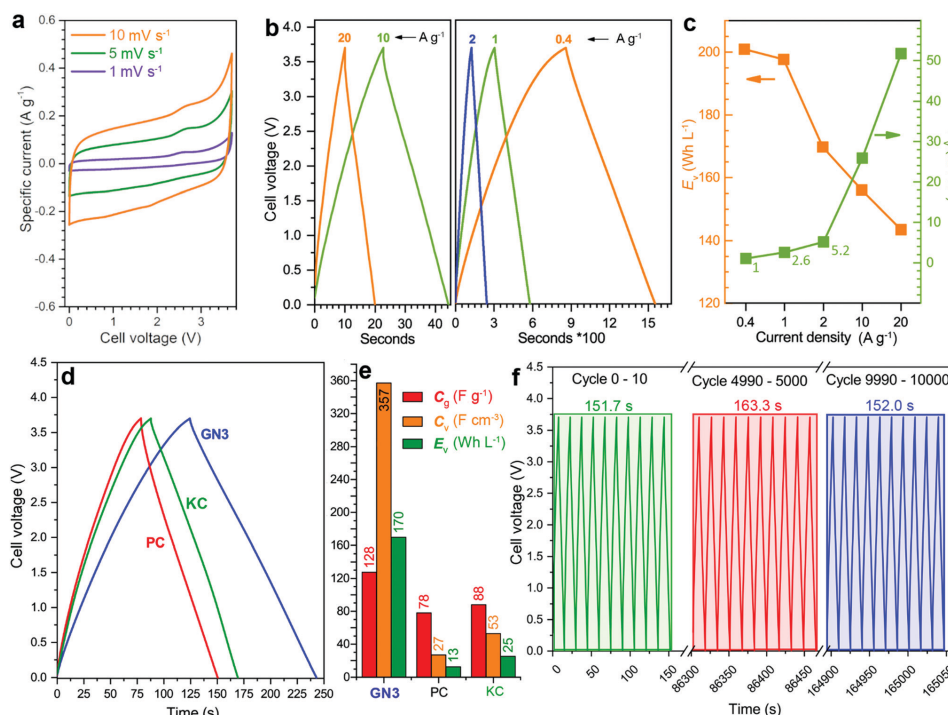
744 | *Energy Environ. Sci.*, 2022, **15**, 740–748

This journal is © The Royal Society of Chemistry 2022

231

Fig. 5 Electrochemical characterization of a symmetric supercapacitor cell with GN3 electrodes. (a) CV curves in the EMIM-BF$_4$ and TTE (9:1) electrolyte at low scan rates. (b) GCD profiles at different specific currents. (c) Energy and power density of GN3 at increasing specific currents. (d) Comparison of the GN3 cell with symmetric cells made using commercial high surface area (2000 m^2 g^{-1}) porous carbons (PC and KC) at 2 A g^{-1} and (e) the performance of these cells. (f) Cyclic stability of GN3 showing the GCD profiles at the beginning, mid-point, and end of a 10 000 cycle test at 20 A g^{-1} current density.

ratio. The cyclic voltammograms (CVs, Fig. 5a) were quasi-rectangular in shape with minor redox peaks, probably due to the nitrogen lattice atoms of the GN3 material.[49] This shape was preserved even at very high scan rates (Fig. S12, ESI†), indicating that the system exhibits predominantly capacitive behaviour[10] with fast charge transport in the material and at the interfaces.[15] These features were verified by galvanostatic charge/discharge measurements (GCD, Fig. 5b), which yielded linear and symmetric profiles (124 s charging, 118 s discharging at 2 A g^{-1}, 95% energy efficiency). The efficiency improved to 100% at 20 A g^{-1} (22 s charging, 22 s discharging). At 1 A g^{-1}, the GN3 cell achieved an ultrahigh energy density of 197.6 W h L^{-1} at a power of 2.6 kW L^{-1}. At 20 A g^{-1}, the energy density remained high at 143.5 W h L^{-1}, while the power density jumped to 51.8 kW L^{-1} (Fig. 5c).

For benchmarking, the carbons PC and KC (the latter widely used in commercial supercapacitors[50]) were evaluated under identical conditions. GN3 had a significantly better discharging time (Fig. 5d) than PC and KC, and its performance was

superior in both volumetric and gravimetric terms (Fig. 5e), which is impressive given the dramatic differences in the materials' BET surface areas. The cycling stability test of the GN3 material showed capacitance retention of 100% after 10 000 cycles at 20 A g^{-1} (Fig. 5f) and 98% after 14 000 cycles at 5 A g^{-1} (Fig. S15, ESI†). Rate testing of the GN3 cell showed that 76% retention of its capacitance at 40 A g^{-1} (Fig. 6a). A similar (70%) capacitance retention was achieved at 40 A g^{-1} for a cell made with exfoliated graphene-mediated HI-reduced graphene oxide (EGM-GO), which contained 50% exfoliated graphene.[23]

For comparative purposes, reported capacitance retention values for other high-performance graphene-based electrodes are *ca.* 65% at 40 A g^{-1} for liquid-mediated densified graphene,[18] 70% at 40 A g^{-1} for holey graphene,[19] 57% at 5 A g^{-1} for capillary-densified graphene,[21] and 77% at 20 A g^{-1} for vertically aligned graphene electrodes[51] (a much more conductive aqueous electrolyte was used in the latter case, which unfortunately keeps energy content low). These
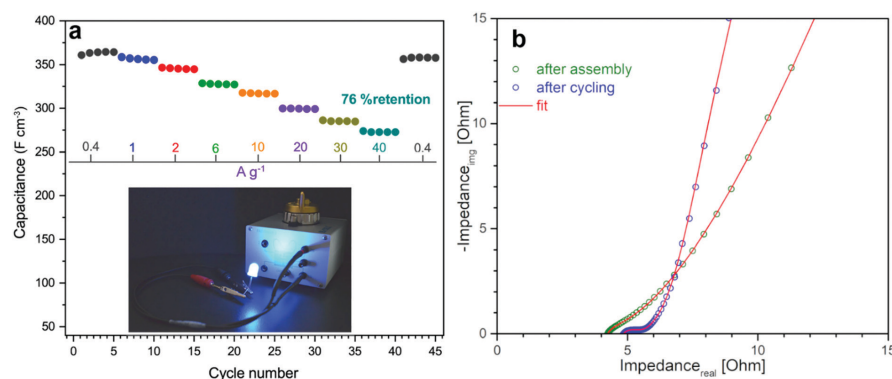
232

Fig. 6 Electrochemical properties of a symmetric supercapacitor cell with GN3 electrodes. (a) Rate test at increasing specific currents. (b) Nyquist plots of GN3 after cell assembly and after cycling in EMIM-BF$_4$ and TTE electrolyte (9 : 1 ratio).

comparisons highlight the excellent charge transport properties of GN3, which are also reflected in its electrochemical impedance spectroscopic features before and after cycling (Fig. 6b). Based on the modified Frumkin–Melik–Gaykazyan circuit (Fig. S17, ESI†), the intersection of the Nyquist plot with the real axis at the start of the high frequency region corresponded to an equivalent series resistance (R_s) of 3.9 Ω before cycling, which was only marginally increased to 4.4 Ω after 10 000 cycles.

Furthermore, the total absence of semicircles in the high frequency region indicated a very low charge transfer resistivity (R_{ct}) in the bulk material and at the interfaces.[19,52] The almost vertical slope of the spectrum in the low frequency region

(on the right of the x-axis) suggested a highly capacitive behaviour and effective ionic charge transport in the bulk of the electrode material.

Volumetric performance is particularly important for devices in the modern portable energy storage landscape;[2,4,13,14,20,23] both energy and power density are desired. The former directly affects the amount of energy that can be stored, while high power density enables fast charging and discharging. Energy density is the Achilles heel of supercapacitors, whereas high power densities are one of their greatest strengths, which must be preserved. The GN3 cell (Fig. 5c and Fig. S18, ESI†) demonstrated ground-breaking performance by delivering both ultrahigh energy density and power density. Specifically, its energy density was *ca.* 200 W h L^{-1} at a
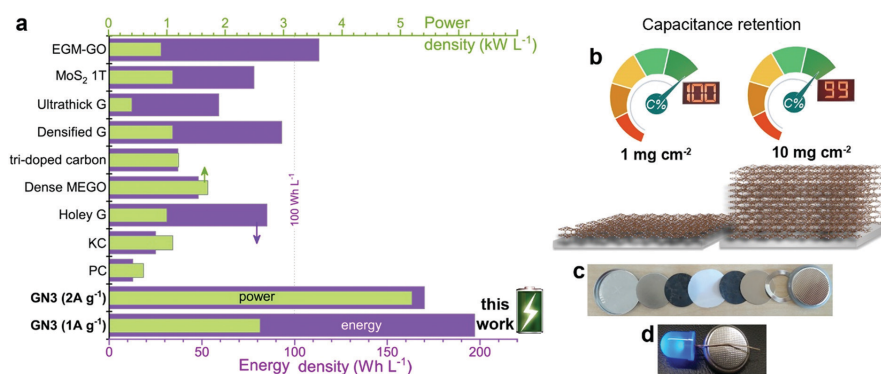

Fig. 7 (a) The energy and power density output achieved with GN3 electrodes compared to electrodes made with commercial 2000 m^2 g^{-1} active carbon and prominent analogues selected from the literature, chosen for their promising features; (holey G: holey graphene;[19] dense MEGO: compressed, microwave expanded and activated reduced graphene oxide;[17] tri-doped carbon;[20] densified G: capillary densified graphene;[18] ultrathick graphene;[14] 1T-MoS$_2$ (ref. 22) and EGM-GO: exfoliated graphene-mediated graphene oxide[23]). (b) Specific capacitance in symmetric full cell at high (10 mg cm^{-2}) mass loading of GN3 was 99% of the recorded capacitance of the low-mass-loading (1 mg cm^{-2}) symmetric full cell. (c),(d) Coin cell GN3 electrodes on aluminium foils before (c) and after assembly (d); the assembled cell was used to operate a 4 V LED diode.

233

power of 2.6 kW L^{-1}, 170 W h L^{-1} at 5.2 kW L^{-1}, and 143 W h L^{-1} at 52 kW L^{-1}. To set these results into the context of the current state of the art, they are presented alongside literature data on top-performing materials in Fig. 7a. When making these comparisons, care was taken to ensure that the same set of equations and metrics were used in all cases.[53–55] The equations from ref. 23 were used, as described in the experimental section. The comparisons highlight the transformative performance of GN3: not only does it have a higher energy density than the previously best-in-class EGM-GO electrode (170 W h L^{-1} for GN3 *vs.* 113 W h L^{-1} for EGM-GO[23]), but this energy could be delivered at a power of 5.2 kW L^{-1} compared to 0.9 kW L^{-1}. Importantly, the GN3 cell could also be operated at mass loadings of up to 10 mg cm^{-2}, demonstrating almost identical capacitance (Fig. 7b) at a temperature of 38 °C, which is in the range typically used to evaluate energy storage devices,[56–59] and 81% retention at the same testing conditions as the low mass-loading supercapacitor cell (see experimental part, ESI†). The coin cell shown in Fig. 7c and d, was constructed with a commercial ultrathin 25 μm membrane operating a 4 V LED lamp. Successful operation of carbon materials with such highly attractive features lays the ground for the fabrication of competitive, commercially relevant cells.

3. Conclusions

We have discovered a new class of carbon-based materials comprising nitrogen doped graphene with diamond-like tetrahedral bonds for high energy density supercapacitor electrodes that are significantly more dense than comparable materials prepared by mechanical compression,[17] capillary densification,[18] and other methods.[19,23] The new materials are prepared by leveraging the radical-based chemistry of fluorographene, which enables the fruitful combination of sp^2 and sp^3 carbon bonds in the same network, along with very high nitrogen doping and vacancies. This hybrid carbon achieves mass densities of 2.8 g cm^{-3}, while retaining efficient charge transport, ion penetration, diffusion, and storage. Therefore, cells with electrodes made from these materials offer ground-breaking energy storage capability at very high charging/discharging rates. The discovery of this class of materials will spur intense research on other high-density conductive carbon materials with different functionalities, with the aim of further increasing the competitiveness of supercapacitors in the portable energy storage landscape.

Conflicts of interest

A European patent with the number EP 3907184 has been published.

Acknowledgements

Notes and references

1 A. S. Aricò, P. Bruce, B. Scrosati, J.-M. Tarascon and W. van Schalkwijk, *Nat. Mater.*, 2005, **4**, 366–377.
2 W. Gu and G. Yushin, *Wiley Interdiscip. Rev.: Energy Environ.*, 2014, **3**, 424–473.
3 Q. Wang, J. Yan and Z. Fan, *Energy Environ. Sci.*, 2016, **9**, 729–762.
4 Y. Gogotsi and P. Simon, *Science*, 2011, **334**, 917–918.
5 J. W. Choi and D. Aurbach, *Nat. Rev. Mater.*, 2016, **1**, 16013.
6 P. Albertus, S. Babinec, S. Litzelman and A. Newman, *Nat. Energy*, 2018, **3**, 16–21.
7 M. Salanne, B. Rotenberg, K. Naoi, K. Kaneko, P.-L. Taberna, C. P. Grey, B. Dunn and P. Simon, *Nat. Energy*, 2016, **1**, 16070.
8 T. Lin, I.-W. Chen, F. Liu, C. Yang, H. Bi, F. Xu and F. Huang, *Science*, 2015, **350**, 1508–1513.
9 J. Hou, C. Cao, F. Idrees and X. Ma, *ACS Nano*, 2015, **9**, 2556–2564.
10 Y. Zhu, S. Murali, M. D. Stoller, K. J. Ganesh, W. Cai, P. J. Ferreira, A. Pirkle, R. M. Wallace, K. A. Cychosz, M. Thommes, D. Su, E. A. Stach and R. S. Ruoff, *Science*, 2011, **332**, 1537–1541.
11 A. Izadi-Najafabadi, S. Yasuda, K. Kobashi, T. Yamada, D. N. Futaba, H. Hatori, M. Yumura, S. Iijima and K. Hata, *Adv. Mater.*, 2010, **22**, E235–E241.
12 *EP2357046B1*, 2013.
13 P. Simon and Y. Gogotsi, *Acc. Chem. Res.*, 2013, **46**, 1094–1103.
14 H. Li, Y. Tao, X. Zheng, J. Luo, F. Kang, H.-M. Cheng and Q.-H. Yang, *Energy Environ. Sci.*, 2016, **9**, 3135–3142.
15 D. Yu, K. Goh, H. Wang, L. Wei, W. Jiang, Q. Zhang, L. Dai and Y. Chen, *Nat. Nanotechnol.*, 2014, **9**, 555–562.
16 R. Weber, M. Genovese, A. J. Louli, S. Hames, C. Martin, I. G. Hill and J. R. Dahn, *Nat. Energy*, 2019, **4**, 683–689.
17 S. Murali, N. Quarles, L. L. Zhang, J. R. Potts, Z. Tan, Y. Lu, Y. Zhu and R. S. Ruoff, *Nano Energy*, 2013, **2**, 764–768.
18 X. Yang, C. Cheng, Y. Wang, L. Qiu and D. Li, *Science*, 2013, **341**, 534–537.

This journal is © The Royal Society of Chemistry 2022

Energy Environ. Sci., 2022, **15**, 740–748 | **747**

19 Y. Xu, Z. Lin, X. Zhong, X. Huang, N. O. Weiss, Y. Huang and X. Duan, *Nat. Commun.*, 2014, **5**, 5554.

20 H. Jin, X. Feng, J. Li, M. Li, Y. Xia, Y. Yuan, C. Yang, B. Dai, Z. Lin, J. Wang, J. Lu and S. Wang, *Angew. Chem., Int. Ed.*, 2019, **58**, 2397–2401.

21 P. Li, H. Li, D. Han, T. Shang, Y. Deng, Y. Tao, W. Lv and Q.-H. Yang, *Adv. Sci.*, 2019, **6**, 1802355.

22 M. Acerce, D. Voiry and M. Chhowalla, *Nat. Nanotechnol.*, 2015, **10**, 313–318.

23 Z. Li, S. Gadipelli, H. Li, C. A. Howard, D. J. L. Brett, P. R. Shearing, Z. Guo, I. P. Parkin and F. Li, *Nat. Energy*, 2020, **5**, 160–168.

24 W. Lai, D. Xu, X. Wang, Z. Wang, Y. Liu, X. Zhang, Y. Li and X. Liu, *Phys. Chem. Chem. Phys.*, 2017, **19**, 24076–24081.

25 U. Rajeena, P. Raveendran and R. M. Ramakrishnan, *J. Fluorine Chem.*, 2020, **235**, 109555.

26 W. A. Yarbrough, *J. Am. Ceram. Soc.*, 1992, **75**, 3179–3200.

27 Z.-J. Liu, S.-J. Ding, P.-F. Wang, D. W. Zhang, J.-Y. Zhang, J.-T. Wang and K. Kohse-Hoinghaus, *Thin Solid Films*, 2000, **368**, 208–210.

28 I. Schmidt and C. Benndorf, *Diamond Relat. Mater.*, 1997, **6**, 964–969.

29 J. Robertson, *Mater. Sci. Eng., R*, 2002, **37**, 129–281.

30 V. Pischedda, S. Radescu, M. Dubois, N. Batisse, F. Balima, C. Cavallari and L. Cardenas, *Carbon*, 2017, **114**, 690–699.

31 H. Touhara, K. Kadono, Y. Fujii and N. Watanabe, *Z. Anorg. Allg. Chem.*, 1987, **544**, 7–20.

32 P. V. Bakharev, M. Huang, M. Saxena, S. W. Lee, S. H. Joo, S. O. Park, J. Dong, D. C. Camacho-Mojica, S. Jin, Y. Kwon, M. Biswal, F. Ding, S. K. Kwak, Z. Lee and R. S. Ruoff, *Nat. Nanotechnol.*, 2020, **15**, 59–66.

33 J. Sivek, O. Leenaerts, B. Partoens and F. M. Peeters, *J. Phys. Chem. C*, 2012, **116**, 19240–19245.

34 F. Karlický, R. D. Kumara, M. Otyepka and R. Zbořil, *ACS Nano*, 2013, **7**, 6434–6464.

35 M. Medveď, G. Zoppellaro, J. Ugolotti, D. Matochová, P. Lazar, T. Pospíšil, A. Bakandritsos, J. Tuček, R. Zbořil and M. Otyepka, *Nanoscale*, 2018, **10**, 4696–4707.

36 D. Zaoralová, V. Hrubý, V. Šedajová, R. Mach, V. Kupka, J. Ugolotti, A. Bakandritsos, M. Medved and M. Otyepka, *ACS Sustainable Chem. Eng.*, 2020, **8**, 4764–4772.

37 G. Zoppellaro, A. Bakandritsos, J. Tuček, P. Błoński, T. Susi, P. Lazar, Z. Bad'ura, T. Steklý, A. Opletalová, M. Otyepka and R. Zbořil, *Adv. Mater.*, 2019, **31**, 1902587.

38 Y. Liu, Y. Shen, L. Sun, J. Li, C. Liu, W. Ren, F. Li, L. Gao, J. Chen, F. Liu, Y. Sun, N. Tang, H.-M. Cheng and Y. Du, *Nat. Commun.*, 2016, **7**, 1–9.

39 A. S. Mazur, M. A. Vovk and P. M. Tolstoy, *Fullerenes, Nanotubes, Carbon Nanostruct.*, 2020, **28**, 202–213.

40 R. L. Johnson, J. M. Anderson, B. H. Shanks and K. Schmidt-Rohr, *Chem. Mater.*, 2014, **26**, 5523–5532.

41 J. Giraudet, M. Dubois, A. Hamwi, W. E. E. Stone, P. Pirotte and F. Masin, *J. Phys. Chem. B*, 2005, **109**, 175–181.

42 S. Stankovich, D. A. Dikin, R. D. Piner, K. A. Kohlhaas, A. Kleinhammes, Y. Jia, Y. Wu, S. T. Nguyen and R. S. Ruoff, *Carbon*, 2007, **45**, 1558–1565.

43 W. Gao, L. B. Alemany, L. Ci and P. M. Ajayan, *Nat. Chem.*, 2009, **1**, 403–408.

44 D. W. Mayo, in *Course Notes on the Interpretation of Infrared and Raman Spectra*, eds. D. W. yo, F. A. Miller and R. W. Hannah, John Wiley & Sons, Inc., 2004, pp. 101–140.

45 J. Senthilnathan, C.-C. Weng, J.-D. Liao and M. Yoshimura, *Sci. Rep.*, 2013, **3**, srep02414.

46 A. Bakandritsos, R. G. Kadam, P. Kumar, G. Zoppellaro, M. Medved', J. Tuček, T. Montini, O. Tomanec, P. Andrýsková, B. Drahoš, R. S. Varma, M. Otyepka, M. B. Gawande, P. Fornasiero and R. Zbořil, *Adv. Mater.*, 2019, **31**, 1900323.

47 P. Lazar, R. Mach and M. Otyepka, *J. Phys. Chem. C*, 2019, **123**, 10695–10702.

48 X. Wu, H. Zhao, J. Pei and D. Yan, *Appl. Phys. Lett.*, 2017, **110**, 133102.

49 D. Hulicova-Jurcakova, M. Seredych, G. Q. Lu and T. J. Bandosz, *Adv. Funct. Mater.*, 2009, **19**, 438–447.

50 L. Weinstein and R. Dash, *Mater. Today*, 2013, **16**, 356–357.

51 Y. Yoon, K. Lee, S. Kwon, S. Seo, H. Yoo, S. Kim, Y. Shin, Y. Park, D. Kim, J.-Y. Choi and H. Lee, *ACS Nano*, 2014, **8**, 4580–4590.

52 J. Wang, J. Tang, B. Ding, V. Malgras, Z. Chang, X. Hao, Y. Wang, H. Dou, X. Zhang and Y. Yamauchi, *Nat. Commun.*, 2017, **8**, 15717.

53 M. D. Stoller and R. S. Ruoff, *Energy Environ. Sci.*, 2010, **3**, 1294–1301.

54 S. Zhang and N. Pan, *Adv. Energy Mater.*, 2015, **5**, 1401401.

55 A. Noori, M. F. El-Kady, M. S. Rahmanifar, R. B. Kaner and M. F. Mousavi, *Chem. Soc. Rev.*, 2019, **48**, 1272–1341.

56 R. Weber, M. Genovese, A. J. Louli, S. Hames, C. Martin, I. G. Hill and J. R. Dahn, *Nat. Energy*, 2019, **4**, 683–689.

57 X. Lin, M. Salari, L. M. R. Arava, P. M. Ajayan and M. W. Grinstaff, *Chem. Soc. Rev.*, 2016, **45**, 5848–5887.

58 L. Timperman, H. Galiano, D. Lemordant and M. Anouti, *Electrochem. Commun.*, 2011, **13**, 1112–1115.

59 J. Alvarado, M. A. Schroeder, M. Zhang, O. Borodin, E. Gobrogge, M. Olguin, M. S. Ding, M. Gobet, S. Greenbaum, Y. S. Meng and K. Xu, *Mater. Today*, 2018, **21**, 341–353.

748 | *Energy Environ. Sci.*, 2022, **15**, 740–748

This journal is © The Royal Society of Chemistry 2022

235